THE UNIVERSITY *of* EDINBURGH

Hypervalent Iodine(III) Oxidants in Gold Catalysis

THE UNIVERSITY *of* EDINBURGH

Magdalene Teh

Doctor of Philosophy

University of Edinburgh

2019

Declaration

I declare that the work in this thesis was carried by me under the supervision of Prof. Guy Lloyd-Jones FRS and is in accordance with the requirements of the University of Edinburgh. This work is original, except where indicated by special reference in the text, and no part of the dissertation has been previously submitted for any other academic award.

Signed …….

Date 18/02/2020

Abstract

Hypervalent iodine oxidants have been used extensively in oxidative metal catalysis, especially in gold catalysis, where the redox potential of gold(I) to gold(III) is large. The reoxidation of gold(I) within an intramolecular gold-catalysed direct arylation reaction developed previously in the group occurs after the turnover-limiting step, and so cannot be studied by analysing the reaction rates. Competition reactions between $ArI^{III}(OR)_2$ oxidants with different electronic parameters have been carried out to gain further understanding into the reoxidation of gold(I) under the following reaction conditions.

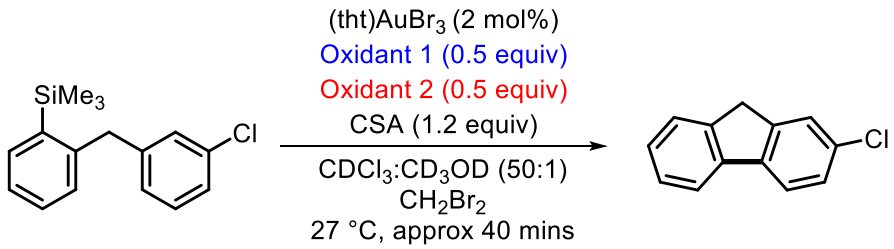

Scheme 1: Summary of oxidant competition carried out under a gold(III)-catalysed direct arylation reaction of an intramolecular substrate.

It was found that the more electron-rich oxidant has a higher relative rate compared to electron-poor oxidants and log k_{rel} gave the best correlation with σ^+ of the para-substituent. This suggests that the oxidant undergoes an initial ligand dissociation step to give an iodonium species before the gold is oxidised, as opposed to forming a π-complex with the gold(I) intermediate.

Contrary to this result, the relative redox potential of these oxidants, calculated by looking at the equilibrium position between an iodine(III) oxidant and an aryl iodide showed that the more electron-deficient oxidant has a higher redox potential, and is therefore the more oxidising oxidant when compared to electron-rich oxidants. This trend has also been illustrated by looking at the electrochemical reduction of the oxidants using square-wave voltammetry.

In an attempt to obtain a system where the absolute rates of oxidation of gold(I) can be obtained, a new experimental setup was utilised. Injection of an oxidant into the reaction mixture within the NMR spectrometer allowed for the monitoring of the oxidation product with very small dead time, and the oxidation of gold(I) generated in the reaction can be monitored.

In addition to this, the oxidation of $(Ph_3P)Au(Cl)$ as a gold(I) example was studied. At low amounts of free CSA, an induction period was observed, and was significantly lengthened by the presence of stoichiometric amount of Cl^-. A tentative mechanism has been proposed, where key observations are described.

Lay Summary

A major goal in chemical synthesis is the ability to transform a molecule completely into a different compound with no by-products or waste. Without the formation of by-products, issues such as separation of the desired products and disposal of the waste products are non-existent. One way of describing the efficiency of a reaction in converting all the atoms in the starting material into product is to use atom economy. Atom economy is expressed as a percentage of the molecular weight of the desired product over the molecular weight of all the reactants used.

One method of improving atom economy is to use catalytic amounts instead of equal (stoichiometric) amount of reagents to aid a reaction. This means that only a small quantity of reagents, relative to the starting material, is required. Furthermore, a catalyst is not consumed in a reaction, and so, the recovery of the catalyst is plausible.

Cross-coupling reactions are typically reactions where two preactivated starting materials are reacted to give a product in a presence of a catalyst. These types of reactions, catalysed by palladium, were awarded the Nobel Prize in Chemistry in 2010. In forming the product, the activating groups on the starting material are not incorporated in the product and are lost as by-products. Furthermore, preactivated starting materials are not typically commercially available, and have to be made. This introduces more steps into the synthesis, generating more waste from the reaction and purification steps.

Strategies to obtain these coupling products where one or both starting materials do not require preactivation have been developed. However, issues such as selectively forming a cross-coupled product (as opposed to a homocoupled product, where two of the same starting material have reacted) or forming a bond in a specific site between the two coupling partners have proven challenging.

This thesis looks at a gold-catalysed reaction where one starting material has been preactivated. Previous work looking into the mechanism of this reaction have led to:

- The development of an improved precatalyst, with shorter reaction times.
- A good understanding of the basis of selectivity for a cross-coupled product.
- The identification of an inhibitor species present in the reaction.
- The prediction of the site of reactivity on the unactivated starting material.

However, a major disadvantage of this reaction was that a stoichiometric amount of reagent, known as the oxidant, was required to regenerate the catalyst during the reaction. This produced a lot of waste and has been a problem during the separation process from the desired product. Other oxidants which have been shown to work in similar reactions result in no product forming, or a much lower yield of product formation.

Thus, the focus of this thesis has been to understand the role of this reagent and how it reacts to regenerate the catalyst and subsequently, explore the possibility of replacing these oxidants to give a reaction with better atom economy. The research has shown that when two variants of this oxidant was used and competed against one another, the stronger oxidant was consumed at a slower rate. This has led to an insight into the requirements of the reagent, where the oxidant was proposed to change its form prior to reacting with the gold.

A more robust experimental setup was explored to gain absolute rates of reactions. This meant that the oxidants competed cannot interact with each other to affect their rate of consumption. In order to carry this out, the equipment used to study these reactions had to be modified so that the time between the start of the reaction and the point where observation of the reaction can begin was shortened, since the reaction studied was expected to be very quick (< 10 seconds). The results from these studies suggest that the gold complex, prior to reactivation, forms an inactive complex outside the catalytic cycle of reaction.

Another study was carried out between the reaction of the oxidant and a different gold complex. This gold complex was previously found to be active in catalysing the above coupling reaction, but had a significant induction period, where the catalyst was being activated. Reacting the gold complex and the oxidant have shown that one of the ligands bonded to the catalyst had to be released before the active catalyst was produced. In this thesis, it was found that a large variety of processes were occurring in order to activate the catalyst, and the use of chloride in the reaction resulted in a separate pathway of reaction.

Acknowledgements

Firstly, I would like to thank Professor Guy Lloyd-Jones for his advice, useful discussions, and extreme patience with me throughout this work. His knowledge and insight into this work have been vital in carrying out this project, and I am grateful for the opportunity to learn from him and his group.

I would also like to acknowledge all past and present members of the GLJ group for their support, advice, and fun times in the last few years. Special thanks go to Dr Ruth Dooley, Dr Eric Keske, Dr Katherine Geogheghan, Dr Alba Collado Martinez, and Dr Jorge González González for all the assistance and knowledge you have given me, including taking the time to read through and give your advice on this thesis from afar.

I would like to thank the people who have kept the department running. In particular, Juraj Bella and Dr Lorna Murray for the NMR facility, Dr Logan Mackay for the mass spectrometry facilities and assistance in setting up the group HPLC, Stuart Johnstone for saving my broken and very expensive Shigemi tube, David Paden and Ted King for assistance in constructing the rapid injection device, Archie Whatley and Dr Steve Hearn for my Dynochem® querries, and Tim Calder, Mark Forrest, and Simon Cummings for the smooth running of stores and waste disposal. I am also very appreciative of the funding received from the ERC.

Finally, I would like to thank my family and Jamie Wilson, my “friend from Leeds”. Your patience, love, and support has kept me going these last few years, and I could not be more excited to marry you.

Contents

Declaration iii

Abstract iv

Lay Summary vi

Acknowledgements viii

Abbreviations xiii

1. Introduction 1

1.1. Gold 2

1.1.1. A brief history 2

1.1.2. Physical properties of gold 2

1.2. Gold complexes 4

1.2.1. Gold(I) 4

1.2.2. Gold(III) 4

1.3. Homogeneous gold catalysis 5

1.4. Activation of C-H bonds 7

1.4.1. Gold(III) complexes 7

1.4.2. Gold(I) complexes 7

1.5. Oxidative gold catalysis 8

1.5.1. Activated coupling partners 13

2. Hypervalent aryliodine(III) oxidants 19

2.1. Hypervalent Iodine(III) Oxidants 20

2.1.1. Overview 20

2.1.2. Ligand exchange 21

2.1.3. Electrochemistry studies 22

2.2. Aims of the chapter 28

2.3. Oxidant equilibration 28

2.3.1. Control reactions 28

2.3.2. Oxidant potentials 32
2.4. Electrochemical Studies 36
2.4.1. Method 36
2.5. Conclusion 39
3. Relative rates of oxidation 41
3.1 Gold(I) oxidation 42
3.1.1. Oxidation of $(Ph_3P)Au(Me)$ 42
3.1.2. Oxidation of *bis*(NHC)-Au(I) complexes 43
3.2 Aims of the chapter 44
3.3 Competition of aryl oxidants 45
3.3.1. Method 47
3.3.2. Reaction profile 48
3.3.3. Relative rates 50
3.3.4. Results 54
3.4. Competition of alkyl oxidants 58
3.4.1. Synthesis 58
3.4.2. Equilibration and competition 59
3.4.3. Validation of method 62
3.5. Proposed mechanism 62
3.6. Conclusions 63
4. Absolute rates of oxidation 65
4.1. Introduction 66
4.2. Preliminary results 66
4.2.1. Monitoring resting state 66
4.2.2. Reoxidation of Gold(I) 72
4.3. Aims of the chapter 75
4.4. Monitoring fast reactions 76
4.4.1. UV-vis spectrometry 77

4.4.2. Rapid injection 78
4.. Conclusion 101
5. Oxidation of phosphine-gold(I) chloride 103
5.1. Introduction 104
5.1.1. Oxidation of $(Ph_3P)Au(OTs)$ 104
5.1.2. Oxidation of $(C_6F_5)Au(PPh_3)$ 105
5.2. Aims of the chapter 107
5.3. Results 108
5.3.1. Changing the nature of oxidant 108
5.3.2. Stoichiometric amount of oxidant 109
5.3.3. Effect of CSA 114
5.3.4. Addition of HCl 119
5.3.5. Addition of chloride 122
5.3.6. Proposed pathway in the presence of free chloride 124
5.4. Conclusion 129
5.4.1. Proposed reaction 130
6. Conclusion and future work 133
7. Experimental 139
7.1. General experimental details 140
7.1.1. Techniques 140
7.1.2. Reagents and solvents 140
7.1.3. Analysis 141
7.2. Synthetic procedures 142
7.3. Procedures and data relevant to Chapter 2 142
7.3.1. Control reactions 142
7.3.2. Reaction monitoring 143
7.3.2. Catalyst screen 144
7.3.3. Reaction of $PhI(OAc)_2$ with *m*-OMeArI (Scheme 25) 144

7.3.4. Oxidant potentials 145
7.3.5. Electrochemistry procedures 147
7.4. Procedures and data relevant to Chapter 3 148
7.4.1. General procedure for competition reactions 148
7.4.2. Procedures relating to the data in Table 6 149
7.4.3. Procedure relating to Figure 31 150
7.5. Procedures and data relevant to Chapter 4 151
7.5.1. Monitoring the resting state 151
7.5.2. Reaction shown in Figure 37 152
7.5.3. Reoxidation of gold 152
7.5.4. Setup 1.0 153
7.5.5. Setup 1.1 155
7.5.6. Setup 2.0 156
7.6. Procedures and data relevant to Chapter 5 159
7.6.1. General considerations 159
7.6.2. Oxidation of $(Ph_3P)Au(X)$ 159
7.6.2. Oxidation of $(Ph_3P)Au(Cl)$ with $ArI(OAc)_2$ 160
7.6.3. Stoichiometric amounts of oxidant 160
7.6.4. Effect of product addition 161
7.6.4. Addition of more starting complex (Figure 71) 161
7.6.5. Changing [CSA] 162
7.6.6. Using HCIB as oxidant 163
7.6.7. Premixing CSA and $(Ph_3P)Au(Cl)$ (Figure 75) 163
7.6.8. Addition of HCl 164
7.6.9. Addition of Bu_4NCl 165
7.6.10. Reaction of $(Ph_3P)Au(Cl)_3$ with $PhI(X)_2$ 165
7.6.11. Effect of $(Ph_3P)Au(Cl)_3$ addition 166
7. References 167

Abbreviations

1,2-DCE	1,2-dichloroethane
Ac	Acetyl
AcOH	Acetic acid
Ar	Aryl
Bn	Benzyl
Bu	Butyl
CSA	Camphorsulfonic acid
CV	Cyclic voltammerty
Cy	Cyclohexyl
DCM	Dichloromethane
DFT	Density functional theory
DMAP	4-Dimethylaminopyridine
EDG	Electron-donating group
Equiv.	Equivalents
EWG	Electron-withdrawing group
Fc	Ferrocene
HCIB	[Hydroxy(camphorsulfonyloxy)iodo]benzene
HRMS	High resolution mass spectrometry
IBDA	Iodobenzene diacetate
IPr	1,3-bis(2,6-diisopropylphenyl)-1,3-dihydro-2H-imidazol-2-ylidene
k	Rate constant
L	Neutral ligand
M	Molar
Me	Methyl
MHz	Megahertz
mM	Millimolar
mmol	Millimole
mol%	Mole percent

NBS	*N*-bromosuccinimide
NHC	*N*-heterocyclic carbene
nm	Nanometer
NMR	Nuclear magnetic resonance
Nu, Nu−	Nucleophile
Ph	Phenyl
ppm	Parts per millioin
R	Alkyl, aryl or heteroatomic substituent
Rt	Room temperautre
SCE	Saturated calomel electrode
SM	Starting material
SWV	Square-wave voltammetry
TFA	Trifluoroacetic acid
THF	Tetrahydrofuran
tht	Tetrahydrothiophene
TLC	Thin-layer chromatography
TLS	Turnover-limiting step
TM	Transition metal
UV	Ultraviolet
X	Halogen substituent, or anionic ligand
μL	microlitre
ρ	Hammett reaction constant
σ	Hammett substituent constant

Chapter 1

Introduction

1.1. Gold

1.1.1. A brief history

Gold, from the Anglo-Saxon word, *geolo* (yellow) is a naturally-occurring element that lies in the transition-metal block of the periodic table. It has the symbol Au, which comes from the Latin name *aurum*, meaning "glowing dawn". It is commonly found in its native state, and typically found alloyed with silver to give electrum.[1]

It is estimated that approximately 190 000 tonnes of gold has been mined,[2] and in 2018, China was the largest producer of gold, mining approximately 400 tonnes of gold and accounting for 12% of the total global gold production.[3]

The chemical inertness of gold, where it is resistant to oxidation and corrosion, as well as its malleability and ductility have made it extremely useful in the electronics and aerospace industry. In addition to this, it's metallic lustre and unique colour have meant that historically, gold has been held at high value as ornaments and jewellery. Even now, gold jewellery is still highly sought after, with over half of the gold produced in 2017 used in the jewellery industry.[4]

1.1.2. Physical properties of gold

Gold has the electron configuration [Xe] $4f^{14}5d^{10}6s^{1}$ and is located in the same group as copper and silver. As it has the largest atomic number of the three, it is expected to have a larger atomic radius as well as lower electronegativity due to increased distance between the valence orbitals and a resulting lower attraction to the positively charged nucleus. However, the opposite is observed, where gold was found to be the most electronegative transition metal,[5] and its radius was found to be comparable to the radius of silver atoms.[6] Table 1 compares the metallic radius[6] and the Pauling electronegativity[7] values of the elements in the same group as gold.

Table 1: Physical properties of elements in the same group as gold.

	Metallic radius / nm	Pauling electronegativity
Cu	0.128	1.90
Ag	0.144	1.93
Au	0.144	2.54

These observations were a result of the lanthanide contraction, where poor shielding from electrons in the 4*f* orbitals coupled with an increase of nuclear charge led to an increase in effective nuclear charge experienced by the electrons in the valence orbitals of gold. The electronegativity of gold has meant that it does not react with other electronegative elements (such as oxygen), has a high redox potential (Au^{I}/Au^{0} = 1.83 V, compared to Pt^{II}/Pt^{0} = 1.19 V, under standard conditions),[8] and the auride anion, Au^{-}, is known and stable.[9]

This has meant that only relatively recently, gold complexes have been utilised in homogeneous catalysis, dominated mostly by gold(I) and gold(III) complexes. As pointed out by Bochmann et al., "the formation of purple gold nanoparticles during the course of unsuccessful reactions is only too familiar",[8] indicating that gold in these oxidation states can be unstable, and reduce down (or disproportionate) to gold(0) and gold(III).

Figure 1 shows the number of publications per year since 1965 that matched the search term "homogeneous", "gold", and catalys*. The wildcard (*) was used to obtain results relating to catalysis as well as catalyst reported. It is only from 2004 onwards that the interest in this field has taken off, with multiple reviews published,[10–19] and it has also been recognised as an important tool in synthesis, with two reviews written on the use of gold in total synthesis.[20,21]

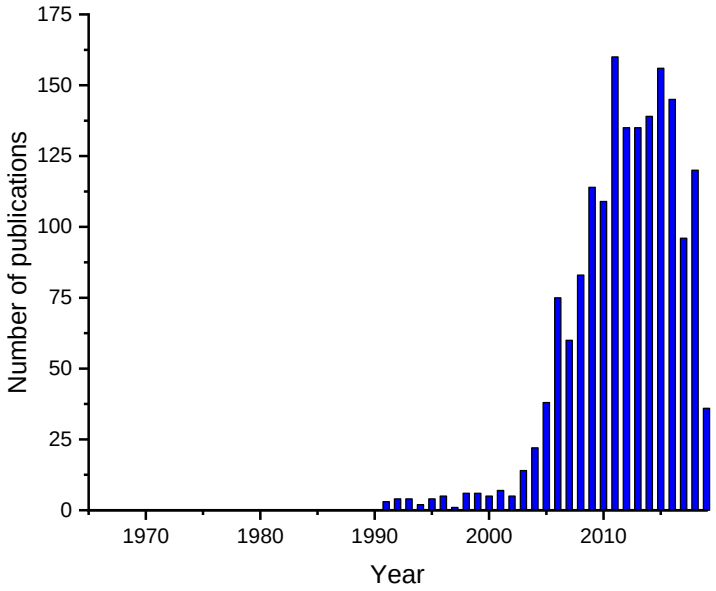

Figure 1: Number of publications per year when the search term "homogeneous", "gold", and catalys* was used in the Web of Science, carried out on the 18th of June 2019.

1.2. Gold complexes

1.2.1. Gold(I)

Gold in the +1 oxidation state has the electron configuration [Xe] $4f^{14}5d^{10}6s^{0}$, and is not considered a transition metal, as its *d*-orbitals are full. This means that bonding with ligands occurs through the s-orbital, which gives rise to two-coordinate, linear complexes with one neutral ligand (typically phosphines or organosulfur) and one anionic ligand ($LAu^{I}X$). Since it has a full shell in the *d*-orbitals, these compounds are found as white solids.Some of the more common, commercially available gold(I) complexes are illustrated in Figure 2.

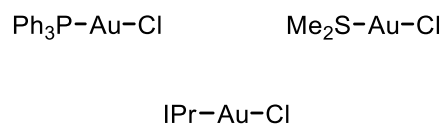

Figure 2: Commercially available gold(I) complexes found on Sigma-Aldrich's website. Search was carried out on the 18th of June 2019.

1.2.2. Gold(III)

In contrast to gold(I) complexes, organogold complexes in the +3 oxidation state are not as common. This is due to a high oxidation potential (Au^{III}/Au^{0} = 1.36 V under standard conditions) and a strong oxidant is typically required to oxidise gold(I) complexes to gold(III) complexes. Gold(III) is a transition metal, and has the electron configuration [Xe] $4f^{14}5d^{8}$. Gold(III) complexes typically have a coordination number of 4 and a square-planar geometry. Figure 3 shows some common gold(III) complexes used as catalyst in reactions. Since these compounds tend to be not very soluble in organic solvents, gold(III) catalysis is typically carried out with the addition of a gold(I) complex and a stoichiometric amount of oxidant.[22]

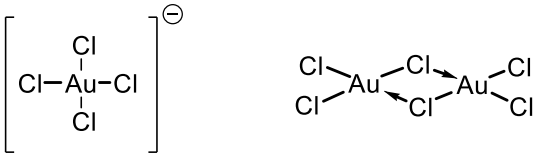

Figure 3: Commonly used gold(III) complexes as precursors to other complexes or catalysts.

1.3. Homogeneous gold catalysis

The first reported homogenous gold catalysed reaction was the asymmetric aldol reaction between aldehydes and isocyanoacetates in 1986.[23] The reaction used a gold(I) catalyst and a chiral ferrocenylphosphine ligand with an amine group The transition state proposed in the reaction involved σ-activation of both the electrophilic and nucleophilic species by the gold(I) catalyst. Using both copper and silver catalysts gave poorer enantioselectivity, and this rationalised to be because gold(I) has a higher affinity to the phosphorus atom on the ligand compared to copper and silver.

The next milestone in the development of homogenous gold catalysis was achieved by Hashmi et al. in 2000, where they employed a gold(III) catalyst for the formation of C-C and C-O bonds.[24]

Allenyl ketones, **A1**, in the presence of a gold(III) catalyst was found to cyclise to give a furan, **A4**, alongside **A3** as a side product from the reaction of **A4** with the starting material, **A1** (Scheme 2). In contrast, the use of a palladium(II) catalyst gave **A2**, the regioisomer of compound **A3**, and comparison of the different catalysts highlighted the high activity of the gold catalyst. 1 mol% of $AuCl_3$ required only one minute at 20 °C for full conversion of the starting material, whereas 1 mol% of $Pd(Cl)_2(MeCN)_2$ had a reaction time of about an hour. Reducing the loading of the gold catalyst to 0.1 mol% still gave complete consumption of **A1**. When **A3** and **A4** were left together in the presence of $AuCl_3$, further reactivity was observed to give compound **A5**, which is a trimer of compound **A1**. This suggested that the reaction of **A4** with other Michael acceptors to form a new C-C bond were possible, something that did not work when using a Pd catalyst. Thus the possibility of developing new C-C bond forming reactions using gold catalysis was realised.

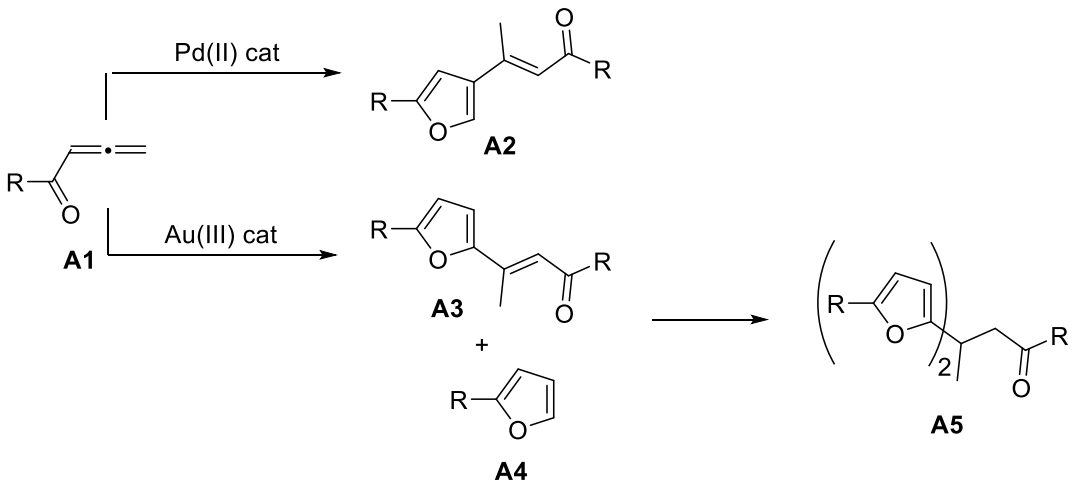

Scheme 2: Difference in regioselectivity between a palladium(II) and gold(III) catalysed reaction. Additional C-C bond formed in the presence of the gold(III) catalyst.

In attempting to extend the scope for the synthesis of the furan shown above, Hashmi et al. discovered that by subjecting a mixture of **A6** and **A7** with $AuCl_3$ (2 mol%) in acetonitrile, the expected furan (**A8**), as well as a phenol product (**A9**) was obtained (Scheme 3).[25] Further experiments carried out with **A8** in $AuCl_3$ showed transformation to the phenol product **A9** at room temperature and without exclusion of air or water.

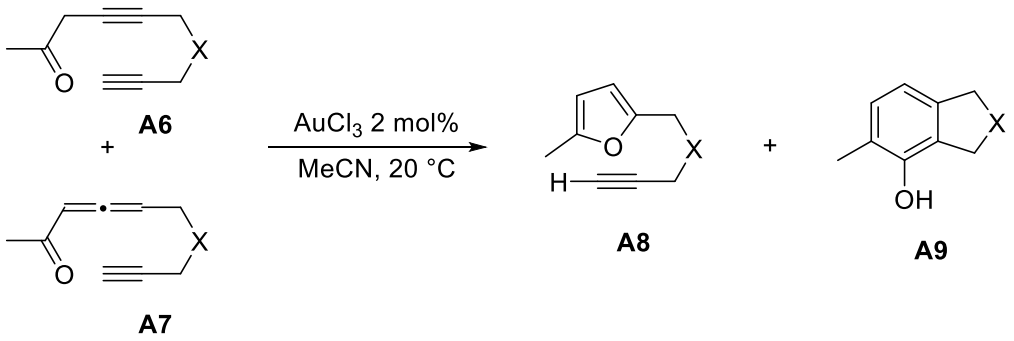

Scheme 3: Gold-catalysed synthesis of phenols.

Less than 1% of ^{18}O incorporation was observed when the reaction was carried out with $H_2{}^{18}O$. This was consistent with the proposal that the reaction proceeded via an intramolecular oxygen transfer with an epoxide intermediate **A10**, as illustrated in Scheme 4. A screening of a few late transition metal complexes found that the reaction proceeded with other d^8 metal complexes including palladium(II) and rhodium(I) and not by metal complexes in other oxidation states such as palladium(0) and rhodium(III), supporting a gold(III) catalysed reaction. Furthermore, $AuCl_3$ was the most active catalyst in the screen, which showed promise for the field of gold catalysis.

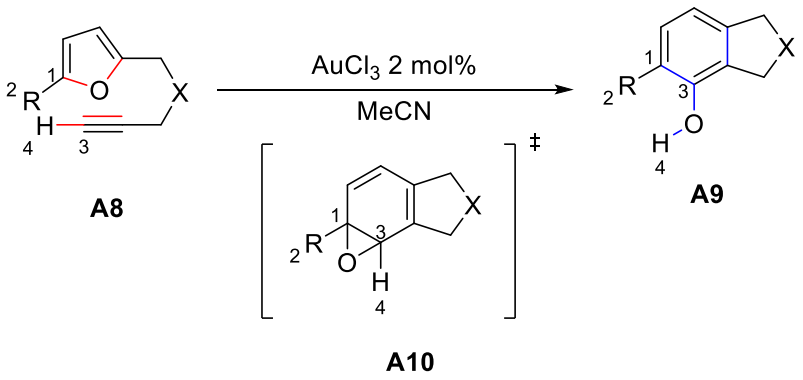

Scheme 4: Intermediate proposed in the gold-catalysed synthesis of phenol.

1.4. Activation of C-H bonds

1.4.1. Gold(III) complexes

The first reported activation of C-H bonds by gold(III) complexes was in 1931. Karasch and Isbell[26] found that reaction of anhydrous auric chloride and benzene gave off hydrogen chloride along with 1,2,4,5-tetrachlorobenzene and gold(I) chloride (Scheme 5). Quenching the reaction after a few minutes with Et_2O allowed for the isolation of an intermediate in the reaction, and this was identified as phenyl auric dichloride **A12**. It was proposed that the activation of C-H bond is by an electrophilic aromatic substitution step to give the phenylgold(III) complex.

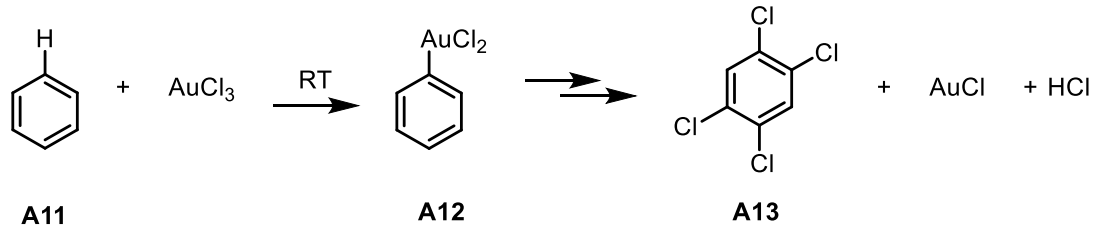

Scheme 5: First reported activation of C-H bonds using gold(III) complexes.

1.4.2. Gold(I) complexes

In contrast to gold(III), it was only recently, in 2010, that gold(I) complexes were shown to activate C-H bonds in electron deficient arenes (Scheme 6).[27] Exploiting the π-acidity of gold(I) complexes, it was proposed that π-complexation followed by σ-bond metathesis routes can be utilised to activate the C-H bond in the arene and form an aryl-gold(I) species.

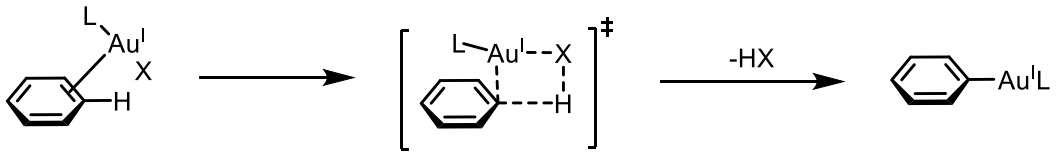

Scheme 6: Activation of C-H bond with gold(I) complexes.

The substitution pattern seen in a range of arenes tested were consistent with activation of the most electron-deficient C-H bond. C-H activation starts to become a challenge when more electron-rich arenes are utilised and no reaction was seen with *p*-fluoroanisole.

The reaction proceeded best with strong donor ligands on the gold, which corresponds to the more stable π-complex formed between the gold and the arene at the start of the activation process.

1.5. Oxidative gold catalysis

One of the reasons gold has only recently become popular as a catalyst is due to its high redox potential. Typical cross-coupling reactions in late transition-metal catalysis involve oxidative addition of the metal complex by the substrate/reagent. Since the oxidation of gold(I) complexes are difficult, gold-catalysed cross-coupling reactions have been less reported.

One of the first few reported use of gold as an oxidative catalyst is by Periana et al.[28] in 2004, where methane was oxidised to methanol, using a selenium(VI) compound as the stoichiometric oxidant. This is summarised in Scheme 7. The gold catalyst activates the C-H bond in methane under acidic conditions, although it is unclear which oxidation state, gold(I) or gold(III), the catalyst is in. DFT calculations carried out on the system showed that both oxidation states are capable of activating the C-H bond and although the pathway via the gold(I) species is more favourable, the concentration of gold(I) complex compared to gold(III) complex is quite low in the presence of excess selenium(VI) oxidants.

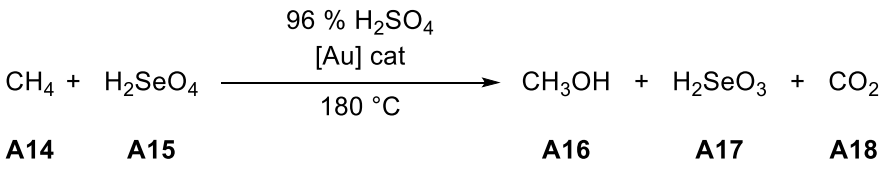

Scheme 7: Oxidative gold catalysis of methane to methanol.

Evidence was obtained, showing the reductive elimination of gold(III) to gold(I) whilst forming a C-C bond was possible as an elementary step in oxidative gold catalysis.[29] It was reported that substituted allenyl carbinols **A19**, in the presence of a gold catalyst can cyclise to form dihydrofurans **A21** (Scheme 8). One of the side products obtained includes a dimerisation of the dihydrofuran compounds, **A23**. It was proposed that the cyclised gold intermediate **A20** can react with itself in a ligand exchange reaction to give compound **A22**, which can then reductively eliminate to form the homocoupled dimer **A23**. In the absence of an external oxidant, the yield of the dimer was found to be less than twice the percentage of the catalyst loading. Increasing the catalyst loading increased this yield.

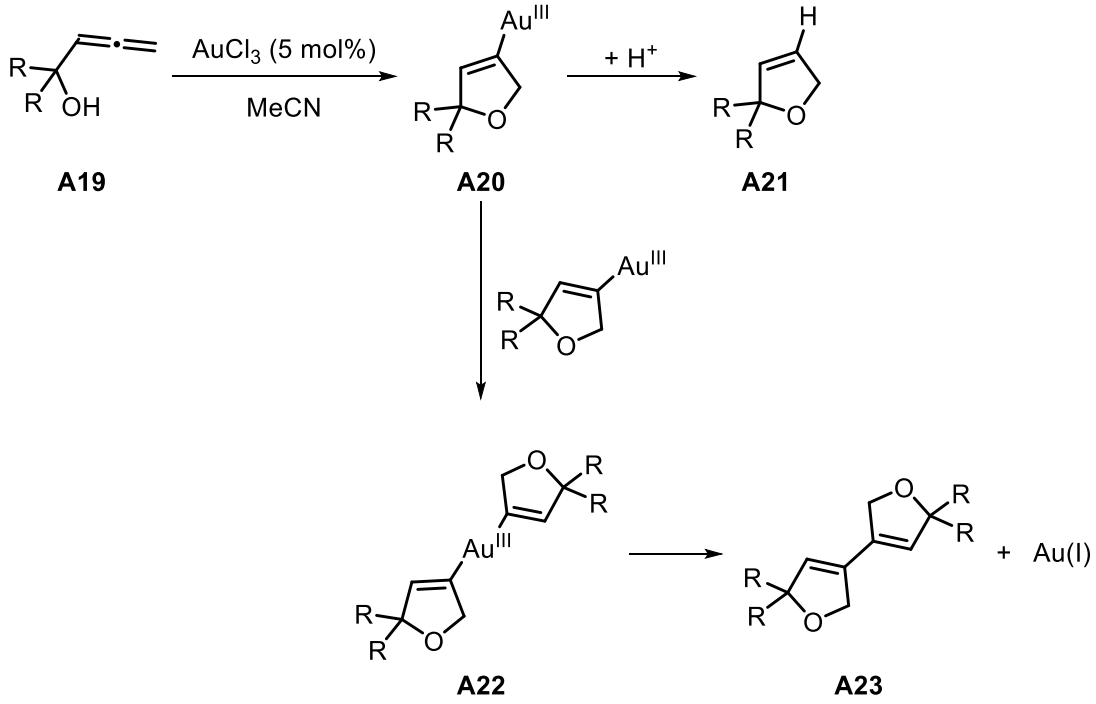

Scheme 8: Gold(III) to gold(I) reduction pathway with the formation of a new C-C bond.

The next advancement from this is to use gold catalytically to form new C-C bonds in biaryls. Using a similar strategy to the oxidation of methane to methanol, a stoichiometric oxidant can be used to reoxidise gold(I) into gold(III). Focusing on forming C-C bonds, Tse et al. developed a gold-catalysed homodimerisation reaction of simple arenes.[30] It was found that p-xylene, **A24,** could dimerise to form the biphenyl **A25** in the presence of 2 mol% of a gold catalyst with a stoichiometric amount of $PhI(OAc)_2$ as the oxidant (Scheme 9)

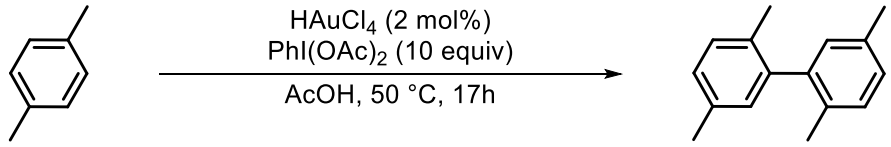

A24 **A25**

Scheme 9: Gold(III) catalysed oxidative homocoupling of p-xylene.

The method was then extended to heterocoupling of halogenated anisoles with benzene (Scheme 10).[31] However, using a 1:1 ratio of halo-anisole to benzene gave a significant amount of biphenyl product **A29**, obtained from the homocoupling of benzene. Tuning the ratio of arene, so that there was an excess of anisole to benzene (15:6), the yield of the heterocoupled product could be increased to 46%. Unfortunately, about 22% of **A29**, the homocoupled product, was still observed.

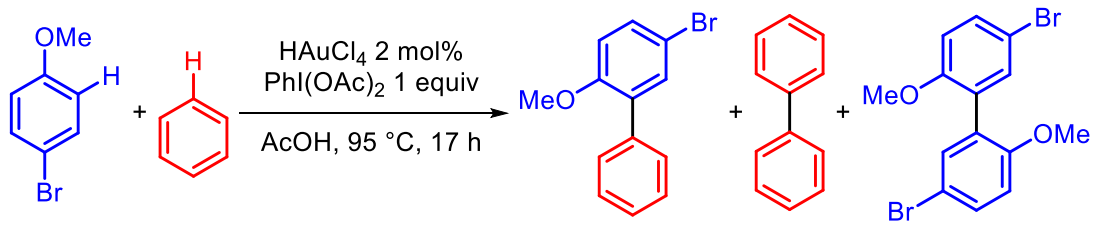

A26 **A27** **A28** **A29** **A30**

Scheme 10: Gold(III) catalysed cross-coupling of bromoanisole and benzene, with a significant amount of homocoupled side product formed

Since the main issue with the reaction is the homocoupling of benzene, rather than the homocoupling of the halo-anisole, it was proposed that the mechanism proceeded via the activation of benzene first. The intermediate formed can then choose to either react with benzene or the halo-anisole to give biphenyl or the desired cross-coupled product.

Using an excess of one of the arenes is not ideal, especially if the material is precious. One method in generating a cross-coupled product is demonstrated by Larrosa et al. in 2013.[32] The difference in selectivities of gold(I) and gold(III) in activating C-H bonds was exploited. Gold(I) complexes can activate the most acidic C-H bonds in arenes with electron withdrawing groups. Conversely, gold(III) complexes tend to activate electron-rich arenes via an S_EAr mechanism.

It was hypothesised that by utilising the change in selectivity between the two oxidation states of gold, a double oxidative C-H coupling can proceed to give cross-coupled products of two

electronically different arenes. A general scheme of the reaction proposed is shown in Scheme 11.

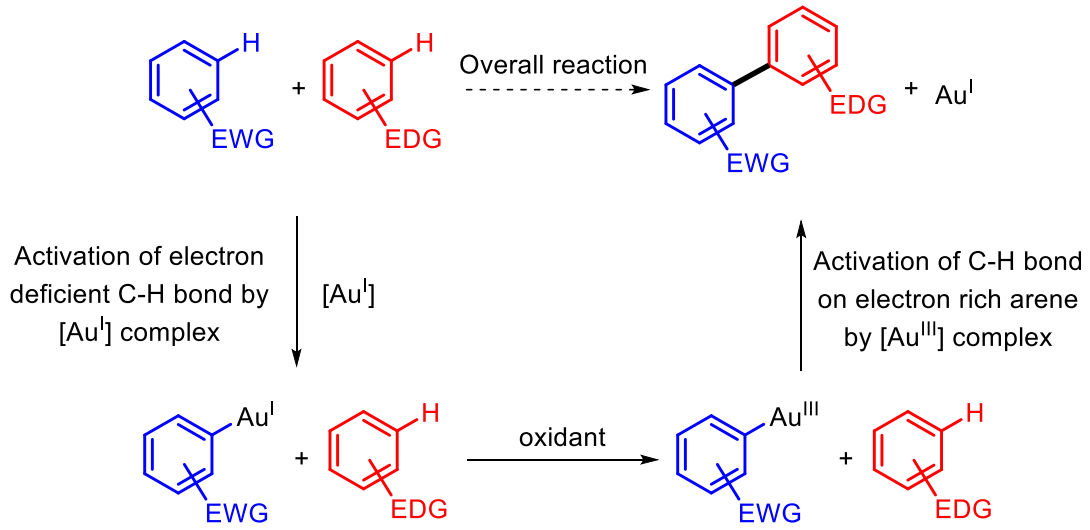

Scheme 11: Proposed strategy in the selective formation of unsymmetrical biaryls.

Firstly, the EWG arene is activated by the gold(I) complex. Following an oxidation of the corresponding aryl-gold(I) to aryl-gold(III) complex, the C-H bond in the EDG arene can be activated. Reductive elimination from the resulting gold(III) complex leads to the desired cross-coupled product and regenerates the gold(I) complex.

The reaction between the aryl-gold(I) complex, an arene and the oxidant was optimised (Scheme 12), and the scope of reaction was tested. It was found that the reaction proceeded to give the cross-coupling product almost exclusively with a range of electron rich arenes. It should be noted that no product was observed when no EWG or when *p*-NO_2 was attached onto the electron-deficient arene. This highlights the limitation of the reaction, where presumably when the aryl group on the gold(I) species is too electron-rich, the corresponding gold(III) species cannot activate C-H bonds from electron-rich arenes. On the other hand, when the aryl-gold(I) species is too electron-poor, oxidation of the gold(I) to gold(III) starts to become challenging.

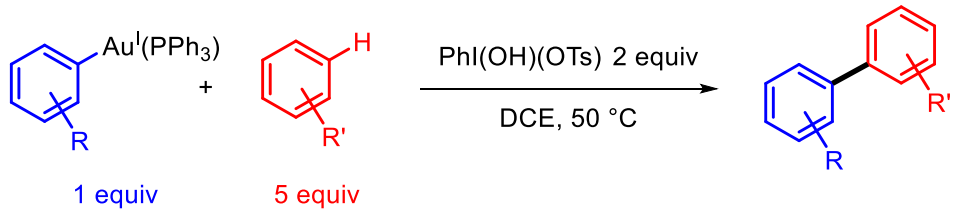

Scheme 12: Optimised reaction conditions for generation of the cross-coupled product.

In trying to determine nature of the aryl-gold(III) complex formed from the oxidation of the corresponding aryl-gold(I) complex, $(C_6F_5)Au^{III}(Cl)_2(PPh_3)$ was used as a catalyst and shown to be unreactive in the presence of 1,3-dimethoxybenzene at 50 °C. Addition of AgOPiv to displace the Cl ligands on the gold with an OPiv group gave the cross-coupled product in similar yields to when the $PhI(OPiv)_2$ oxidant was used, suggesting the formation of a more electrophilic gold(III)-pivalate complex is required. This supports the proposal that the second C-H activation step of electron-rich arenes is activated by an aryl-gold(III) complex.

Although the procedure for this coupling is not a one-pot process, the gold(I) complex from the first activation can be obtained via simple filtration, and the reaction continued with the addition of oxidant. However, the need for five equivalents of the electron-rich arene is not ideal.

In 2015, the same group reported an extension of the method.[33] By using a sub-stoichiometric amount of AgOPiv as an additive, the cross-coupling reaction of an electron-rich and electron-deficient aryl group can be achieved, and this is summarised in Scheme 13. Although optimum yields were obtained with an excess of five equivalents of the electron rich arene, using 1.5 equivalents still gave the cross-coupled product selectively, although with a slight decrease in yield (from 85%).

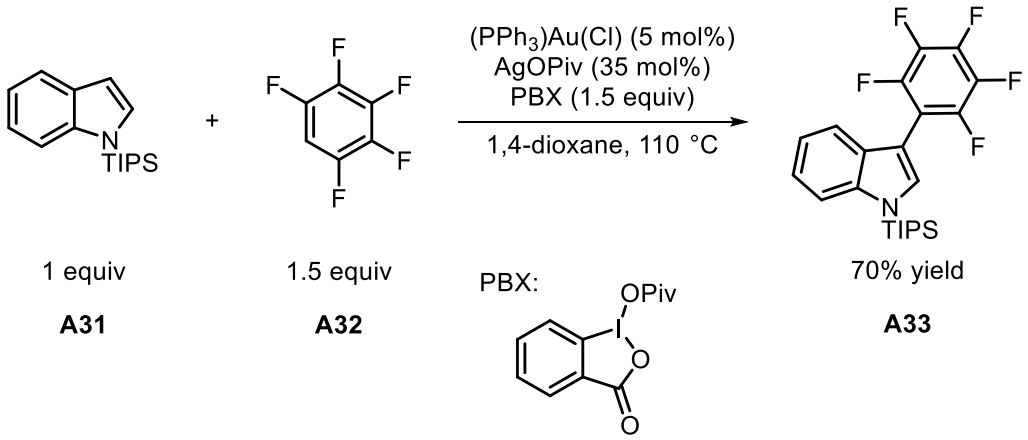

Scheme 13: One-pot cross-coupling of an electron-rich and electron-deficient aryl groups in high yields with an added AgOPiv additive

However, the reaction conditions are quite harsh, requiring high temperatures for the coupling to proceed. Furthermore, the substrate scope is limited to reactions between electron-rich and electron-poor arenes.

1.5.1. Activated coupling partners

Another method of generating unsymmetrical biaryls is to use a preactivated coupling partner. Using inspiration from Pd cross-coupling reactions, arylboronic acids[34–39] (Suzuki-Miyaura reaction) and arylsilanes[40–43] (Hiyama coupling reaction) can be utilised for direct arylation reactions.

A gold-catalysed direct arylation of arenes and arylsilane was reported in 2012.[42] The reaction proceeded under mild conditions at room temperature. A range of moderately electron-rich arenes and electron-rich and electron-deficient arylsilanes could be coupled, where functional groups including halogens, primary alcohols, amides and amines were tolerated. This allows for further functionalisation of the substrate, for example, the C-Hal groups can be used as a handle for palladium cross-coupling methodologies, highlighting the complementary reactivity of gold(III) with palladium(0) complexes.

A stoichiometric amount of iodine(III) oxidant was required, and this was generated in situ from $PhI(OAc)_2$ and camphorsulfonic acid (CSA). A general scheme of reaction is shown in Scheme 14.

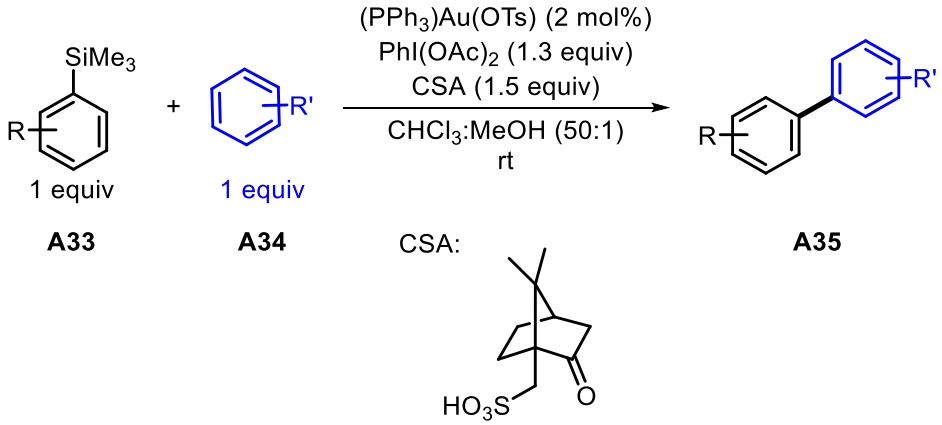

Scheme 14: Gold(III)-catalysed direct arylation of arylsilanes and arenes in the presence of a stoichiometric external oxidant.

A detailed mechanistic study was carried out on the reaction[43] and a catalytic cycle was proposed. Using $(tht)Au(Br)_3$ as the precatalyst instead of $(PPh_3)Au(OTs)$ gave a shorter induction period (and will be further explored in Chapter 5). Furthermore, $(tht)Au(Br)_3$ is soluble in organic solvents and stable under air, moisture and light conditions, and is highly selective for the heterocoupled product.

A simplified version of the catalytic cycle is shown in Scheme 15.

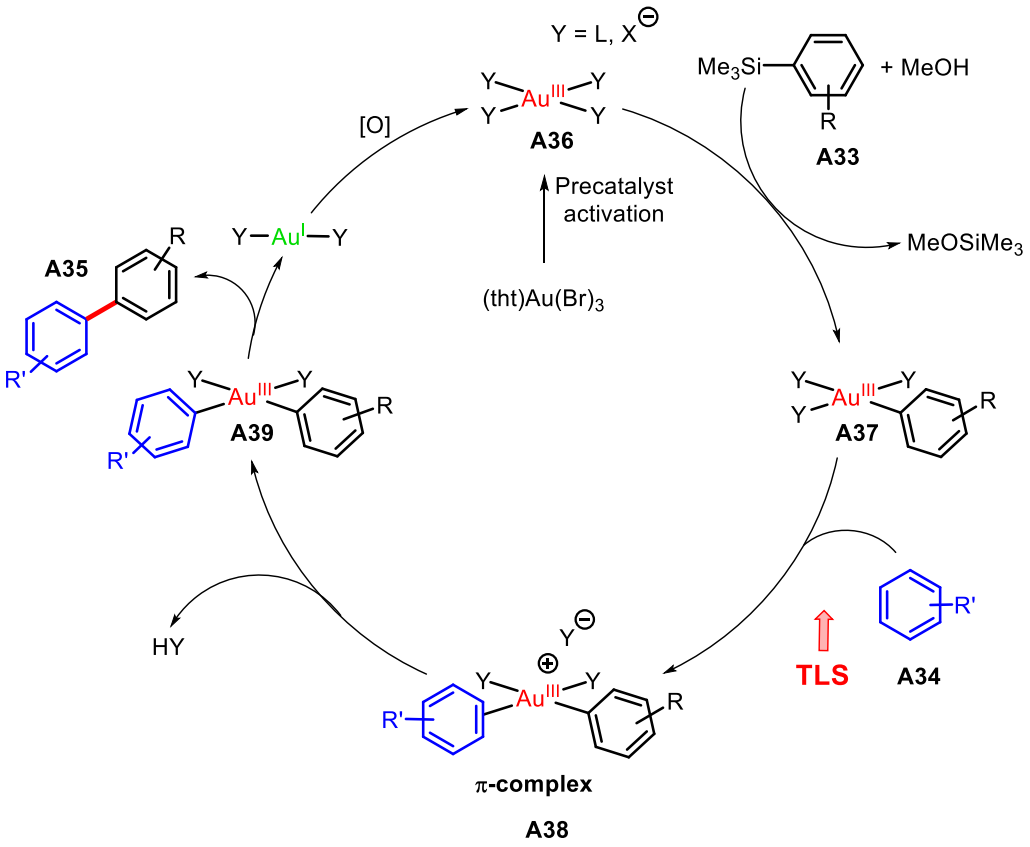

Scheme 15: Simplified catalytic cycle of the direct arylation of arylsilanes and arenes.

The reaction first proceeds via the activation of the precatalyst, where the tetrahydrothiophene (tht) ligand is lost irreversibly. The nature of the active catalyst is unknown and is proposed to change throughout the cycle depending on the electronic and steric requirements of the catalyst.

The next step involves a C-Si auration via an S_EAr mechanism, where the formation of a wheland intermediate **A40** is proposed (Scheme 16). The position of substitution is consistent with this as arylsilanes are known to undergo substitution at the ipso position due to the ability of silicon to stabilise β carbocations. This also means that the arylsilane will preferentially react with the catalyst, instead of the arene to form **A37**.

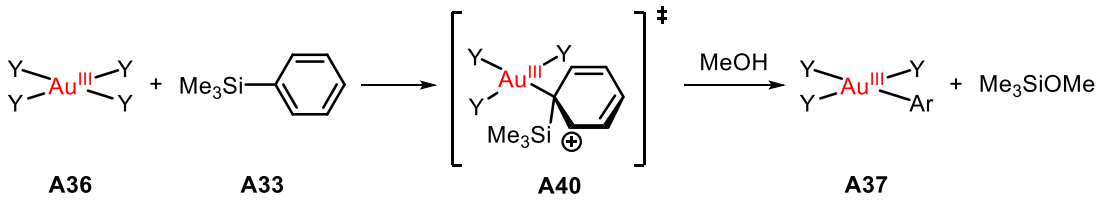

Scheme 16: Proposed intermediate formed from the reaction between a gold(III) catalyst and an arylsilane.

Substituting one of the ligands on complex **A37** with a camphorsulfonate species gives a more electrophilic gold centre, which can then selectively form a π-complex with the electron-rich arene **A34**. This complexation is found to be the turnover-limiting step and is irreversible, thus complex **A37** is the catalyst resting state in the cycle. From this, the gold(III) complex can then activate the C-H bond via an S_EAr mechanism through another wheland intermediate to give complex **A39**, where both the aryl groups attached onto the gold.

Reductive elimination from **A39** will give the desired cross-coupled product and a gold(I) species which can then be oxidised to regenerate the active gold(III) catalyst, **A36**.

An extension of the substrate scope was reported in 2016 by the same group (Scheme 17).[44] Using a bulky hypervalent iodine(III) oxidant (**A41**) and a silyl group tethered to an alcohol (**A42**) on the silane coupling partner, the formation of diaryliodonium salts, a by-product from the reaction of the oxidant with electron-rich arenes was reduced. Furthermore, the yield of product obtained was increased, and a shorter reaction time was required.

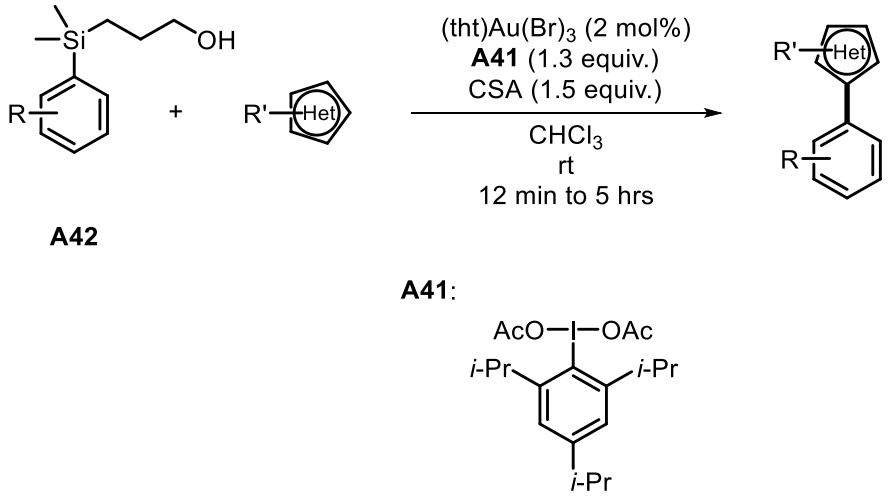

Scheme 17: Modifications to the gold(III)-catalysed direct arylation reaction.

The steric bulk around the oxidant was proposed to slow down its reaction with the arene, and the use of silane **A42** meant that methanol was no longer required as a co-solvent. Since

methanol was found previously to inhibit the catalysis,[43] the exclusion of methanol resulted in increased rates of reactivity.

In 2017, Hofer, Genoux, Kumar, and Nevado reported an oxidative direct arylation reaction between arenes (**A34**) and electron-deficient aryl boronates (**A43**) as the preactivated coupling partner.[45] The reaction utilised an "internal base", where an acetate ligand was attached to the gold(I) catalyst to prevent protodeboronation of the electron-deficient boronates.[46–49] A summary of the reaction is shown in Scheme 18.

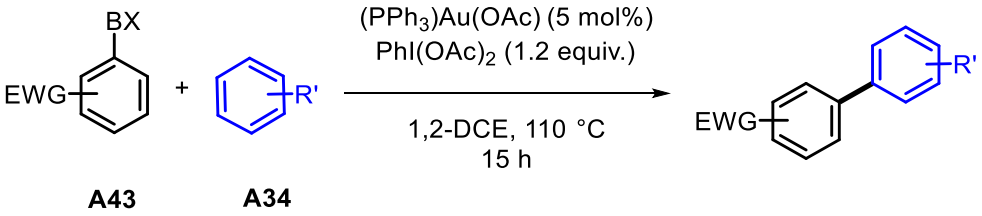

Scheme 18: Summary of a gold-catalysed coupling reaction between electron-deficient aryl boronates and arenes. X = 2,4-pentanediol ester or pinacol ester.

Studies on the mechanism were carried out using stoichiometric amounts of gold. Firstly, the transmetallation step between the gold(I) catalyst and the boronic ester was probed, and this is summarised in Scheme 19. Both $(Ph_3P)Au(Cl)$ and $(Ph_3P)Au(OAc)$ were reacted separately with **A46**, and transmetallation product was only detected when $(Ph_3P)Au(OAc)$ was used, indicating the importance of the acetate ligand. Only electron-deficient aryl groups on the boronic esters were transferred onto the gold(I) complex, and the reaction of **A47** was unsuccessful. The reaction between **A44** and **A46** was repeated in the presence of *p*-xylene (two equiv.) and no change was observed in the product distribution, highlighting the selectivity of this step, where the boronic ester coupling partners are reacting.

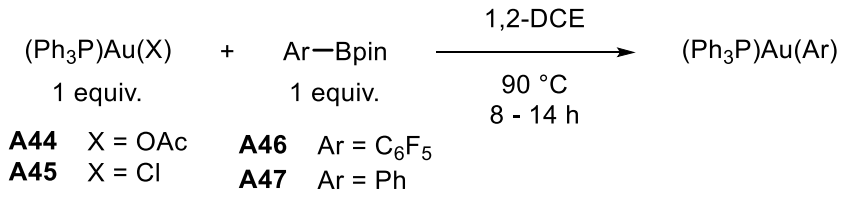

Scheme 19: Stoichiometric reactions carried out between a gold(I) complex and the aryl boronic ester.

The oxidation step was examined next. Reaction of $(Ph_3P)Au(C_6F_5)$ with 3 equiv. of $PhI(OAc)_2$ was carried out in C_6F_6/C_6H_6 (1:1) at 80 °C. The resulting gold(III) product

obtained is shown in Figure 4. The two additional acetate ligands are *trans* to each other, and **A48** was characterised by X-Ray crystallography.

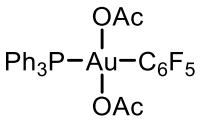

A48

Figure 4: Gold(III) product obtained from the oxidation of $(Ph_3P)Au(C_6F_5)$ with $PhI(OAc)_2$.

Finally, complex **A48** reacted with *p*-xylene (1 equiv.) to give the expected coupled product in 59% yield.

The reaction shown in Scheme 20 was monitored under both stoichiometric and catalytic gold(I) conditions by ^{19}F NMR spectroscopy. Both intermediates identified in the stoichiometric studies described previously $(Ph_3P)Au(C_6F_5)$ and **A48** were observe.

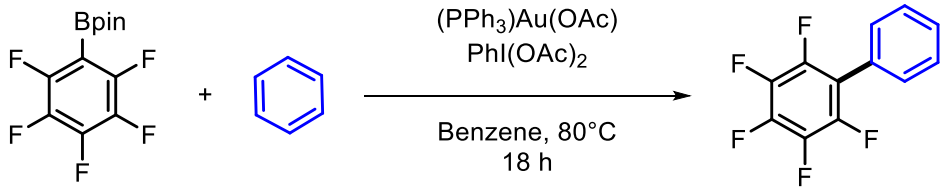

A46 **A49**

Scheme 20: Reaction monitored by ^{19}F NMR spectroscopy.

A few months later, Lloyd-Jones et al. reported an extension on the mechanistic study of the gold-catalysed direct arylation reaction of arenes and arylsilanes.[50] In this study, intramolecular substrates where the arene and silane were tethered together by a linker was examined. The general reaction is shown in Scheme 21.

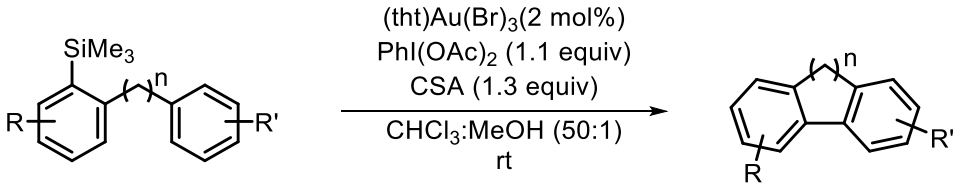

Scheme 21: Intramolecular gold-catalysed direct-arylation reaction of aryl silanes and arenes that are tethered together.

It was found that using these substrates, where n = 1, and R' is not strongly electron-withdrawing gave pseudo-zero-order kinetic profiles in the consumption of starting material. A Hammett plot was constructed on the substrates where n = 1 to give fluorene

products. It was found that the rate of reaction was faster when electron-donating groups (R or R') were used and was independent of whether the same substituent was on the silane ring (R) or the arene ring (R'). This indicates that both substrates go through the same intermediate before, or during the turnover-limiting step.

Along with an Eyring analysis and labelling studies, it was concluded that the reductive elimination step from a diaryl-gold(III) complex was the turnover-limiting step, and coordination of the arene to the resting state (**A39**) occurred irreversibly. The shift in the TLS was proposed to be a result of increased local concentration of the arene resulting in faster rates of π-complexation.

Chapter 2

Hypervalent aryliodine(III) oxidants

2.1. Hypervalent Iodine(III) Oxidants

2.1.1. Overview

Hypervalent iodine(III) species (λ^3-iodanes) have been found to be a mild oxidant for reactions involving oxidative metal catalysis.[51–54] These species typically have the general structure shown below in Figure 5, with some main classes illustrated.

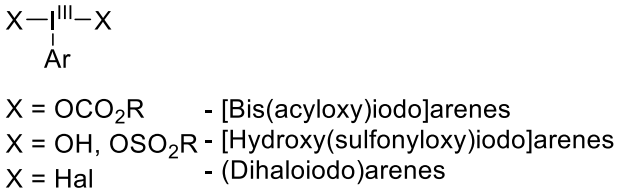

Figure 5: General structure of hypervalent aryliodine(III) oxidants.

The iodine centre has 10 valance e^- and a trigonal bipyramidal geometry, where the ligands form a T-shaped structure. The equatorial position is occupied by the least electronegative ligand (Ar) and two lone pairs of electrons, with the other two ligands (X) occupying the axial positions.

The X–I–X bond is proposed to be a three-centre, four-electron (3c-4e) bond utilising the filled *5p* orbital on iodine and the half-filled orbitals of ligands that are *trans* to each other. Compared to a regular covalent bond, this hypervalent bond is found to be longer and therefore weaker.[55] A molecular orbital bonding diagram illustrating the bonding, non-bonding and antibonding interactions are shown below in Figure 6.

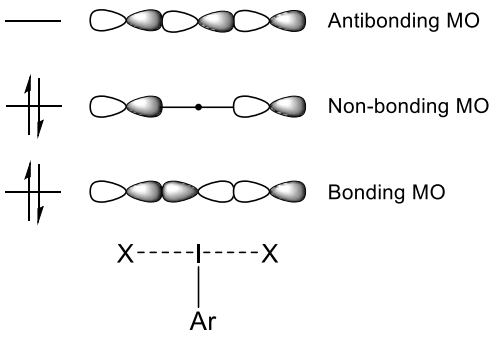

Figure 6: Molecular orbital diagram showing the 3c-4e bond between iodine and the two axial ligands, X.

The highest occupied molecular orbital (HOMO) features a node at the iodine centre, and thus the hypervalent bond is highly polarised, where the electrons are more localised on the ligands. The HOMO can also be thought of as a pair of bonding electrons delocalised on the ligands. Thus, the axial ligands are typically the more electronegative ligands, compared to the ligand in the equatorial position, resulting in a highly electrophilic iodine centre.

The role of *trans* influence in hypervalent aryliodine(III) compounds has been studied by examining the I–X bond lengths in their crystal structures, since both the X ligands share the *5p* orbital on iodine.[56] *Trans* influence is a thermodynamic property which describes how much a ligand can weaken the bond *trans* to itself. It was found that ligands that had higher *trans* influence had smaller Hammett inductive parameters and were more electron donating. Iodine(III) compounds with two strongly *trans* influencing X ligands ($PhI(OMe)_2$ and $PhI(OO^tBu)_2$) were correctly predicted to be unstable, whereas oxidants with two moderately *trans* influencing ligands ($PhI(OAc)_2$) or ligands with a mixture of strong and weak *trans* influence (PhI(OH)(OTs)) resulted in stable iodine(III) compounds.

2.1.2. Ligand exchange

The X ligands on the iodine centre are susceptible to ligand exchange upon reaction with a nucleophile. Two mechanistic pathways have been proposed; the associative and the dissociative mechanisms.[57] These are summarised in Scheme 22 shown below, starting from a general aryliodine(III) compound with two X ligands, **B1**.

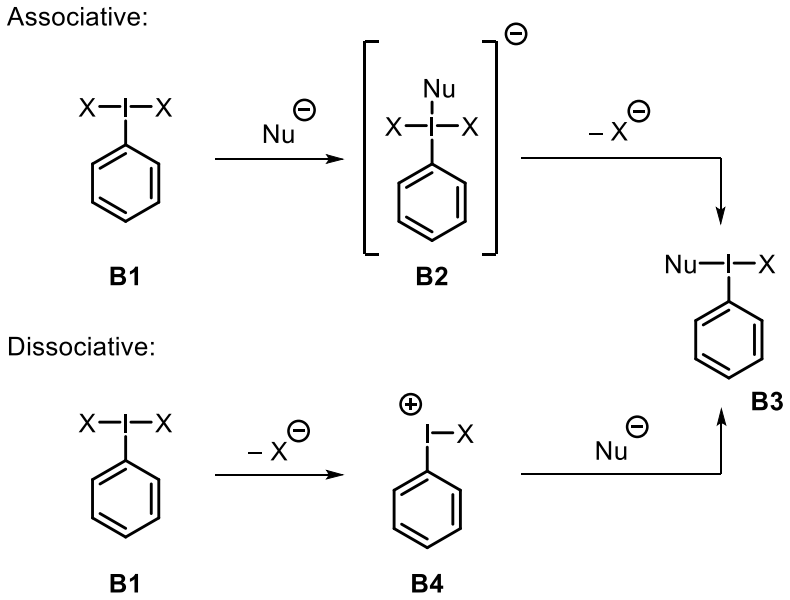

Scheme 22: Two proposed pathways for the exchange of the axial ligands in hypervalent aryliodine(III) compounds.

The associative pathway gives rise to the formation of a 12 e^-, tetracoordinated iodate resulting from attack of the nucleophile into the C–I σ* orbital to give a square planar intermediate, **B2**. Following isomerisation and loss of ligand X, the new aryliodine(III) species **B3** is generated. The dissociation pathway starts with an initial loss of ligand X to give an 8 e^- iodonium species **B4**, which then reacts with the nucleophile, Nu^- to give compound **B3**.

It has been suggested that ligand exchange occurs through an associative mechanism, as tetracoordinate[58–60] and pentacoordinate[61] iodine centres have been observed previously. For example, the tetrachloroiodate anion has been characterised and crystallised,[59] and there have been observed secondary bonding in the crystal structures of iodobenzene diacetate, **B5**[61] and (dichloroiodo)benzene, **B6**.[60] These are illustrated in Figure 7. It should be noted that the bonding in the latter two compounds has been described as more of an electrostatic interaction, rather than a covalent bonding interaction.

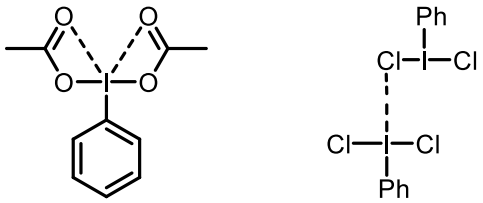

B5 **B6**

Figure 7: Secondary bonding in $PhI(OAc)_2$ and $PhI(Cl)_2$, as observed in the crystal structures of these compounds.

2.1.3. Electrochemistry studies

In 1988, Varvoglis, Kokkinidis, and Papadopoulou analysed the reduction of [bis(acyloxy)iodo]arenes electrochemically in order to understand their oxidising properties.[62]

Electrochemistry involves studying the interrelation of chemical and electrical effects. For example, the measurement of electrical parameters due to chemical changes, as well as the use of electrical properties to bring about a chemical reaction.

The electrochemical experiments conducted in this chapter concerns methods where the voltage (or potential) is controlled and current is an observed parameter. Figure 8 illustrates a reduction process.[63]

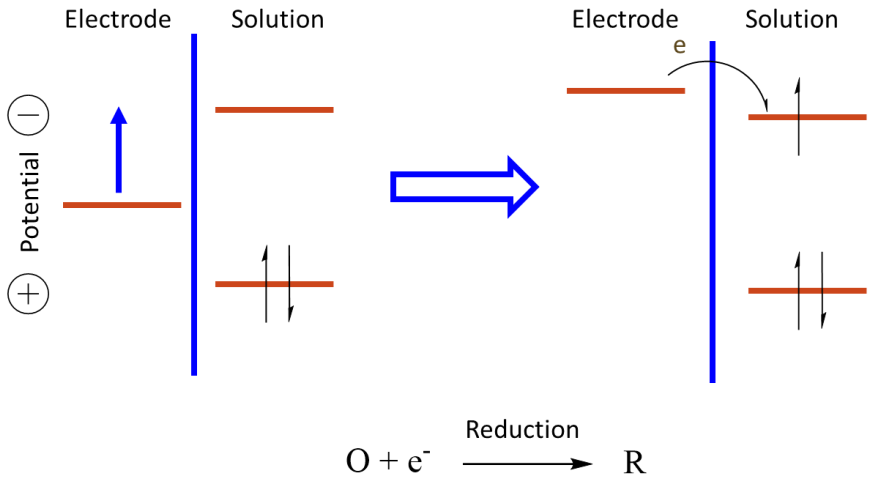

Figure 8: Illustration of a reduction process by increasing the potential of the electrode.[63]

When the electrode is driven to a more negative potential, the energy of the electrons is raised to the point where electron transfer is thermodynamically favoured from the electrode to the analyte near the surface of the electrode. This results in a net movement of electrons out of the electrode, which produces a current response. As current is the rate of movement of charge, in this case, the current is as a result of the movement of electrons.

Cyclic voltammetry

One of the most popular techniques in electrochemistry and a technique used in this chapter is cyclic voltammetry (CV). This technique is typically the first electrochemical study carried out in an experiment and can provide a lot of useful qualitative information by monitoring the current response as a result of a potential sweep, as illustrated in Figure 9.

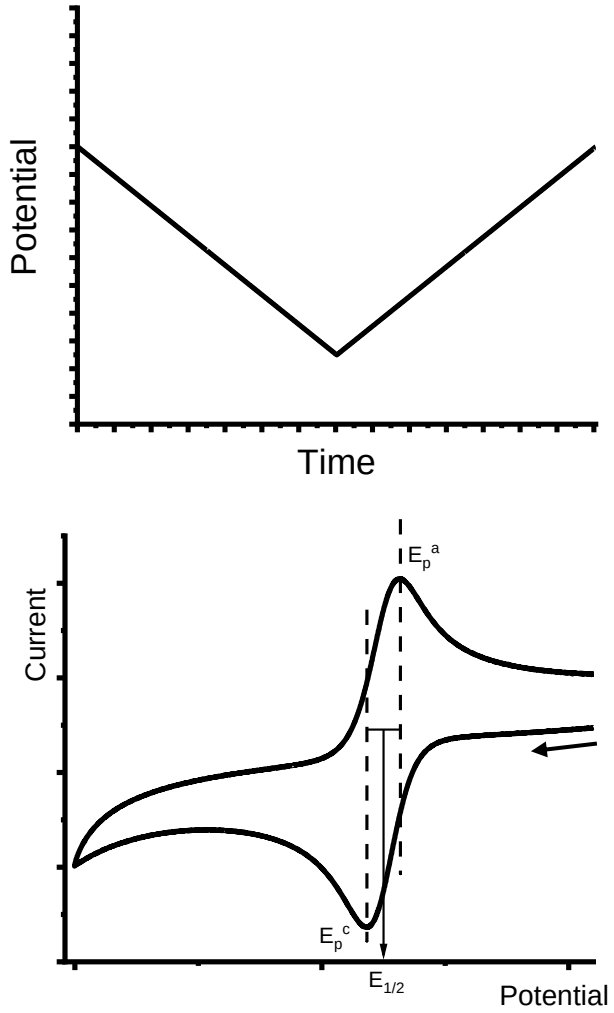

Figure 9: Top: sweep of potential versus time for a cyclic voltammetry experiment. Bottom: current response as a result of a potential sweep, to give a cyclic voltammogram. E_p^c is the cathodic peak potential, and E_p^a is the anodic peak potential. The mid-point of the two peak potential is known as $E_{1/2}$, the half-wave potential.

As the potential is swept to a more negative voltage, a small initial increase in the magnitude of current is observed. This is due to the build-up of an electrical double layer, resulting in a background current or charging current. Increasing the potential further leads to a point where a large reduction current is seen, and the potential at which the peak current occurs is labelled E_p^c.

If the reduction is reversible and the reduced species is sufficiently stable and long-lived in solution, sweeping the voltage back to a more positive potential will result in a similar curve, but with a positive current response, as the reduced species is reoxidised. In a fully reversible system, the halfway point between the two peak currents is known as $E_{1/2}$, or the half-wave potential.

Although it is a qualitative method, cyclic voltammetry is able to provide a large amount of useful information in short periods of time. For example, redox active species within a potential window can be identified, including whether coupled homogenous chemical reactions occur before or after a redox process.[63] Furthermore, the method serves as a simple means to identify the potentials required to drive a redox reaction, both for kinetic studies[64,65] and bulk electroredox processes.[66–68]

In the study carried out by Varvoglis et al.,[62] the authors utilise cyclic voltammetry in order to verify that a secondary reduction peak, observed in the reduction of [bis(acyloxy)iodo]benzene, is due to the reduction of iodobenzene generated from the first reduction wave (Figure 10).

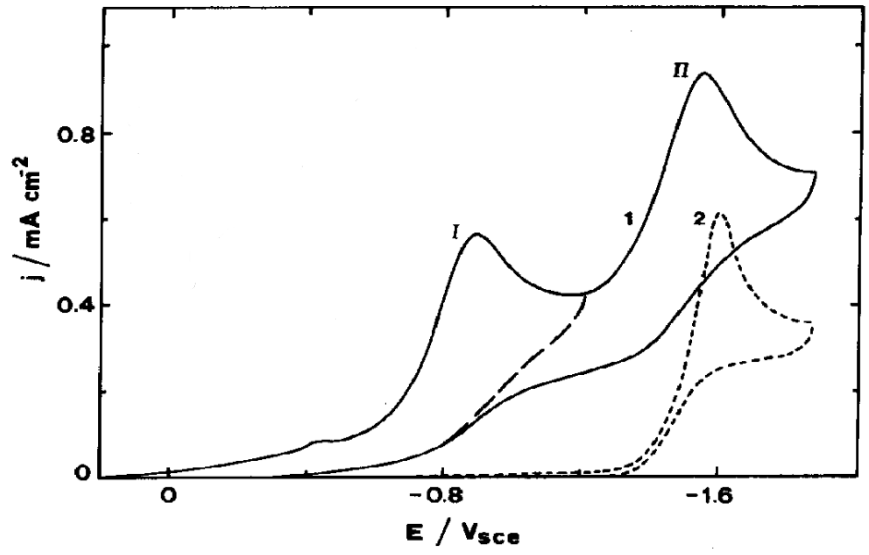

Figure 10: Cyclic voltammograms of $PhI(OAc)_2$ (curve 1) and PhI (curve 2) carried out on an Au electrode, in 0.1 M Et_4NClO_4 in acetonitrile, with a scan rate of 200 mV s^{-1}. Peak I refers to the reduction of $PhI(OAc)_2$, and peak II refers to the reduction of PhI.[62]

Square-wave voltammetry

Another technique utilised in this chapter is square-wave voltammetry (SWV), devised by Ramaley and Krause.[69] This pulse voltammetry method is carried out on a stationary electrode, and the potential waveform applied is illustrated below in Figure 11. Each cycle consists of two pulses, forward and reverse, and the current is sampled twice in each cycle at the end of the pulses (at the points labelled as • in Figure 11). This allows for the charging current from an electrical double layer to decay, resulting in a more sensitive technique compared to CV.

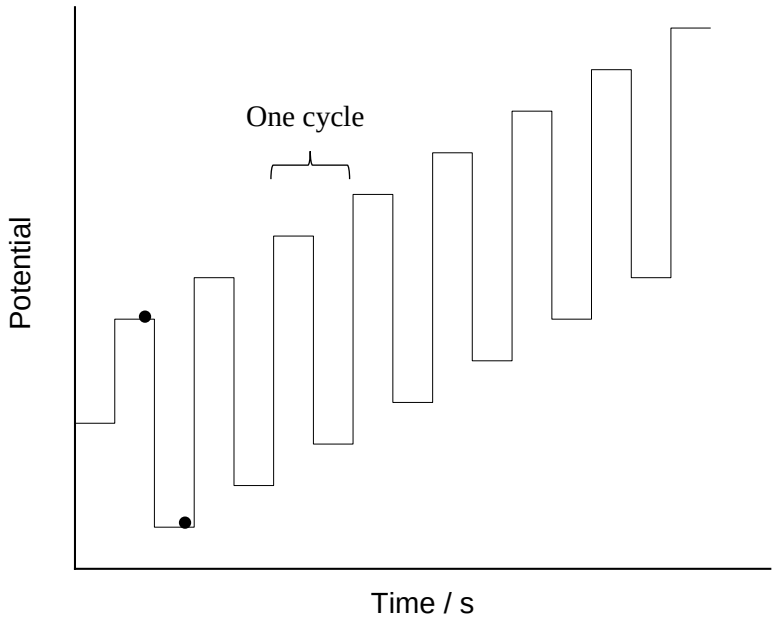

Figure 11: Applied potential versus time for a square-wave voltammetry experiment.

The theoretical current response for a reversible system is shown in Figure 12, where the responses for the forward pulse (A) is separated from the response for the backwards pulse (B). The curve labelled as C is known as the difference current and is calculated by subtracting the resulting reverse current from the forward current, as a function of potential. Curve C is the observed output obtained in a SWV experiment, and the peak current is known as $E_{1/2}$.

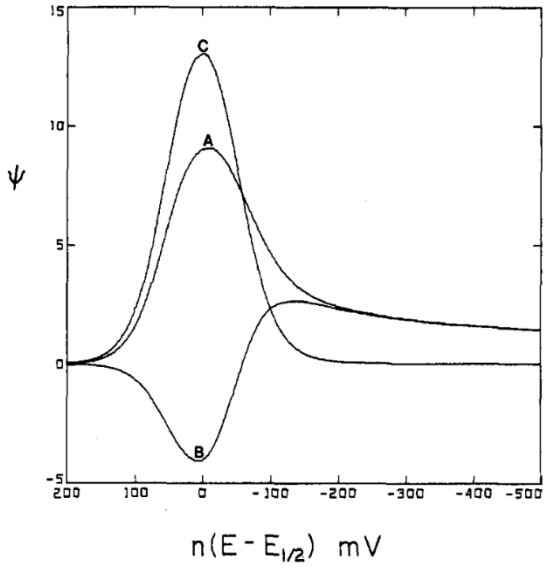

Figure 12: Current response (ψ) versus potential, separated into current response as a result of the forward pulse (A) and the backwards pulse (B). Expected observed current (C) is obtained by subtracting curve B from curve A.[70]. n = number of electrons transferred.

Following the study on the electrochemical reduction of iodoarene diacetates, Varvoglis et al. published another paper looking at the electrochemical reduction of the hypervalent iodine compounds shown in Figure 13.[71] Using slightly different conditions, it was found that the reduction of **B7**, **B8**, and **B9** were reduced at potentials that were outside the solvent window. It was estimated that the reduction potentials for these compounds were higher than 1.35 V versus a saturated calomel electrode (SCE). In comparison, the reduction of iodobenzene diacetate occurred at − 0.24 V (versus SCE)[62] and the reduction of compounds **B10** and **B11** at approximately − 0.12 V (versus SCE). This shows that in the terms of thermodynamics, these [(hydroxysulfonyloxy)iodo]benzene compounds are more oxidising compared to the iodoarene diacetates and their cyclic analogues.

B7 R = 10-camphoryl
B8 R = p-tolyl
B9 R = 2-napthyl

B10 X = OH
B11 X = CH_3COO

Figure 13: Range of oxidants studied by Varvoglis et al. by electrochemistry.[71]

2.2. Aims of the chapter

This chapter focuses on probing the relative oxidising power of aryliodine(III) oxidants. Previous studies carried out using electrochemistry have shown that the electron-poor oxidants have higher redox potentials and therefore are stronger oxidants. Using the chemical equilibrium between the oxidised (iodine(III)) and reduced (iodine(I)) form of the oxidant, relative oxidising powers can be quantified and compared to the electrochemically measured values.

2.3. Oxidant equilibration

2.3.1. Control reactions

Control experiments were carried out prior to the competition studies discussed in Chapter 3. From this, it was discovered that aryliodine(III) oxidants are able to oxidise aryl iodides to give the general equilibrium shown in Scheme 23, under the oxidative gold catalysis conditions.[43]

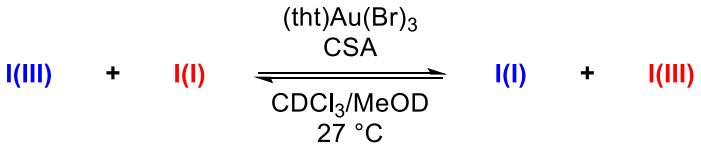

Scheme 23: Equilibrium of aryliodine(III) and iodine(I) species, under oxidative gold conditions.

When one equivalent of both *p*-MeArI(OAc)$_2$ (**B12**) and PhI (**B13**) were mixed in $CDCl_3$ and $CDCl_3$/CD_3OD, no oxidant exchange was observed after 17.5 hours. Adding 1.3 equivalents of camphorsulfonic acid (CSA), which generates the ArI(OH)(OR) oxidant, gave a small amount of the corresponding PhI(OH)(OR) oxidant (**B1**) when left for 48 hours.

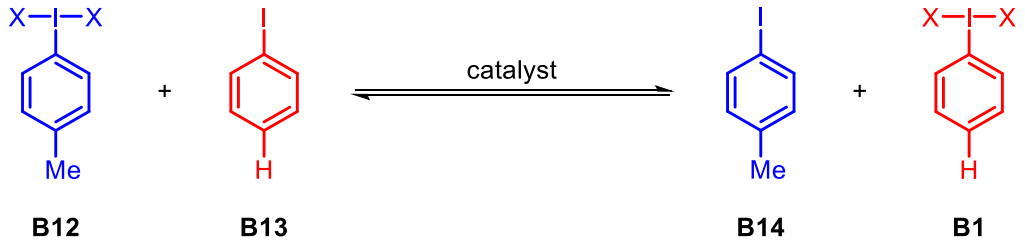

Scheme 24: Equilibration of *p*-MeArIX$_2$ (**B12**) with PhI (**B13**) in the presence of catalytic amounts of (tht)Au(Br)$_3$.

Reaction profile

Addition of 2 mol% of gold catalyst, (tht)Au(Br)$_3$ resulted in the formation of a significant amount of oxidised PhI product, **B1** within 500 seconds, and a stable equilibrium by 1000 seconds (Scheme 26). The equilibrium was monitored by ^{1}H NMR spectroscopy, and the concentration profile versus time is shown below in Figure 14.

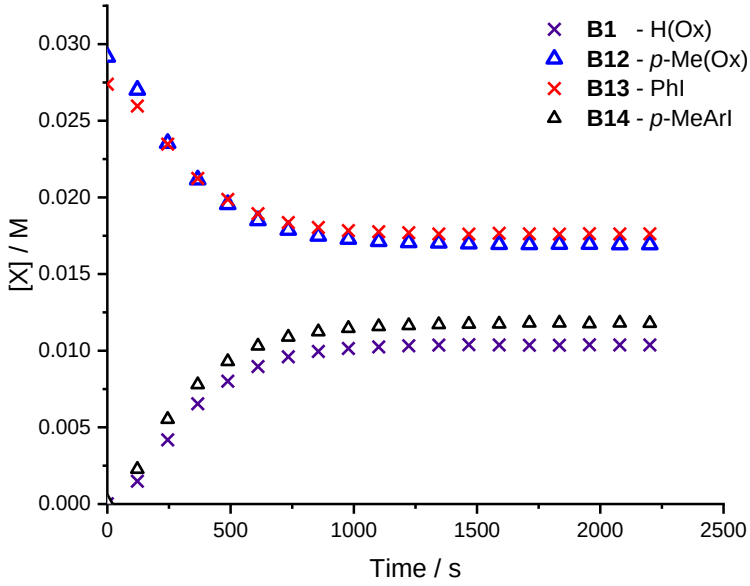

Figure 14: Concentration versus time profile for the reaction in Scheme 24, 0.03 M *p*-Me(Ox) (**B12**), 0.03 M PhI (**B13**) and 0.04 M CSA in $CDCl_3/CD_3OD$ (50:1), with 1 mol% (tht)Au(Br)$_3$.

More of the oxidant (*p*-Me(Ox), **B12**) was consumed relative to the aryl iodide (PhI, **B13**). This is possibly due to the activation of the precatalyst, (tht)Au(Br)$_3$, where it was previously reported that five equivalents of oxidant reacts with one equivalent of gold precatalyst.[43] Consequently, the amount of *p*-MeArI (**B14**) product formed was slightly greater than the amount of oxidant **B1** formed. This difference in product formation (Δ) is found to be largest with higher catalyst loadings (Table 1). However, the relative amounts of each component at equilibrium is the same across all catalyst loadings.

Table 2: Equilibrium constant $K_{eq} = \frac{\text{product}}{\text{reactant}}$ and difference in the amount of the two products (**B14** and **B1**) formed (Δ).

Catalyst / mol%	K_{eq}	Δ / M × 1000
1.0	0.41	0.679
0.5	0.41	0.490
0.3	0.40	0.214
0.2	0.41	0.089

Catalysts

A variety of gold complexes and halide salts were tested as catalysts, in order to identify the requirements of the reaction. The results are illustrated in Table 3.

Table 3: Results from testing gold complexes and halide salts as potential catalysts for the equilibrium shown in Scheme 24.

No.	Catalyst	Equilibrate?
1	(tht)Au(Br)$_3$	✓
2	(PPh$_3$)Au(Br)	✓
3	(IPr)Au(Br)	✓
4	(IPr)Au(Cl)	✗
5	(tht)Au(Cl)	✗
6	KBr	✓
7	NBS	✓
8	Bu$_4$NBr	✓
9	NaI	✗

From entries 1-5 in Table 3, it was found that not all gold complexes were able to catalyse the equilibration shown in Scheme 24, and only complexes with bromide ligands present were active. Further testing of bromide containing compounds (entries 6-8) showed that the equilibration reaction could be catalysed in the absence of gold. This suggests that bromonium (generated from the reaction of bromide and aryliodine(III) oxidants) was the active species responsible for catalysing the equilibration reaction shown in Scheme 24. Finally, NaI was not an active catalyst for the reaction, as shown in entry 9, highlighting the importance of the presence of bromide.

When the equilibration was carried out in chloroform stabilised with amylenes instead of ethanol-stabilised, or unstabilised chloroform, no reaction occurred. This was possibly due to a reaction between amylenes and a generated bromonium species. To test this further, the following reaction shown in Scheme 25 was carried out.

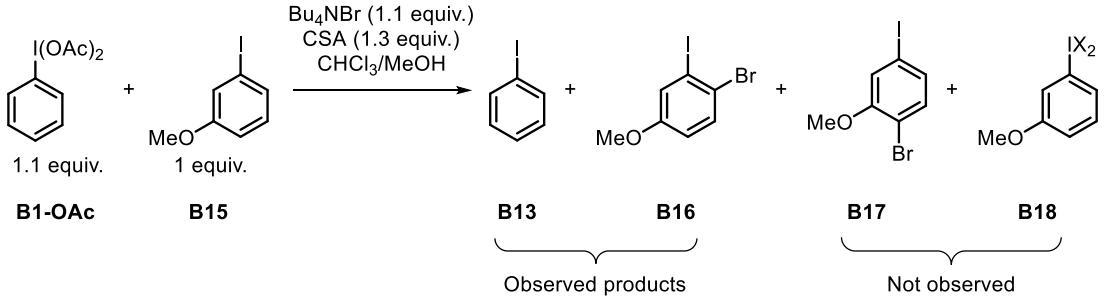

Scheme 25: Possible product distribution from the reaction of **B1-OAc** and **B15** in the presence of a stoichiometric amount of bromide.

The crude mixture was analysed, and only PhI (**B13**) and compound **B16** were observed by ^{1}H NMR spectroscopy.[72] No oxidation of the *m*-OMeArI to give **B18** was observed, indicating that bromonium required in catalysing the equilibration is no longer available and has been consumed by **B15** in a bromination reaction.

Proposed mechanism

A tentative mechanism was proposed in Scheme 26, given that bromonium is thought to be responsible for catalysing the equilibration. Upon oxidation of bromide by the ArI(III) oxidant, the generated bromonium could react with aryl iodide in solution to give an iodonium(III) compound with a bromide attached.[73] This could undergo ligand exchange *via* an associative-type intermediate with the added ArI(III) oxidant to form the new oxidant, and regenerate an iodonium(III) compound, which can then undergo ligand exchange again to give an equilibrated mixture of the oxidants.

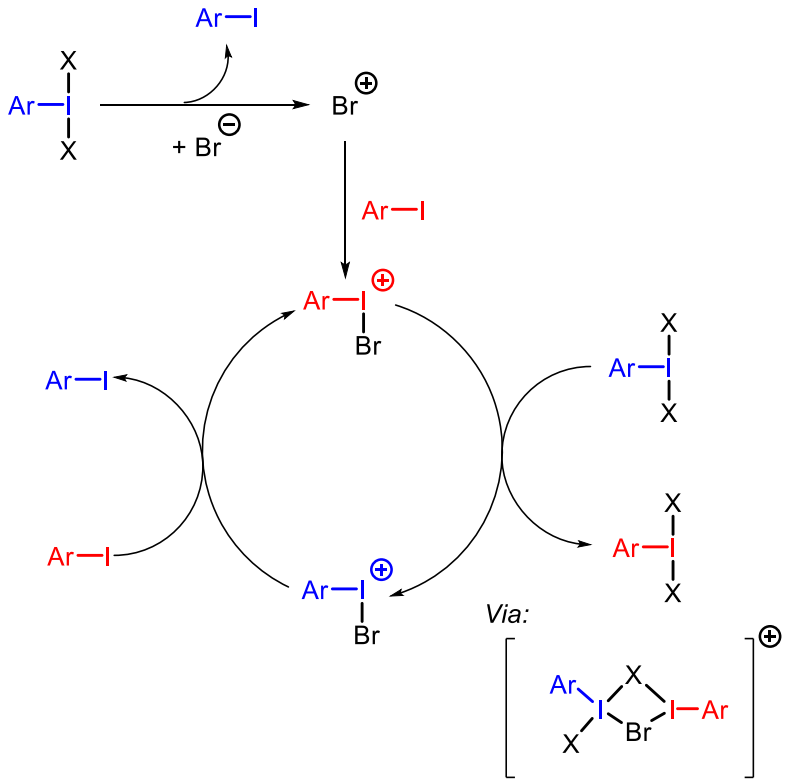

Scheme 26: Proposed mechanism for a bromonium-catalysed equilibration of ArI(III) oxidants.

2.3.2. Oxidant potentials

Using the equilibration reaction, the relative oxidising power of substituted ArI(III) oxidants can be examined. This is summarised in Scheme 27. The position of equilibrium between a range of substituted aryl iodides (**B**) with the unsubstituted oxidant (**AO**) was determined using ^{1}H NMR spectroscopy. The equilibrium constant (K) for these reactions were calculated, using Eq. 1, and the results are summarised in Table 4.

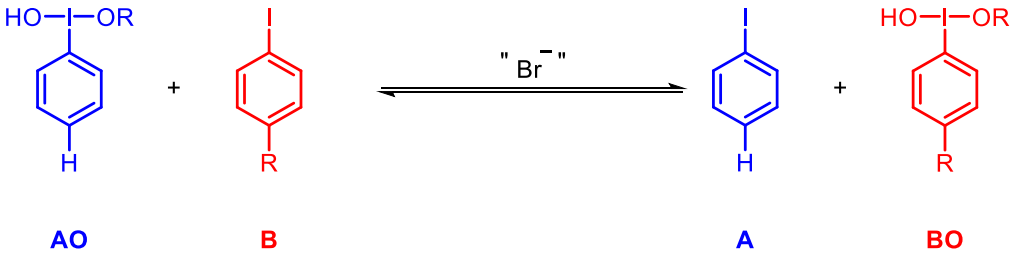

Scheme 27: Equilibration of substituted aryl iodides with $PhI(X)_2$ oxidants, catalysed by 1 mol% of $(tht)Au(Br)_3$ in $CDCl_3/CD_3OD$ (50:1 mixture).

$$K = \frac{[\boldsymbol{AO}][\boldsymbol{B}]}{[\boldsymbol{A}][\boldsymbol{BO}]} \qquad \text{Equation 1}$$

Table 4: Equilibrium constants (*K*) and calculated redox potentials (E) for various substituted aryliodine(III) oxidants. All concentrations were calculated by ^{1}H NMR spectroscopy at 300 K with CH_2Br_2 as an internal standard. The concentrations of each species obtained approximately after 30 minutes, 1 hour, and overnight remained constant.

No.	R	σ	*K*	E / v
1	*p*-CF3	0.54	11.12	0.031
2	*p*-NO2	0.78	40.35	0.048
3	*p*-^{t}Bu	− 0.20	0.30	− 0.015
4	*p*-Me	− 0.17	0.41	− 0.011
5	*p*-Cl	0.23	2.75	0.013
6	*p*-Br	0.23	2.92	0.014
7	*p*-OMe	− 0.27	0.24	− 0.019
8	*p*-F	0.06	1.54	0.006
9	*m*-NO2	0.71	29.29	0.044

K values greater than one were obtained when aryl iodides with electron-withdrawing groups were used, and values of less than one with electron-donating groups. This is consistent with the proposal that electron-withdrawing groups result in a more electrophilic iodine(III) centre. These oxidants therefore have a higher affinity for electrons, and thus are the stronger oxidants, and will more readily reduce to the aryl iodides compared to iodine(III) oxidants with electron-donating groups attached.

Once the equilibrium constants have been obtained, the Nernst equation (Eq. 2) can be used to calculate the relative redox potential (E) of the substituted oxidant (**BO**).

$$ln\ K = \frac{nFE^0}{RT}$$ Equation 2

Where: n (number of electrons transferred) = 2

F (Faraday constant) = 96485 C mol^{-1}

R (gas constant) = 8.312 J K^{-1} mol^{-1}

T (Temperature) = 298 K

Hammett Plot

The relative potentials were plotted against the Hammett substituent constant (σ)[74] for the corresponding R groups and a good linear correlation was obtained, shown in Figure 15. These results were compared against those obtained by Varvoglis et al.,[62] where the electrochemical reduction of various substituted aryliodine diacetates were studied. The electrochemical measurements were made in acetonitrile, with a three-electrode cell: a rotating Au disc electrode, a calomel reference electrode and a Pt counter electrode with Et_4NClO_4 as the electrolyte.

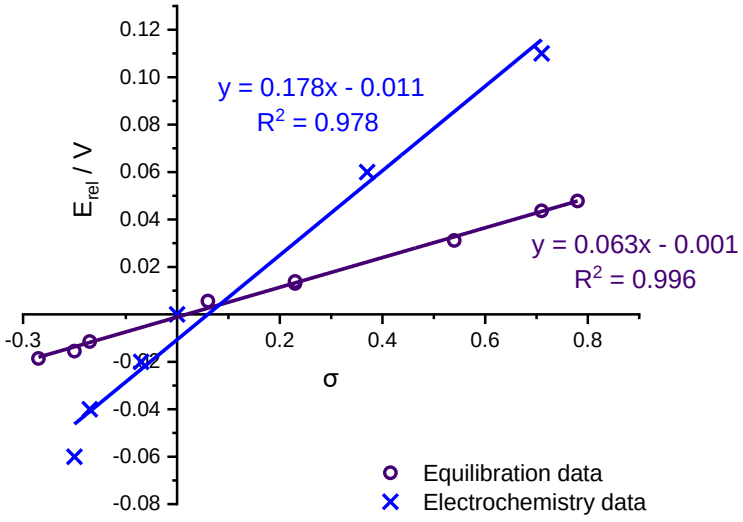

Figure 15: Hammett plot of redox potential (E_{rel}) versus Hammett constant (σ) for the calculated potentials from the equilibration studies (Table 4) and the electrochemical reduction[62]. All values have been adjusted so that the unsubstituted oxidant, $PhI(X)_2$ has a redox potential of zero volts.

Although both sets of data agree that the more electron deficient oxidant has a higher redox potential, the electrochemical data suggests that the substituents have a larger effect on the redox potentials than the calculated potentials from equilibration studies show. To investigate this difference, the conditions in which the equilibration reactions were carried out in were modified, so that they were more similar to the electrochemical conditions.

Firstly, the reactions in chloroform/methanol (50:1) and CSA were repeated, to ensure reproducibility. Removing CSA from the reaction media resulted in equilibration of the aryliodine diacetate species rather than the hydroxycamphorsulfonate oxidants, which is the class of oxidants examined electrochemically.

Figure 16 (run 4) shows the resulting Hammett plot from equilibrating aryliodine diacetates. The obtained gradient is similar to that found previously when CSA was added (runs 1 and 2). This is because the different axial ligands on the iodine centre should only affect the absolute redox potential, rather than the relative redox potentials. Similarly, the reaction was repeated in acetonitrile (run 3), the solvent that was utilised in the electrochemical study,[62] but gave negligible effects as the plot still matches the other runs.

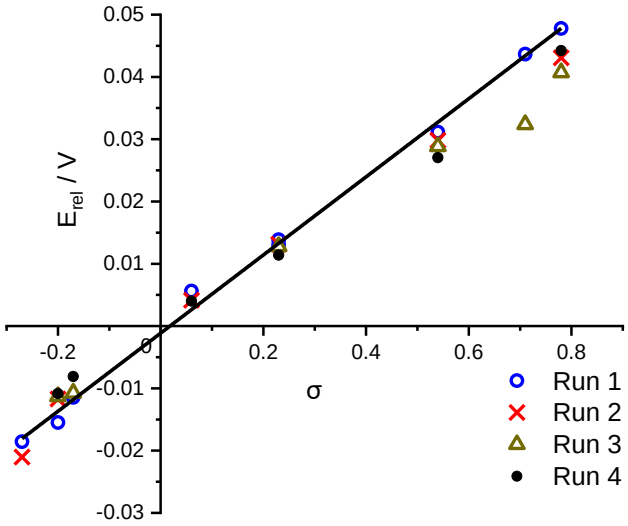

Figure 16: Hammett plot obtained from calculated redox potentials based on the position of equilibrium in the reaction illustrated in Scheme 27. Conditions: 0.06 M $PhI(OAc)_2$ and 0.06 M RArI. Runs 1 & 2 were in $CDCl_3/CD_3OD$ (50:1) solvent mixture, with added CSA and $(tht)Au(Br)_3$ (1 mol%) as the catalyst. Run 3 was carried out in MeCN-d_3/CD_3OD (50:1) solvent mixture, with added CSA and Bu_4NBr (2 mol%) as the catalyst. Run 4 was carried out in $CDCl_3$ and $(tht)Au(Br)_3$ (2 mol%) as the catalyst. All concentrations were calculated by ^1H NMR at 300 K with CH_2Br_2 as an internal standard.

Repeating the analysis of the equilibrium position under various conditions shows that the values calculated for the relative redox potentials of these oxidants are reproducible and are minimally affected by the solvent or the X ligands on the iodine(III) centre.

2.4. Electrochemical Studies

2.4.1. Method

The electrochemical analysis of the aryliodine diacetate oxidants was then repeated. A three-electrode setup was used, with a glassy-carbon disc as the working electrode, a platinum gauze as the counter electrode, and Ag/AgCl as the quasi-reference electrode. $[^nBu_4N][PF_6]$ was used as the electrolyte.

A cyclic voltammogram of $PhI(OAc)_2$ in dichloromethane was obtained, in order to determine the window where reduction of the compound occurred. It was found that $PhI(OAc)_2$ undergoes an irreversible reduction process at $E_p^c = -1.6$ V versus Ag/AgCl quasi-reference electrode. Previous analysis had determined that the reduction corresponds to a two-electron reduction process.[62]

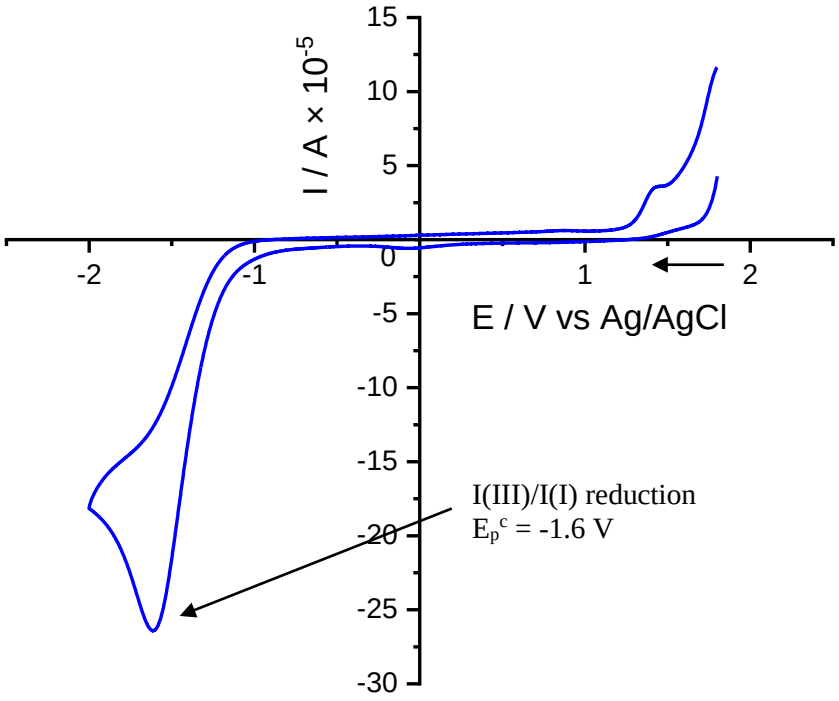

Figure 17 : Cyclic voltammogram for $PhI(OAc)_2$ as a 5 mM solution in DCM with 0.1 M $[^nBu_4N][PF_6]$, using a glassy-carbon working electrode, a Pt gauze counter electrode and a Ag/AgCl quasi-reference electrode. A scan rate of 100 mV s^{-1} was used.

Square-wave voltammetry was used to obtain a more accurate reading of the reduction potential of $PhI(OAc)_2$. Ferrocene was added as the internal standard, and the resulting output is illustrated in Figure 18. The reduction potential, E_p^c was obtained at − 1.47 V versus Fc^+/Fc.

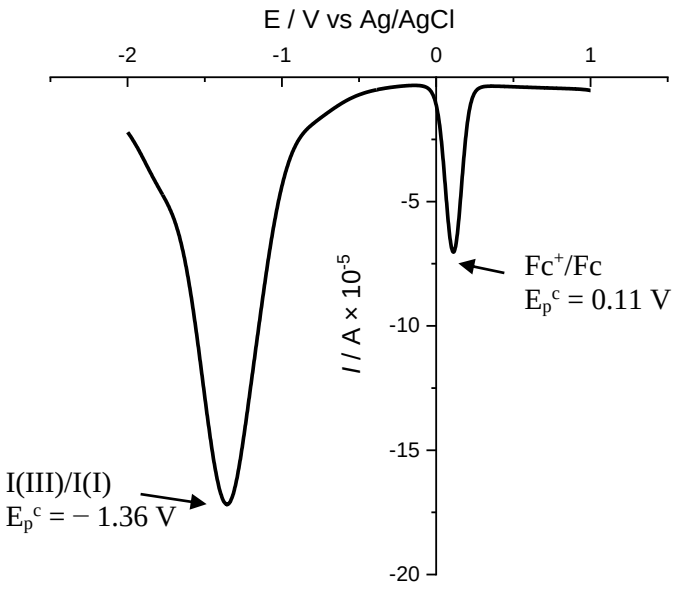

Figure 18: SWV of $PhI(OAc)_2$ as a 1 mM solution in DCM, with 0.1 M [$^nBu_4N$][PF_6], using a glassy-carbon working electrode, a Pt gauze counter electrode and a Ag/AgCl quasi-reference electrode. A scan rate of 100 mVs^{-1} was used.

Performing square wave voltammetry on different electron rich and electron poor aryliodine(III) oxidants allowed for the Hammett plot analysis shown in Figure 19. Both sets of data were normalised so that the unsubstituted oxidant is referenced at zero volts.

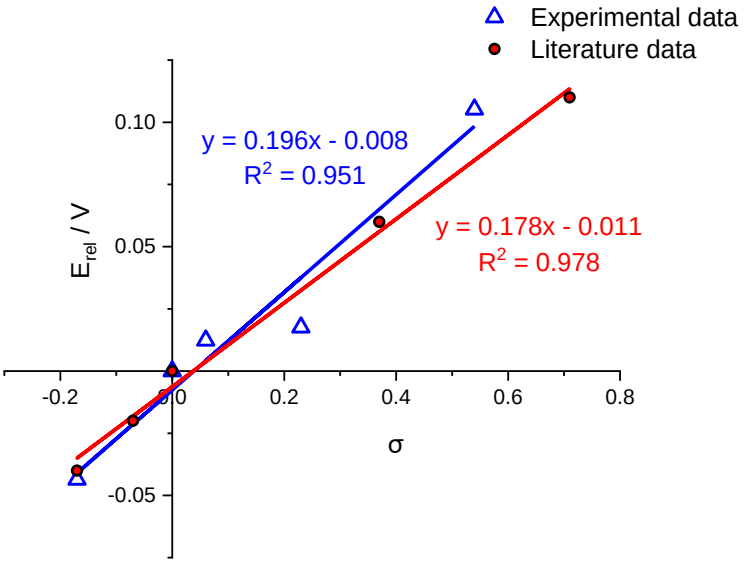

Figure 19: Hammett plot of relative redox potentials (E_{rel}) obtained electrochemically versus Hammett substituent constants (σ). Plot of data obtained compared with literature data.[62]

Although the conditions used by Varvoglis et al.[62] to obtain the electrochemical reduction potential of $ArI(OAc)_2$ oxidants were very different to the conditions described above, the resulting Hammett plots of the relative potentials have similar gradients. These results show that there appears to be an inherent difference between measuring the redox potentials electrochemically and by analysing the equilibrium positions. This could be attributed to the fact that more than one oxidant species is present under the equilibrating conditions, and formation of dimers or aggregates may impact the position of equilibrium. Even though the cause for the different gradients obtained is unclear, the general trend that electron poor oxidants are the stronger oxidants remains the same for both sets of data.

2.5. Conclusion

The presence of catalytic amount of bromide in a solution containing aryliodine(III) oxidants and iodobenzene causes an equilibration reaction to occur, where a mixture of the starting materials, reduced iodoarene compounds, and oxidised phenyliodine(III) oxidants are observed, as illustrated in Scheme 24. The position of equilibrium was utilised in the Nernst equation to calculate the relative redox potentials of these aryliodine(III) oxidants. The potentials were plotted against the Hammett constants of the corresponding substituent on the ring, and it was found that the more electron-deficient oxidants have a higher redox potential and are therefore more potent oxidants. The relative redox potentials obtained were independent of the X ligands of the aryliodine(III) oxidants, as well as the solvent the reaction was carried out in.

Comparison of the Hammett plot of calculated potentials with potentials obtained from electrochemical reduction of these oxidants showed a substantially different gradient. Although the direction of the gradient was the same, the electrochemistry data implied that the substituents on the aryl ring of these oxidants have a larger impact on the relative potential of these aryliodine(III) oxidants. However, the equilibrium studies were carried out under similar conditions to the gold-catalysed coupling reaction. In this case, both reactions occur in the solution state. In comparison, the electrochemical studies rely on an electron-transfer process between the solution at the surface of the electrode and the solid electrode, which may result in a less accurate description for the oxidants in the context of our studies, the oxidation of the gold(I) generated from a gold(III)-catalysed direct-arylation reaction.

Chapter 3

Relative rates of oxidation

3.1 Gold(I) oxidation

Hypervalent iodine oxidants are commonly used in oxidative metal catalysis, where a stoichiometric amount of external oxidant is required to complete the catalytic cycle. Typical oxidants used in oxidative gold catalysis include fluoronium oxidants[36–39,75–77] and hypervalent iodine oxidants.[31–33,42,78–81]

Interestingly, it was found that both oxidants give different products when reacted with $(C_6F_5)Au^I(PPh_3)$, **C1**.[82] A summary of the results are shown in Scheme 28.

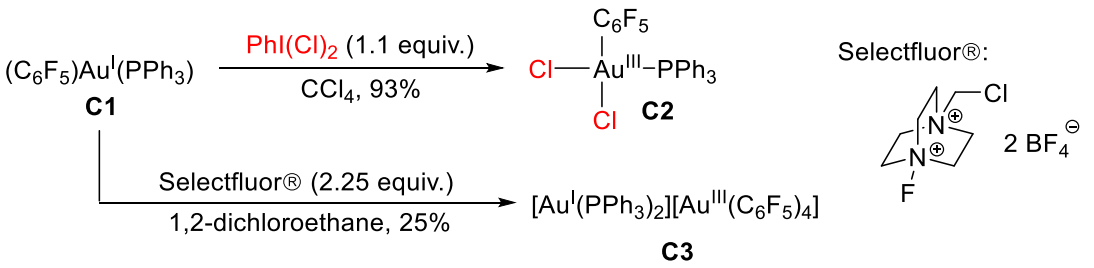

Scheme 28: Difference in observed reactivity oxidation of an electron-deficient Au(I) species with iodine(III) oxidants and fluoronium oxidants.

With $PhI(Cl)_2$ as the oxidant, the only product that was formed was **C2**, a gold(III) complex with the Cl ligands *cis* to each other. The complex was characterised by single-crystal X-ray crystallography as well as NMR spectroscopy. Using Selectfluor® however, gave an unanticipated gold(I)-gold(III) complex, **C3**, which was characterised by single-crystal X-ray crystallography. **C3** was proposed to have formed via the oxidation of the starting material, followed by ligand exchange with the starting material **C1**, due to the instability of electron-deficient fluorinated gold(III) complex.[83]

3.1.1. Oxidation of $(Ph_3P)Au(Me)$

In 2009, Muñiz and Iglesias studied the stoichiometric oxidation of a gold(I) complex with $PhI(OAc)_2$ in the context of a gold-catalysed diamination reaction of alkenes.[78] The authors selected the methyl gold complex **C4** as a probe for an alkyl gold complex, which was proposed as an intermediate within their catalytic cycle. The resulting products were identified as gold(III) complex *cis*-**C5** and *trans*-**C5** shown in Scheme 29, and characterised by ^{31}P NMR spectroscopy and HRMS. A 90:10 mixture of the isomers (*cis*/*trans*) was obtained when a stoichiometric amount of oxidant was added, and a 58:42 mixture obtained when an excess of oxidant was utilised. Further reaction of the gold(III) mixture with an anionic urea to mimic the final step of the proposed catalytic cycle led to the expected *N*-methylated product, indicating the relevance of this stoichiometric step to the overall catalytic reaction.

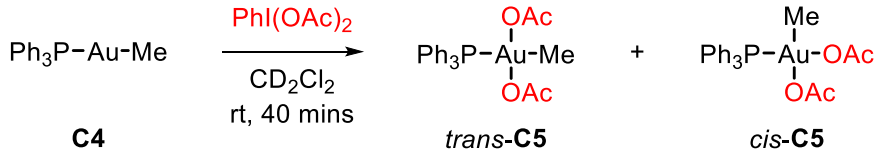

Scheme 29: Stoichiometric reaction of $PhI(OAc)_2$ with alkyl phosphinegold(I) complex (**C4**) to give gold(III) complexes with acetate ligands either *cis* or *trans* to each other.

3.1.2. Oxidation of *bis*(NHC)-Au(I) complexes

A study on the oxidation of various gold(I) complexes with two *N*-heterocyclic carbene (NHC) ligands coordinated, with hypervalent iodine(III) compounds was carried out in 2016.[84] It was found that these complexes reacted with $PhI(Cl)_2$ to give a gold(III) complex with two NHC ligands and two Cl ligands, where both NHC ligands are *trans* to each other.

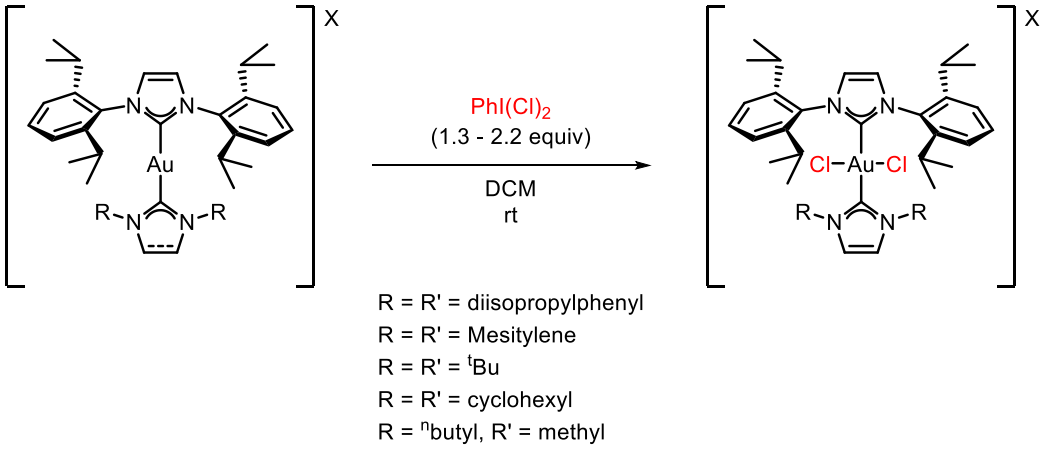

Scheme 30: Reaction of *bis*(NHC) gold(I) complexes with $PhI(Cl)_2$ as the oxidant, carried out at room temperature to give a gold(III) complex with Cl ligands *trans* to each other.

Initial studies investigated the oxidation of gold(I) complexes with two NHC ligands attached and $PhI(Cl)_2$ as the oxidant (Scheme 30). By varying one of the NHC ligands on the gold, the time taken for full conversion was analysed by NMR spectroscopy and compared with the steric descriptors of the varied NHC ligand. This parameter is known as the percent buried volume ($\%V_{burr}$) and describes the percentage of the total volume of a defined sphere that is occupied by ligands, with the centre of the sphere on the metal.[85] It was found that smaller and more electron-donating NHC ligands had shorter reaction times and higher yields.

In particular, the complex with two IPr (*N*,*N*'-*bis*(2,6-diisopropylphenyl)imidazol-2-ylidine) NHC ligands, which had the largest $\%V_{burr}$ (38.2%), required a larger excess of oxidant (2.2 equivalents) and 7 days at room temperature to reach full conversion. This is in contrast to the results obtained when one of the IPr NHC ligands was replaced with an ICy (*N*,*N*'-dicyclohexylimidazol-2-ylidene) NHC ligand, which had a $\%V_{burr}$ of 27.2% and required 1.3 equivalents of oxidant and 3.5 hours to reach full conversion. This was attributed to steric hindrance from the ligands on the gold centre slowing down the oxidation reaction.

The reactions between gold(I)-*bis*(NHC) complexes and $PhI(OAc)_2$ as well as $PhI(OCH_2CF_3)_2$ as oxidants were also studied. The complexes containing an IPr NHC ligand as shown in Scheme 30 gave no reaction with these oxidants. Instead, complex **C6** featuring two smaller NHC ligands ($\%V_{burr}$ = 27.8% and 27.4%) was synthesised and oxidised with $PhI(OAc)_2$ and $PhI(OCH_2CF_3)_2$. The resulting gold(III) complexes obtained (**C7** and **C8**) had two NHC ligands bound *trans* to each other, and both the X ligands from the hypervalent iodine species attached, as illustrated in Scheme 31.

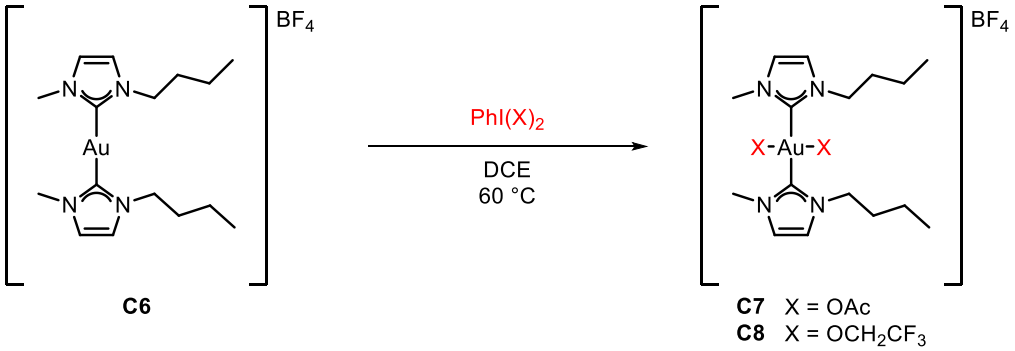

Scheme 31: Oxidation of complex **C6** with $PhI(OAc)_2$ and $PhI(OCH_2CF_3)$.

The examples above have shown that in general, the oxidation of gold(I) complexes to gold(III) is accompanied by the transfer of the X ligands from the hypervalent aryliodine(III) oxidants to the gold centre. However, the precise mechanism of this oxidation is currently unknown.

3.2 Aims of the chapter

This chapter probes the mechanism of the oxidation of gold(I) complexes within the context of an oxidative direct arylation reaction, covered in Chapter 1.[42,43,50] It was found previously[42] that hypervalent iodine oxidants with sulfonyloxy and hydroxy X ligands gave the highest yield of product, whereas the iodine(III) oxidants with two acetate ligands were less effective. Furthermore, fluoronium based oxidants (Selectfluor™ and [PyrF][BF_4]) gave no reaction.

Other reports where hypervalent iodine oxidants were superior as oxidants over other oxidants such as fluoronium based oxidants, peroxides, and Oxone® have also been reported.[31,32,86,87] It was therefore of interest to understand the mechanism of reaction of these hypervalent iodine(III) oxidants with gold(I).

3.3 Competition of aryl oxidants

Direct observation of the rate of reaction in Scheme 32 gives no information on the oxidation of gold(I) under the reaction conditions, as the turnover-limiting step occurs prior to oxidation.[50] Instead, competition reactions can be designed to probe the oxidation, where the oxidant with favourable properties will be consumed preferentially. Scheme 32 shows a summary of the reaction studied, where substrate **C9** was chosen, since it had a suitable reaction time in giving the product **C10**.

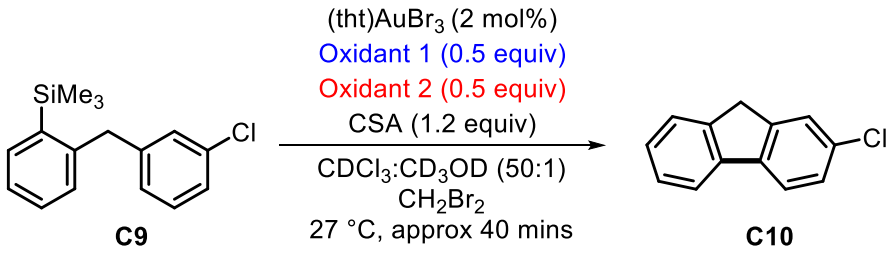

Scheme 32: Intramolecular cyclisation of aryl silane **C9**. Two oxidants are competed against one another to obtain relative rates of reaction.

Modelling

The competition reaction was modelled in Dynochem® to obtain examples of the concentration versus time profiles for these reactions. A simplified catalytic cycle shown in Scheme 33 was constructed, where the active catalyst first reacts with the starting material to form an intermediate (INT). The next step from the intermediate (INT) to the gold(I) species ([Au^{I}])was set with a small *k* value (k_2) compared to the rest of the processes and is therefore the turnover limiting step. The gold(I) species is then reoxidised by either OX 1 or OX 2.

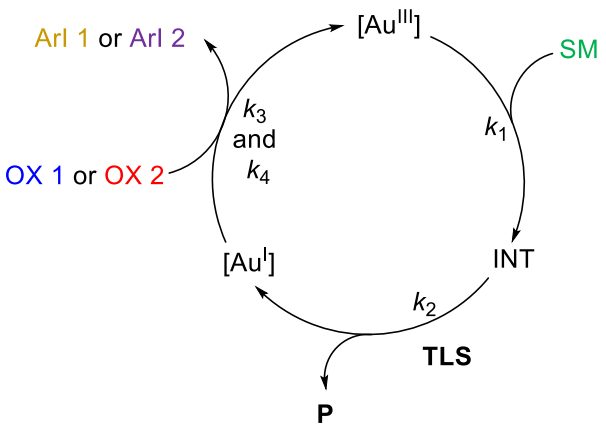

Input values:

k_1 = 100 mol^{-1} dm^3 s^{-1}
k_2 = 0.01 s^{-1}
k_3 = 1000 mol^{-1} dm^3 s^{-1}
k_4 = 2000 mol^{-1} dm^3 s^{-1}

Scheme 33: Simplified catalytic cycle that was modelled in Dynochem® to represent the reaction studied in Scheme 32.

Following the simplified catalytic cycle and setting one of the oxidants to react at twice the rate of the other, the concentrations of all components during the reaction can be simulated. The resulting plot is shown in Figure 20.

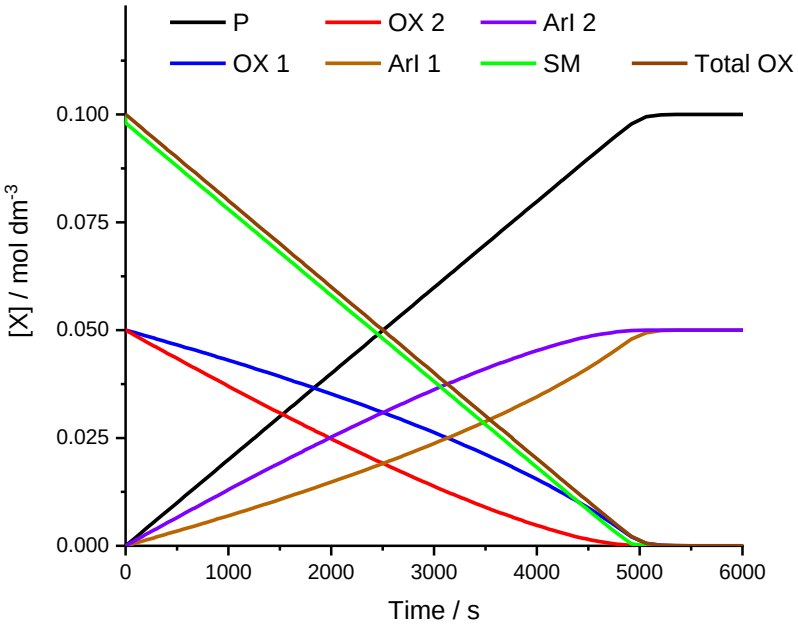

Figure 20: Reaction profile generated from modelling the catalytic cycle in Scheme 33. 0.1 M of starting material (SM) and 0.05 M of both oxidants (OX 1 and OX 2) were used as the starting point of the model. P is product of the cyclisation, ArI 1 and ArI 2 are formed from reducing the oxidant. Total Ox shows the concentration versus time profile of both oxidants together, where the decay of total oxidant is pseudo zero-order.

As the reaction proceeds, the oxidant which is set to react at a faster rate constant (OX 2) is consumed faster (red line). A difference in the relative rates of consumption is seen, where the concentration of OX 2 decreases quicker than the concentration of OX 1. However, as the oxidant is consumed, the relative probability of reacting with OX 2 is reduced compared to OX 1, increasing the rate of consumption of OX 1.

It should be noted that the overall rate of consumption of the oxidants remain tied to the turnover-limiting step, and so by looking at the total concentration of oxidant, the overall consumption of oxidant follows the same rate as the consumption of starting material.

3.3.1. Method

Monitoring reactions using ^{1}H NMR Spectroscopy

The consumption of oxidant was monitored via ^{1}H NMR spectroscopy under the reaction conditions described in Scheme 32. Figure 21 shows the stacked temporal ^{1}H NMR spectra for the competition between *p*-BrArI(OAc)$_2$ and *p*-OMeArI(OAc)$_2$, and it was observed that the peaks for the ortho protons on these oxidants are distinct and separated from the rest of the other proton peaks. This is because the iodine centre itself is in the +3 oxidation state, resulting in a more electron-poor aromatic ring, thus the protons around the aromatic ring are more deshielded and are shifted downfield. Therefore, utilising ^{1}H NMR spectroscopy, accurate concentration values were obtainable, even towards the end of the reaction, where the concentration of these oxidants are low and have small peak areas.

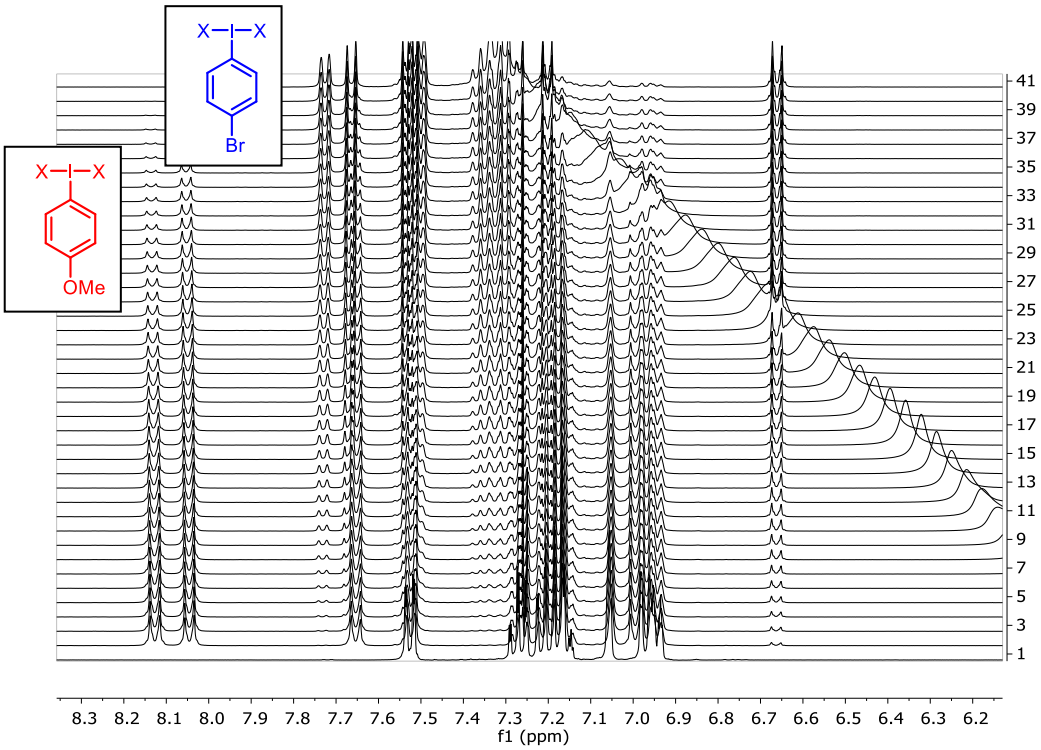

Figure 21: Stacked temporal ^{1}H NMR spectra of the reaction shown in Scheme 32, with 0.05 M *p*-BrArI(OAc)$_2$ and 0.05 M *p*-OMeArI(OAc)$_2$ as oxidant 1 and oxidant 2. 0.1 M of **C9** was used, with 2 mol% of (tht)Au(Br)$_3$ catalyst in $CDCl_3$/CD_3OD (50:1) with CH_2Br_2 as the internal standard. Each spectrum was obtained after a 60 second delay, with the first delay at 125 seconds.

3.3.2. Reaction profile

Equimolar amounts of the oxidants *p*-OMeArI(OAc)$_2$, **OMe(Ox)** and *p*-BrArI(OAc)$_2$, **Br(Ox)** were competed together to study the effect of electronics on the oxidation of gold(I) under the reaction conditions. Oxidant **OMe(Ox)** represented the electron-rich oxidant, and oxidant **Br(Ox)** represented the electron-deficient oxidant. The temporal concentration plot of both oxidants and the starting material **C9** was obtained and is shown in Figure 22.

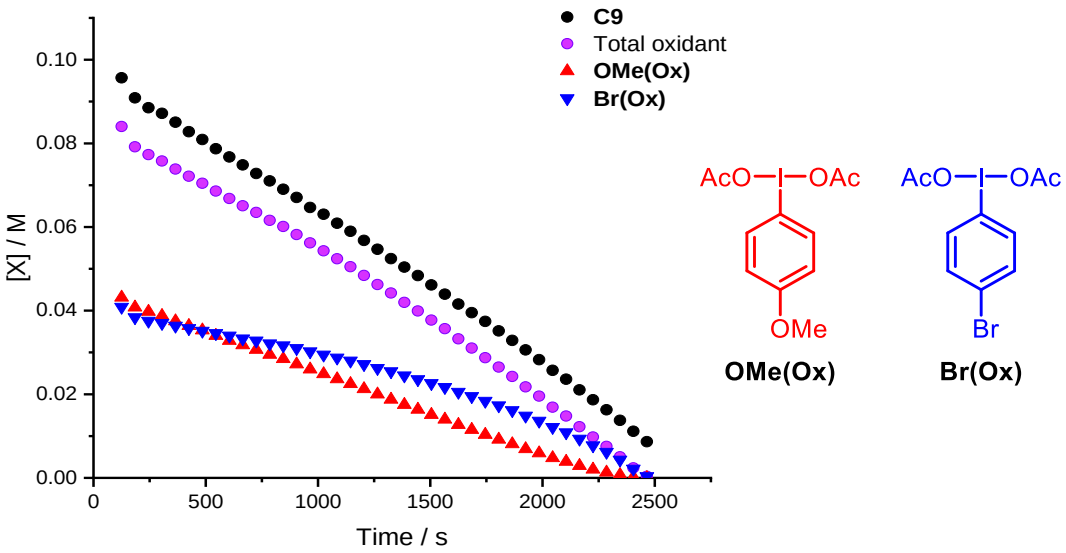

Figure 22: Intramolecular direct arylation reaction of **C9** under the conditions shown in Scheme 32, with 0.1 M starting material. Data points were obtained by ^{1}H NMR spectroscopy every 60 seconds, with CH_2Br_2 as an internal standard.

From the graph in Figure 22, the consumption of both oxidants together follows the profile for starting material consumption, in agreement that the nature of the oxidant plays no role in the overall rate of reaction. The initial drop in concentration of total oxidant is as a result of activation of the precatalyst, where five equivalents of oxidant are consumed.[43] There is also a smaller drop in the concentration of the starting material observed. This is due to a known bromodesilylation side reaction, where two of the bromides on the gold precatalyst are oxidised to bromonium, which can then react with the silane in the starting material.[50]

Focusing on the consumption of the individual oxidants, **OMe(Ox)** and **Br(Ox)**, it was found that the more electron-rich oxidant **OMe(Ox)** is consumed faster in the presence of the electron-deficient oxidant **Br(Ox)**, which is contradictory to the results from both the electrochemical and equilibration study discussed in Chapter 2. The measured and calculated potentials indicate that the electron-deficient oxidants have a higher reduction potential and are therefore more oxidising. However, initial results from the competition reactions have shown that the more oxidising oxidant does not react preferentially, indicating that the oxidation of gold(I) under these reaction conditions is under kinetic, rather than thermodynamic control.

From these observations, two preliminary hypotheses were proposed. Figure 23a illustrates the formation of an initial π-complexation between the gold(I) complex and the aromatic ring of the oxidant, prior to the reoxidation step,[88] where an oxidant with an electron-rich aromatic ring would be favoured. The second proposal (Figure 23b)[89,90] shows the dissociation of a ligand from the iodine centre, to form a more electrophilic iodonium species, which would then be the active species responsible for the oxidation of gold(I).

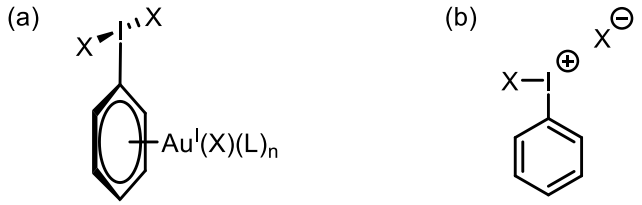

Figure 23: Two possible intermediates for the oxidation of gold(I). (a): Formation of a π-complex and (b): Dissociation of an X ligand from the iodine(III) centre.

3.3.3. Relative rates

In order to differentiate between the two hypotheses shown in Figure 23, a Hammett correlation was investigated. Correlation of the logarithm of relative rate to σ is expected to support the formation of a π-complex, whereas correlation to σ^+, where resonance from a *para* substituent to the I^+ centre is considered, would support initial ligand dissociation from the iodine(III) centre.

To quantify relative rates of oxidation, it was anticipated that Eq. 3 utilised by Singleton and Thomas[91] could be applied. In the equation, the ratio of the competing reactants (r) is dependent on the initial ratio of reactants (r_0), the fractional conversion of total competing reactants, F (between 0 and 1, where 1 represents the total consumption of both competing reactants), and the relative rate of reaction (k_{rel}). The equation can then be fitted to a plot of ratio versus conversion by varying k_{rel}.

Equation 3

$$r_{calc} = r_0 \times (1 - F)^{\left(\frac{1}{k_{rel}} - 1\right)}$$

It should be noted that the equation has been derived to be used for the calculation of natural abundance KIE; where the concentration of one competing component is significantly less than the other competing component. Thus, an approximation is used in Eq. 3, and this is discussed later on.

To test the validity of utilising Eq. 3 to calculate relative rates for the competition reactions, a plot of calculated ratio versus conversion of both components at very different rates was created and displayed in Figure 24.

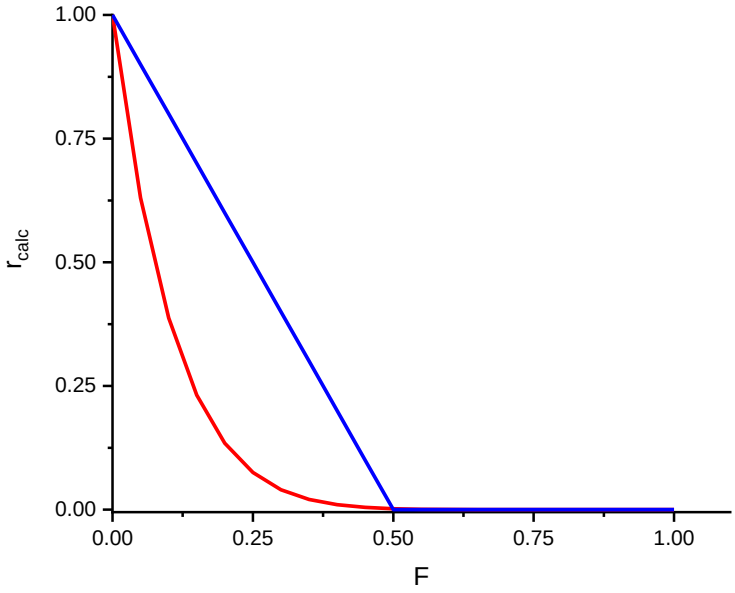

Figure 24: Graphs showing calculated ratios (r) versus conversion (F). Blue line indicates maximum ratio change calculated for a completely selective process ($k_{rel} = \infty$), and the red line indicates calculated ratios obtained using Eq. 3, when $r_0 = 1$, and $k_{rel} = 0.1$.

The resulting red curve is shown in comparison with a theoretical maximum ratio change shown in blue. This line was obtained as a result of a totally selective system (illustrated in Table 5), where one competing component (A) is consumed completely before the other competing component (B). It was observed that the ratio change shown by the red curve decreases too quickly at conversions below 0.5.

Table 5: Calculation of ratios where the competition is completely selective for the consumption of compound A.

$$A \xrightarrow[k_1]{X} C$$

$$B \xrightarrow[k_2]{X} C$$

A	:	B	r	F
0.5	:	0.5	1.0	0.0
0.3	:	0.5	0.6	0.2
0.0	:	0.5	0.0	0.5

Wolfsburg and Beigeleisen

Using an equation derived by Wolfsburg and Beigeleisen[92] from two first order reactions in A and B, shown in Table 5, the ratio of rate constants can be expressed as shown in Eq. 4.

$$\frac{k_1}{k_2} = \frac{\ln\left({}^{A}/_{A_0}\right)}{\ln\left({}^{B}/_{B_0}\right)} \qquad \text{Equation 4}$$

$$\left(\frac{k_1}{k_2} - 1\right)\ln\left({}^{B}/_{B_0}\right) = \ln\left(\frac{{}^{A}/_{B}}{{}^{A_0}/_{B_0}}\right) \qquad \text{Equation 5}$$

When r is the ratio of A and B, r= $\frac{A}{B}$,

$$\left(\frac{k_1}{k_2} - 1\right)\ln\left({}^{B}/_{B_0}\right) = \ln\left(\frac{r}{r_0}\right) \qquad \text{Equation 6}$$

And the fractional conversion, F, follows the expression where $1 - F = \frac{A+B}{A_0+B_0}$.

$$\left(\frac{k_1}{k_2} - 1\right) = \frac{\ln\left({}^{r}/_{r_0}\right)}{\ln\left[(1-F)\frac{(1+r_0)}{(1+r)}\right]} \qquad \text{Equation 7}$$

Eq. 7 was developed by Wolfsburg and Beigeleisen and relates the ratio between A and B to the initial ratio (r_0), the fractional conversion of A and B, and their relative rates of reaction $k_{rel} = \left(\frac{k_1}{k_2}\right)$.

When the abundance of one of the competing components is much lower compared to the other component, as is the case with natural abundance KIE calculations, the ratio $\frac{(1+r_0)}{(1+r)}$ can be assumed to equal to 1, and Eq. 7 simplifies to Eq. 8 and rearranges to give Eq. 3', a rearranged form of Eq. 3.

$$(k_{rel} - 1) = \frac{\ln\left({}^{r}/_{r_0}\right)}{\ln(1-F)} \qquad \text{Equation 8}$$

$$(k_{rel} - 1)\ln\,(1 - \mathrm{F}) = \ln\left({}^{r}/_{r_0}\right)$$

$$(1 - \mathrm{F})^{(k_{rel}-1)} = \frac{r}{r_0} \qquad \text{Equation 3'}$$

Eq. 7 was rearranged so that F is the subject of the equation and is shown in Eq. 9.

$$\ln(1-F)+\ln\left(\frac{1+r_0}{1+r}\right)=\frac{\ln\left({}^{r}/_{r_0}\right)}{k_{rel}-1}$$

$$\ln(1-F)=ln\frac{\left(\frac{r}{r_0}\right)^{\frac{1}{(k_{rel}-1)}}}{\frac{1+r_0}{1+r}}$$

$$F=1-\frac{\left(\frac{r}{r_0}\right)^{\frac{1}{k_{rel}-1}}}{\frac{1+r_0}{1+r}} \qquad \text{Equation 9}$$

The same test as used with Eq. 3 can used in this scenario to test the validity of Eq. 9. Using the same initial ratio and relative rates, the analogous plot to Figure 24 was constructed and displayed in Figure 25. In this case, the red curve occurs above the line representing the maximum ratio change and shows a feasible situation.

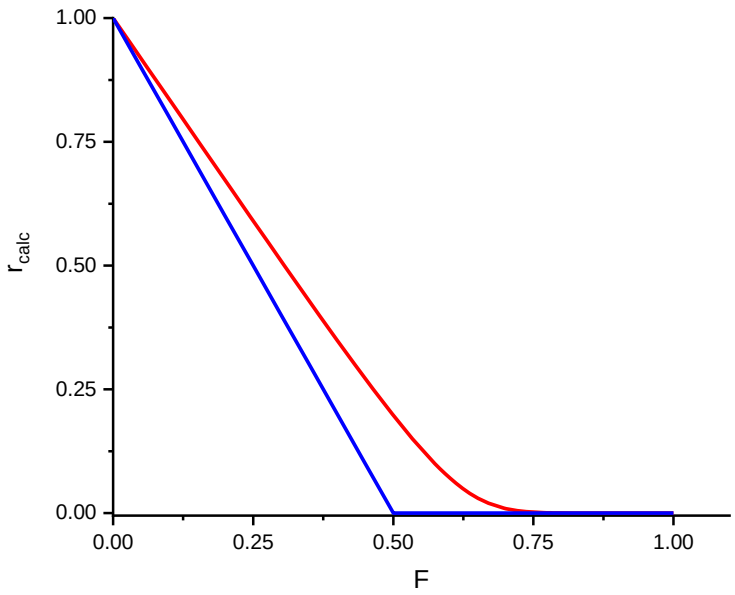

Figure 25: Graphs showing calculated ratios (r) vs conversion (F). Blue line indicates maximum ratio change calculated for a completely selective process ($k_{rel} = \infty$), and the red line indicates calculated ratios obtained using Eq. 9, when $r_0 = 1$, and $k_{rel} = 0.1$.

3.3.4. Results

Ratio versus conversion

The relative rate of oxidation of **OMe(Ox)** versus **Br(Ox)** can be obtained by fitting Eq. 9 to experimentally obtained ratios and conversion. This was carried out by calculating F and adjusting the relative rate (k_{rel}) until a good fit is achieved. The resulting plot is shown in Figure 26.

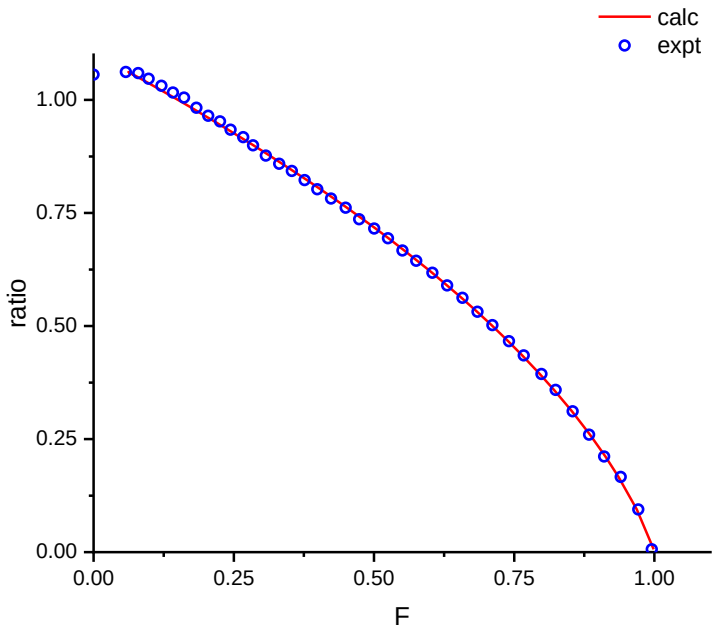

Figure 26: Ratio versus conversion plot for the competition of **OMe(Ox)** and **C4** in an intramolecular direct arylation reaction. Blue datapoints represent experimental ratios. Red line represents data calculated using Eq. 9. $k_{rel} = k_{OMe}/k_{Br} = 1.88$, r = [**OMe(Ox)**]/[**Br(Ox)**].

The best fit of the equation to experimental data was obtained when $k_{rel} = 1.88$, showing that the relative rate of consumption of **OMe(Ox)** was nearly twice as fast as the relative rate of consumption of the *p*-Br substituted oxidant, **Br(Ox)**. The initial portion of the graph, where consumption of total oxidant is low, deviates from the fitted curve and has a flatter profile. This could be due to the oxidants undergoing equilibration (discussed in Chapter 2) in the initial portion of the reaction, where bromide or bromonium from the precatalyst is still present in the reaction mixture and have not yet been removed by the starting silane to give the bromodesilylated product, as described in Section 2. An alternative reason could be that the activation of the catalyst involves the consumption of these oxidants, and their relative rates are unknown.

To ensure that the equilibration process is not occurring throughout the reaction, *p*-MeArI(OAc)$_2$ (**Me(Ox)**) and *p*-ClArI(OAc)$_2$ (**Cl(Ox)**) were competed in the presence of 2-bromothiophene, which has been previously shown to stop the equilibration between the oxidants by reacting with bromonium generated from the precatalyst.[43] The results are displayed in Table 6, entry 3.

Table 6: Comparison of relative rates obtained under different conditions to observe the effect of oxidant equilibration. $k_{rel} = k_X/k_{Me}$.

No.	Oxidant	Catalyst	k_{rel}
1	**Me(Ox)** **Cl(Ox)**	(tht)Au(Br)$_3$	0.83
2		(tht)Au(Cl)	0.86
3		(tht)Au(Br)$_3$ + 2-bromothiophene (7 mol%)	0.80
4	**Me(Ox)** **CF$_3$(Ox)**	(tht)Au(Br)$_3$	0.60
5		(tht)Au(Cl)	0.62

Competition reactions between **Me(Ox)** and **Cl(Ox)** as well as **Me(Ox)** and *p*-CF$_3$ArI(OAc)$_2$ (**CF$_3$(Ox)**) with (tht)Au(Cl) as a catalyst were carried out. (tht)Au(Cl) was previously tested in Chapter 2 and was shown to not catalyse the equilibration between these iodine(III) oxidants.

The relative rates obtained under both of the modified conditions (entries 2, 3, and 5) gave similar relative rates of reaction to the original conditions (entries 1 and 4). However, it was unexpected that the reaction with (tht)Au(Cl) (entries 2 and 5) gave a higher k_{rel} compared to the reaction with (tht)Au(Br)$_3$ (entries 1 and 4) which is known to undergo equilibration. If equilibration is occurring throughout the reaction where the oxidants are competing, the k_{rel} value was expected to be closer to one, as the equilibration favours formation of the more electron-poor oxidant.

However, the reactions for entries 2, 3, and 5 were not monitored to completion, and it is only towards full conversion where the fitting is most sensitive to changes in k_{rel} and will therefore provide a more accurate value for the relative rate of reaction.

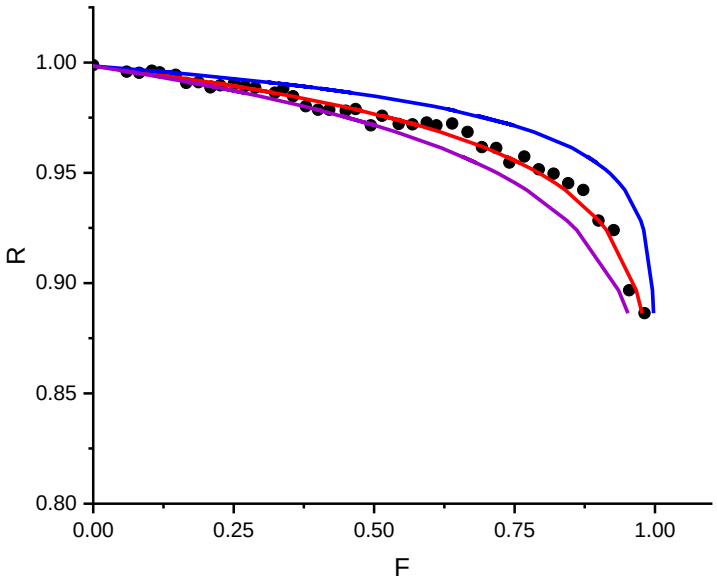

Figure 27: Graph indicating the accuracy of the k_{rel} values obtained, where the red line shows the best fit obtained (k_{rel} = 0.97) based on the experimental data (black circles). The blue line shows the resulting curve when k_{rel} = 0.98, and the black line shows the situation where k_{rel} = 0.96.

Hammett correlation

With a method of quantifying relative rates of reaction for competition reactions in hand, a Hammett plot was constructed by competing a range of *para*-substituted ArI(OAc)$_2$ oxidants against *p*-BrArI(OAc)$_2$. It was found that log (k_{rel}) correlated best with σ^+ values (Figure 28), indicating that the proposal where a ligand dissociates from the iodine centre to form an iodonium species was more likely than the formation of a π-complex, as illustrated in Figure 23.

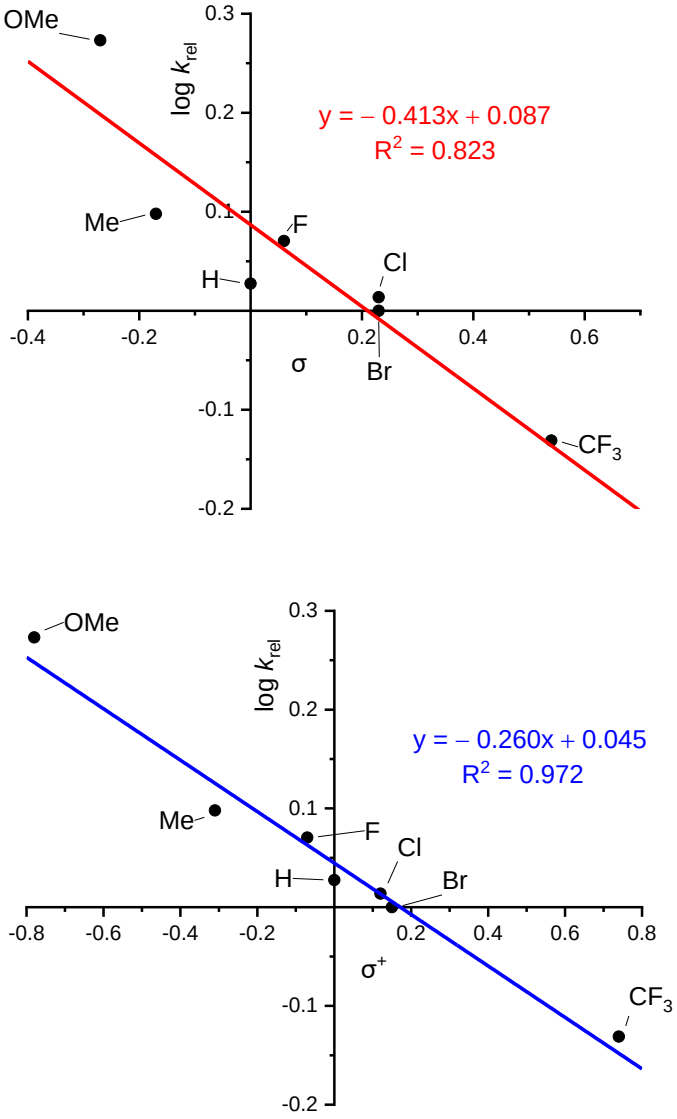

Figure 28: Comparison of Hammett plots using σ and σ^+ values. Top: log k_{rel} versus σ, bottom: log k_{rel} versus σ^+.

Furthermore, Swain-Lupton parameters[74] were utilised, where the value on the x-axis (σ_{SL}) is derived from a mix of induction (F) and resonance (R) parameters, as shown in Equation 10, where x is between 0 and 1. The best fit was obtained when x = 0.36, and the value is weighted towards the resonance component.

$$\sigma_{SL} = xF + (1 - x)R \qquad \text{Equation 10}$$

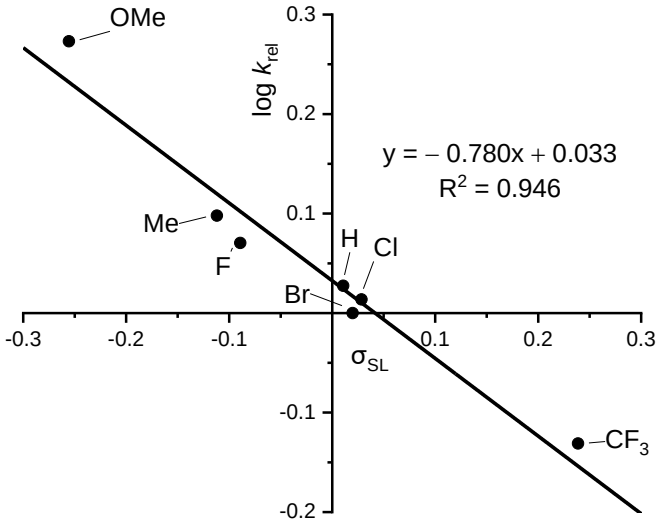

Figure 29: log k_{rel} versus σ_{SL} obtained for the competition of substituted aryl oxidants.

$\sigma_{SL} = xF + (1 - x)R$, where $x = 0.36$.

3.4. Competition of alkyl oxidants

To completely rule out the possibility of needing π-complexation prior to oxidation of the gold(I) intermediate, as shown in Figure 23, the reactivity of an alkyl oxidant was analysed. Since these oxidants have no aromatic rings, if the alkyl oxidant is active under the reaction conditions, this would further illustrate that the oxidation occurs initially via the dissociation of a ligand attached to the iodine centre to form an iodonium species, as drawn in Figure 23.

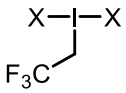

Alkyl(Ox)

Figure 30: Hypervalent iodine(III) oxidant with an alkyl group in the equatorial position.

3.4.1. Synthesis

Alkyl hypervalent iodine(III) oxidants shown in Figure 30 can be synthesised from the oxidation of trifluoroethyliodide (**C11)** with trifluoroperacetic acid.[93,94] From the generated bistrifluoroacetate compound **C12**, the sulfonate analogues, such as tosylate **C13** or mesylate **C14** can be synthesised by reacting with the corresponding sulfonic acids, as illustrated in Scheme 34. These compounds were found to be stable and could be stored in the refrigerator for several months without observable degradation.

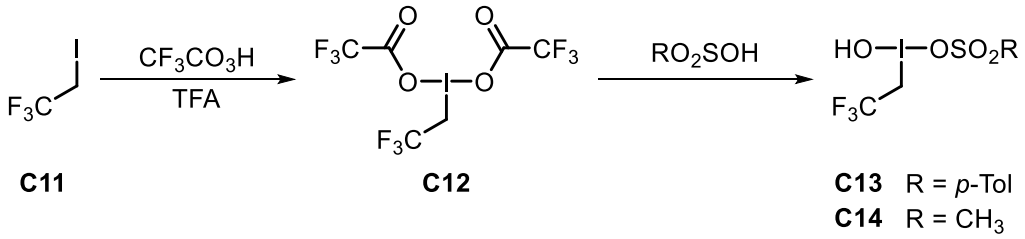

Scheme 34: Synthetic route towards the synthesis of a hypervalent iodine(III) oxidant with an alkyl group in the equatorial position.[93]

However, the use of trifluoroperacetic acid is undesirable, as it is potentially explosive.[95] Other methods have been developed, where trifluoroperacetic acid is generated in-situ from trifluoroacetic anhydride and hydrogen peroxide,[96] but the avoidance of forming any trifluoroperacetic acid was favourable.

An initial attempt at utilising sodium perborate in acetic acid[97] did not give any hypervalent iodine(III) product when analysed by ^{1}H NMR spectroscopy. It was then thought that we could take advantage of the equilibration reaction (discussed in Chapter 2) and use an aryl oxidant to oxidise the alkyl iodide within the coupling reaction. Since it was seen in Figure 26 that equilibration does occur at the very beginning when using (tht)Au(Br)$_3$ as a catalyst, a small amount of the alkyl oxidant could be generated, and subsequently competed against the initial aryl oxidant added when equilibration was halted.

3.4.2. Equilibration and competition

When the reaction shown in Scheme 35 was carried out, it was found that an insignificant amount of alkyl oxidant (less than 1%) was generated during the reaction.

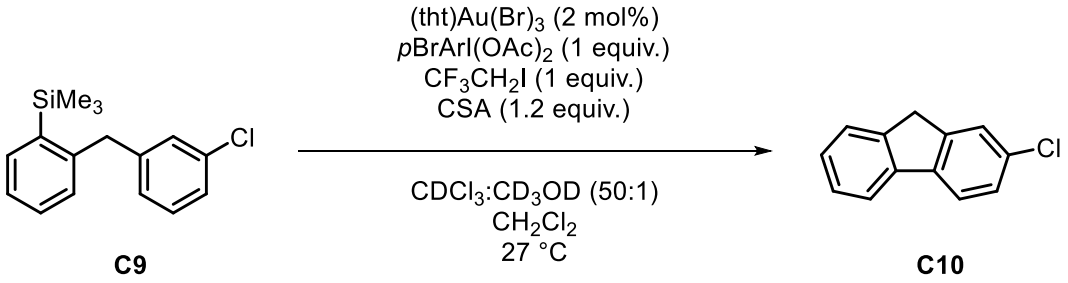

Scheme 35: Intramolecular cyclisation of **C9** catalysed by gold(III), with **Br(Ox)** and alkyl iodide in an attempt to generate some alkyl iodine(III) oxidant.

Since relying on the equilibration reaction within the coupling reaction was unsuccessful, the equilibration was carried out in a separate vial. The equilibration reaction was then halted by the addition of an electron-rich aromatic compound (*m*-OMeArI), which removes bromonium,

the species assumed to catalyse the equilibration reaction. Aryl silane **C9** and the gold(III) catalyst were then added to this mixture, and the consumption of both the alkyl oxidant and the aryl oxidant were monitored. Figure 31 summarises the experiment carried out.

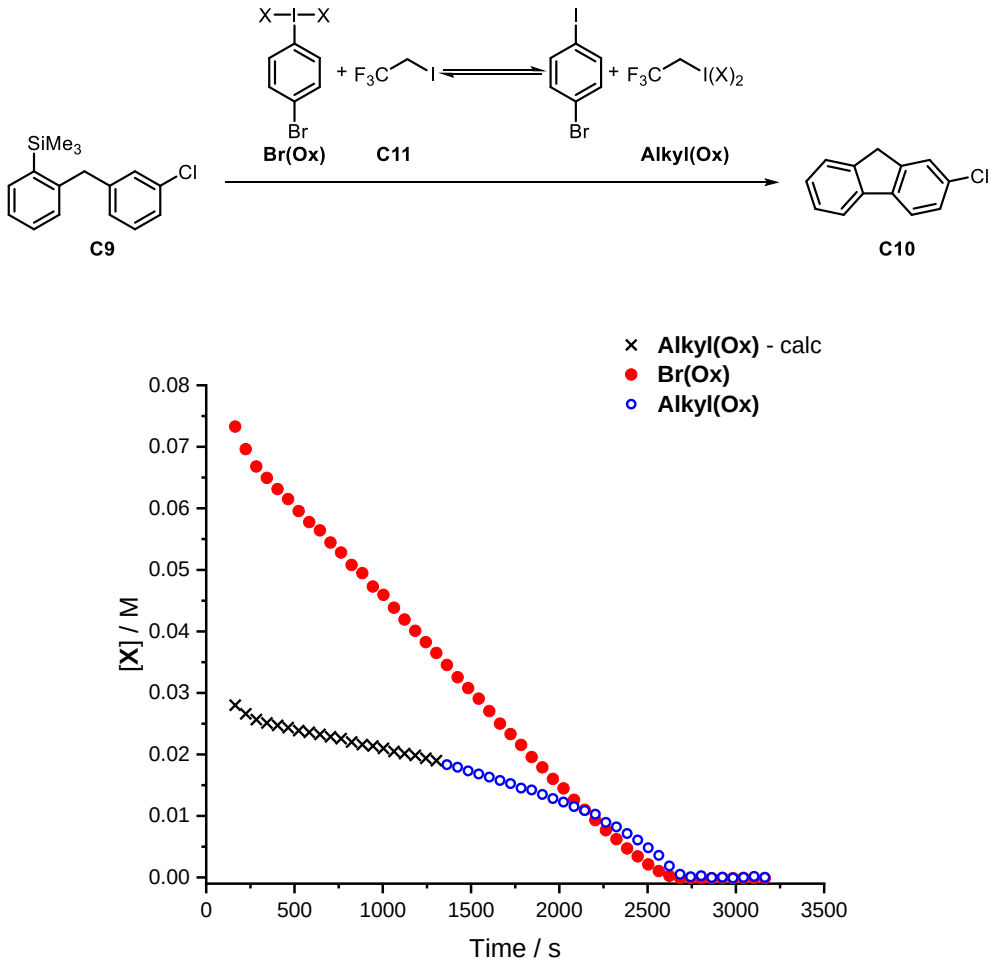

Figure 31: Intramolecular cyclisation of compound **C9**, with 2 mol% (tht)Au(Br)$_3$ as the catalyst. **Br(Ox)** (1 equiv.) and CF_3CH_2I (1 equiv.) were equilibrated with Bu_4NBr (1 mol%) in $CDCl_3/CD_3OD$, and the equilibration was halted with *m*-OMeArI. Silane **C9** and (tht)Au(Br)$_3$ were added to the mixture. All concentrations were obtained relative to CH_2Cl_2 as a standard. Circle datapoints were directly obtained based on the integrations of the corresponding peaks, and cross datapoints were obtained based on the alkyl iodide integration.

The integrations of **Alkyl(Ox)** at the start of the reaction was not directly possible due to an overlapping peak, originating from camphorsulfonic acid. This peak shifts to a higher frequency as the reaction progresses when more of the acid is liberated as the iodine oxidant is consumed. As a result, **Alkyl(Ox)** can be monitored from the latter half of the reaction onwards. However, the initial profile for **Alkyl(Ox)** can be estimated by back calculating from the alkyl iodide (**C11**) peak.

The graph in Figure 31 shows that although **Alkyl(Ox)** reacts at a significantly slower rate when compared to **Br(Ox)**, it is still active in reoxidising gold(I) under the reaction conditions. Its activity is highlighted towards the end of the reaction, (between 2500 s and 3000 s) and as the concentration of **Br(Ox)** drops, the rate of consumption of **Alkyl(Ox)** increases to maintain a constant turnover rate for the catalyst.

Plotting the ratio versus conversion for the competition of **Alkyl(Ox)** and **Br(Ox)**, it was found that the relative rate of reaction of **Alkyl(Ox)** versus **Br(Ox)** is 0.49 (Figure 32).

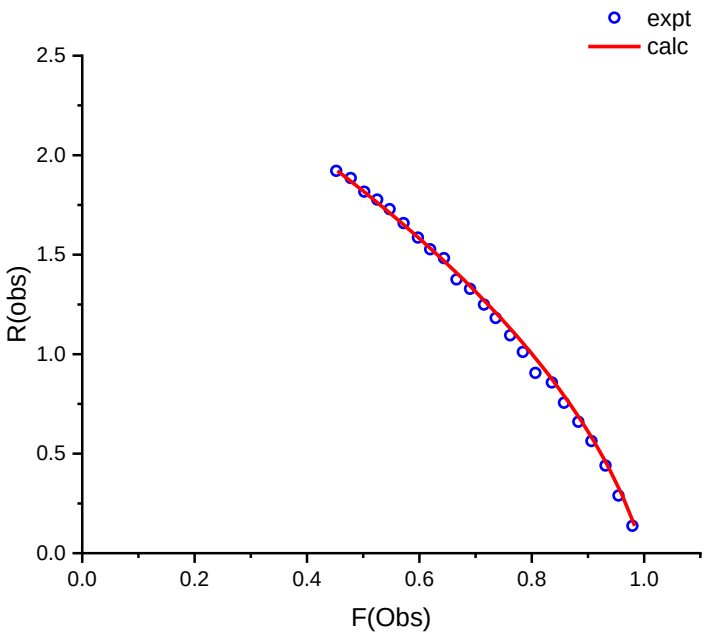

Figure 32: Graph showing the ratio versus conversion from the data in Figure 31. Experimental values illustrated by the circles, and calculated fit using Eq.97 shown with the red line, where $k_{rel} = k_{alkyl}/k_{Br} = 0.49$, r = [**Alkyl(Ox)**]/[**Br(Ox)**].

3.4.3. Validation of method

In an attempt to validate this method for competing oxidants, the same procedure as illustrated in Figure 31 was carried out, where **Cl(Ox)** and **Me(Ox)** were competed. Unfortunately, only the oxidant integrations during the first half of the reaction was obtainable, due to the camphorsulfonic acid peak, which shifts towards the oxidant peaks as the reaction proceeds, resulting in a less accurate value of k_{rel} obtained.

These oxidants were also competed, where equilibration was carried out whilst the direct arylation reaction was occurring. The results are summarised in Table 7.

Table 7: Comparison of k_{rel} values obtained with the competition of **Me(Ox)** and **Cl(Ox)** under different conditions: **Me(Ox)** and **Cl(Ox)** added as oxidants, **Me(Ox)** and ClArI equilibrated prior to the reaction (as described in Figure 31) and **Me(Ox)** and ClArI equilibrated as the intramolecular cyclisation was carried out, as attempted in Scheme 35.

No.	Conditions	k_{rel}
1	Me(Ox) and Cl(Ox)	0.83
2	Me(Ox) and ClArI, preequilibrated	0.84
3	Me(Ox) and ClArI, equilibrate in situ	0.83

3.5. Proposed mechanism

Based on the results of this chapter, a tentative mechanism has been proposed (Scheme 36) for the oxidation of the gold(I) complex formed under the reaction conditions shown in Scheme 32. Initial dissociation of an X ligand on the iodine(III) oxidant is proposed to occur, and this is supported by electron-rich oxidants having a higher k_{rel}. Furthermore, log k_{rel} correlates best with σ^+ compared to σ, as well as resonance-weighted Swain-Lupton parameters, indicating that resonance towards a positive charge is important.

From this, the X ligand could coordinate to the gold(I) centre to give an anionic complex, which is then oxidised by the iodonium compound generated to give a reduced iodoarene and an oxidised gold(III) complex with the second X ligand from the oxidant attached.

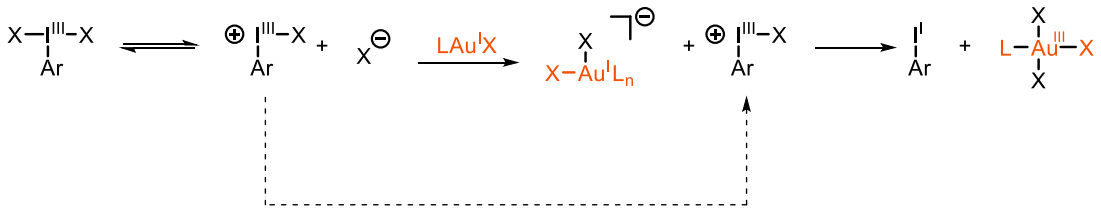

Scheme 36: Proposed mechanism of gold(I) oxidation with hypervalent iodine(III) oxidants under the gold(III) catalysed direct arylation conditions. Initial dissociation of the X ligand from the oxidant is thought to occur prior to oxidation of the gold(I) complex.

3.6. Conclusions

Competition experiments between different oxidants within a gold(III) catalysed direct arylation reaction have shown that electron-rich hypervalent iodine(III) oxidants have a higher relative rate of reaction, when compared to electron-poor oxidants. This is contrary to the results obtained in Chapter 2, where electron-deficient oxidants were found to be stronger oxidants, with higher reduction potentials. Therefore, it is suggested that the oxidation of gold(I) within the reaction conditions studied is under kinetic control, rather than thermodynamic control.

Quantitative relative rate data was obtained using a modified version of an equation derived by Wolfsburg and Beigeleisen.[92] Fitting of this equation to experimentally obtained data allowed for k_{rel} to be obtained, and log k_{rel} was found to correlate better to σ^+ when compared to σ values for substituents on the aromatic ring of the oxidant. This led to the proposal that dissociation of an X ligand from the iodine(III) centre was occurring prior to oxidation of gold(I).

To investigate the necessity of π-complexation of the oxidant to the gold centre for oxidation, an alkyl iodine(III) oxidant was synthesised via an equilibration reaction with **Br(Ox)** (described in Chapter 2), and the two oxidants were subsequently competed in a direct arylation reaction. It was found that the alkyl oxidant was active in turning over the catalyst, which disfavours the proposal that π-complexation of the oxidant to gold(I) was required prior to oxidation. These observations led us to propose the mechanism in Scheme 36.

Chapter 4

Absolute rates of oxidation

4.1. Introduction

In the previous chapter, it was highlighted that the rate of oxidation within a gold(III) catalysed intramolecular reaction of arylsilanes could not directly be monitored, as the turnover-limiting step of the catalytic cycle does not involve the oxidation of gold(I).[50] Instead, competition studies were carried out where two hypervalent iodine(III) oxidants were co-reacted and the relative rates of one oxidant over the other could be analysed. It was found that electron-rich oxidants had higher relative rates over electron-deficient oxidants, even though the studies in Chapter 2 indicated that the more electron-deficient oxidants have a higher redox potential, and are therefore are the stronger oxidants, thermodynamically. It was proposed that dissociation of an X ligand from the iodine(III) centre occurred prior to oxidation of the gold(I) complex.

However, there are several issues associated with the competition studies. Firstly, interactions between the hypervalent iodine(III) species cannot be ruled out, and this may have affected the results obtained. Furthermore, as described in Chapter 2, hypervalent aryliodine(III) oxidants and aryl iodides can equilibrate to form a mixture of hypervalent aryliodine(III) species under the reaction conditions studied for the intramolecular arylation reaction.

Therefore, different approaches of obtaining absolute rate of reactions were considered and will be discussed in this chapter.

4.2. Preliminary results

4.2.1. Monitoring resting state

Previous studies

Prior to exploring the reoxidation of gold(I) generated from the intramolecular cyclisation reaction of arylsilanes such as **D1** in Scheme 37 to give **D2**, the resting state of the catalyst in the catalytic cycle was examined. Previous work[50] indicated that the turnover limiting step was likely to be a reductive elimination process from the gold(III) complex, **D3**.

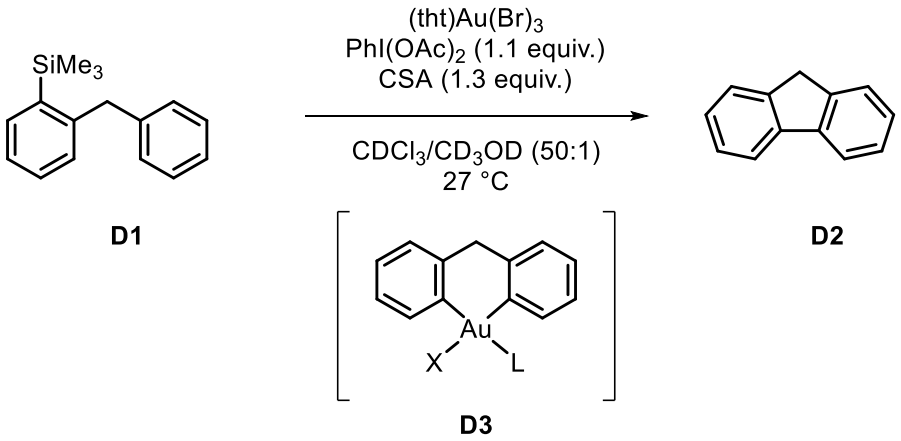

Scheme 37: Summary of previous studies carried out on the reaction of a gold(III) catalysed intramolecular arylation reaction of substrate **D1** to give **D2**. Complex **D3** is proposed to be the resting state of the catalyst.[50]

Current studies

The resting state was previously observed by ^{1}H NMR spectroscopy, where a peak at approximately 4 ppm was observed, with an integration equating to the concentration of catalyst added.[50] Similar analysis was carried out on the reaction of compound **D4** to give **D5** (Figure 33, top) and the reaction was monitored by ^{19}F NMR spectroscopy. The observed peak corresponding to the resting state (**Au-int**) was found to be at approximately −116 ppm, as illustrated in Figure 33.

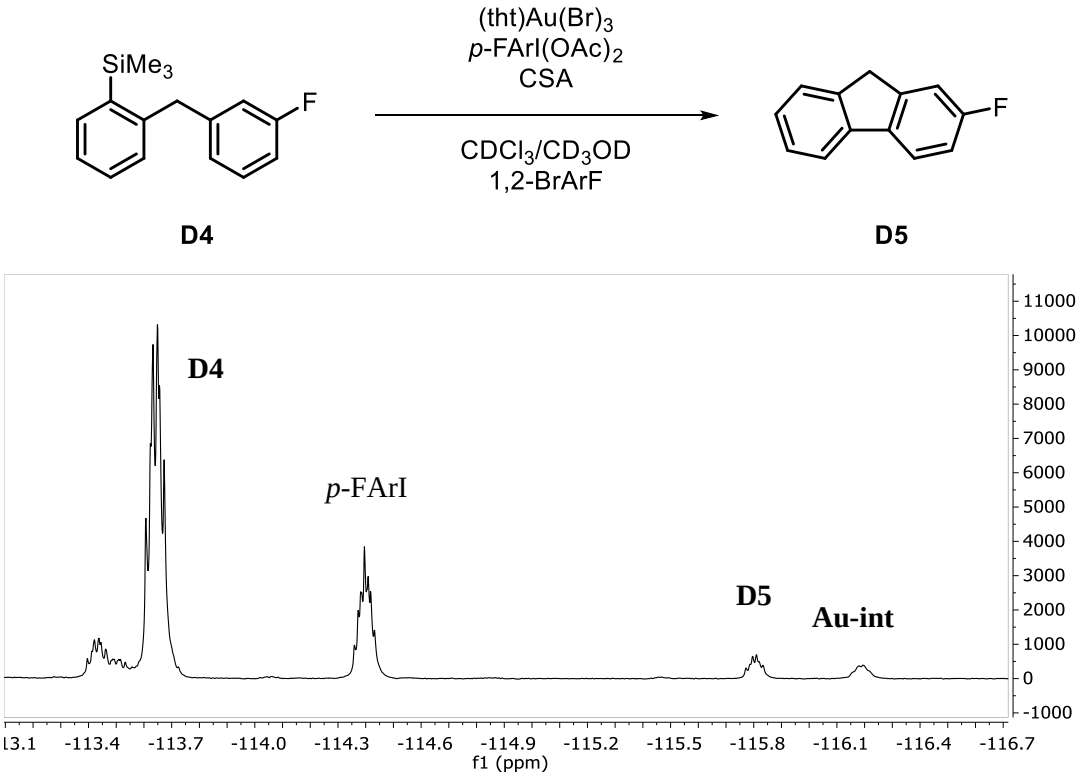

Figure 33: Top – Reaction monitored by ^{19}F NMR spectroscopy. Bottom – ^{19}F NMR spectra obtained at 159 s into the reaction illustrated at the top, with 0.2 M **D4**, 5 mol% (tht)Au(Br)$_3$, 0.75 equiv. *p*-FArI(OAc)$_2$ and 0.8 equiv. CSA in 0.5 mL $CDCl_3/CD_3OD$ (50:1). Approximately 10% conversion was observed from the spectra above.

Addition of a standard (2-BrArF) to the gold pre-catalyst stock solution in a 1:1 ratio allowed for a more accurate insight into the amount of gold added to the reaction mixture prior to initiation of the reaction. The volume of the gold stock solution added was varied and the results are shown in Figure 34. All three datasets have the same profile and start with an increase in the concentration of the resting state, as the catalyst is activated. The flat profile in the middle shows the steady-state concentration of this intermediate, and it was found that its integration equated to the same concentration as the integration of the standard. This is consistent when the volume of the stock solution was changed, and thus the amount of (tht)Au(Br)$_3$ and standard added.

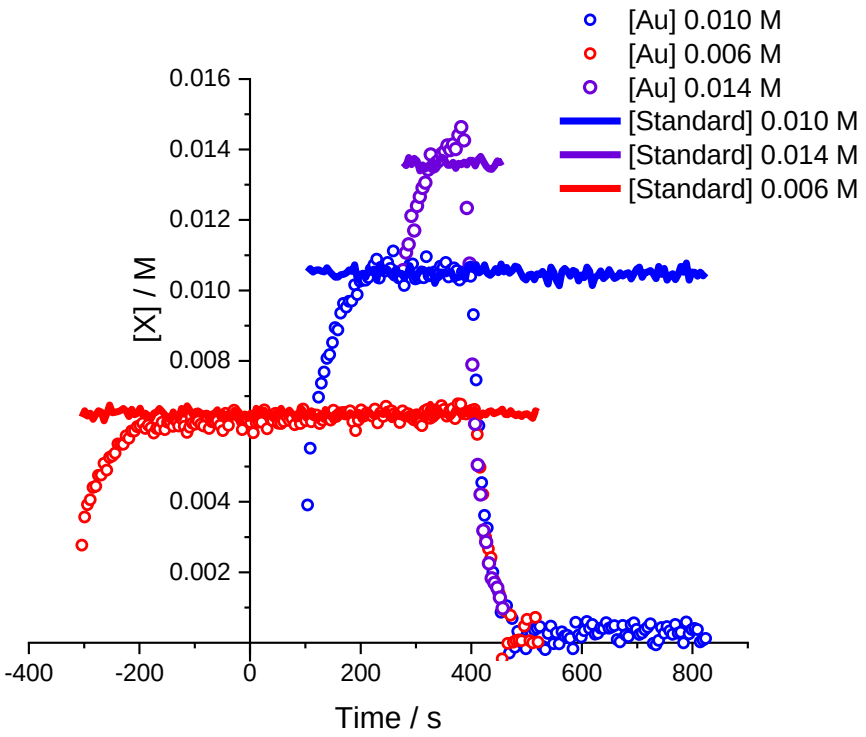

Figure 34: Temporal concentration plot showing the intermediate thought to be the resting state of the catalyst and the standard (2-BrArF) added. Three different concentrations of catalyst were used, and the time scale for the red and the purple data was adjusted. Reaction carried out is illustrated at the top of Figure 33 with 0.2 M **D4**, 0.75 equiv. *p*-FArI(OAc)$_2$, 0.8 equiv. CSA in 0.5 mL $CDCl_3$/CD_3OD (50:1). Red data corresponds to 3 mol% (tht)Au(Br)$_3$, blue data corresponds to 5 mol% (tht)Au(Br)$_3$, and purple data corresponds to 7 mol% (tht)Au(Br)$_3$ used.

Decay of resting state

The graph shown in Figure 34 shows the temporal concentration profiles of the resting state of the catalysts and the standard added. The time scale of the runs for 0.006 M and 0.014 M of [Au] were adjusted so that the decay profile of the formed intermediate overlapped, illustrating a first order decay. Furthermore, as shown in Figure 35, the data fits well to a first order profile.

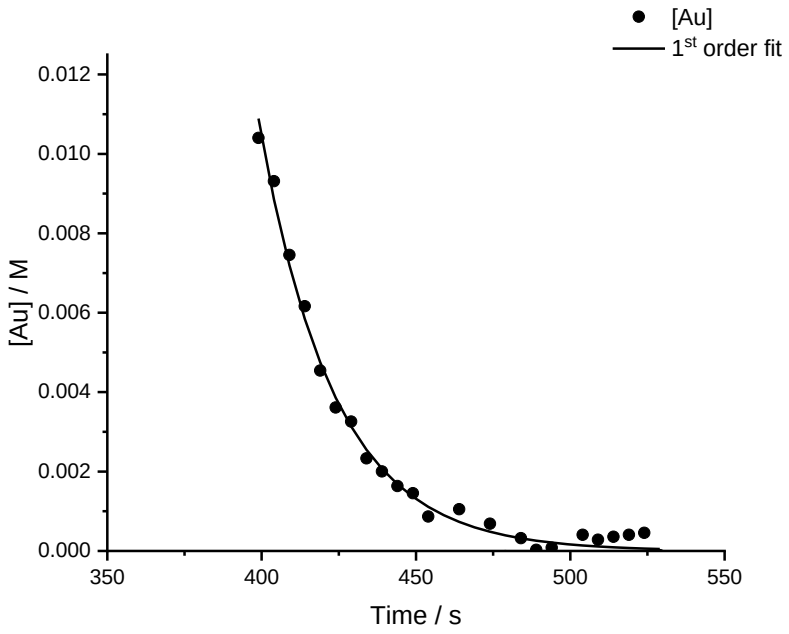

Figure 35: First order fit to the decay observed in Figure 34, [Au] = 0.010 M.

Nature of resting state

It was previously proposed that the turnover-limiting step of the reaction was a reductive elimination process from a biaryl gold(III) complex, where the resting state of the catalyst is bound by both rings of the starting material shown below in Figure 36.[50]

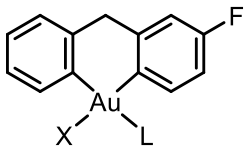

D6

Figure 36: Proposed intermediate for the resting state of gold in the intramolecular cyclisation reaction of **D4**, catalysed by (tht)Au(Br)$_3$. The X and L ligands attached to the gold are unknown.

To further probe the nature of the resting state, two different arylsilanes were compared as starting materials, as shown in Scheme 38. Both these starting materials contain a fluorine label on them, but on the different aryl rings. These starting materials would converge on the same intermediate, if the above proposed resting state was true.

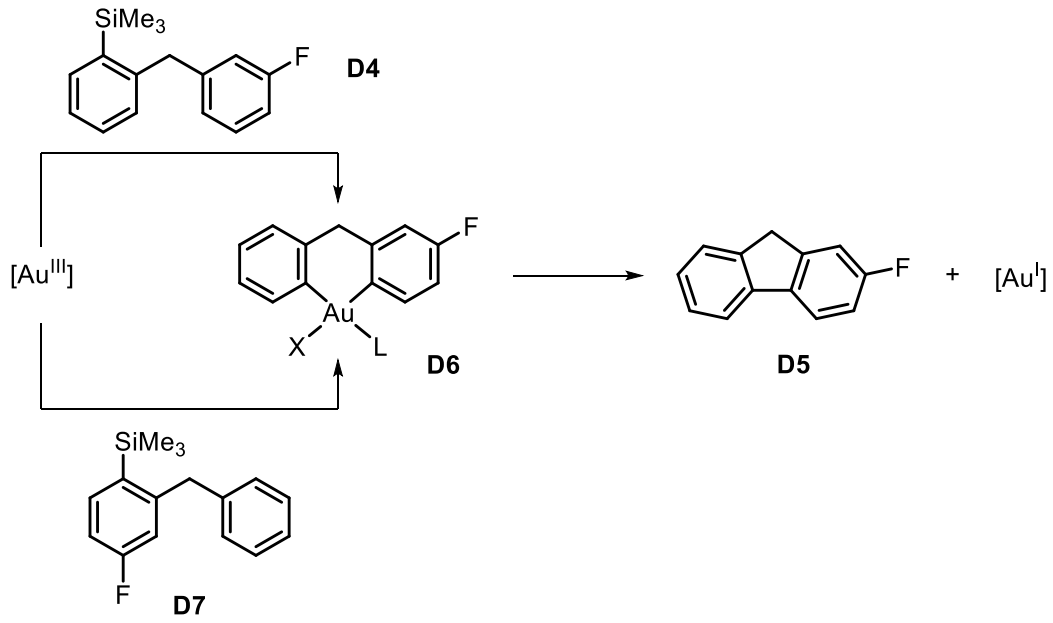

Scheme 38: Comparison of the cyclisation reaction of **D4** and **D7** via intermediate **D6**.

The ^{19}F NMR spectra for both reactions, obtained after the reactions indicated in Scheme 38 were initiated, are illustrated in Figure 37. The peaks relating to both starting materials are shown on the spectra. It should be noted that the product peak is identical in both reactions, as expected. Furthermore, the peak for the resting state of the catalyst previously identified in Figure 33 occur with identical chemical shifts in both reactions. This shows that they either converge on the same intermediate, or that both intermediates have the fluorine label at very similar chemical environments.

Considering the chemical shifts in the first reaction with compound **D4** as the starting material, the fluorine in the bromodesilylation side product has a chemical shift of −113.4 ppm, where the silane itself has its fluorine chemical shift at −113.6 ppm. This shows that even a change in the silane ring has a visible impact on the chemical shift of the fluorine on the arene ring. Therefore, it is more likely that the resting state identified in both reactions are the same.

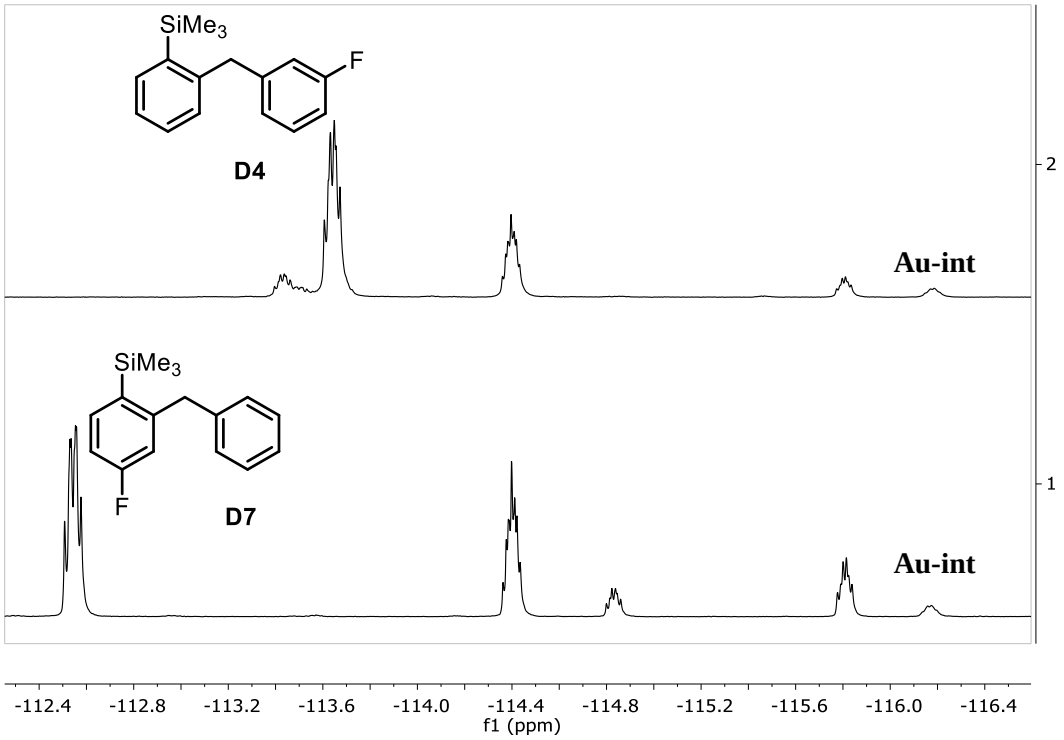

Figure 37: ^{19}F NMR spectra obtained for the reaction of **D4** (top) and **D7** (bottom) under the reaction conditions described in Figure 33, obtained after 159 s and 390 s respectively.

4.2.2. Reoxidation of Gold(I)

It was previously suspected that the resulting gold(I) species formed after reductive elimination had a very short lifetime, with the reaction mixture forming significant amounts of colloidal gold ("gold black") when there is insufficient oxidant present.[43]

To probe the lifetime of the gold(I) species generated under the reaction conditions described in Scheme 39, experiments were carried out where sub-stoichiometric amounts of oxidant were added, and the consumption of oxidant was monitored by ^{1}H NMR spectroscopy. When all the oxidant had been consumed, additional portions of oxidant were then added to the reaction mixture at different time intervals. The reaction mixture was then monitored further to examine whether the catalyst was still active. This is summarised in Scheme 39.

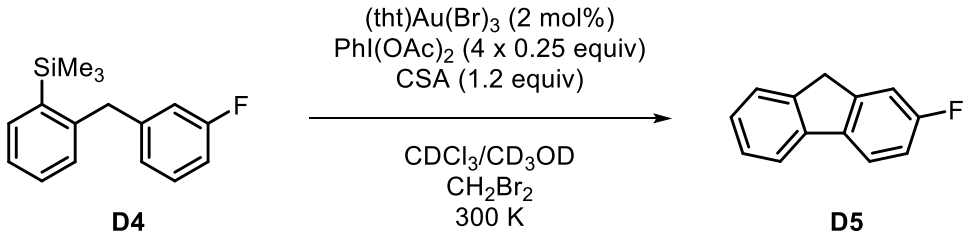

Scheme 39: Intramolecular cyclisation of substrate **D4**, with multiple addition of sub-stoichiometric amounts of oxidant.

The graph in Figure 38 shows the consumption of oxidant versus time, where the lines indicate when more oxidant was added to the reaction mixture. With subsequent additions of oxidant, the rate of reaction decreases. This is consistent with the suggestion that the catalyst, in absence of the oxidant is metastable. Therefore, each time more oxidant is added, a smaller amount of catalyst is reactivated.

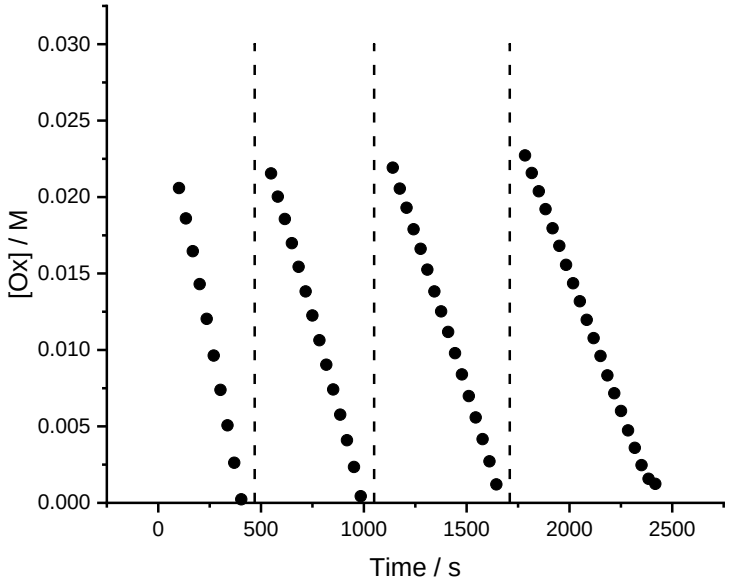

Figure 38: Temporal concentration plot of the oxidant in the reaction illustrated in Scheme 39. The black data points represent the oxidant monitored, and the vertical dotted lines show the times when more oxidant was added. Conditions used: 0.1 M **D4** in 1.0 mL $CDCl_3/CD_3OD$ (50:1). Delay times where no oxidant was present were at 58 s, 47 s, and 30 s in order.

The relative rates of reaction after each addition were plotted against the cumulative length of time the reaction mixture was left without oxidant, and the data from Figure 38 is shown as Run 1. The experiment was repeated with increasing and decreasing delay times, and the relative rates of the reactions are shown in Figure 39. In general, a longer delay results in a lower amount of reactivated catalyst.

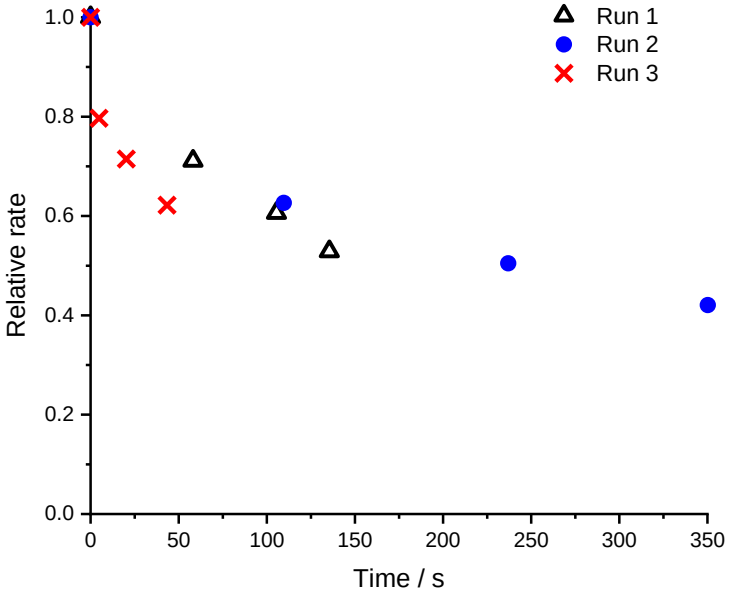

Figure 39: Graph showing the relative rate of reaction versus total time the reaction shown in Scheme 39 was left without oxidant.

By comparing the relative rates of reaction after the first addition of oxidant across the three runs, the amount of reactivated catalyst is lower for the longer delays (Run 2). However, there seems to be a shallower drop in reaction rate when comparing the first data point of Run 3 and Run 2. Approximately 20% of the catalyst was lost in 5 seconds of Run 3 and approximately double that amount, 40% of the catalyst, was lost in 120 seconds in Run 2. This indicates that a larger amount of catalyst is deactivating as soon as the reaction runs out of oxidant, and the rate of deactivation slows down the longer the reaction is left without any oxidant present.

Interestingly, the amount of time the reaction mixture was left without oxidant does not directly correlate with the amount of catalyst reactivated, and instead, this was affected also by the number of times it was reactivated. For example, in Run 3, there was 60% of the active catalyst remaining in the reaction by the third reoxidation, and the total amount of time the reaction mixture has been left in the absence of oxidant is approximately 50 seconds. However, in Run 2, the first reoxidation, which occurs after approximately 120 seconds also results in 60% of the active catalyst remaining. This could be a result of the addition process, where impurities, such as water could introduced alongside the oxidant, which may aid the decomposition of the catalyst.[98]

4.3. Aims of the chapter

These sets of experiments have indicated that the resulting gold(I) species is stable for long enough under the reaction conditions to be reoxidised, and therefore, the oxidation of gold(I) can be studied. Scheme 40 summarises the approach in monitoring this oxidation, based on the known mechanism of this reaction. [43,50]

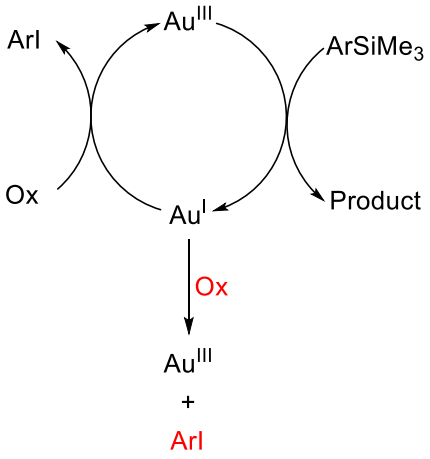

Scheme 40: Summary of the method used in monitoring the oxidation of gold(I) under the intramolecular direct arylation reaction catalysed by (tht)Au(Br)$_3$.

In this proposed approach, the gold(III) catalytic cycle is initiated where with an excess of starting material (ArSiMe$_3$) over the oxidant (Ox). Once the oxidant has been fully consumed, the catalytic cycle stops at the gold(I) complex following reductive elimination to release the product. A second oxidant can then be added to the mixture, and the subsequent reaction can then be monitored to directly observe the kinetics of oxidation of the generated gold(I) complex.

4.4. Monitoring fast reactions

Previous studies[50] have indicated that the rate of gold(I) oxidation is too rapid[i] to be observed by NMR spectroscopy via the method illustrated in Scheme 39 and Figure 38, where the time between addition of oxidant and the first acquired spectra was approximately 80 seconds.

Furthermore, the results in Figure 38 indicate that all of the catalyst that can be reactivated has already been oxidised by the time the first spectra was obtained. This was seen in the concentration versus time profile of the starting material shown in Figure 40. Since the rate of reaction follows zero-order kinetics, the consumption of starting material will show a straight-line profile. If more gold is reactivated after the first spectra has been taken, the rate of reaction for the latter sections of the reaction will be faster. However, the spectra were collected with a 30 second interval between data points, and small changes in the rate may not be observable at this resolution.

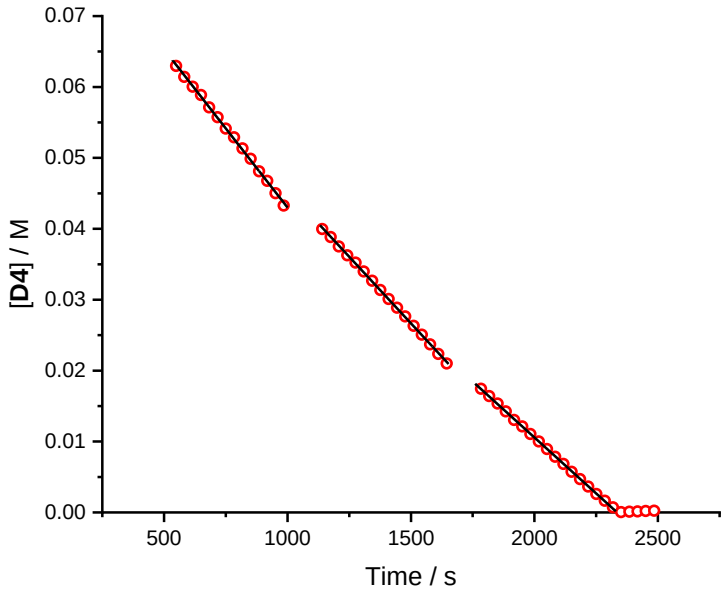

Figure 40: Temporal concentration plot of starting material, **D4** in the reaction shown in Scheme 39 under the reaction conditions described in Figure 38.

[i] Fastest reaction carried out achieved 95% conversion to product in 10 minutes using 1 mol% catalyst. This gave 1 turnover every 6.5 seconds.

4.4.1. UV-vis spectrometry

Since the reaction between the generated gold(I) complex and hypervalent iodine(III) oxidants is thought to be rapid, it was proposed that the oxidation reaction could be monitored by UV-spectroscopy, as data can be acquired on the millisecond timescale.[99] Furthermore, it was found that reagents can be easily added to cuvettes via an adder-mixer,[100–102] which consists of a rod with a square or rectangular attachment at one end. A small amount of reagent (approximately 100 μL)[102] can be placed on the attachment at the end of the rod, and the solutions are mixed by vertical movements of the rod, achieving dead times of a few seconds.[100]

The plots shown in Figure 41 shows an overlay of the UV spectrum obtain for the gold(III) precatalyst, the arylsilane **B4**, and $PhI(OAc)_2$ with CSA. From this, it was proposed that the growth of the gold(III) complex (product from oxidation of gold(I)) could be monitored, as the peak at approximately 400 nm occurs in the absence of any other absorbance peaks.

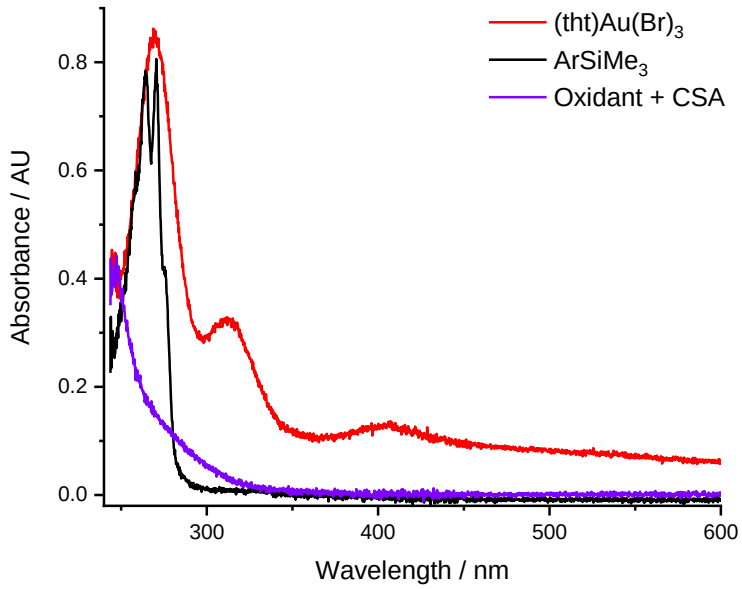

Figure 41: Overlay of UV-vis absorbance spectra of $(tht)Au(Br)_3$ (0.033 mM), **D4** (0.5 mM), and $PhI(OAc)_2$ (0.05 mM) with CSA (0.06 mM). All compounds were made in a solution of $CHCl_3$.

However, further testing on the reaction conditions showed that the absorbance of catalytic amounts of gold resulted in an almost negligible peak at around 400 nm. Increasing the amount of gold used in the reaction would result in increasing the amount of oxidant used, and the saturation limit of the UV-vis detector would be reached. The graph shown in Figure 42 illustrates the t_0 time-point of the reaction, where only starting material **B4** and (tht)Au(Br)$_3$ are present, and the t_1 time-point of the reaction, where the oxidant has been added to the mixture to start the reaction.

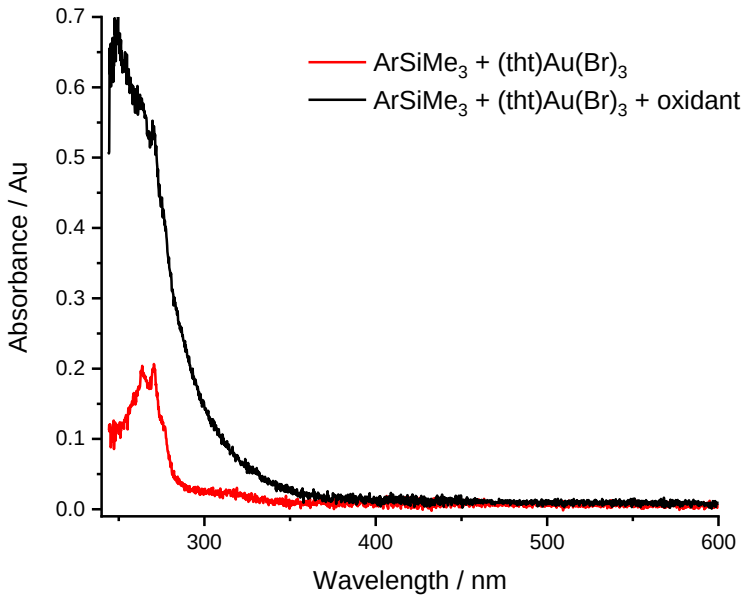

Figure 42: Overlay of UV-vis absorbance spectra of the reaction shown Figure 33 (0.3 mM **D4** and 10 mol% (tht)Au(Br)$_3$). Red line shows the t_0 spectra and the black line shows the t_1 spectra obtained following initiation by addition of oxidant (0.45 mM oxidant).

4.4.2. Rapid injection

Setup 1.0

Having had little success in utilising UV-vis spectroscopy in monitoring the oxidation of gold(I), it was proposed that NMR spectroscopy could be utilised, and reagents could be added whilst the reaction was inside the magnet of the NMR spectrometer to reduce the dead time obtained. A schematic of the NMR tube design is shown in Figure 43.

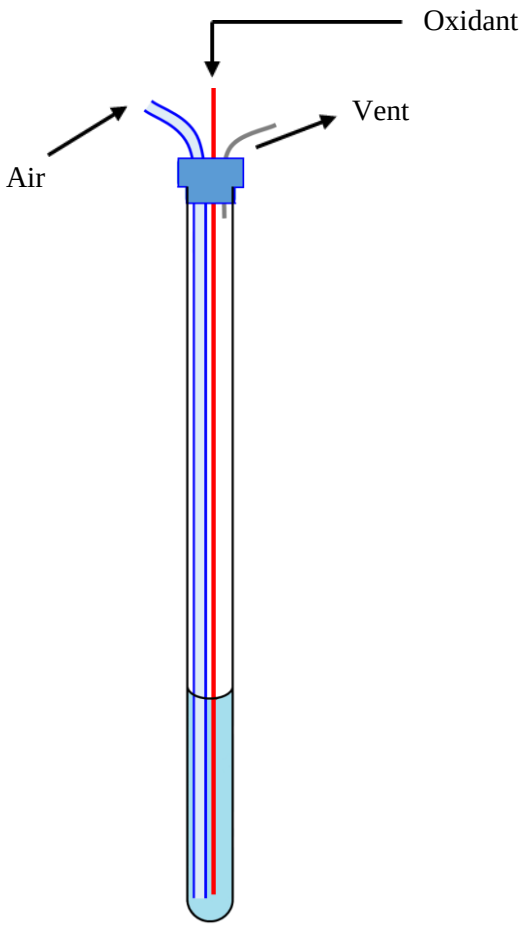

Figure 43: Summary of design utilised to add and mix reagents inside the NMR magnet. Three pieces of tubing were inserted through a standard plastic NMR cap. Oxidant was added via the tubing shown in red, air was bubbled through the light blue tubing to mix the reagents. The grey tubing was used as a vent. Reaction mixture illustrated as pale blue at the bottom of the tube.

Three pieces of tubing were inserted into the lid of the NMR tube, with two of them going to the bottom of the tube. The oxidant was delivered through the reagent tubing (red in Figure 43) and the second tube was used to deliver air bubbles to the reaction mixture. This was to allow for mixing to take place when the new oxidant was added within the magnet of the NMR spectrometer. The third piece of tubing acted as a vent to prevent a build-up of pressure within the tube.

At the other end of the reagent tubing, a three-way valve was attached to allow for a reservoir syringe and a loading syringe to be connected. The movement of reagent is shown in Figure 44. The reservoir syringe was used fill the loading syringe (red arrow) and subsequently used to prime the reagent tubing (blue arrow). This helps prevent the formation of air bubbles within the reagent tube.

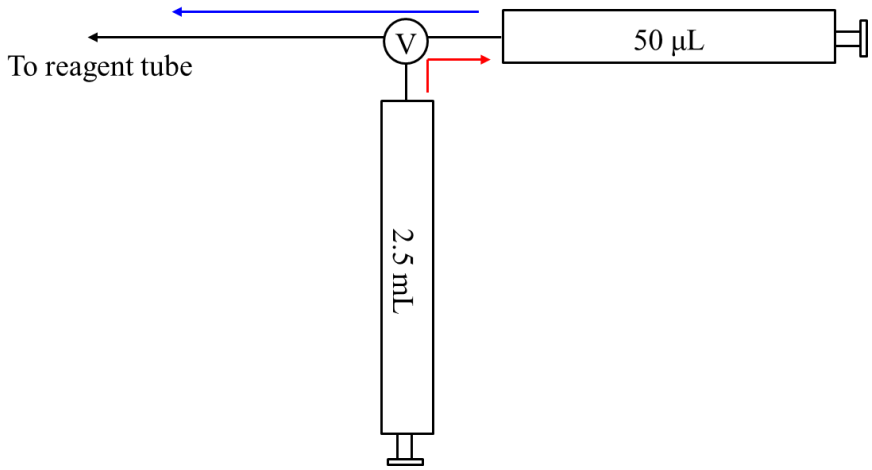

Figure 44: Syringe setup that was connected to the end of the reagent tube (red in Figure 43). The 2.5 mL syringe was used as the reservoir syringe, and the 50 µL syringe was used as the loading syringe which injected the reagent into the NMR tube. Movement of reagent followed the red arrow first, then the blue.

Using this setup, the mixing efficiency was tested using a blue solution in chloroform injected into chloroform. Figure 45 shows the results taken after the bubbling has stopped, which occurs at approximately 4 seconds after the bubbler was turned off. The blue solution was injected just before the bubbler was turned off.

Figure 45: Injection of a blue solution into chloroform. Image was taken approximately 4 seconds after the addition of the blue solution, and after bubbling has stopped.

Reaction monitoring using setup 1.0

From Figure 45, it appears that the solution is fully mixed by the time the bubbling stops. The setup shown in Figure 43 and Figure 44 was then used to study the reoxidation of gold(I) by addition of a new oxidant to the reaction mixture, as discussed in Scheme 40.

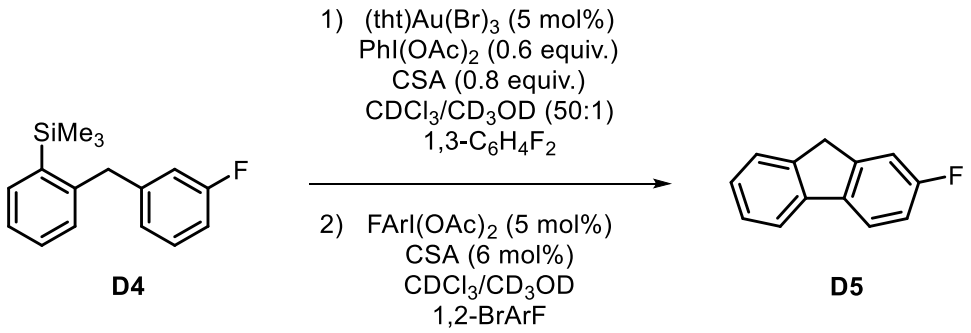

Scheme 41: Intramolecular cyclisation of substrate **D4** with substoichiometric amounts of oxidant. A second oxidant was added after the reaction ran out of initial oxidant.

The reaction shown in Scheme 41 was carried out to obtain preliminary results. In the first part of the reaction, intramolecular cyclisation of **D4** was carried out with sub-stoichiometric amounts of oxidant. Once the oxidant was used up, a fluorine-labelled oxidant (*p*-FArI(OAc)$_2$) was added, and the formation of the *p*-FArI was monitored.

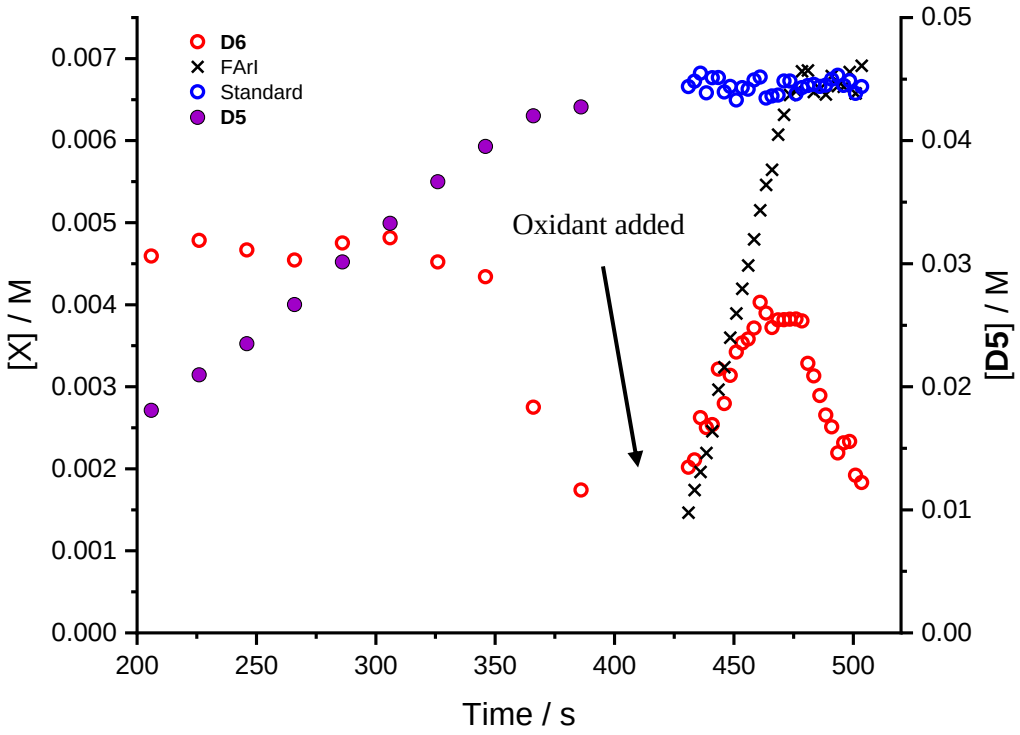

Figure 46: Graph showing the temporal concentration of the product from the intramolecular cyclisation reaction, **D5** (Scheme 41), the product from the added oxidant, *p*-FArI, the proposed resting state of the catalyst (**D6**) and the internal standard (2-BrArF) added in a 1:1 ratio with *p*-FArI(OAc)$_2$. Data obtained every 20 seconds before addition of oxidant, and every 2.5 seconds after addition of oxidant. All integrals were obtained by ^{19}F NMR spectroscopy relative to 1,3-difluorobenzene.

The graph in Figure 46 shows the temporal concentration plot of the reaction in Scheme 41. The first portion of the graph (up to 400 s) shows the growth of the product, and the concentration of the resting state of the catalyst. As discussed previously, the profile of the resting state matches that shown in Figure 34. When the formation of product **D5** stops, the bubbler was turned on, and more oxidant was added. The next timepoint obtained was when the bubbling had halted, and this can be seen by monitoring the concentration of the standard (1,3-$C_6H_4F_2$) added at the very beginning of the reaction. During the bubbling, the concentration of this standard drops, as air is introduced into the sample, and the solution is displaced from the active volume in the NMR probe head. This is shown in Figure 47 where the absolute integration of the standard is plotted against time.

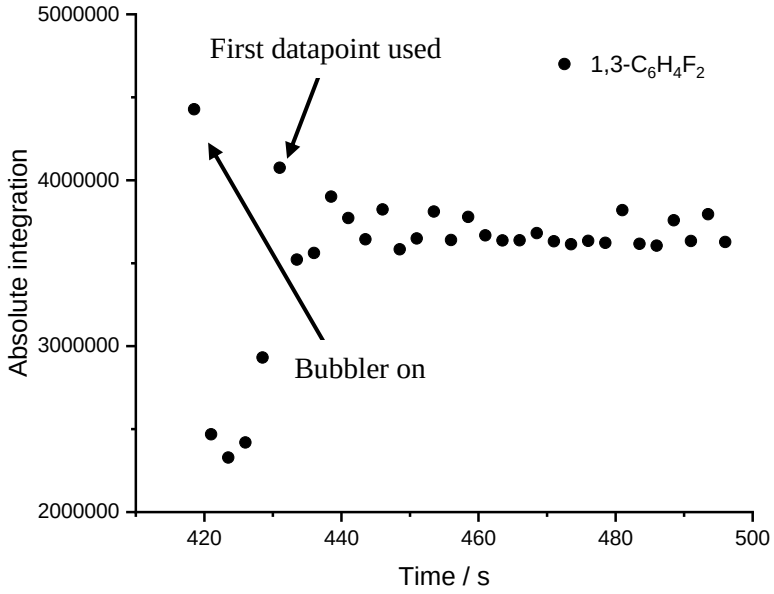

Figure 47: Absolute integration of 1,3-difluorobenzene obtained by ^{19}F NMR spectroscopy as the bubbling was started.

From the graph shown in Figure 46, after addition of the oxidant, the formation of reduced oxidant (*p*-FArI) was monitored, along with the concentration of the gold resting state (**D6**) and the standard added together with the oxidant (1,2-BrArF). It was observed that the growth of *p*-FArI was linear, which was unexpected as this indicates that the concentration of oxidant, at this point in the reaction described in Scheme 42, plays no role in the rate of gold(I) oxidation. It was then thought that the added oxidant was not mixed well when added to the reaction in the NMR tube, and that the production of *p*-FArI was controlled by mixing. However, the concentration of the standard added together with the oxidant indicates that the mixture within the receiver coils have a constant concentration over the monitored time.

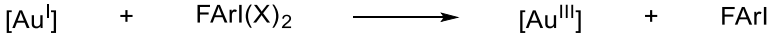

Scheme 42: Summary of expected reaction between the gold(I) complex formed and the added oxidant.

Setup 1.1

A drawback from the design shown in Figure 44 was that the time of oxidant addition was not known. Furthermore, the point when more oxidant was added was not observable by NMR spectroscopy as the signals obtained during bubbling was too weak. A modification of this design was carried out, where a trigger was accommodated into the setup so that the addition of oxidant resulted in the start of NMR acquisition. This is illustrated in Figure 48.

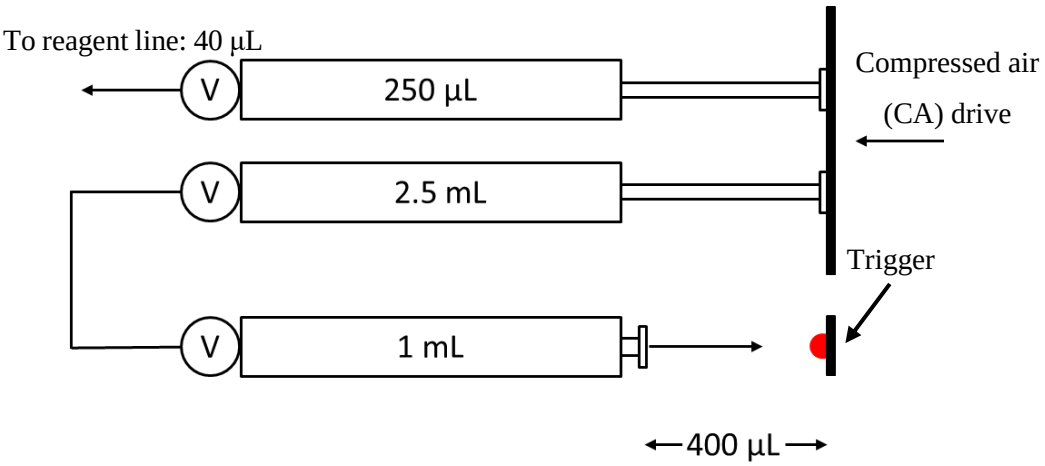

Figure 48: Syringe setup with a trigger to start spectra acquisition on the NMR spectrometer. Three-way valves are shown as V in a circle.

The design shown in Figure 48 has three syringes, with one of the syringes as the waste syringe (1 mL). The 250 µL syringe (reagent syringe) directly connects to the reagent line to deliver oxidant inside the NMR tube, and the 2.5 mL syringe (trigger syringe) was filled with water and connects directly to the waste syringe. The trigger syringe pushes out the plunger of the waste syringe so that the trigger is pushed. A three-way valve was used to load and unload the syringes and to prime the reagent line, similar to that shown in Figure 44.

Both the reagent syringe and the trigger syringe are connected to the same push plate and is driven by a compressed air (CA) drive. This allows for a faster flow of reagent to the reaction inside an NMR tube, which would assist in the mixing.

The waste syringe was positioned at a distance which required 400 µL of solution from the trigger syringe to completely extend the syringe plunger so that it meets the trigger. Using the syringe sizes as shown in Figure 48, this equates to 40 µL of reagent added to the NMR tube.

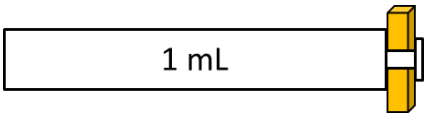

Figure 49: Setup of spaces on the plunger of the waste syringe. Larger spaces result in less volume required to push the trigger.

Spacers were made to reduce the distance between the plunger of the waste syringe and the trigger as shown in Figure 49. This reduces the amount of water required from the trigger syringe, and thus allows for a variable amount of reagent added. The spacers were designed so that 5 µL – 40 µL of reagent can be added, with 5 µL increments.

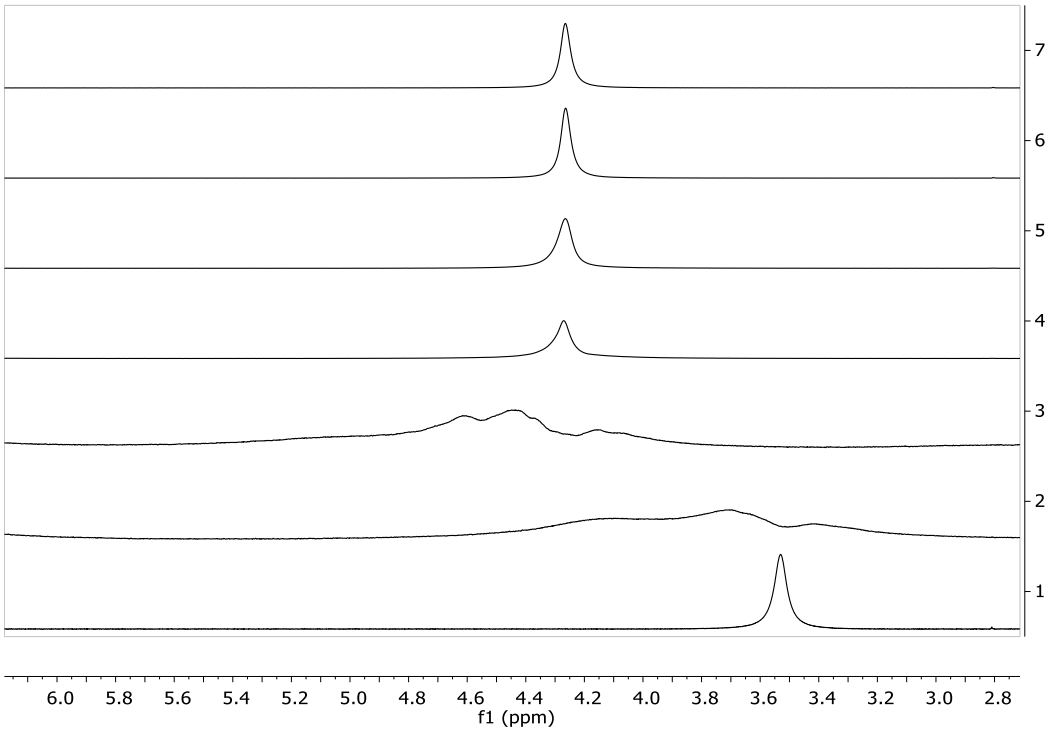

Figure 50: ^{1}H NMR spectra obtained from the injection of AcOH in $CDCl_3$ (20 μL) into a 0.5 mL solution of *p*-fluoroaniline in $CDCl_3$.

The mixing of the setup shown in Figure 48 with bubbling was tested using an acid-base reaction between *p*-fluoroaniline and acetic acid (AcOH) in $CDCl_3$. The ^{1}H NMR spectra obtained are shown as a stack in Figure 50, where the first spectrum was obtained before addition of acetic acid, the second spectrum was obtained as soon as the trigger started acquisition and subsequent spectra (3-7) were obtained at intervals of 3 seconds. The bubbler was turned off approximately 2 seconds after acetic acid was added.

Figure 50 shows that the sample inside the NMR tube was fully mixed by spectrum 4, at which point, the bubbling has stopped. This occurs at approximately 6 seconds after the addition of AcOH.

Reaction monitoring using setup 1.1

The reaction shown in Scheme 41 was repeated with the current setup and varying the amount of oxidant added. Unfortunately, problems were encountered with the wire connecting the trigger and the NMR spectrometer, which meant that the exact time point the new oxidant was added could not be recovered. However, using the information gained from Figure 50, the point of oxidant addition could be estimated to be within a 3 second interval. An example of this is shown below in Figure 51. Acquisition was started before bubbling and addition of the new oxidant. The point at which bubbling began can be seen in the broadening of the peaks (spectrum 9, Figure 51) and ceases by spectrum 17. Oxidant can be seen appearing in spectrum 16, so spectrum 15 was taken as t = 0. The peaks for oxidant and the 1,2-BrArF standard seen prior to oxidant addition was attributed to the reagents within the tubing setup in the NMR tube.

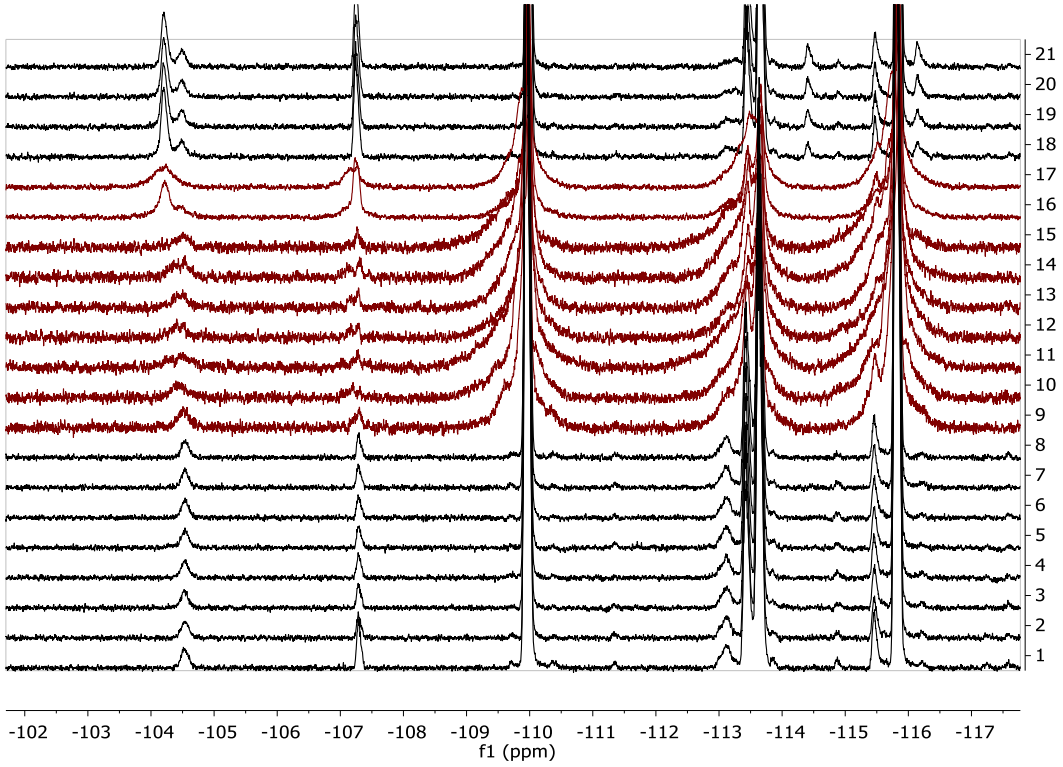

Figure 51: ^{19}F NMR spectra obtained from the reaction in Scheme 41 (0.2 M **D4**). Spectra 1-8 were obtained prior to bubbling and addition of new oxidant. The spectra shown in red were obtained when bubbling occured. Spectra 18-21 were obtained following the addition of *p*-FArI(OAc)$_2$ (0.005 mmol). From left to right, the peaks correspond to: oxidant in solution (−104.2 ppm), oxidant in tube (−104.5 ppm), 1,2-BrArF (−107.3 ppm), 1,3-difluorobenzene (−110.0 ppm), **D4** (−113.7 ppm), *p*-FArI (−114.4 ppm), **D5** (−115.9 ppm) and **Au-int** (−116.2 ppm).

The amount of oxidant added was modified by injection of different volumes of the same stock solution from the reagent syringe (Figure 48). This was achieved by using the spacers described in Figure 49 to adjust the starting point of the plunger from the waste syringe. The product from the oxidant added was monitored, and the results are illustrated in Figure 52.

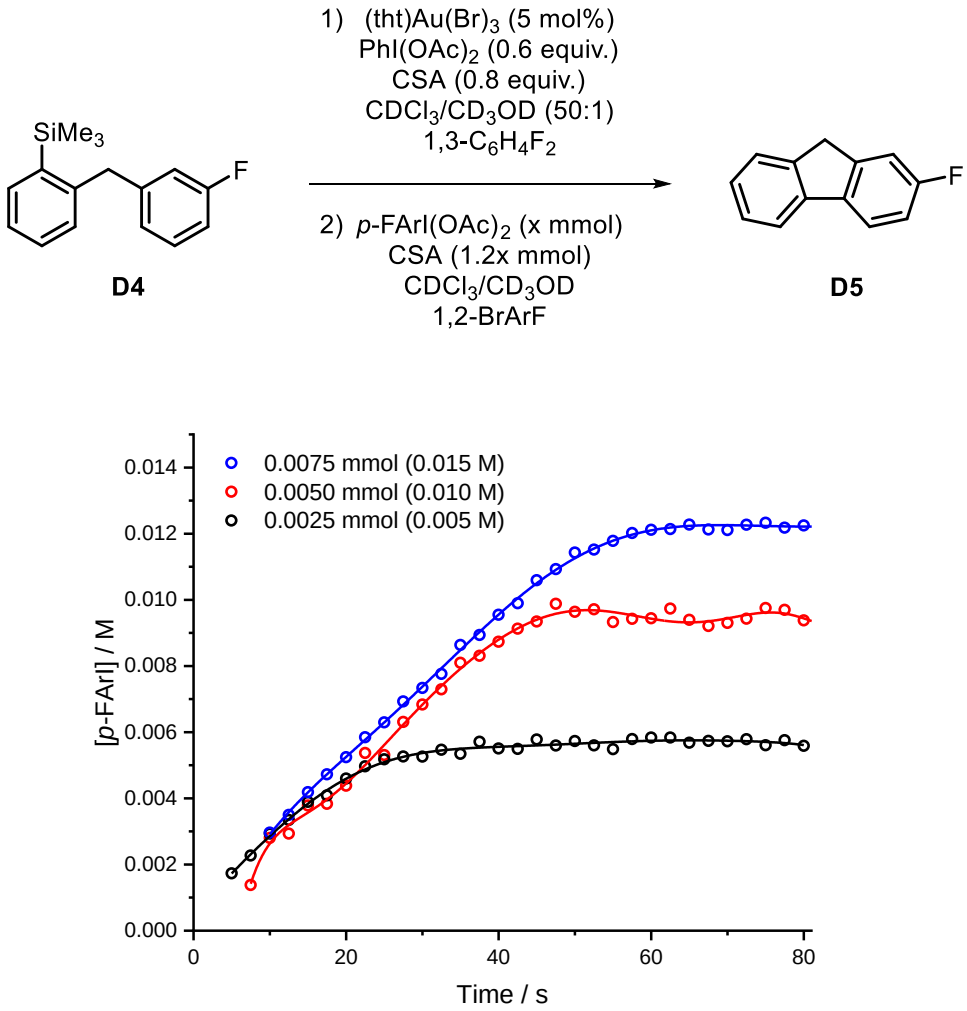

Figure 52: Top – summary of reaction monitored by ^{19}F NMR spectroscopy with 0.2 M **D4**. Bottom – temporal concentration plot of *p*-FArI, product from the oxidation of gold(I).

The growth in *p*-FArI follows a linear profile with similar gradients across the three different amounts of oxidant added. This was similar to the results obtained in Figure 46, where a linear increase in *p*-FArI was also observed. However, in Figure 52, the growth of product has more of a curvature towards the end. This is highlighted when a high-order polynomial fit was applied, and with the data from the addition of 0.0025 mmol of oxidant.

The final amounts of product obtained for addition of 0.005 mmol and 0.0075 mmol of oxidant was found to be lower than the amount added. This was possibly as a result from a small leak between the syringe and the three-way valve which played a bigger role when a larger force (compressed air drive) was used to push the reagents out. However, the concentration of *p*-FArI obtained at the end was found to be the same as the amount of standard added (in a 1:1 ratio) together with the oxidant.

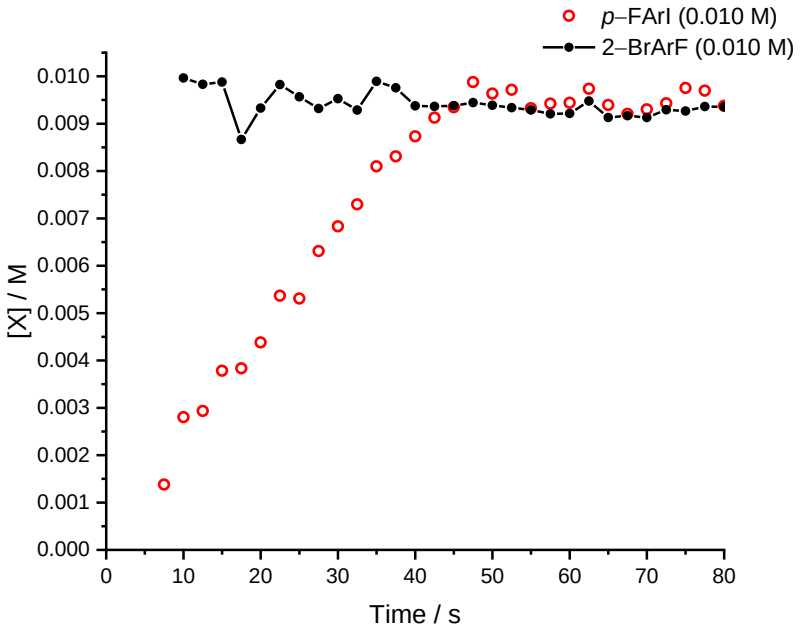

Figure 53: Graph showing the concentration of *p*-FArI and 2-BrArF as the internal standard versus time of the reaction shown in Figure 52, top, after the addition of 0.10 M *p*-FArI(OAc)$_2$.

With the exception from the addition of 0.0050 mmol of oxidant (red), results from both the addition of 0.0075 mmol (blue) and 0.0025 mmol (black) of oxidant appear to have an initial jump in the concentration of *p*-FArI generated. This may have resulted from an initial region of high concentration of oxidant before the sparging of air mixes the solution. The mixing of a blue solution into chloroform shown in Figure 54 was obtained approximately one second after addition, and a clear gradient can be seen between the bottom and top of the solution in the NMR tube. However, it is still important to note that the exact time of oxidant addition is unknown, and therefore this jump could have been a result of an inaccurate setting of t = 0.

Figure 54: Injection of 20 uL of blue solution into chloroform. Approximately one second after injection and turning off the bubbler. A concentration gradient can be seen where the colour is deeper at the bottom of the NMR tube.

Furthermore, when the temporal concentration plot of the oxidant and aryl iodide were overlaid (Figure 55), the initial concentration of oxidant was seen to be a lot higher than the concentration of its product obtained at the end of the reaction.

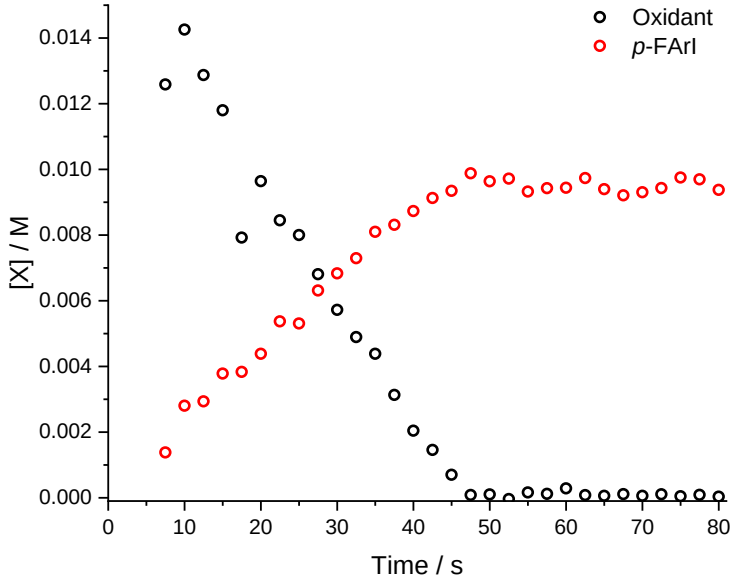

Figure 55: Graph showing the concentration change of added oxidant and *p*-FArI over time of the reaction shown at the top of Figure 52, after the addition of 0.10 M *p*-FArI(OAc)$_2$.

Although the exact timepoint that oxidant was added cannot be accurately determined, the resulting concentration gradient within the NMR tube may still have affected the results shown in Figure 52. Alternative design setups were explored, firstly to achieve a thoroughly mixed solution in less than 1 s, and to enable the start of the reaction to be monitored. Since the latter issue was as a result of recovery from bubbling, rapid injection methods using the setup shown in Figure 48 with a compressed air drive was considered, where the injection of the new reagent would be the method for mixing.

Setup 2.0

In 2003, a rapid sample-mixing technique was developed in order to monitor real-time protein folding inside an NMR spectrometer.[103] A few years later, the technique was developed further,[104] and Figure 56 below summarises the insert used inside the NMR tube.

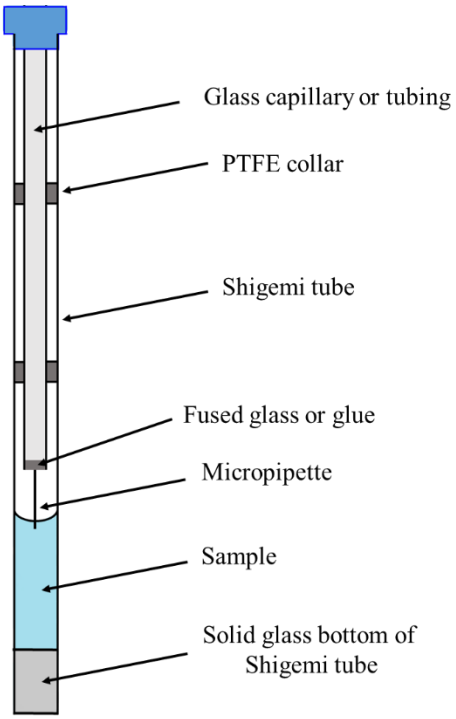

Figure 56: Summary of the design used for rapid sample-mixing.[103,104]

A glass capillary or a coaxial tube insert was used to hold and deliver reagents inside the NMR tube, with a glass micropipette attached to the end to allow for a collimated jet of liquid to be injected. The tip of the micropipette was positioned just above the radiofrequency coil in the magnet, and just below the surface of the solution in the tube. A Shigemi tube was used, which allowed a smaller sample volume to be used without affecting the lineshape of the spectra obtained. Furthermore, it was proposed that the flat bottom of the tube produced greater turbulence when compared to a round bottom.[103] The whole insert was held in place within the tube with PTFE collars, and was supported by the NMR cap at the top.

A Y-connector was attached to the top of the tubing (or glass capillary) and a PTFE transfer line was attached to carry reagents to the inside of the NMR tube. The transfer line was then connected to a glass syringe, which was mounted onto a pneumatic injector.

The mixing efficiency of the device was tested using injection of a fluorescent dye into water, with pH jump experiments, and with the injection of H_2O into D_2O. It was found that complete mixing was achieved within 100 ms, when 50 µL of solution was injected into 280 µL inside the NMR tube.[103]

In comparison, the system we developed used a larger volume of solution in the tube (500 µL) and injected 10-30 µL of reagent. As highlighted in Figure 54, mixing along the length of the NMR tube proved problematic. Using the information from the rapid-injection device developed,[103,104] we adjusted our design so that efficient mixing could be achieved without bubbling air through the solution. The insert is illustrated in Figure 57.

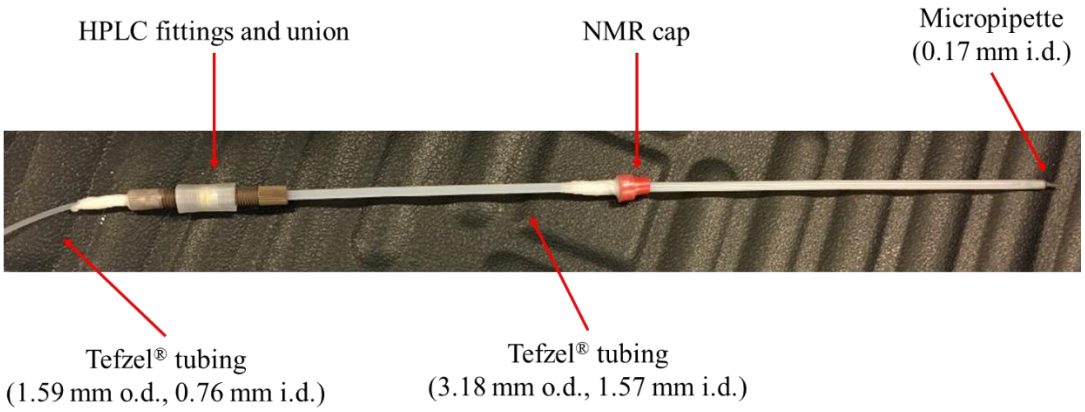

Figure 57: Setup of tubing used for rapid-injection inside the NMR magnet.

Similar to the rapid-injection design discussed previously,[103,104] the insert consists of a piece of Tefzel® tubing connected to a micropipette at one end, and a narrower piece of tubing on the other, which leads to the syringe setup shown in Figure 48. The two pieces of tubing were connected via HPLC fittings, joined together by a threaded union. This allowed for the inset to be swapped over for different designs during the testing phase, without having to waste long pieces of tubing. The NMR cap was used to hold the insert in place at a set height from the bottom of the tube, and the micropipette was used to direct the jet flow of reagent into the NMR tube.

The insert shown in Figure 57 was placed inside a Shigemi tube matched to $CDCl_3$, so that a smaller amount of reaction mixture could be used. Swapping the reagent syringe from the 250 µL to a 500 µL syringe meant that 10 µL – 80 µL of reagents could be added with the current syringe setup.

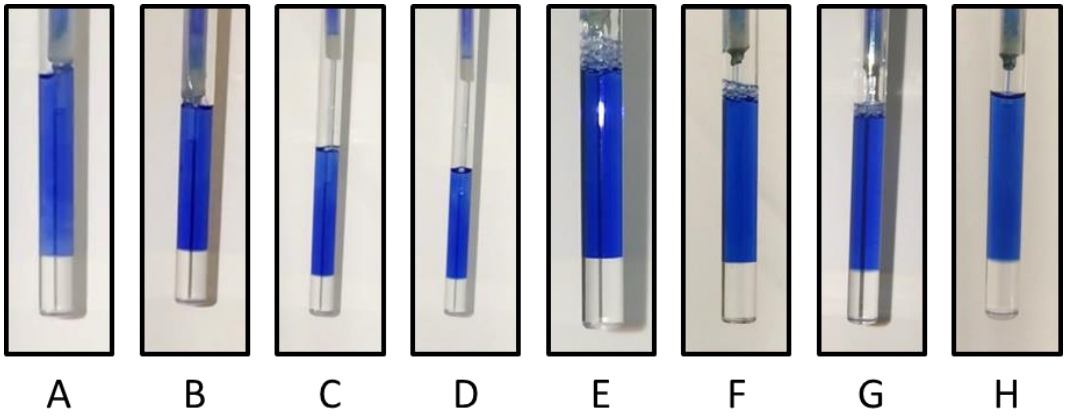

Figure 58: Injection of a blue solution into chloroform. All images were obtained approximately 3 seconds after injection. Pressure values refer to the driven pressure from the compressed air drive. Medium tip has a length of 0.7 cm, and the long tip has a length of 2.5 cm. From left to right: A: 300 µL chloroform, 60 µL blue solution, 5 bar, medium tip in solution. B: 250 µL chloroform, 60 µL blue solution, 5 bar, medium tip in solution. C: 300 µL chloroform, 60 µL blue solution, 8 bar, long tip in solution. D: 300 µL chloroform, 50 µL blue solution, 8 bar, long tip in solution. E + F: 250 µL chloroform, 60 µL blue solution, 9 bar, medium tip above solution. G + H: 250 µL chloroform, 60 µL blue solution, 5 bar, medium tip above solution.

The mixing efficiency was studied by injecting a solution of blue dye in chloroform and monitoring the spread of the colour in chloroform inside the NMR tube (Figure 58). The first test (A) carried out was injection of 60 µL of dye into 300 µL of solvent. This gave poor mixing, with areas of low dye concentration at the bottom and near the top of the solution.

Decreasing the volume of solvent used from 300 μL to 250 μL improved the mixing at the bottom of the tube, but the top of the solution remained poorly mixed. This was because solution inside the NMR tube was rising around the Tefzel® tubing, and it was thought that this tubing was hindering mixing at the top. A longer micropipette tip was tested (C and D) but there were still issues with the mixing at the top of the solution. The micropipette tip was removed from the solution and placed just above the top of the solvent. This was shown to have the best mixing efficiency, even with lower pressures on the compressed air drive (G and H). However, since the jet injected was hitting the surface of the solution, a significant amount of bubbles were formed during injection.

This setup (Figure 58, G and H) was further tested inside the magnet of the NMR spectrometer, where AcOH was injected into a solution of *p*-fluoroaniline in $CDCl_3$. The results are shown in Figure 59, where the reaction was monitored by ^{1}H NMR spectroscopy.

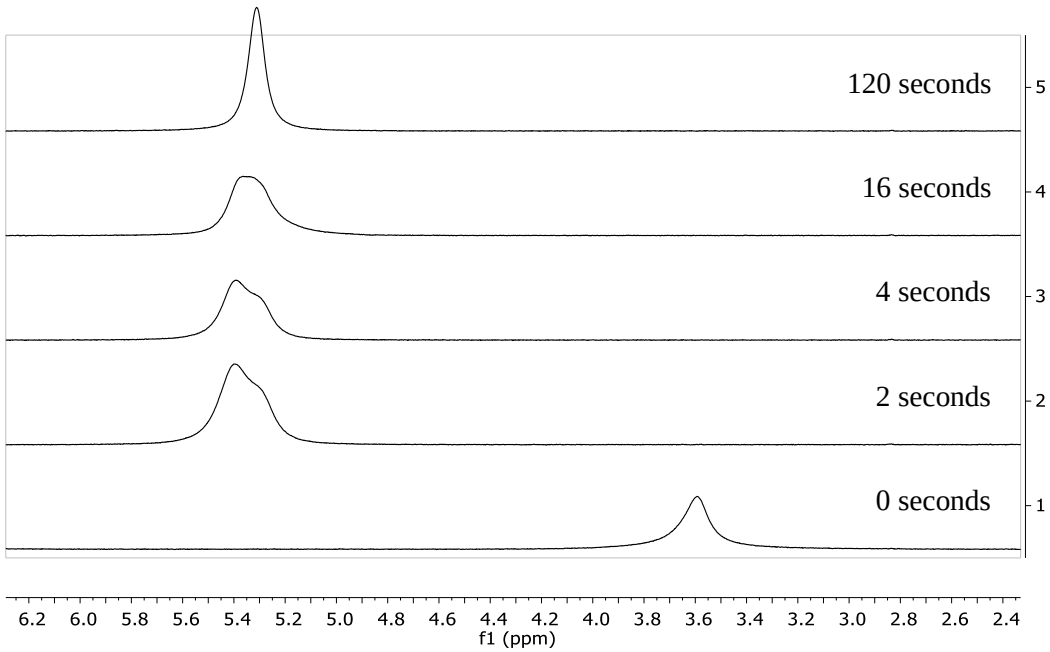

Figure 59: Stacked ^{1}H NMR spectra showing the injection of 60 μL of AcOH (0.5 M solution in $CDCl_3$) into a 250 μL solution of *p*-fluoroaniline in $CDCl_3$ (0.16 M) using setup G (and H) shown in Figure 58. Addition occurred between 0 – 2 seconds.

It was seen that mixing was achieved within 2 seconds from injection, with a slight overshoot by 0.1 ppm when compared to the spectra obtained at 120 seconds. This overshoot is small when considering the initial change in chemical shift, which was 1.8 ppm obtained when 0.75 equiv. of AcOH was added.

Reaction monitoring using setup 2.0

The reoxidation of gold(I) was then monitored, where the reaction shown at the top of Figure 52 was observed by ^{19}F NMR spectroscopy. When the formation of product **D5** stopped, more oxidant (*p*-FArI(OAc)$_2$) was added whilst the reaction was still in the magnet of the NMR spectrometer using the series of tubing illustrated in Figure 56 and Figure 57, and following setup G (and H) shown in Figure 58. The resulting temporal concentration plot of *p*-FArI is shown in Figure 60.

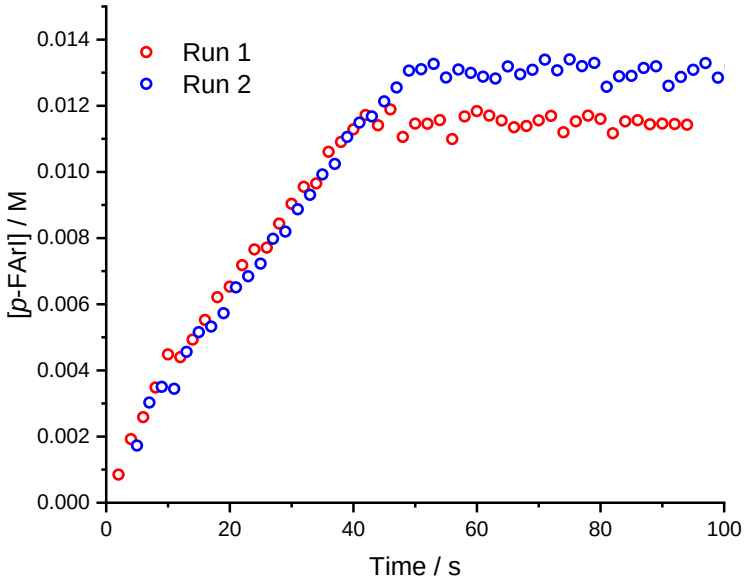

Figure 60: Graph showing the formation of *p*-FArI over time following the reaction shown at the top of Figure 52, after the addition of 0.0025 mmol *p*-FArI(OAc)$_2$.

Figure 60 shows the growth in *p*-FArI, the product from oxidation of gold(I) over two identical runs. It can be seen that there was an issue with the volume of oxidant stock solution added. The target amount to be added was 0.0025 mmol (0.008 M) of oxidant in 60 µL of solution, but from Figure 60, in both cases, the amount of oxidant added was higher than expected. From the final amount of *p*-FArI obtained in Run 1 (0.0035 mmol), the volume of oxidant stock added to the NMR tube worked out to be 88 µL, which is nearly 50% more than expected.

Both Run 1 and Run 2 indicate that the amounts of oxidant added does not affect the rate of *p*-FArI production. This is similar to the results obtained in Figure 52.

Focusing on the profile obtained of *p*-FArI in Run 1, there appears to be two separate regions of growth. This is highlighted in Figure 61, where two linear fits were applied to the different regions of data.

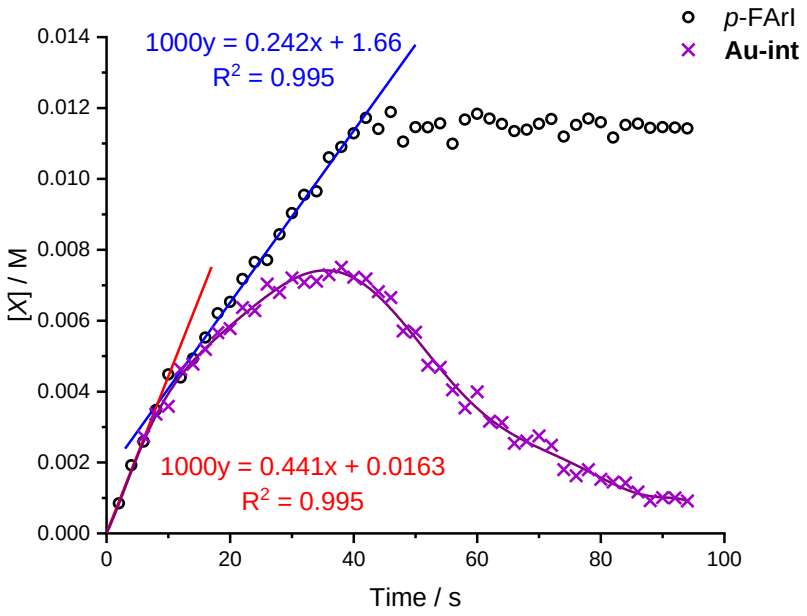

Figure 61: Graph showing the temporal concentration of the oxidation product, *p*-FArI and the resting state of the catalyst, **Au-int** from the reaction shown at the top of Figure 52 following the addition of *p*-FArI(OAc)$_2$ (0.0025 mmol).

A higher rate of *p*-FArI production was seen at the start of the graph shown in Figure 61, compared to the rate observed after 10 seconds. Assuming a straight-line fit could be applied to the growth of aryl iodide, the rate after 10 seconds was nearly half of that observed before 10 seconds. The concentration of the resting state (**Au-int**) versus time was also plotted in Figure 61. It appears that the initial growth of **Au-int** overlays with the growth of *p*-FArI, which also coincides with the fast region described earlier. This implies that the rate of oxidation (Scheme 43, equation 1) is slower or comparable with the rate of C-Si auration of starting material **D4** to obtain **Au-int** (Scheme 43, equation 2).

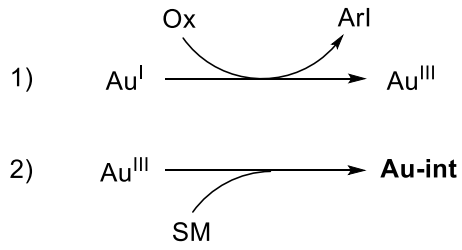

Scheme 43: 1) Reaction of a gold(I) complex with oxidant to give the corresponding aryl iodide product and a gold(III) complex. 2) Reaction of a gold(III) complex with the arylsilane starting material (**D4**) to give the resting state of the catalyst.

The decrease in rate of *p*-FArI formation seen could be a result of a decreased concentration of the initial gold(I) complex in solution. This is accompanied by a decrease in the rate of **Au-int** formation, although this decrease is much greater. However, it should be noted that the oxidant will also be consumed when **Au-int** reacts to release **D5** and more gold(I), which will then be oxidised, to produce more *p*-FArI.

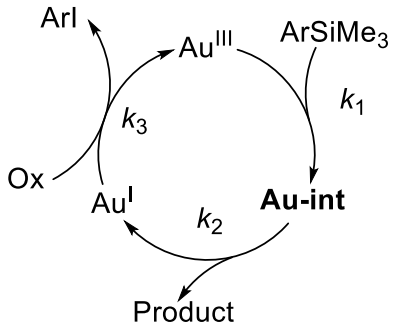

Input values:

k_1 = 10 mol^{-1} dm^3 s^{-1}
k_2 = 0.01 s^{-1}
k_3 = 10 mol^{-1} dm^3 s^{-1}
[Ox] = 0.0030 M

Scheme 44: Simplified catalytic cycle for the gold(III) catalysed intramolecular cyclisation of arylsilanes. Input values for the model are shown on the right.

A simple catalytic cycle was simulated (Scheme 44) and the resulting graph in Figure 62 shows the expected profile for *p*-FArI and **Au-int**. The starting point used for the model is the gold(I) complex (Au^I) and oxidant (Ox). These react to give a gold(III) species (Au^{III}) which reacts with arylsilane ($ArSiMe_3$) to give the resting state of the catalytic cycle, **Au-int**. The release of product from **Au-int** was set to have a small rate constant and is the turnover-limiting step. Once product is released, the Au^I is regenerated to react with more oxidant.

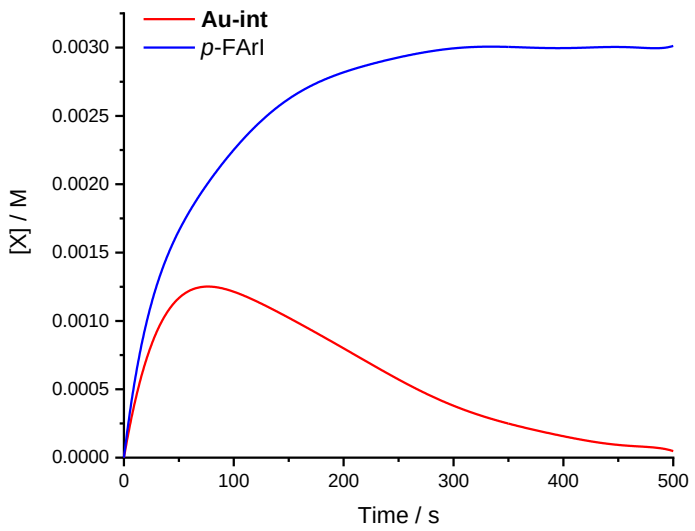

Figure 62: Graph showing the temporal concentration of *p*-FArI and **Au-int** obtained from modelling the catalytic cycle shown in Scheme 44.

Under the conditions described in Scheme 44, the initial portion of the curves in Figure 62 match the profile obtained in Figure 61. However, the rate of oxidation compared to the rate of turnover is too slow, showing significant curvature towards the end. This is contrary to studies carried out previously on the reaction shown in Scheme 37, where pseudo-zero order kinetics were observed for the production of aryl iodide.[50]

However, increasing the rate of oxidation used in the model so that a pseudo-zero order profile is obtained for *p*-FArI results in an initial jump in [*p*-FArI]. This is shown in Figure 63. The graph shows the temporal concentration profile of *p*-FArI and **Au-int**, and the insert shows the same graph, but expanded on the first 15 seconds of reaction.

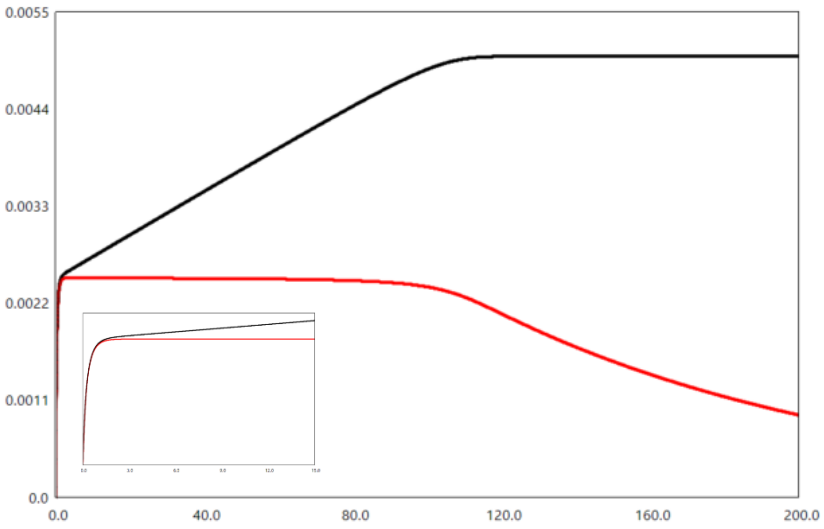

Figure 63: Graph showing the change in concentration versus time profile of *p*-FArI and **Au-int** as a result of increasing k_1 and k_3 to 1000 mol^{-1} dm^3 s^{-1}. The concentration of Ox used in the model was increased to 0.005 M for clarity.

A second model was developed, where the Au^I intermediate is proposed to be in equilibrium with an off-cycle species, AuX (Scheme 45). Using this model, the rate of *p*-FArI formation would be controlled by the rate of Au^I production.

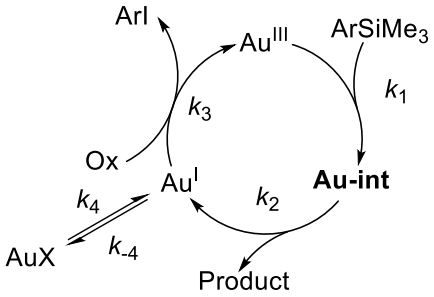

Scheme 45: Modified catalytic cycle used in Dynochem® to include the possibility of an off-cycle species which releases Au^I, which can then react with the oxidant.

The model shown in Scheme 44 and Scheme 45 were fitted to experimental data, and the results of these fits are illustrated in Figure 64.

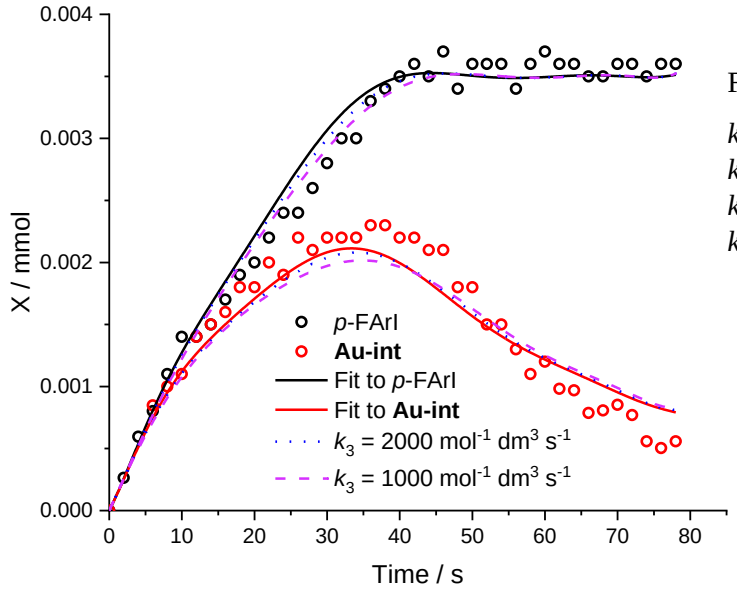

Fitted values:

k_1 = 2490 mol^{-1} dm^3 s^{-1}
k_2 = 0.0247 s^{-1}
k_3 = 9710 mol^{-1} dm^3 s^{-1}
k_4 = 0.0589 s^{-1}

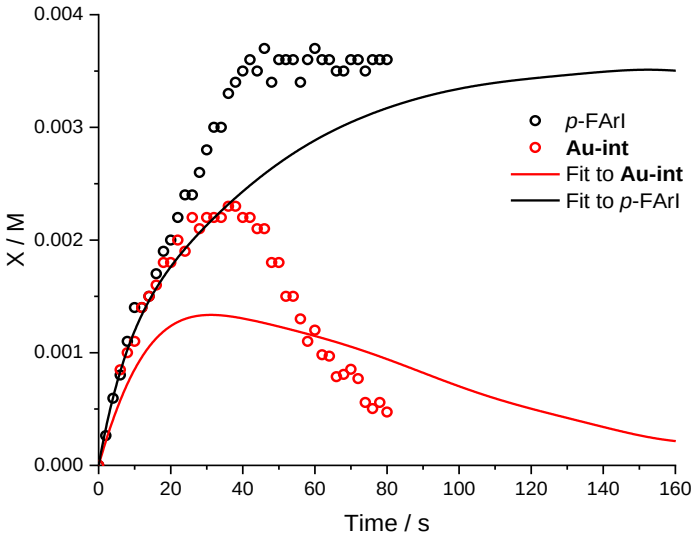

Fitted values:

k_1 = 7 mol^{-1} dm^3 s^{-1}
k_2 = 0.0252 s^{-1}
k_3 = 7 mol^{-1} dm^3 s^{-1}
[Ox] = 0.0011 M

Figure 64: Top: Fitting of the model shown in Scheme 45 to experimental data. Lower limit of the fitting obtained from k_3 are shown by the blue dotted lines When k_3 is less than k_1, the fitting of the intermediate starts to deviate, and a lower peak concentration of **Au-int** obtained. The purple dashed line illustrates a more extreme version of this decrease to emphasise the flattening of the **Au-int** profile. Bottom: Fitting of the model shown in Scheme 44 to experimental data. Fitted values obtained are shown at the side of each graph.

The graph at the top of Figure 64 illustrates the fit obtained to experimental data using the model shown in Scheme 45. The first 40 seconds of the plot shows a reasonable fit for both *p*-FArI and **Au-int** and the rate constants obtained are displayed to the right of the plot. Both the oxidation step and the C-Si auration reaction have very large rate constants, especially when compared to the turnover-limiting step. In this model however, the rate of *p*-FArI production is now controlled by the release of Au^{I} from its inactive form, AuX. (k_4 and k_{-4}). Therefore, the initial jump in concentration of both *p*-FArI and **Au-int** as described in Figure 63 does not occur.

In contrast, the graph displayed at the bottom of Figure 64 shows a poor fit between the modelled data and the experimental data. Rate constants obtained from the fit showed large differences (in comparison to the results at the top) in the rate for the oxidation step and the C-Si auration step. Furthermore, the shape of the graph obtained for the concentration of both species, as described previously, is different when compared to the shape of the experimental data.

The temporal concentration of the added oxidant and standard (2-BrArF) was plotted alongside the concentration of *p*-FArI and displayed in Figure 65.

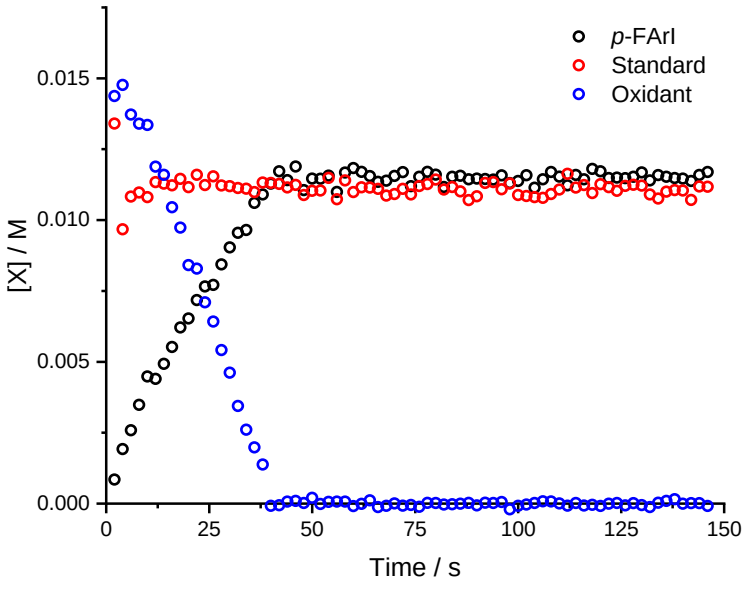

Figure 65: Graph showing the change in concentration of the added oxidant, *p*-FArI and standard over time of the reaction shown at the top of Figure 52 obtained after the addition of oxidant.

Similar to the results obtained from setup 1.1 shown in Figure 55, the concentration of the oxidant at the start of the addition is higher than the final concentration of *p*-FArI added. In addition, the concentration of the standard added follows the same pattern for the first datapoint. Although no visible concentration gradient was observed for this setup when tests with injection of a blue solution was carried out (Figure 58, G and H), the addition of AcOH to *p*-fluoroaniline displayed a small increase in acid concentration in the first few seconds after addition when compared to the end spectra obtained after 2 minutes (Figure 59). Therefore, regions of high concentration of oxidant within the reaction mixture inside the NMR tube may have been responsible for the higher rate of *p*-FArI production at the start.

4.. Conclusion

The study of the oxidation step in a gold(III)-catalysed direct arylation reaction (Scheme 37) was carried out, where direct observation of the rate of oxidation was the objective. In order to achieve this, the stability of the resulting gold(I) complex was probed, and it was found that when insufficient amounts of oxidant was added, the arylation reaction could be partially reactivated by addition of more hypervalent iodine(III) oxidant. Interestingly, most of the deactivation of the catalyst occurred as soon as the reaction ran out of oxidant, and it was calculated that 80% of the catalyst could be reactivated after the reaction mixture was left for 5 seconds without oxidant. In contrast, leaving the reaction without oxidant for 120 seconds resulted in only 40% of the catalyst deactivating.

Methods into monitoring the oxidation step were then explored. It was initially proposed that this could be monitored using UV-vis spectroscopy. However, it was found that the UV spectra for the gold(III) catalyst was too weak under catalytic conditions. Increasing the amounts of catalyst used meant that an increasing amount of oxidant was required to activate the catalyst, and this posed a problem as the saturation limit on the UV-vis detector was reached.

Rapid-injection methods of reagents into an NMR tube inside the NMR magnet were then considered. Using the design shown in Figure 43, the oxidant was added via a piece of tubing, and air was bubbled through a separate piece of tubing to mix the reagents together. However, this design had two main disadvantages: the reaction could not be monitored while bubbling occurred as the concentration within the coils of the NMR spectrometer was too low and mixing of the added reagent was too slow.

Using a design developed by Hore et. al.[103,104] a similar design was created to achieve rapid mixing without bubbling. This also involved reducing the amount of solvent in the NMR tube, increasing the amount of reagent injected, and using a flat-bottomed Shigemi tube to improve

mixing efficiency. Different positions of the new tubing were tested along with different volumes of solvent and reagents to achieve good mixing. It was found that injection of 60 μL of reagent into 250 μL with the tip of the reagent tubing just above the solvent line gave the best mixing when tested with the injection of a blue solution into a clear solution.

Further testing of this setup was carried out with the injection of AcOH into *p*-fluoroaniline, and the mixing efficiency was monitored by ^{1}H NMR spectroscopy. It was found that the solution was mostly mixed within 2 seconds from injection, where a slightly higher acid concentration was seen when compared to a spectrum obtained after 120 seconds.

This setup was used to monitor the oxidation of gold(I) within the intramolecular direct arylation reaction of **D4**. Focusing on the product from the oxidant, *p*-FArI, it appeared that the rate of its formation was higher in the first 10 seconds after addition of oxidant. Two models of the catalytic cycle were generated (Scheme 44 and Scheme 45). The first was a simple model with three steps: C-Si auration of the starting material to the gold(III) catalyst, release of product from the resting state of the catalyst, and the oxidation of gold(I).

The first model had a poor fit to the experimental data, where the profile of *p*-FArI generation modelled was too curved. Increasing the rate of oxidation in this model gave an initial jump in *p*-FArI seen, which is inconsistent with the experimental data. The second model had an additional equilibrium between the gold(I) complex and an off-cycle, inactive species, labelled AuX. The second model accounted for the slow growth in *p*-FArI seen, where the rate of oxidation was controlled by the release of gold(I) from AuX, where X is unknown, and could be a result of water in the reaction mixture. This model gave a better fit to the experimental data obtained.

Chapter 5

Oxidation of phosphine-gold(I) chloride

5.1. Introduction

5.1.1. Oxidation of $(Ph_3P)Au(OTs)$

Previous discussion and studies on the gold-catalysed oxidative coupling reaction between aryl silanes and arenes have been focused on the catalytic cycle involving the activated form of the precatalyst, $(tht)Au(Br)_3$.[43,50] Prior to using $(tht)Au(Br)_3$ as the catalyst, a phosphine-ligated gold(I) complex, $(Ph_3P)Au(OTs)$ (**E1**)[42] was used as the precatalyst for the coupling reaction. It was found that a significant induction period of approximately 45 minutes[43] resulted from the use of **E1**.

The reaction of **E1** with excess oxidant (**E2-F**) and CSA was studied in the absence of the coupling substrates (arylsilane and arene), as shown in Scheme 46.

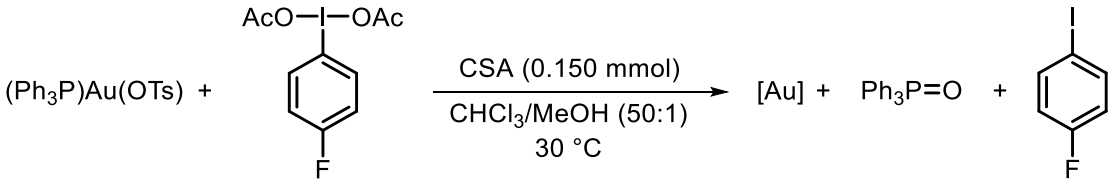

E1 0.002 mmol

E2-F 0.130 mmol

Scheme 46: Oxidation of **E1** with hypervalent iodine(III) oxidant under catalytic gold conditions.

Monitoring the reaction by ^1H NMR spectroscopy and $^{31}P\{^1H\}$ NMR spectroscopy showed that two equivalents (relative to **E1**) of oxidant were consumed (Figure 66). This was accompanied by the production of one equivalent of triphenylphosphine oxide, and it was suggested that the oxidation of both the gold(I) and the phosphine ligand was responsible for the induction period seen.

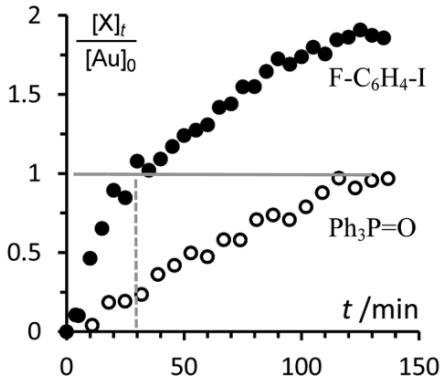

Figure 66: Graph showing the formation of Ph_3PO and aryl iodide relative to the amount of gold complex **E1** added over time.[43]

Three different pathways for the activation of **E1** were proposed.[43] The length of induction period obtained when using electron-rich and electron-poor phosphines coordinated to the gold tosylate complex ((*p*-$RC_6H_4)_3Au(OTs)$) was analysed. It was found that the use of an electron-rich phosphine (R = Me) resulted in a shorter induction period when compared to using an electron-poor phosphine (R = CF_3). This suggested that an initial oxidation of **E1** occurs to give the corresponding gold(III) complex, rather than an initial dissociation of phosphine from the gold.

From this gold(III) complex, two pathways were considered: the dissociation of phosphine to produce phosphine oxide and the active catalyst; and the reductive elimination of a phosphonium(V) salt to give a gold(I) complex, which can then be oxidised to the active catalyst. Increasing the steric bulk on the phosphine ligand (from *p*-tolyl to *o*-tolyl) resulted in an increase in the length of the induction period. This supports the proposal that reductive elimination of a phosphonium salt is occurring (Scheme 47).

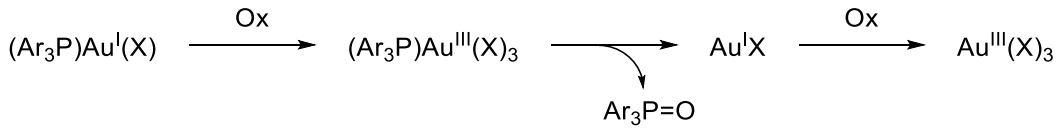

Scheme 47: Proposed pathway for the oxidation of **E1** with a hypervalent iodine(III) oxidant.[43]

5.1.2. Oxidation of $(C_6F_5)Au(PPh_3)$

The oxidation of phosphine-gold(I) complexes has been studied previously,[78,82] and the reaction shown in Scheme 48 was studied by Hofer and Nevado.[82]

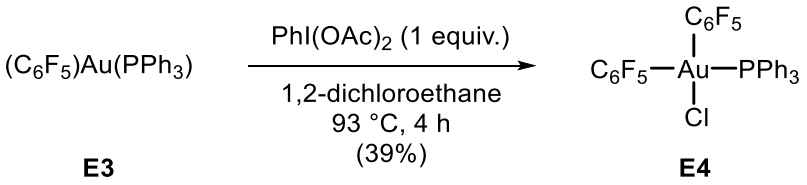

E3 **E4**

Scheme 48: Oxidation reaction of **E3** and $PhI(OAc)_2$ to give complex **E4**.[82]

The oxidation of complex **E3** was carried out in the presence of one equivalent of $PhI(OAc)_2$ as the oxidant, in 1,2-dichloroethane as the solvent. The reaction was carried out at 93 °C, as no reactivity was seen at room temperature. Previous discussion on the reactivity of gold(I) complexes with hypervalent iodine(III) oxidants in Chapter 3 indicated that the expected product from the reaction shown in Scheme 48 would be a gold(III) complex with two additional ligands from the iodine oxidant coordinated, $(C_6F_5)Au(PPh_3)(OAc)_2$, where both OAc ligands have originated from the iodine(III). However, the product observed was complex **E4**, with no acetate ligands attached. Changing the solvent used in the reaction from 1,2-dichlorethane to benzene produced the expected gold(III) complex, $(C_6F_5)Au(PPh_3)(OAc)_2$.[45]

To probe the formation of complex **E4**, the reaction in Scheme 48 was monitored by $^{31}P\{^1H\}$ NMR spectroscopy which revealed the presence of several intermediates, including $[Au(PPh_3)_2]^+$ at 46 ppm, as well as Ph_3PO and/or $AuCl(PPh_3)_2$ at 29 ppm. The former was found to increase in concentration at the start of the reaction, and decay as the reaction proceeded towards full consumption of the starting material.

The effect of the anionic ligand on the reaction shown in Scheme 48 was probed by addition of one equivalent of $(Ph_3P)Au(Cl)$ (**E5**). It was found that the formation of product **E4** was accelerated, as well as the consumption of both the starting material, **E2** and the intermediate $[Au(PPh_3)_2]^+$.

From these results, two pathways for the formation of **E4** were proposed. The first pathway shown in Scheme 49 involves ligand dissociation of the anionic ligand to give the intermediate $[Au(PPh_3)_2]^+$, which was then oxidised by $PhI(OAc)_2$ in solution to give $[AuX_4]^-$, where X = OAc or Cl (from solvent activation). It was also stated that the redox potential of $[Au(PPh_3)_2]^+$ was more negative when compared to neutral gold(I) complexes. From complex $[AuX_4]^-$, it was suggested that either transmetallation or ligand exchange with the starting complex **E3** occurred to give the final product **E4**.

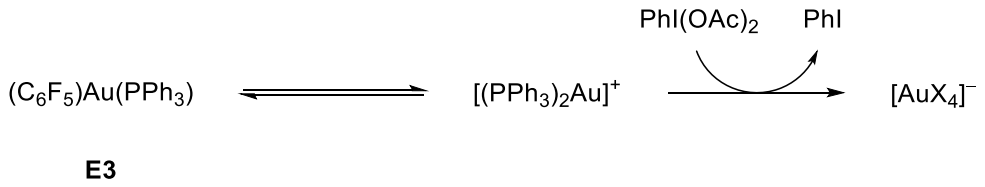

Scheme 49: Proposed pathway for the oxidation of **E3**, with an initial ligand dissociation step. X = OAc or Cl.

The second pathway suggested that the oxidation occurred directly from complex **E3** to give $(PPh_3)Au^{III}(C_6F_5)(X)_2$, which can also undergo transmetallation or ligand exchange with **E3**.

The studies described above have shown that the oxidation of gold(I) complexes are not necessarily as simple and straightforward as described in Chapter 3. Multiple steps have been shown to occur with the observation of intermediates such as $[Au(PPh_3P)_2]^+$, moreover the ligands coordinated to the gold centre are not always clear.

5.2. Aims of the chapter

This chapter focuses on studying the mechanism of the reaction shown in Scheme 50. The reaction was monitored by ^1H NMR spectroscopy to follow the consumption of the oxidant and formation of iodobenzene, as well as by $^{31}P\{^1H\}$ NMR spectroscopy to monitor the formation of triphenylphosphine oxide.

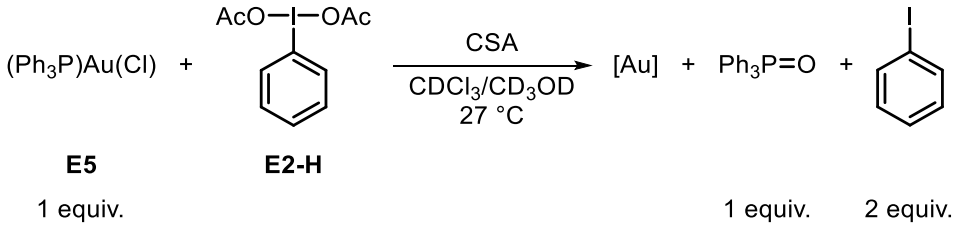

Scheme 50: Reaction studied to probe the oxidation of phosphine-gold(I) complex **E5** with $PhI(OAc)_2$ and CSA.

5.3. Results

Similar to the oxidation reaction carried out with $(Ph_3P)Au(OTs)$ (**E1**), the oxidation of complex **E5** consumed two equivalents of oxidant for each gold(I) complex to give one equivalent of triphenylphosphine oxide and two equivalents of aryl iodide. However, in contrast to the oxidation of complex **E1**, the reaction with complex **E5** was significantly faster, with the formation of two equivalents of iodobenzene complete in 60 minutes in comparison to 120 minutes obtained with complex **E1**. The graph showing the growth of aryl iodide relative to the amount of gold complex added for the reaction from both complexes is shown in Figure 67.

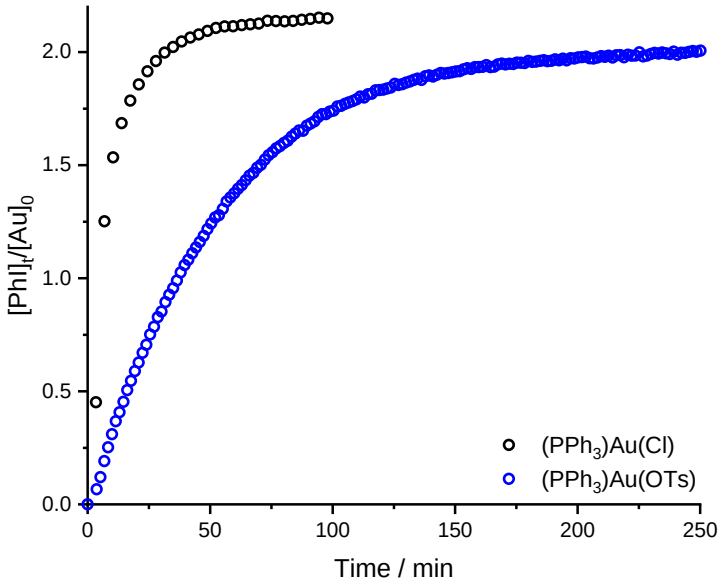

Figure 67: Graph showing the comparison on the rate of growth of PhI relative to amount of gold(I) complex added for **E1** and **E5**. The reaction was carried out as summarised in Scheme 50 with 0.005 mmol gold complex, 0.10 mmol $PhI(OAc)_2$ and 0.12 mmol CSA in 0.715 mL $CDCl_3/CD_3OD$ (50:1).

5.3.1. Changing the nature of oxidant

The role of the oxidant was probed using a hypervalent iodine(III) oxidant with a *p*-CF_3 group on the aromatic ring, and comparing the results when the reaction was carried out with the unsubstituted hypervalent iodine(III) oxidant. This is summarised in Figure 68 (top). The rates of aryl iodide formation as well as production of triphenylphosphine oxide were identical for both oxidants, even though the electronics on the oxidants were very different. This suggests that the oxidant is not involved in the rate-determining step of the reaction, or that the electronic nature of the oxidants do not affect its reactivity. As examined in Chapter 2, the

oxidant with a *p*-CF_3 group has a higher reduction potential and is thermodynamically more oxidising than the unsubstituted oxidant. However, under these conditions, a large excess of oxidant was used when compared to complex **E5**.

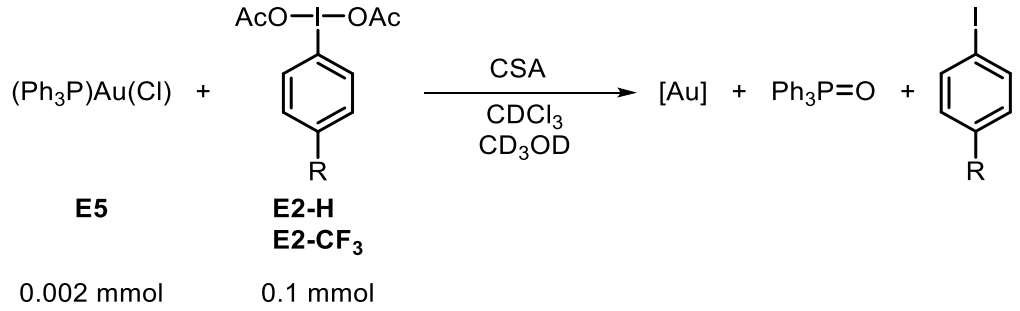

E5 **E2-H** **E2-CF_3**

0.002 mmol 0.1 mmol

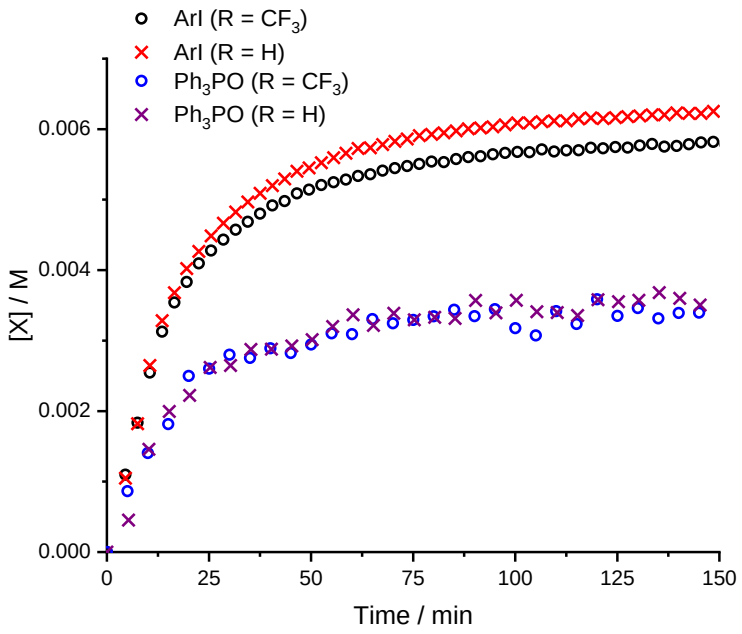

Figure 68: Top: Scheme of reaction carried out. Bottom: Concentration versus time graph showing the growth of aryl iodide and triphenylphosphine oxide, comparing the effects of using **E2-H** and **E2-CF_3** as oxidants. The reaction was carried out with 0.002 mmol **E5**, 0.10 mmol oxidant and 0.12 mmol CSA in 0.715 mL $CDCl_3$/CD_3OD (50:1).

5.3.2. Stoichiometric amount of oxidant

The oxidation reactions of gold complexes **E1** and **E5** were carried out with an excess of oxidant. To study the effect of the amount of oxidant added, a reaction with 1:2 ratio of gold(I) complex to oxidant was carried out. In this case, the growth of aryl iodide and triphenylphosphine oxide showed a significant induction period.

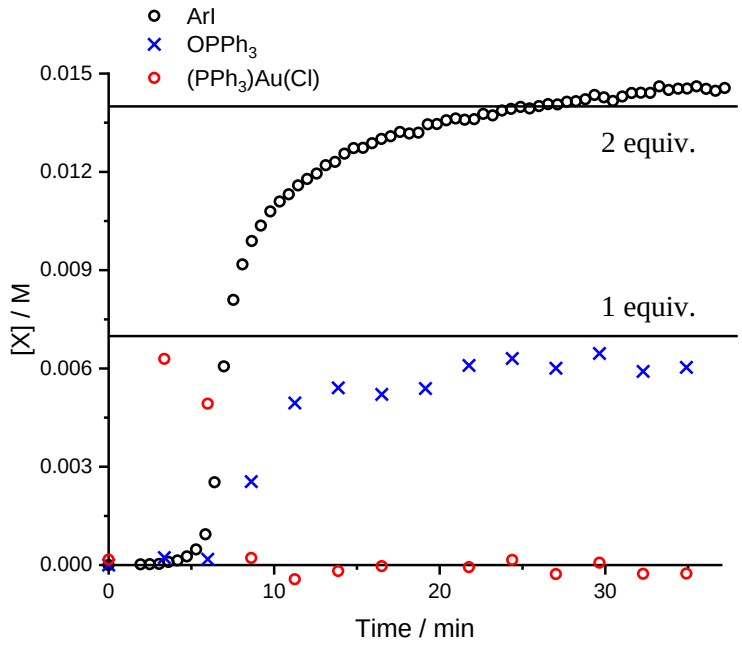

Figure 69: Graph showing the concentration change over time of complex **E5**, aryl iodide, and triphenylphosphine oxide. The horizontal lines indicate concentrations that are equal to one and two equivalents of the starting complex **E5** added. The reaction was carried out with 0.005 mmol **E5**, 0.010 mmol **E2-H**, and 0.012 mmol CSA in 0.715 mL $CDCl_3/CD_3OD$ (50:1).

Figure 69 shows how the concentration of complex **E5**, Ph_3PO, and ArI changes over time. As expected, the final concentrations of ArI reaches two equivalents relative to the amount of **E5** added, and one equivalent of Ph_3PO is formed. Interestingly, in the first 5 minutes of the reaction, there is very little formation of product or consumption of the starting complex **E5**. After this induction period, the rate of reaction increases, and most of the reaction is complete in the next 5 minutes. The gold complex **E5** was fully consumed in this time although not all the phosphine oxide or aryl iodide has been formed. Following this burst in product formation, the formation of ArI slows down as it reaches full conversion, taking approximately another 30 minutes.

Effect of product addition

The initial two regions (10 minutes) of the profile obtained for the growth of aryl iodide could indicate that the reaction is autocatalytic, where small amounts of product formation could catalyse its formation and thus lead to a rapid increase in the rate of reaction. Another explanation could be that there is an inhibitor present, and that the inhibitor has to react before complex **E5** reacts. To test the former hypothesis, both products, triphenylphosphine oxide (1 equiv.) and aryl iodide (1 equiv.) were tested as catalysts by adding these compounds to the start of the reaction.

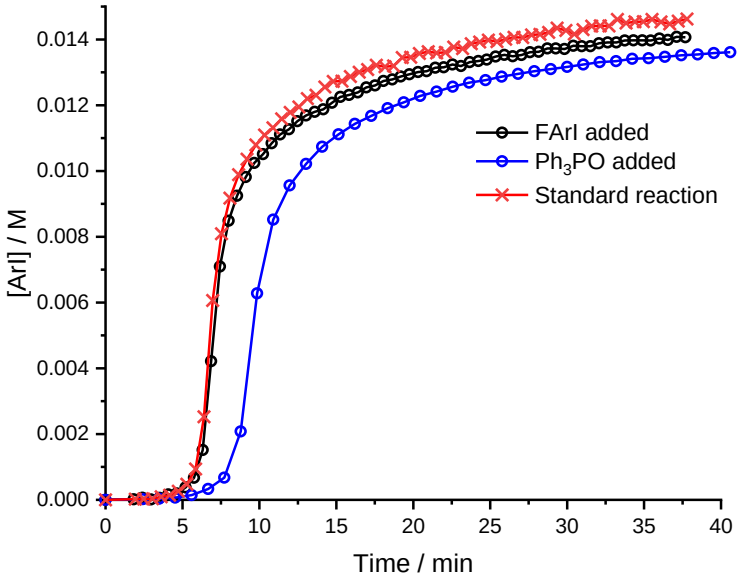

Figure 70: Overlay of the growth of ArI over time from three different reactions to test the effect of ArI and Ph_3PO in the reaction. Reaction conditions used were 0.005 mmol of **E5**, 0.010 mmol $PhI(OAc)_2$, and 0.012 mmol CSA in 0.715 mL $CDCl_3/CD_3OD$ (50:1). 0.005 mmol Ph_3PO or 0.010 mmol *p*-FArI were added in the appropriate runs. All concentrations were obtained relative to CH_2Br_2 as a standard.

The addition of an aryl iodide (*p*-FArI) to the reaction shown in Scheme 50 gave a very similar plot as the reaction without added aryl iodide. Similarly, addition of triphenylphosphine oxide to the start of the reaction resulted in a similar growth of aryl iodide, even though a slightly longer induction period was seen. This could be a result of experimental error, where a different stock solution of complex **E5** was used for this run. These results indicate that both the aryl iodide product (PhI) and triphenylphosphine oxide do not function as a catalyst for the reaction of complex **E5**.

To further probe the induction period observed in the reaction of complex **E5** and hypervalent iodine(III) oxidant, the reaction in Scheme 51 was carried out, where more of complex **E5** was added.

*Addition of more starting complex, **E5***

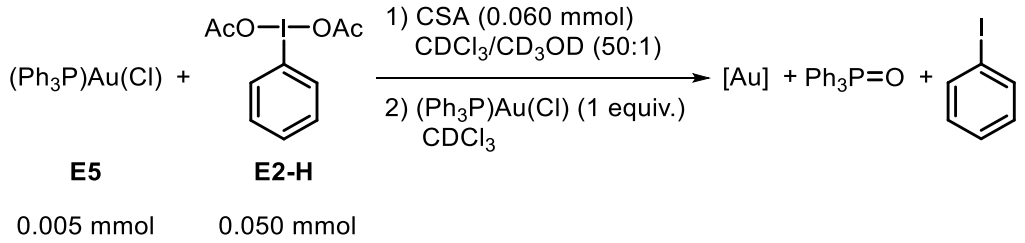

Scheme 51: Summary of reaction carried out with addition of more starting material **E5** when the production of ArI stops.

Figure 71 shows the temporal concentration of aryl iodide in three separate reactions. Run 1 was carried out as described in Scheme 51, where the reaction between (Ph_3P)Au(Cl) (**E5**) and oxidant was carried out. When the formation of aryl iodide stops, more of complex **E5** was added, at the timepoint indicated by the vertical dotted line. Run 2 shows the profile for the concentration of aryl iodide without the addition of complex **E5** and Run 3 shows the reaction profile for the formation of aryl iodide when the reaction was carried out under the same conditions as the second half of Run 1. The change in conditions for Run 3 included increasing the volume of solvent used, which was due to addition of complex **E5** as a stock solution. The amount of oxidant in the second half of Run 1 and consequently the start of Run 3 was reduced, as two equivalents (0.010 mmol) of oxidant were consumed. It should be noted that the graph for Run 3 has been adjusted so that t_0 occurs at the point of complex **E5** addition, and that the concentration has been elevated so that it overlays with the graph from Run 1.

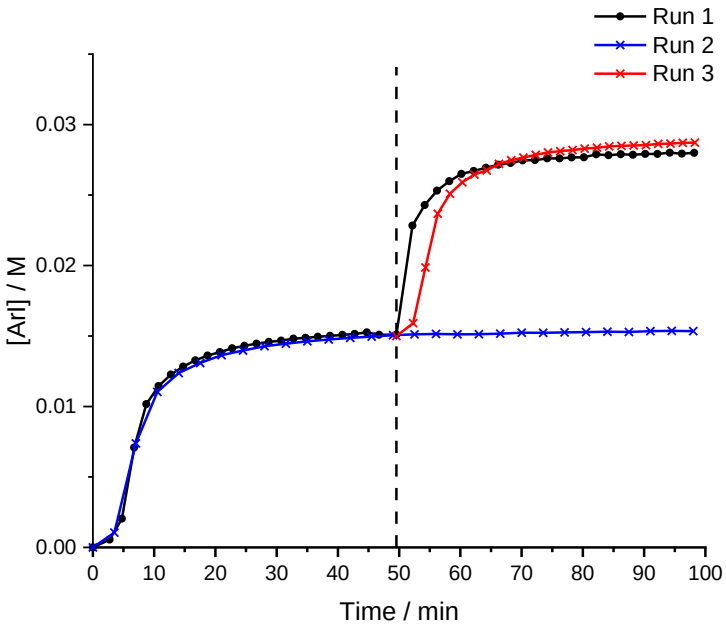

Figure 71: Run 1: Reaction carried out as illustrated in Scheme 51 in 0.715 mL $CDCl_3/CD_3OD$ (50:1) with the addition of more **E5** (0.005 mmol, 100 µL in $CDCl_3$) , represented by the vertical dotted line. Run 2: 0.005 mmol **E5**, 0.050 mmol $PhI(OAc)_2$, and 0.060 mmol CSA in 0.715 mL $CDCl_3/CD_3OD$ (50:1). Run 3: 0.005 mmol **E5**, 0.040 mmol $PhI(OAc)_2$, and 0.060 mmol CSA in 0.8 mL $CDCl_3$ and 15 µL CD_3OD.

Focusing on the graph of Run 1 in Figure 71, the growth of aryl iodide proceeds as expected, with a short induction period at the beginning. However, upon addition of more **E5**, this induction period is no longer present, and most of the aryl iodide has formed by the time the next spectrum was taken. Comparison of this section of the graph to Run 3 highlights the loss of induction period. This indicates that the reaction forms a compound that is capable of increasing the rate of its reaction, or that the inhibitor present is not in the stock solution of complex **E5**.

The reaction carried out with ten equivalents of oxidant (Scheme 51) was compared to the reaction carried out with two equivalents of oxidant (Figure 70). This is shown in Figure 72.

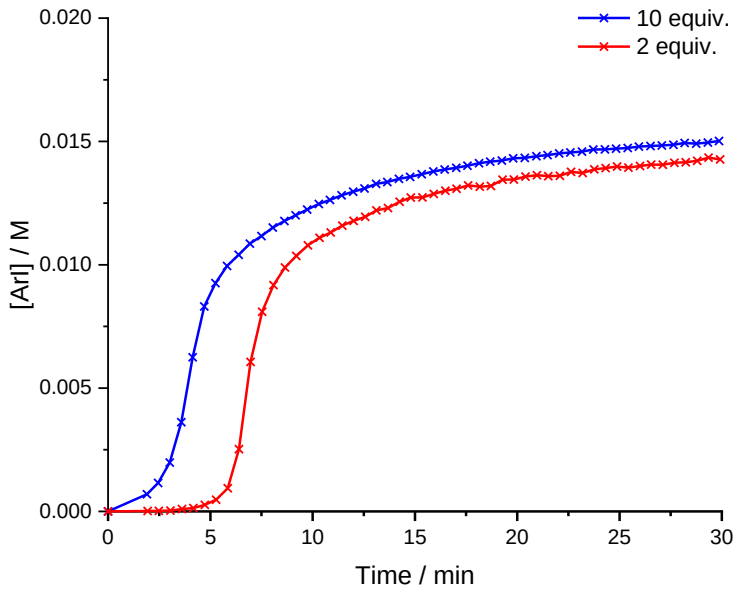

Figure 72: Graph comparing the growth in ArI formation with excess and stoichiometric amount of oxidant ($PhI(OAc)_2$). Conditions used: 0.005 mmol **E5**, 0.050 mmol (10 equiv.) or 0.010 mmol (2 equiv.) $PhI(OAc)_2$, and 0.060 mmol (24 equiv.) or 0.012 mmol (2.4 equiv.) CSA in 0.715 mL $CDCl_3/CD_3OD$ (50:1).

The graph in Figure 72 shows that increasing the amount of oxidant added decreases the induction period observed. However, under these conditions, the amount of CSA added was relative to the amount of oxidant added (1.2 equiv. amount of oxidant). CSA reacts with hypervalent iodine(III) diacetates to give the hydroxycamphorsulfunate oxidants,[105] where the two acetate ligands on the iodine centre have been replaced (Chapter 2). A slight excess of CSA was used to ensure that all the hypervalent iodine(III) diacetate exists as the hydroxycamphorsulfunate oxidant. Therefore, the amount of free CSA in solution changes with changing amounts of oxidant added, which led to the study on the effects of CSA on the reaction.

5.3.3. Effect of CSA

Changing CSA concentration

Scheme 52 summarises the reaction carried out to probe the role of CSA in the reaction of complex **E5** with hypervalent iodine(III) oxidant. The amount of oxidant used was kept constant, and the amount of CSA added was varied. This gives a situation where the amount of free CSA in solution at the start of the reaction changes.

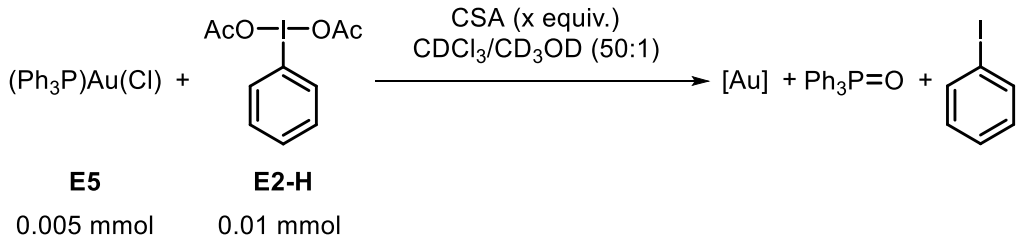

Scheme 52: Reaction conditions used to probe the role of CSA.

The graph in Figure 73 shows the change in aryl iodide concentration over time for reactions with different amounts of CSA added. Increasing the amount of CSA added while keeping the oxidant concentration constant reduces the induction period observed in the growth of aryl iodide. However, it is unlikely that CSA was playing a direct role in the sudden increase in rate, and this is highlighted when comparing the profiles where 0.030 mmol and 0.012 mmol of CSA was added.

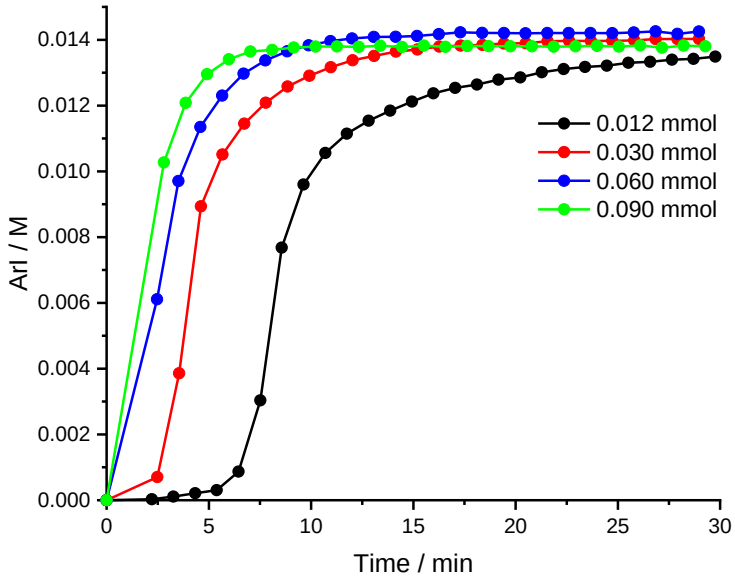

Figure 73: Graph showing the growth of ArI over four separate runs with different amounts of CSA, as illustrated in Scheme 52. Conditions used: 0.005 mmol **E5**, 0.010 mmol $PhI(OAc)_2$, and 0.012 mmol to 0.090 mmol of CSA in 0.715 mL $CDCl_3/CD_3OD$ (50:1).

Looking at the approximate values, the point where the rate increases with 0.012 mmol of CSA occurs around the moment when 0.001 M of aryl iodide has been generated. This equates to about 0.001 mmol of CSA released from the oxidant, which gives a total of 0.003 mmol of free CSA in solution. Focusing back on the plot with 0.030 mmol of CSA added, at the start of this reaction, approximately 0.02 mmol of free CSA exists in solution. This value is greater than five times the amount of CSA in solution when the profile for the black datapoints (0.012 mmol) increases in rate. In spite of the large excess of free CSA in the solution, a significant induction period was still observed (Figure 73, red datapoints).

However, in this analysis, the possible equilibrium shown in Scheme 53 was not considered. This was because there was an insignificant amount of $PhI(OAc)_2$ detected by ^1H NMR spectroscopy, indicating that the equilibrium lies heavily to the left of the equilibrium. Therefore, it is unlikely that the formation of CSA via this equilibrium would influence the discussion relating to Figure 73.

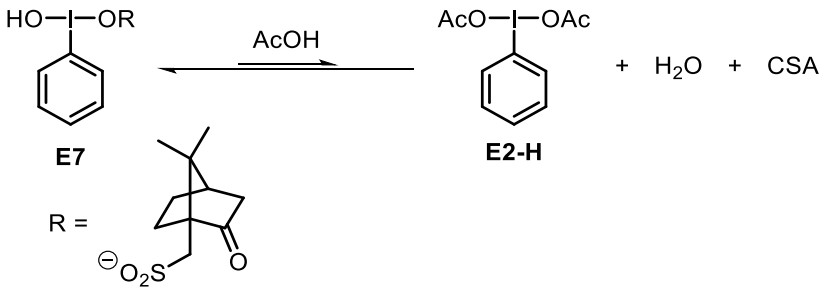

Scheme 53: Equilibrium between hydroxycamphorsulfonate and diacetate hypervalent iodine(III) oxidants.

*Use of **E7** as oxidant*

Further testing on the importance of free CSA was carried out by the use of compound **E7** as the oxidant. In this case, all the oxidant exists as compound **E7**, and no free CSA was present in the solution.

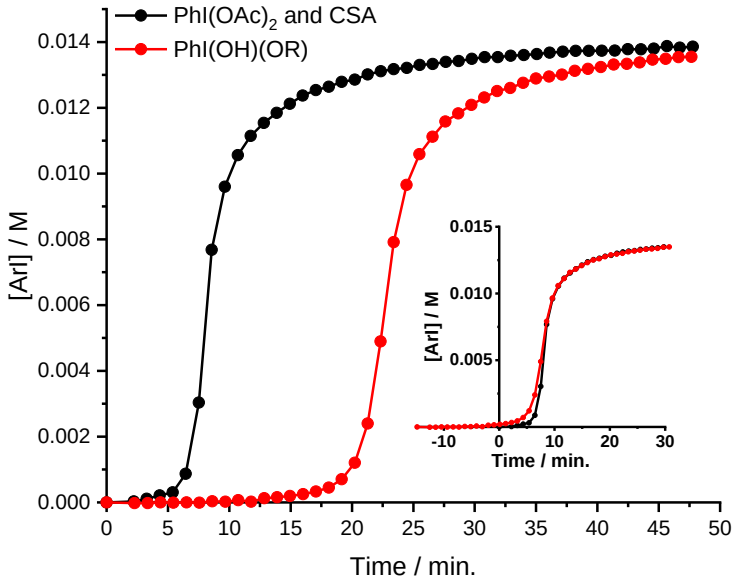

Figure 74: Comparison of the growth of ArI when using the preformed oxidant **E7** and when using $PhI(OAc)_2$ and CSA to form **E7** in-situ. Reaction conditions: 0.005 mmol **E5**, 0.010 mmol $PhI(OAc)_2$ with 0.012 mmol CSA or 0.010 mmol **E7** in 0.715 mL $CDCl_3/CD_3OD$ (50:1). Insert: Time adjusted profile for the red line so that the growth section showing the burst in reactivity is overlaid.

The graph in Figure 74 shows the temporal concentration of aryl iodide with and without added CSA. The red datapoints display the results from the addition of compound **E7** without any excess CSA present. The induction period obtained as a result was significantly longer when compared to the results obtained in Figure 73 (the black datapoint correlates to the addition of 0.012 mmol of CSA as indicated in Figure 73). Despite the long induction period, the rest of the profile obtained under both the conditions described are identical (Figure 74, insert).

This could indicate that CSA is involved in an initiation or activation of complex **E5**, or that CSA was involved in removing the inhibitor in the reaction, and the rate this occurs is dependent on the concentration of CSA in solution.

*Premixing CSA and **E5***

To test whether CSA reacts or removes an inhibitor, the reaction mixture without oxidant was left standing for 20 minutes, then $PhI(OAc)_2$ was added, and the formation of aryl iodide was monitored. This reaction was carried out for two different concentrations of CSA (with 1.2 equiv. of oxidant that was subsequently added). This is summarised in Scheme 54.

Scheme 54: Summary of the reaction carried out where CSA and **E5** were premixed before the addition of $PhI(OAc)_2$ to initiate the reaction.

Premixing the gold complex **E5** with CSA before addition of oxidant produced almost identical results to that obtained when CSA and oxidant were added at the same time. This is shown in Figure 75, where the cross datapoints and the line of the same colour indicates identical concentrations of all components added.

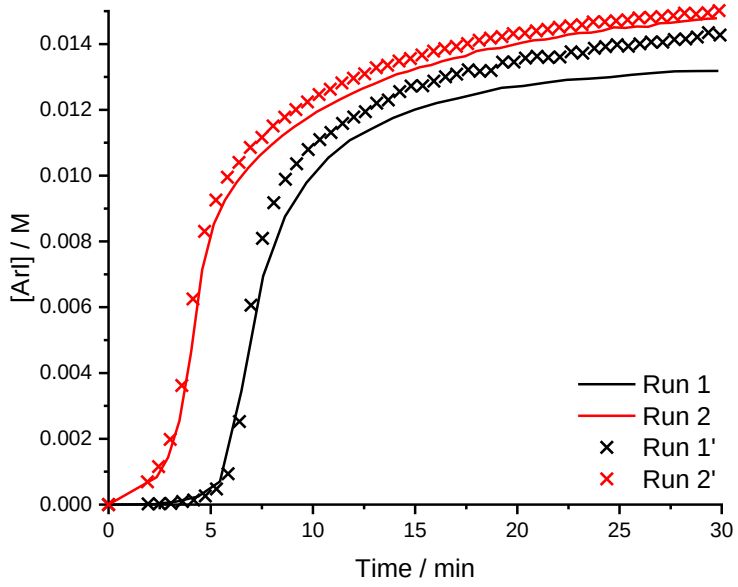

Figure 75: Graph comparing the growth of ArI where $PhI(OAc)_2$ and CSA were added at the same time (crosses) with the reaction where **E5** and CSA were premixed before the addition of $PhI(OAc)_2$ (line). Run 1 and Run 1': 0.005 mmol **E5**, 0.010 mmol $PhI(OAc)_2$, and 0.012 mmol CSA. Run 2 and Run 2': 0.005 mmol E5, 0.05 mmol $PhI(OAc)_2$, and 0.06 mmol CSA. All reactions were carried out in 0.715 mL $CDCl_3/CD_3OD$ (50:1).

5.3.4. Addition of HCl

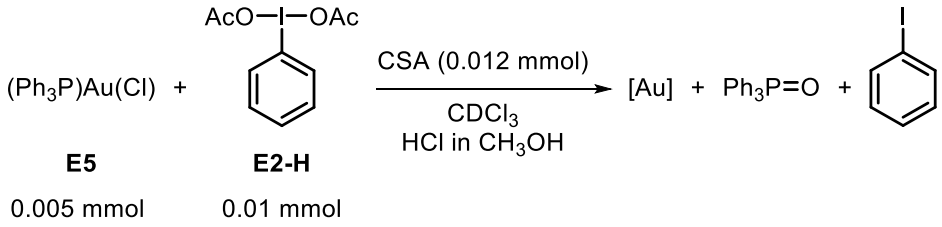

Scheme 55: Summary of reaction carried out with HCl added.

The effect of adding acid to the reaction profile obtained was tested, since CSA also behaves as a Brönsted acid (Scheme 55). This was carried out by substituting CD_3OD with a solution of hydrochloric acid in methanol (1.25 M).

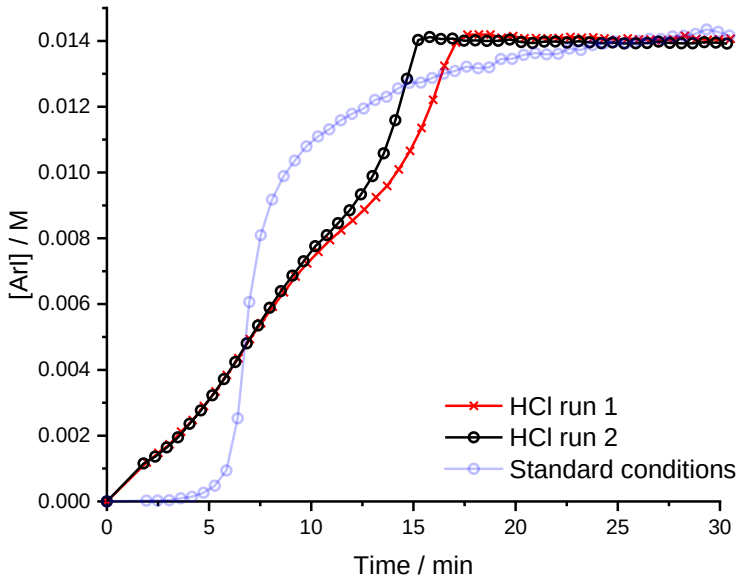

Figure 76: Graph showing the change in ArI concentration over time for two identical runs with HCl added and comparing this to the same reaction without HCl. Reaction conditions: 0.005 M **E5**, 0.010 M $PhI(OAc)_2$, and 0.012 M CSA in 0.7 mL $CDCl_3$ with 15 µL HCl in methanol (1.25 M) for the HCl runs, and in 0.715 mL $CDCl_3/CD_3OD$ (50:1) for the standard run.

The growth of aryl iodide over time is shown in Figure 76. The test with HCl was carried out twice to check for reproducibility, and the reaction carried out without any HCl was overlaid for comparison. The concentration changes over time showed a very different profile to that observed previously. The induction period seen under the standard conditions is not present in the reaction profile when HCl was added, and the burst in rate of aryl iodide formation does not occur. Furthermore, the decrease in rate towards the end of the reaction does not occur.

Instead, the profile shows four different regions: an initial slow growth of aryl iodide (< 5 min), a slight increase in rate (5 – 10 min), another slower period of aryl iodide production (10 – 13 min), and finally, a larger jump in rate of reaction towards the end. Both HCl runs follow the same profile and overlay fairly well, with the exception of the final rate increase. Run 2 has a smaller rate jump at the end when compared to Run 1.

Monitoring by $^{31}P\{^{1}H\}$ NMR spectroscopy

When the reaction with HCl was monitored by $^{31}P\{^{1}H\}$ NMR spectroscopy, three additional peaks were observed (Figure 77) in addition to the starting material (complex **E5**) and product (Ph_3PO).

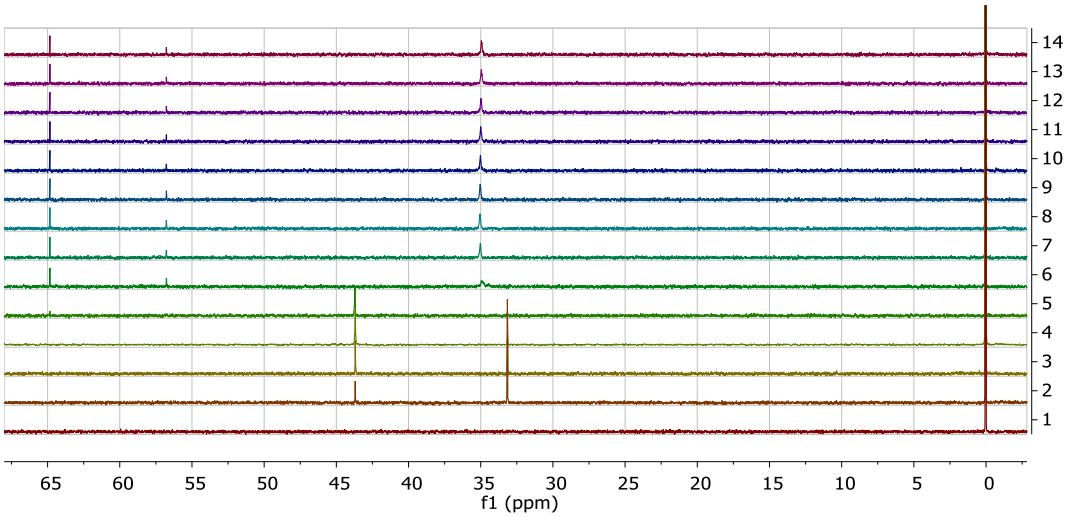

Figure 77: Stacked temporal $^{31}P\{^{1}H\}$ NMR spectra of the reaction shown in Scheme 55, obtained under the conditions described in Figure 76. Each spectrum was obtained after a 2.5 min delay, with the first spectrum obtained before initiation of the reaction (t_0). δ = 64.8 ppm, 56.8 ppm, 43.7 ppm, 35.0 ppm (Ph_3PO), 33.1 ppm (**E5**). The peak at 0 ppm is from an external capillary standard containing H_3PO_4.

Both the peaks at 64.8 ppm and 56.8 ppm in the $^{31}P\{^{1}H\}$ NMR spectra shown in Figure 77 appear together with the product from the reaction, triphenylphosphine oxide, whereas the peak at 43.7 ppm forms after initiation and disappears by the time the product signal starts to appear. This suggests that the compound at 43.7 ppm may be an intermediate in the reaction and is sufficiently stable under the conditions described in Scheme 55.

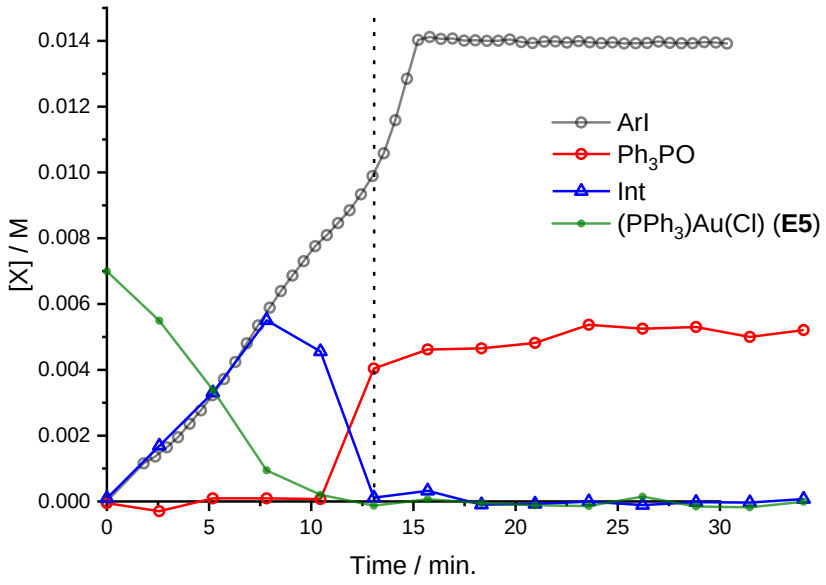

Figure 78: Graph describing the temporal concentration change of ArI, Ph_3PO, **E5,** and the intermediate (int) detected at 43.7 ppm for the reaction shown in Scheme 55 and the stacked $^{31}P\{^{1}H\}$ NMR spectra shown in Figure 77.

The temporal concentration of complex **E5**, triphenylphosphine oxide and the intermediate are shown in Figure 78, with the graph for aryl iodide growth overlaid in the background. In the first 7 minutes of the reaction, the intermediate grows together with the decay of the starting complex **E5**, and no triphenylphosphine oxide is observed. This is accompanied by the formation of aryl iodide. As the intermediate starts decaying, triphenylphosphine oxide is produced, together with more aryl iodide. Interestingly, the rate of aryl iodide formation increases after all of the phosphine oxide has formed, highlighted by the vertical dotted line in Figure 78.

5.3.5. Addition of chloride

It was thought that chloride in the solution[43] was responsible for the intermediate seen at 43.7 ppm (Figure 77). Therefore, the effect of adding Bu_4NCl was explored (Scheme 56).

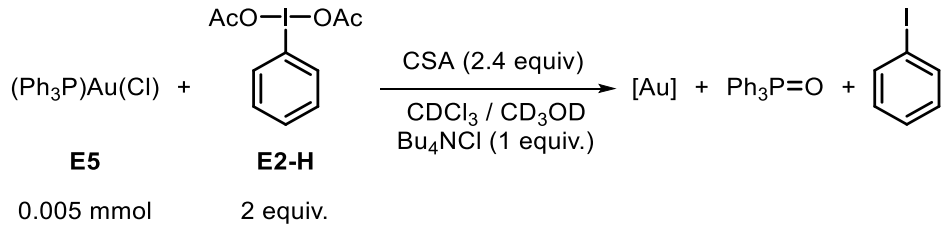

Scheme 56: Reaction carried out where the addition of chloride as Bu_4NCl was tested.

The stacked temporal $^{31}P\{^1H\}$ NMR spectra are shown in Figure 79. As with Figure 77, the peak at 43.7 ppm corresponding to an intermediate was found to be present. However, the other two side products (Figure 77, 64.8 ppm and 56.8 ppm) were not detected. Furthermore, unlike the spectra seen in Figure 77, Ph_3PO starts to form before all the intermediate is consumed.

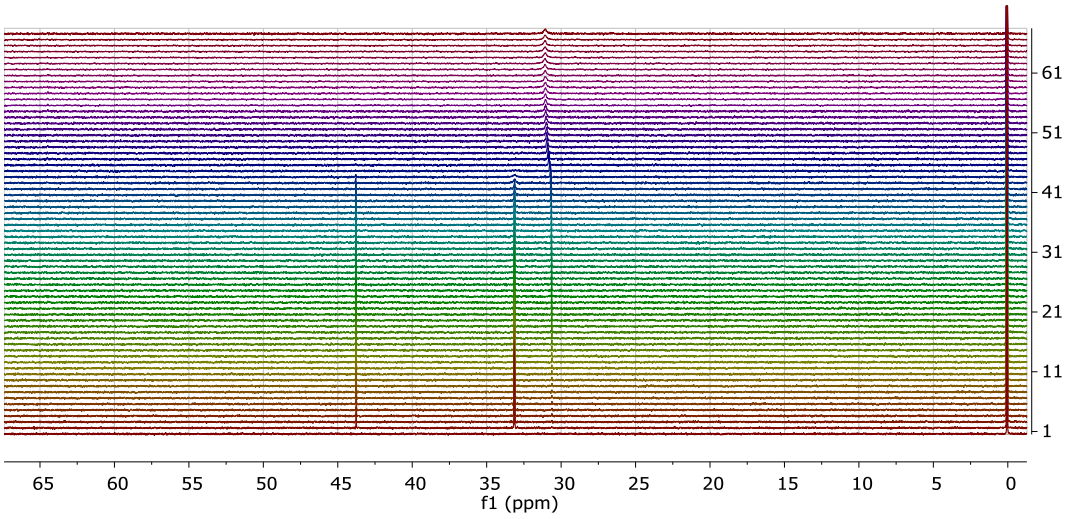

Figure 79: Stacked temporal $^{31}P\{^1H\}$ NMR spectra obtained for the reaction described in Scheme 56. Each spectrum was obtained after 2.5 min, with the first spectra taken at t_0, and the second spectra obtained at 3.5 min after initiation of the reaction. δ = 43.7 ppm (int), 33.1 ppm (**E5**), and 30.6 ppm (Ph_3PO). The peak at 0 ppm is from an external capillary standard containing $(OH)_3PO$.

The signals seen in Figure 79 were plotted as concentration against time, and the resulting graph is shown in Figure 80.

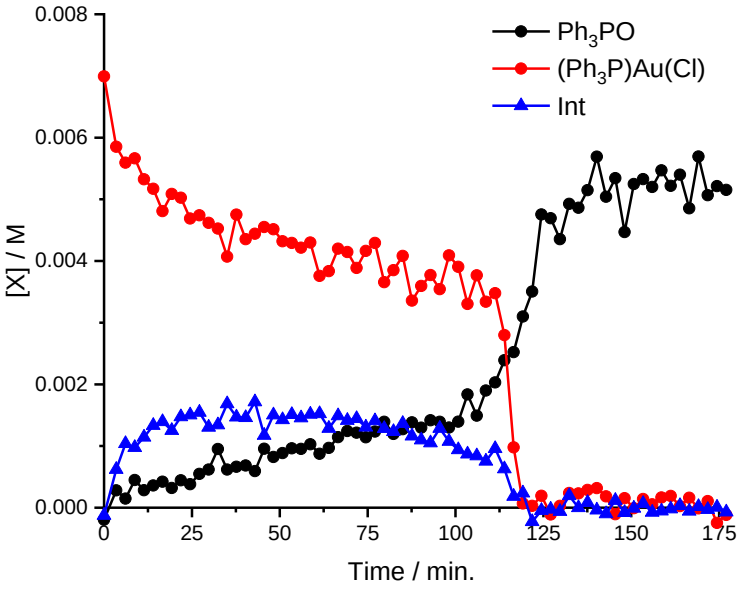

Figure 80: Graph showing the temporal concentration of the $^{31}P\{^{1}H\}$ NMR peaks observed in the spectra shown in Figure 79 based on the reaction summarised in Scheme 56, where 0.005 mmol of **E5**, 0.010 mmol $PhI(OAc)_2$, 0.012 mmol CSA, and 0.005 mmol of Bu_4NCl were dissolved in 0.715 mL CDC_3/CD_3OD (50:1).

Similar to the plots obtained in Figure 69, the reaction follows a similar pattern. An initial induction period was seen in the first 100 minutes, followed by a burst in reactivity to give Ph_3PO and consume both the starting gold complex **E5** and the intermediate. Finally, the reaction rate drops towards the end of the reaction (> 125 min) to give a curved profile at the end.

However, unlike the plots shown previously, the induction period obtained was a lot longer (100 min versus 5 min) and in this time, there was a small but significant formation of Ph_3PO. Furthermore, during the induction period, the intermediate discussed previously was formed and had a steady state concentration until the increase in rate was seen.

Nature of intermediate formed

Since the intermediate was only observed in the presence of chloride in solution (with the addition of HCl and Bu_4NCl), it was postulated that the identity of the intermediate was a gold(III) complex with three Cl^- ligands and a triphenylphosphine ligand (Figure 81). Comparison with literature data showed that complex **E8** has a $^{31}P\{^1H\}$ NMR signal at 44.3 ppm[106] in $CDCl_3$ whereas the intermediate formed has a peak at 43.7 ppm. This suggests that the intermediate formed is feasibly complex **E8**, based on its chemical shift and the reaction conditions where the intermediate was observed.

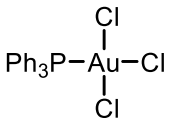

E8

Figure 81: Proposed identity of the intermediate observed with the addition of chloride into the reaction.

5.3.6. Proposed pathway in the presence of free chloride

It was proposed that under the reaction conditions where free chloride is present in solution (either by the addition of Bu_4NCl or HCl), the reaction takes a separate pathway via **E8**, which forms from the reaction of complex **E5** (Scheme 57). **E8** then reacts to give triphenylphosphine oxide as a product. As with the plot obtained in Figure 69, after the induction period, triphenylphosphine oxide is then formed at a significantly faster rate, which could be as a result of a switch in the pathways, so that the same pathway as observed without additional chloride present is now operating.

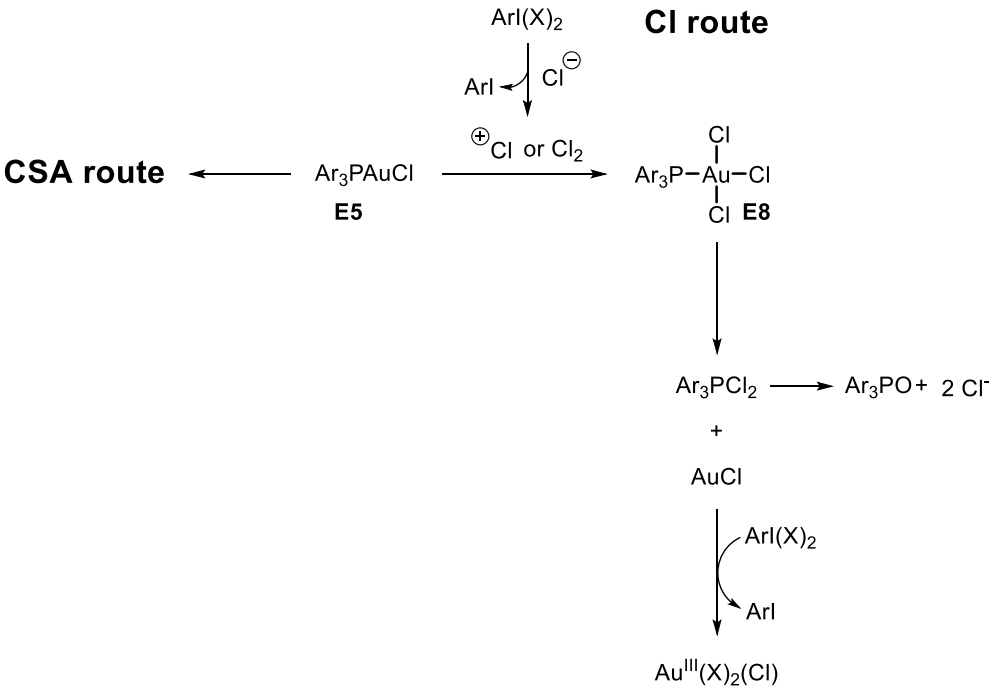

Scheme 57: Proposed pathway for the reaction of **E5** with hypervalent iodine(III) oxidants in the presence of free chloride. X = OCSA, OH, or Cl.

*Reaction of **E8***

To probe the pathway proposed in Scheme 57, complex **E8** was synthesised and tested in a reaction with $PhI(OAc)_2$ and CSA. The reaction was monitored by both $^{31}P\{^{1}H\}$ and ^{1}H NMR spectroscopy and the results are illustrated in Figure 82.

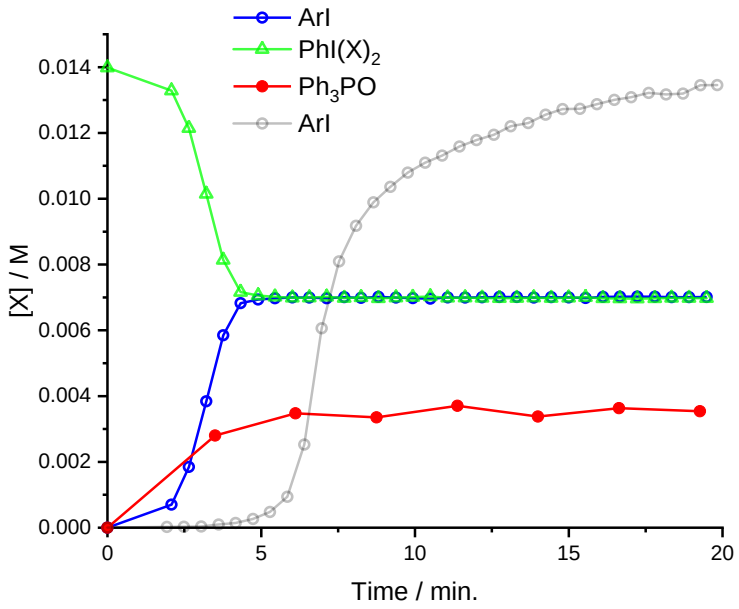

Figure 82: Graph showing the consumption of the oxidant and the formation of the aryl iodide during the reaction of complex **E8** (0.005 mmol) with $PhI(OAc)_2$ (0.010 mmol) and CSA (0.012 mmol) in 0.715 mL $CDCl_3/CD_3OD$ (50:1). The line in the background shows the growth of ArI obtained from the reaction described in Figure 69.

The graph shown in Figure 82 illustrates the change in concentration seen for the oxidant as well as the products, aryl iodide and triphenylphosphine oxide. The intermediate **E8** was not detected in the $^{31}P\{^{1}H\}$ NMR spectra as the reaction occurred, indicating that the reaction from **E8** is rapid. Overall, only one equivalent of oxidant relative to gold complex added was consumed, and one equivalent of triphenylphosphine oxide was formed. In comparison to the reaction carried out under the same conditions but with $(Ph_3P)Au(Cl)$ (**E5)** as the starting gold complex, the induction period observed for $(Ph_3P)Au(Cl)_3$ **E8** was a lot shorter, agreeing with the previous statement that the reaction from **E8** was observed to be faster than the oxidation of **E5** to give **E8**. However, the origin of the induction period for the reaction of **E8** is unclear.

*Effect of **E8***

Further test of the proposed pathway was carried out by spiking complex **E8** into the reaction shown in Scheme 56. This was to confirm that the intermediate observed was assigned correctly to complex **E8**.

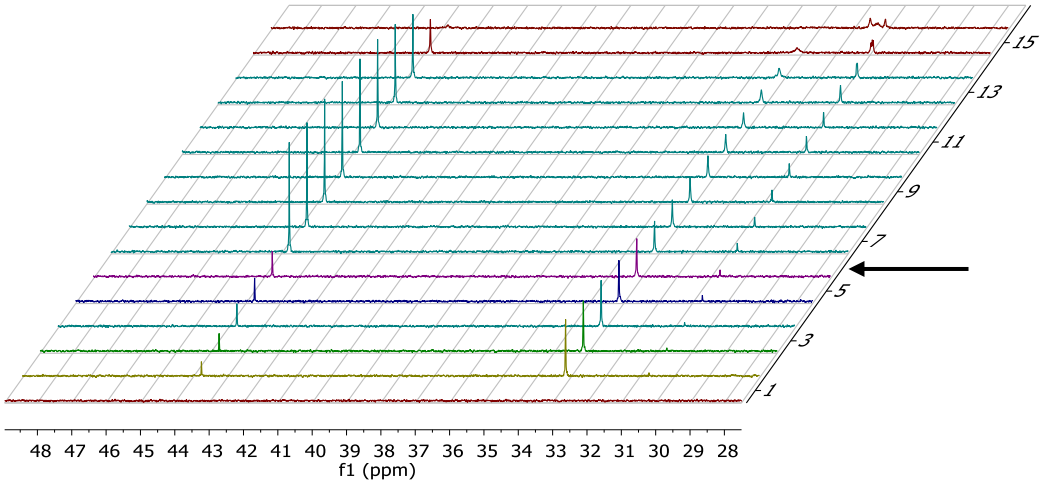

Figure 83: Stacked $^{31}P\{^{1}H\}$NMR spectra of the reaction described in Scheme 56 with the addition of complex **E8** prior to the acquisition of spectra 6. Spectra 1 corresponds to the spectra obtained at t_0, and spectra 2 was obtained with a delay of 3 minutes. The time gap between each spectra is 2.5 minutes, with the exception of the gap between spectra 6 and spectra 7, which had a delay of 6 minutes. The black arrow indicates addition of $(Ph_3P)Au(Cl)_3$ (**E8**).

The three signals observed in the stacked $^{31}P\{^{1}H\}$ NMR spectra shown in Figure 83 were plotted against time, and the resulting graph is displayed in Figure 84.

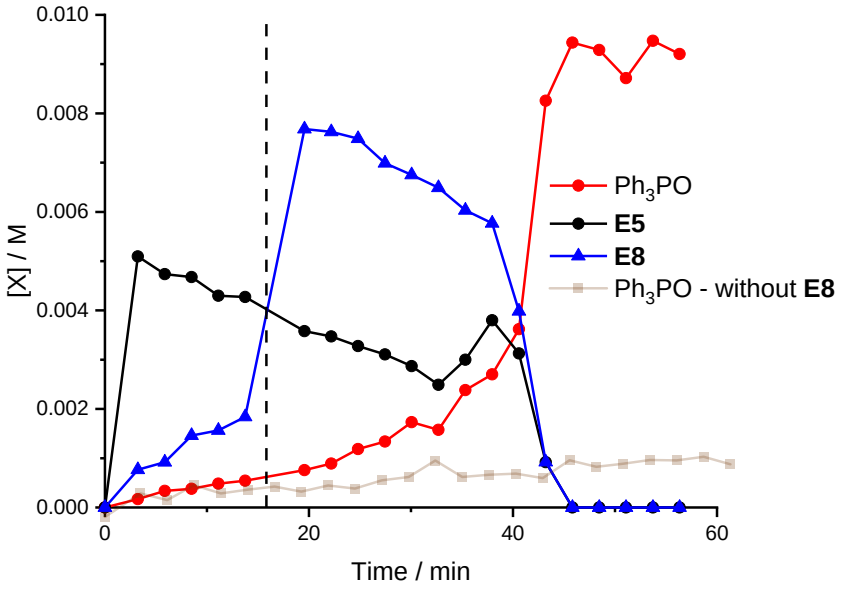

Figure 84: Graph showing the change in concentration of complex **E5**, **E8,** and triphenylphosphine oxide for the reaction shown in Scheme 56, with one equivalent of complex **E8** added in at 16 min. The reaction was carried out with 0.005 mmol **E5**, 0.010 mmol $PhI(OAc)_2$, 0.012 mmol CSA in 0.715 mL $CDCl_3/CD_3OD$ (50:1). The line in the background represents the growth of triphenylphosphine oxide without the addition of **E8**, as observed in Figure 80.

The graph in Figure 84 shows the temporal concentration plot of **E5**, **E8,** and triphenylphosphine oxide. The dotted line indicates the point where one equivalent of **E8** was added to the reaction mixture, and the plot in the background illustrates how the reaction would behave without spiking in **E8**. It can be seen that the introduction of **E8** decreases the induction period dramatically from 100 min which agrees with the previous observation that the reaction from **E8** occurs faster than the reaction from **E5** to form **E8**. Assuming that both **E8** and **E5** results in the formation of the same products, and that the reaction from **E5** goes via **E8**, this observation suggests that the reaction from **E8** produces the component responsible for increasing the rate of reaction of $(Ph_3P)Au(Cl)$ (**E5**).

5.4. Conclusion

The oxidation of phosphine-gold(I) chloride complexes with hypervalent iodine(III) oxidant was studied. Similar to the phosphine-gold(I) tosylate complex, the reaction consumed two equivalents of oxidant to produce two equivalents of aryl iodide and one equivalent of phosphine oxide. However, the chloride complex reacted at a much faster rate when compared to the tosylate complex. (Figure 67)

Using two equivalents of oxidant to gold(I) complex and 2.4 equivalents of CSA (Figure 69), an induction period was observed, followed by a burst in aryl iodide production. As the amount of aryl iodide formed reached two equivalents, the reaction slowed down significantly, and curved towards the end.

Keeping the concentration of oxidant the same but increasing the amount of CSA added, the role of free CSA was explored. It was found that higher concentrations of free CSA within the solution reduced the length of the induction period (Figure 73). The use of the preformed oxidant, **E7**, which meant that no free CSA was present in solution resulted in a very long induction period. However, beyond the induction period, the profile obtained for the growth of aryl iodide overlaid well with previous reactions where free CSA was present (Figure 74).

The dramatic increase in reaction rate suggested that either the reaction was autocatalytic, or there was a background reaction where an inhibitor had to be consumed before the reaction could proceed. The former was tested by addition of known products (iodobenzene and triphenylphosphine oxide, Figure 70) to the start of the reaction and the latter was tested by premixing CSA with the gold(I) complex before the reaction was initiated (Figure 75). These experiments revealed identical rates of aryl iodide growth.

HCl was added to assess the effect of a Brönsted acid on the reaction rate. A new intermediate was detected by $^{31}P\{^{1}H\}$ NMR spectroscopy at 43.7 ppm, and the reaction was further probed by addition of a chloride salt, Bu_4NCl. The formation of this intermediate was observed under these conditions, and the length of the induction period was dramatically increased. The intermediate was assigned to a gold(III) complex with three Cl^- and one triphenylphosphine ligand bound (**E8**). This complex was synthesised separately and tested in a reaction with an hypervalent iodine(III) oxidant. Only one equivalent of oxidant was consumed, which resulted in the formation of one equivalent of aryl iodide (Figure 82).

Addition of **E8** to an initiated reaction with Bu_4NCl decreased the length of the induction period, suggesting that reaction from **E8** also produced a product that could increase the rate of phosphine-gold(I) chloride oxidation.

5.4.1. Proposed reaction

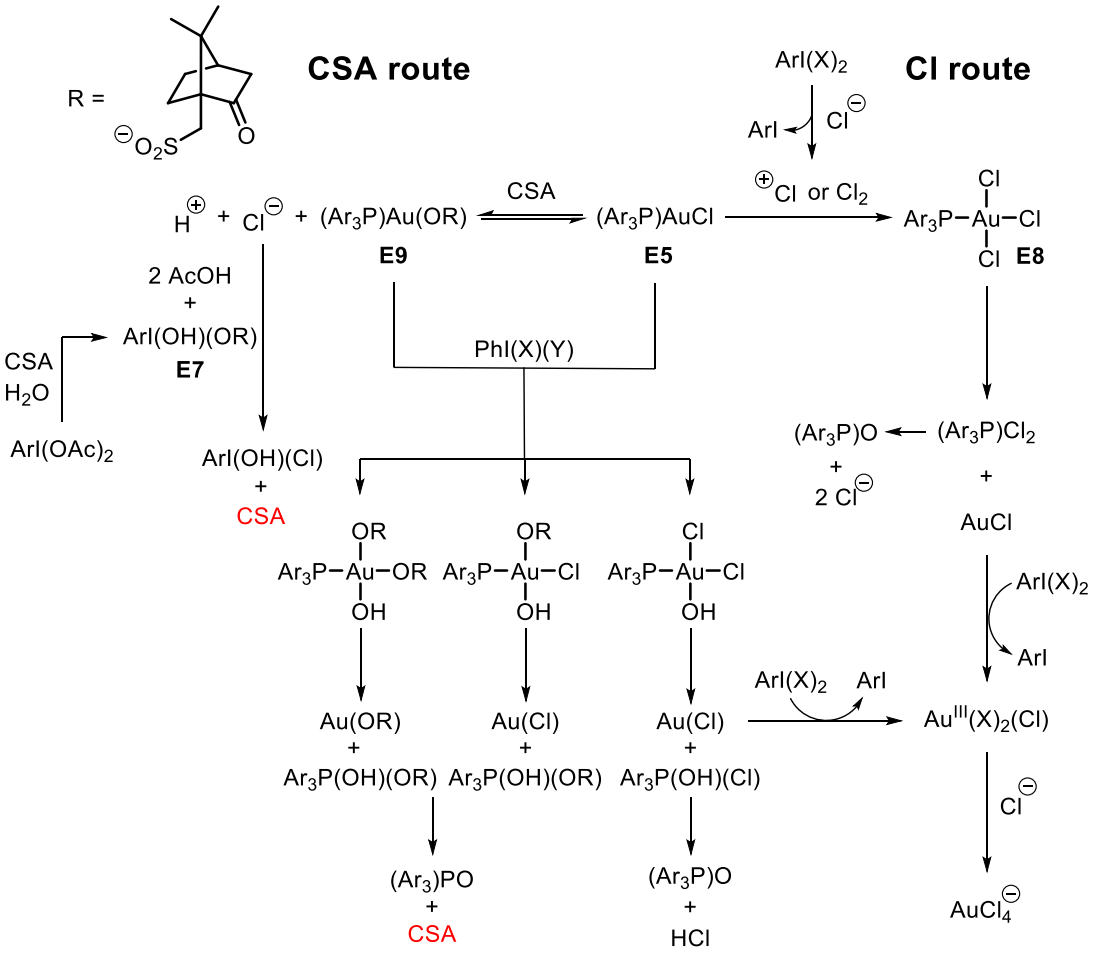

Scheme 58: Proposed reaction pathway for the oxidation of **E5**. PPh_3 has been abbreviated to P for clarity, X = OH, OR, Cl.

Based on the experiments carried out in this chapter, a tentative pathway for the reaction of $(Ph_3P)Au(Cl)$ (**E5**) with hypervalent iodine(III) oxidants has been proposed (Scheme 58). Focusing first on the Cl route, **E5** reacts with either "Cl^+" or Cl_2 to give complex **E8**, which has been synthesised independently and tested under the reaction conditions explored. Complex **E8** could then reductive eliminate, as proposed previously with the oxidation of $(Ph_3P)Au(OTs)$ (**E1**)[43] to give PCl_2, which can hydrolyse to give phosphine oxide and two equivalents of chloride as well as AuCl. This can then react with $ArI(X)_2$ to give a gold(III) complex and another equivalent of ArI. Since the phosphine ligand is no longer on the final gold complex formed here, the nature of this complex is unclear, and could have reacted with free chloride in solution to give $AuCl_4^-$, which is a known and stable anion.[107,108] The first step of this pathway was considered to be the slower step when compared to the reductive

elimination step, as the reaction from complex **E8** was a lot quicker, and addition of **E8** midway through the reaction shown in Scheme 56 resulted in a shorter induction period.

Following the reaction via the CSA route, an initial equilibrium between **E5** and CSA was proposed, to give complex **E9**. From this, the Cl^- ligand formerly on the gold could be oxidised to give a species that could react with gold more quickly, or the resulting complex **E9** could react with hypervalent iodine(III) oxidants at a greater rate when compared to complex **E5**. These suggestions could explain the role of CSA in reducing the induction period. Although CSA was not suggested to be directly catalysing the reaction, if new pathways involving CSA were provided where the formation of products as well as the species responsible for increasing the rate of reaction of **E5** were accelerated, the shorter induction period seen for higher free CSA concentration could be reasoned.

In Scheme 58, following the CSA pathway, multiple gold(III) products[8] were proposed based on the reaction of **E5** and/or **E9** with hypervalent iodine(III) oxidants. This is consistent with the fact that the peak for **E5** observed in $^{31}P\{^1H\}$ NMR spectroscopy shrinks before the peak for triphenylphosphine oxide is seen (Figure 69), suggesting that multiple, low concentration species are formed, and it is possible that these species are in equilibrium with each other.

The species highlighted in red indicates the formation of free CSA, which could be a factor in the accelerating rate of reaction. Finally, the removal of free chloride in solution to give $AuCl_4^-$ could explain the switch from the Cl pathway to the CSA pathway, which appears to be observed in Figure 80. Furthermore, removal of chloride will reduce the formation of ArI(OH)(Cl) proposed previously, and thus slow down the reaction as it approaches completion.

Chapter 6

Conclusion and future work

The work carried out in this thesis have focused on the role of hypervalent aryliodine(III) oxidants and its reactivity with gold(I) complexes. Chapters 2 and 3 have shown that the oxidant with a higher redox potential, and thus the stronger oxidant thermodynamically reacted slower in a gold(III)-catalysed direct arylation reaction, when competed with the oxidants that had lower redox potentials. Together with the construction of a Hammett plot against σ^+ values, it was proposed that ligand dissociation from the iodine(III) centre was occurring prior to the oxidation of gold(I). This is illustrated in Scheme 59.

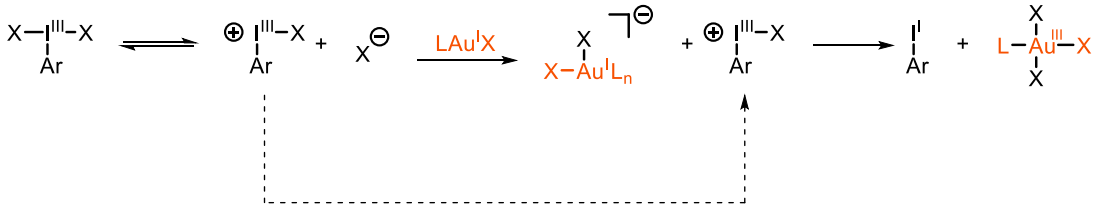

Scheme 59: Summary of proposed mechanism for the oxidation of gold(I) with hypervalent iodine(III) oxidants.

Due to several issues associated with the nature of competition studies, approaches towards obtaining absolute rates of oxidation were considered, and discussed in Chapter 4. A rapid injection system was developed to deliver oxidant to an NMR tube inside the NMR spectrometer. This reduces the dead-time observed previously, allowing for the observation of gold(I) oxidation. The results obtained indicated a possible equilibrium between the gold(I) species and an off-cycle species, AuX. This step was probed with the aid of a chemical modelling software, Dynochem®, and the simplified catalytic cycle shown in Scheme 60 was modelled.

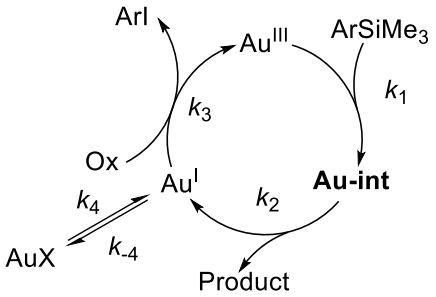

Scheme 60: Summary of model fitted to the experimental observation for the growth of ArI. The best fit was obtained when an equilibrium with an off-cycle species, AuX, where X is not known, was added in.

Further development into the rapid injection system would prove beneficial for this study. For example, the resolving the issue surrounding the trigger button would allow for a more accurate t_1 determination. This will provide more accurate analysis of the reaction, including a better fit of the reaction model to the experimental data. In addition to this, the issue regarding the volume of reagent added during the reaction has to be determined and repaired. This will ensure full control over the reaction conditions tested, as well as to ensure a broader applicability of the rapid-mixing device.

Additional insight into the mixing distribution of the rapid injection device would provide better understanding and allow identification of areas for improving mixing efficiency. The testing carried out in Chapter 4 showed that mixing with the final setup was complete after approximately 3 seconds. However, the spatial distribution of the injected component over time has not been identified. Hore et. al.[103] utilised NMR imaging techniques to observe the radial and axial mixing of their device. This was carried out by injecting a small amount of H_2O into D_2O and observing the flow of injected liquid along the x-axis and z-axis of the tube. From these experiments, they concluded that the injected liquid flows down the middle and up the sides of the tube for efficient mixing, and the solution was completely mixed between 40 and 50 ms.

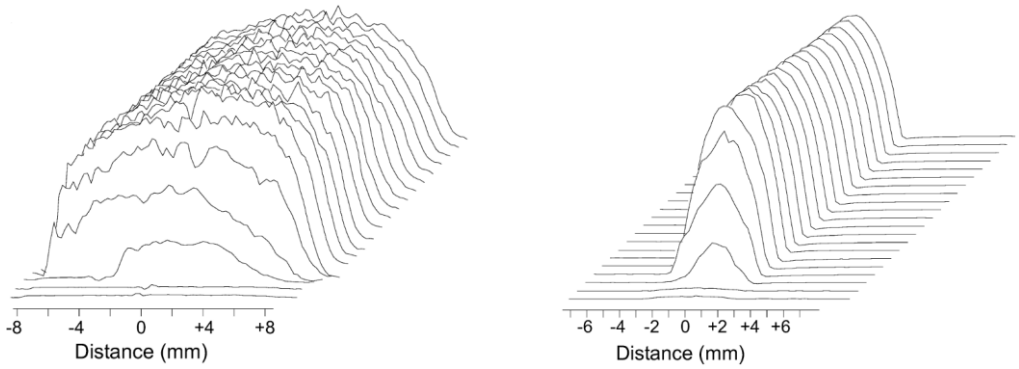

Figure 85: Stacked ^{1}H NMR spectra showing the one-dimensional NMR images, where the spectra were recorded at 10 ms interval. Left: real-time NMR images obtained along the z-axis (right-hand side shows the top of the NMR sample), right: images obtained along the x-axis of the tube.[103]

Furthermore, the identification of the unknown gold-complex, AuX, will assist in understanding the proposed equilibrium, as shown in Scheme 60. The oxidation of Au(I) can be more accurately studied if the kinetic parameters of the equilibration can be obtained. Currently, it is thought that X could originate from water within the reaction mixture. This is a complicated issue, as the active oxidant produces water as it is consumed. Studying the independent reactivity of the active oxidant will allow quantification of water produced, and thus the effect of water can be probed, both experimentally as well as using Dynochem®. In addition, the identity of X can be dictated by utilising potential trapping ligands to stabilise the gold(I) complex.

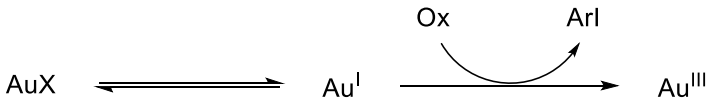

Scheme 61: Proposed method of observing the oxidation of gold(I) complex formed under the direct arylation reaction conditions.

Another main issue surrounding the study into the mechanism of gold(I) oxidation within the direct arylation reaction is that the identity of the gold(I) species is unknown. Throughout the direct arylation reaction, the ligands around the gold complex are proposed to change.[43] However, it has been found that the use of ortho-substituted silanes are able to trap the gold complex before it undergoes reductive elimination.[109] Obtaining crystal structures of these complex will aid in the identification of potential ligands around the gold complex.

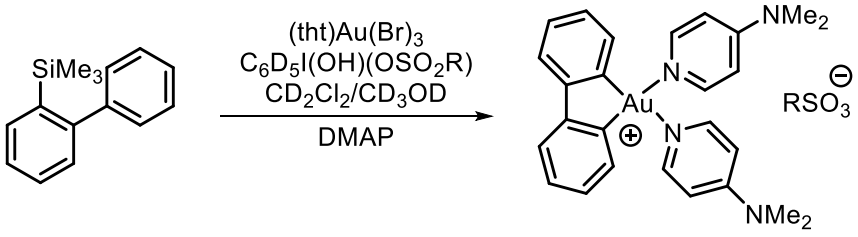

Scheme 62: Crystal structure of a trapped gold(III) complex obtained by addition of DMAP to the reaction mixture.

In contrast to catalytic conditions in the direct arylation reaction, the oxidation of phosphine-gold(I) chloride with stoichiometric amounts of oxidant was probed, where the starting reagents could be monitored by ^{1}H NMR and ^{31}P NMR spectroscopy. Two equivalents of oxidant relative to gold(I) were consumed to give two equivalents of aryl iodide and one equivalent of triphenylphosphine oxide, both of which could also be monitored by NMR spectroscopy.

It was found that the length of induction period observed was dependent on the amount of free CSA as well as free chloride in solution. The latter resulted in the observation of a new intermediate, proposed to be $(Ph_3P)Au(Cl)_3$. This was confirmed with the independent synthesis of the complex as well as spiking the complex into an already initiated reaction mixture.

A complex reaction pathway was proposed with two distinct routes suggested: a chloride pathway which is dominant in the presence of additional chloride, and a CSA pathway which the complex takes in absence of additional chloride. This is summarised in Scheme 58, Chapter 5). The proposed reaction could be systematically probed by synthesis of the intermediates (or similar complexes) and observing their behaviour under the reaction conditions.

The reaction of $(Ph_3P)Au(OTs)$ with $PhI(OAc)_2$ and CSA was found to give PhI and Ph_3PO at a much slower rate when compared to the oxidation of $(Ph_3P)Au(Cl)$. This suggests that the pathway from the proposed complex **E9** ($(Ar_3P)Au(OCSA)$ with HCIB as the oxidant is slower compared to oxidation with $PhI(Cl)_2$[109] or PhI(OH)(Cl). The rate of reaction between complex **E9** and $PhI(Cl)_2$[82] will allow for the proposed CSA route to be studied further.

In addition, similar studies could be carried out on different analogues of phosphine-gold(I) complexes, where a variety of phosphines with different electronic and steric properties can be explored. Similarly, the reactivity of phosphine-gold(I) complexes with different anionic ligands can be probed. This study was previously carried out under catalytic, direct arylation conditions.[43] Stoichiometric studies of these reactions could provide further insight into the mechanism of phosphine-gold oxidations.

Chapter 7

Experimental

7.1. General experimental details

7.1.1. Techniques

Analytical thin-layer chromatography was performed on precoated aluminum-backed plates (Silica Gel 60 F254; Merck), and visualised using a combination of UV light (254 nm). Column chromatography was performed using Davisil® 60A silica gel (35-70 μm; Fisher Scientific) or Geduran® Silica Gel 60 (40-63 μm; Merck).

7.1.2. Reagents and solvents

All commercial reagents were obtained from Sigma-Aldrich, Fluorochem, Fisher Scientific, Acros Organics or Alfa Aeser. $(Ph_3P)Au(Cl)$ and $AuBr_3$ were purchased from Sigma Aldrich. $HAuCl_4$ was purchased from Fisher Scientific. (IPr)Au(Cl) was generously donated by Umicore AG & Co. KG. The following gold complexes were synthesised according to literature procedures: $(tht)Au(Br)_3$,[111] $(Ph_3P)Au(OTs)$,[112] (tht)Au(Cl)[113], (IPr)Au(Br)[114]. All arylsilane compounds[50] and hypervalent aryliodine(diacetate) compounds[97] were synthesised according to literature procedure.

Deuterated solvents were purchased from Sigma-Aldrich and Cambridge Isotopes Limited. Anhydrous organic solvents were obtained from a solvent purification system (MBraun SPS 800) situated in the School of Chemistry, University of Edinburgh. Commercial grade solvents were used for extractions, TLC analysis and flash column chromatography. Deionised water was obtained through a membrane filtration system.

7.1.3. Analysis

NMR spectroscopy

NMR spectra were recorded at 27 °C unless stated otherwise; ^{1}H, $^{13}C\{^{1}H\}$, and ^{19}F NMR spectra were recorded at 600/500/400 MHz, 125/100 MHz and 470/376/282 MHz, respectively, using Bruker Avance I 600, Bruker Avance I 400, Bruker Avance III 500 and Bruker Avance III+ 400 spectrometers. ^{1}H and $^{13}C\{^{1}H\}$ NMR spectra were referenced to residual solvent peaks ($CHCl_3$, δ_H 7.26 ppm; $CDCl_3$, δ_C 77.16 ppm); chemical shifts are reported in ppm relative to tetramethylsilane standard. ^{19}F NMR spectra are reported in ppm relative to a $BF_3{\cdot}OEt_2$ external standard. $^{31}P\{^{1}H\}$ NMR spectra are reported in ppm relative to a 85% aqueous H_3PO_4 external standard. Coupling constants, J, were calculated using Mestrenova versions 10, and are reported to the nearest 0.1 Hz. Coupling constants that did not match as a result of digitization are reported as rounded averages. The following abbreviations (and their combinations) are used to label the multiplicities: s (singlet), d (doublet), t (triplet), q (quartet), m (multiplet) and br (broad).

IR spectroscopy

Infrared spectra of neat compounds were recorded over the range 4000-600 cm^{-1} using a Perkin-Elmer Spectrum 1000 Series FTIR spectrophotometer with an ATR diamond cell.

Melting point analysis

Melting points were measured using Stuart SMP3 melting point apparatus in open capillaries and are uncorrected.

Electrochemistry

Electrochemical measurements were made using 1 mM of the analyte in 12 mL of degassed acetonitrile or DCM, using 0.1 M [n Bu_4N][PF_6] as the supporting electrolyte, under a flow of dry N_2 gas. An Autolab ECO Chemie PGSTAT potentiostat was used, with a glassy-carbon disk (d = 3 mm) working electrode, Pt-gauze counter electrode, Ag-wire quasi-reference electrode, and ferrocenium/ferrocene standard (Fc^+ /Fc = 0 V). Data were processed using GPES Manager 4.9. Cyclic voltammograms were recorded for quiescent solution at variable scan rates between 100 – 500 mV s^{-1}. Square-wave voltammograms were recorded using a frequency of 25 Hz, a step potential of 5 mV and an amplitude of 20 mV, giving a scan rate of 124 mV s^{-1}.

UV spectroscopy

All UV spectroscopy experiments were carried out in an ultraviolet–visible cuvette (pathlength 10 mm) with 3 mL of solvents, with concentrations ranging from 0.03 mM to 0.5 mM. Spectra were collected using Ocean Optics USB4000 detector and the data processed in Kinetic Studio, TgK Scientific.

Videos of rapid injection

Filmed in slow motion (240 frames per second) on an iPhone SE.

7.2. Synthetic procedures

$(Ph_3P)Au(Cl)_3$

$(Ph_3P)Au(Cl)$ (46.6 mg, 0.1 mmol) was dissolved in DCM (1 mL) and stirred under nitrogen in a round-bottom flask wrapped with foil. $NaBO_3.4H_2O$ (30.8 mg, 0.2 mmol) and $HCl_{(aq)}$ (20 µL, 30.5% concentration) were added to the flask, and more DCM (1 mL) was used to wash down the sides of the flask. The reaction was left to stir for 2 hours, and ice-cold water (5 mL) and DCM (5 mL) was added. The organic layer was separated and washed with more water (5 mL), then dried with $MgSO_4$ and filtered. The filtrate was concentrated by blowing a stream of nitrogen over the solution. The resulting solid was dissolved in the minimum amount of DCM and pentane was added. The flask was left to cool in the freezer. The resulting solid was filtered off and washed with pentane, then dried under vacuum to give $(Ph_3P)Au(Cl)_3$ as a yellow solid (30 mg, 53% yield). The compound was stored in a vial wrapped with foil in the freezer.

^{1}H NMR (400 MHz, Chloroform-*d*) δ 7.77 – 7.63 (m, 9H), 7.61 – 7.51 (m, 6H). ^{13}C NMR (101 MHz, Chloroform-*d*) δ 135.25 (d, *J* = 10.3 Hz), 133.91 (d, *J* = 3.3 Hz), 129.36 (d, *J* = 12.9 Hz), 123.42 (d, *J* = 69.5 Hz). ^{31}P NMR (162 MHz, Chloroform-*d*) δ 43.59 (s).[106]

7.3. Procedures and data relevant to Chapter 2

7.3.1. Control reactions

General Procedure

$MeArI(OAc)_2$ (10.5 mg, 0.0312 mmol) was dissolved in $CDCl_3$ (1 mL) and PhI (3.50 µL, 0.0312 mmol), CD_3OD (200 µL), CSA (9.46 mg, 0.0406 mmol, 1.3 equiv) and $(tht)Au(Br)_3$ (31 µL from a 0.01 M solution in $CDCl_3$, 2 mol%) were added depending on the experiment.

7.3.2. Reaction monitoring

A: MeArI(OAc)$_2$ (52.4 mg, 0.155 mmol), PhI (17.5 µL, 0.155 mmol) and CH_2Br_2 (5.50 µL, 0.078 mmol) were combined. The mixture was made up to 5 mL with a 50:1 solution of $CDCl_3$/CD_3OD.

1.0 mL of stock solution **A** was added Ph camphorsulfonic acid (9.46 mg, 0.041 mmol, 1.3 equiv) in an NMR tube. The ^{1}H NMR spectrum at t_0 was obtained at this point. (tht)Au(Br)$_3$ (62.4 µL of a 0.005 M solution in $CDCl_3$, 1 mol%) and $CDCl_3$ (37.6 µL) were added to the tube, and the tube was shaken vigorously. A ^{1}H NMR spectrum at t_1 was then obtained, where t_1 is the time between mixing all the components and the midpoint of the time it takes to acquire the first spectrum. A ^{1}H NMR spectrum is then obtained every 2 minutes.

1.0 mL of stock solution **A** was added to camphorsulfonic acid (9.46 mg, 0.041 mmol, 1.3 equiv) in an NMR tube. The ^{1}H NMR spectrum at t_0 was obtained at this point. (tht)Au(Br)$_3$ (31.2 µL of a 0.005 M solution in $CDCl_3$, 0.5 mol%) and $CDCl_3$ (68.8 µL) were added to the tube, and the tube was shaken vigorously. A ^{1}H NMR spectrum at t_1 was then obtained, where t_1 is the time between mixing all the components and the midpoint of the time it takes to acquire the first spectrum. A ^{1}H NMR spectrum is then obtained every 2 minutes.

1.0 mL of stock solution **A** was added to camphorsulfonic acid (9.46 mg, 0.041 mmol, 1.3 equiv) in an NMR tube. The ^{1}H NMR spectrum at t_0 was obtained at this point. (tht)Au(Br)$_3$ (18.7 µL of a 0.005 M solution in $CDCl_3$, 0.3 mol%) and $CDCl_3$ (81.3 µL) were added to the tube, and the tube was shaken vigorously. A ^{1}H NMR spectrum at t_1 was then obtained, where t_1 is the time between mixing all the components and the midpoint of the time it takes to acquire the first spectrum. A ^{1}H NMR spectrum is then obtained every 2 minutes.

1.0 mL of stock solution **A** was added to camphorsulfonic acid (9.46 mg, 0.041 mmol, 1.3 equiv) in an NMR tube. The ^{1}H NMR spectrum at t_0 was obtained at this point. (tht)Au(Br)$_3$ (12.5 µL of a 0.005 M solution in $CDCl_3$, 0.2 mol%) and $CDCl_3$ (87.5 µL) were added to the tube, and the tube was shaken vigorously. A ^{1}H NMR spectrum at t_1 was then obtained, where t_1 is the time between mixing all the components and the midpoint of the time it takes to acquire the first spectrum. A ^{1}H NMR spectrum is then obtained every 2 minutes.

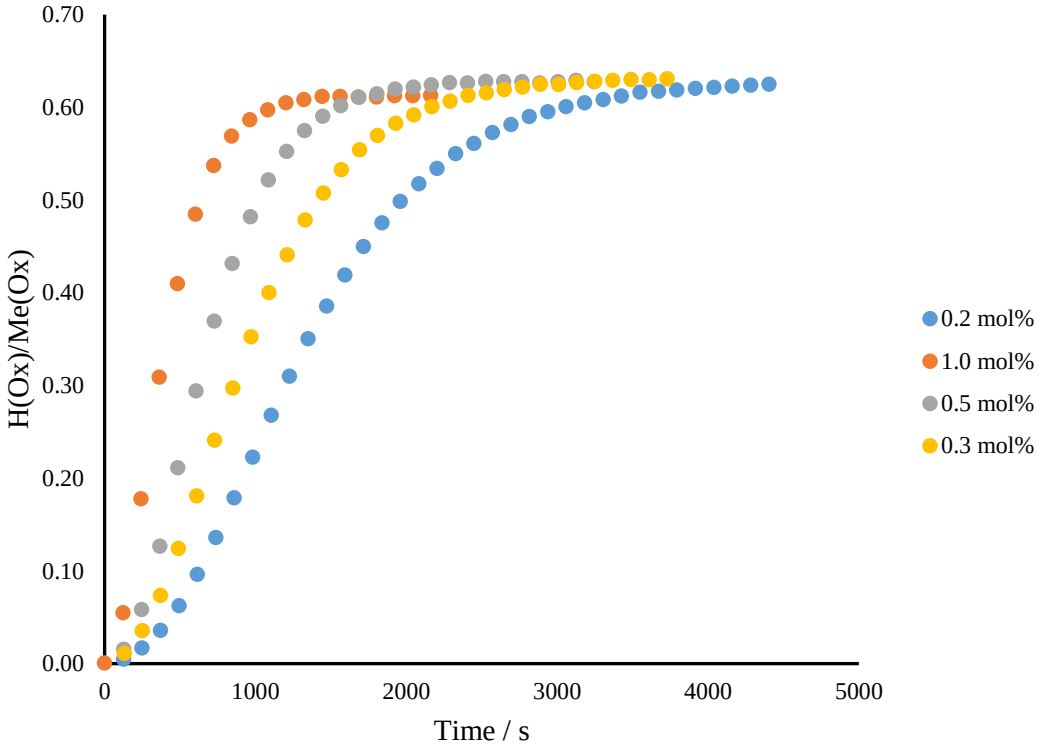

Figure 86: Graph showing the change in ratio between H(Ox) and Me(Ox) over time with different catalyst loadings.

7.3.2. Catalyst screen

MeArI(OAc)$_2$ (10.5 mg, 0.0312 mmol), CSA (9.46 mg, 0.0406 mmol, 1.3 equiv) and PhI (3.50 µL, 0.0312 mmol was dissolved in $CDCl_3$/CD_3OD (50:1, 1 mL). Catalyst (2 mol%) was added.

7.3.3. Reaction of PhI(OAc)$_2$ with *m*-OMeArI (Scheme 25)

m-OMeArI (59.5 µL, 0.50 mmol), PhI(OAc)$_2$ (177 mg, 0.55 mmol, 1.1 equiv) and camphorsulfonic acid (151.65 mg, 0.65 mmol, 1.3 equiv) were dissolved in $CHCl_3$/MeOH (50:1 mixture, 1 mL). Bu_4NBr (177 mg, 0.55 mmol, 1.1 equiv) was added, and the mixture was left for 90 minutes. The solvent was removed, and the crude mixture analysed by ^{1}H NMR spectroscopy. The aromatic region of the spectra is shown below in Figure 87.

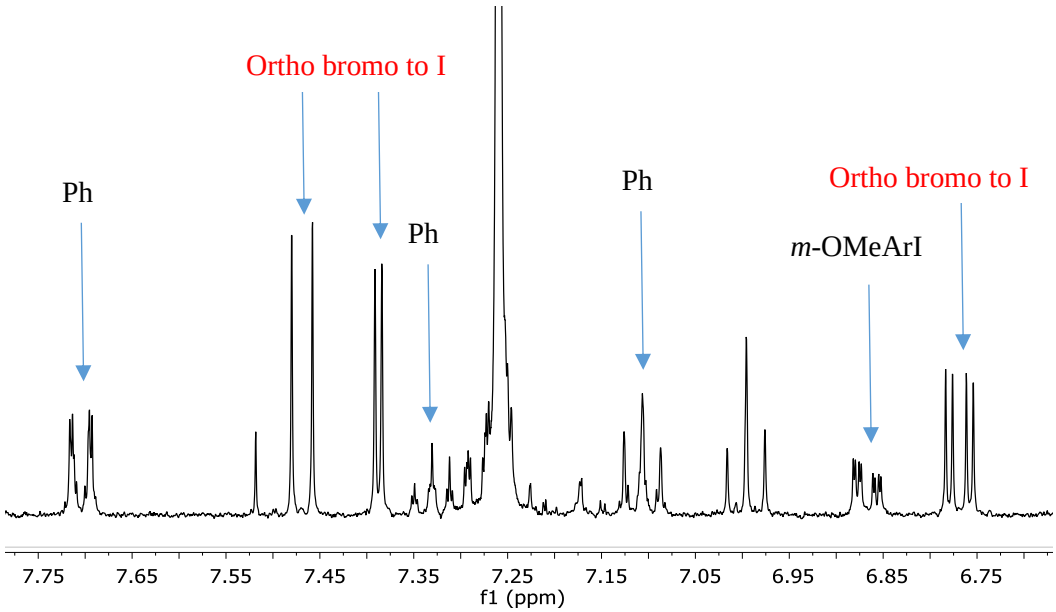

Figure 87: ^{1}H NMR spectra of the crude reaction mixture for the reaction shown in Scheme 25.

7.3.4. Oxidant potentials

General procedures for each run are shown below. A summary of the calculated equilibrium constant (*K*) and the calculated potentials are shown in Table 8.

Run 1 and run 2:

$PhI(OAc)_2$ (101 mg, 0.310 mmol), camphorsulfonic acid (94.6 mg, 0.40 mmol, 1.3 equiv) and CH_2Br_2 (11 µL, 0.15 mmol, 0.5 equiv) were combined. The mixture was made up to 5 mL with a 50:1 solution of $CDCl_3/CD_3OD$.

0.5 mL of the stock solution above was added to the appropriate ArI (0.0312 mmol, 1 equiv) and $(tht)Au(Br)_3$ (62 µL of a 0.005 M solution in $CDCl_3$, 1 mol%). The mixture was left overnight, then analysed by ^{1}H NMR. All peaks were integrated relative to the CH_2Br_2 standard.

Run 3:

$PhI(OAc)_2$ (100 mg, 0.310 mmol), camphorsulfonic acid (94.6 mg, 0.40 mmol, 1.3 equiv) and CH_2Br_2 (11.0 µL, 0.156 mmol, 0.5 equiv) were combined. The mixture was made up to 5 mL with a 50:1 solution of $MeCN\text{-}d_3/CD_3OD$.

0.5 mL of the stock solution above was added to the appropriate ArI (0.1 mmol, 1 equiv) and Bu_4NBr (62 µL of a 0.010 M solution in MeCN, 2 mol%). The mixture was left overnight, then analysed by ^{1}H NMR. All peaks were integrated relative to the CH_2Br_2 standard.

Run 4:

$PhI(OAc)_2$ (322 mg, 1.0 mmol) and CH_2Br_2 (35.3 µL, 0.50 mmol, 0.5 equiv) were combined. The mixture was made up to 5 mL with $CDCl_3$.

0.5 mL of the stock solution above was added to the appropriate ArI (0.1 mmol, 1 equiv) and $(tht)Au(Br)_3$ (200 µL of a 0.005 M solution in $CDCl_3$, 1 mol%). The mixture was left for two days, then analysed by ^1H NMR. All peaks were integrated relative to the CH_2Br_2 standard.

Table 8: Calculated potentials obtained relative to $PhI(X)_2$ of various substituted hypervalent aryliodine(III) oxidants

	No.	R	σ	*K*	E / v
Run 1	1	*p*-CF_3	0.54	11.12	0.0311
	2	*p*-NO_2	0.78	40.35	0.0478
	3	*p*-^{t}Bu	-0.20	0.30	-0.0155
	4	*p*-Me	-0.17	0.41	-0.0115
	5	*p*-Cl	0.23	2.75	0.0131
	6	*p*-Br	0.23	2.92	0.0139
	7	*p*-OMe	-0.27	0.24	-0.0186
	8	*p*-F	0.06	1.54	0.0056
	9	*m*-NO_2	0.71	29.29	0.0437
Run 2	1	*p*-F	0.06	1.38	0.0042
	2	*p*-CF_3	0.54	10.04	0.0298
	3	*p*-NO_2	0.78	27.98	0.0431
	4	*p*-^{t}Bu	-0.20	0.40	-0.0117
	5	*p*-OMe	-0.27	0.20	-0.0210
	6	*p*-Br	0.23	2.76	0.0131
Run 3	1	*p*-CF_3	0.54	9.46	0.0289
	2	*p*-NO_2	0.78	23.84	0.0407
	3	*m*-NO_2	0.71	12.45	0.0324
	4	*p*-^{t}Bu	-0.20	0.41	-0.0113
	5	*p*-Me	-0.17	0.43	-0.0107
	6	*p*-Br	0.23	2.71	0.0128
Run 4	1	*p*-F	0.06	1.36	0.0040
	2	*p*-CF_3	0.54	8.10	0.0270
	3	*p*-NO_2	0.78	30.61	0.0442
	4	*p*-^{t}Bu	-0.20	0.43	-0.0108
	5	*p*-Br	0.23	2.41	0.0114
	6	*p*-Me	-0.17	0.53	-0.0081

7.3.5. Electrochemistry procedures

The reduction potential for hypervalent aryliodine(III) diacetates were obtained as described in the general experimental for electrochemistry experiments in DCM.

The cyclic voltammogram and square-wave voltammograms of these oxidants are shown below.

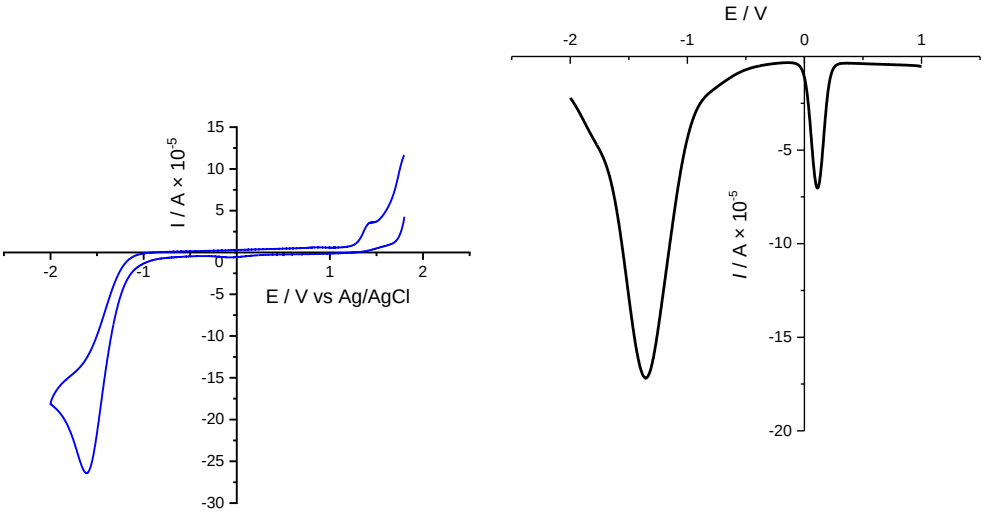

Figure 88: Left: Cyclic voltammogram of $PhI(OAc)_2$. Right: Square-wave voltammogram of $PhI(OAc)_2$.

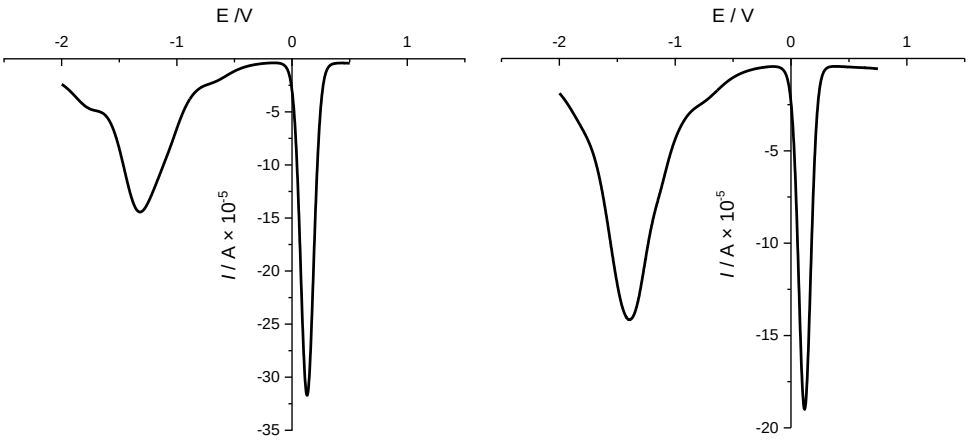

Figure 89: Left: Square-wave voltammogram of *p*-$ClArI(OAc)_2$. Right: Square-wave voltammogram of *p*-$MeArI(OAc)_2$.

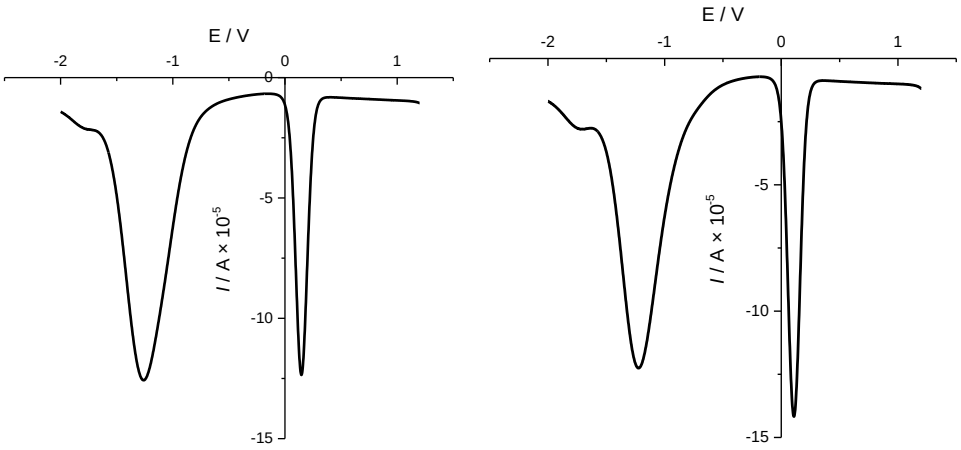

Figure 90: Left: Square-wave voltammogram of *p*-FArI(OAc)$_2$. Right: Square-wave voltammogram of *p*-CF$_3$ArI(OAc)$_2$.

7.4. Procedures and data relevant to Chapter 3

7.4.1. General procedure for competition reactions

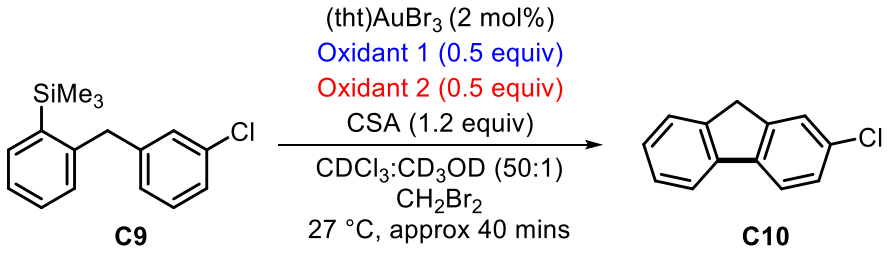

A: **C9** (344 mg, 1.25 mmol) and CD_3OD (245 μL) were mixed, and the solution made up to 10 mL with $CDCl_3$.

B: (tht)Au(Br)$_3$ (26.2 mg, 0.05 mmol) was dissolved and made up to 5 mL with $CDCl_3$.

Stock solution **A** (0.80 mL) and stock solution **B** (0.20 mL) were combined in an NMR tube. The ^{1}H NMR spectrum at t_0 was obtained at this point, and the spectrometer was tuned and shimmed. The solution was emptied into a vial containing oxidant 1 (0.5 mmol), oxidant 2 (0.5 mmol), and CSA (27.9 mg, 0.12 mmol) and the mixture was shaken, then pipetted back into the NMR tube. A ^{1}H NMR spectrum at t_1 was then obtained, where t_1 is the time between mixing all the components and the midpoint of the time it takes to acquire the first spectrum. A ^{1}H NMR spectrum was then obtained every 60 seconds, with 1 scan.

7.4.2. Procedures relating to the data in Table 6

Reaction 1

As described in the general procedure

Reaction 2

A: **C9** (344 mg, 1.25 mmol) and CD_3OD (245 μL) were mixed, and the solution made up to 10 mL with $CDCl_3$.

Stock solution **A** and (tht)Au(Cl) (0.64 mg, 2 mol%) were combined in an NMR tube. The ^1H NMR spectrum at t_0 was obtained at this point, and the spectrometer was tuned and shimmed. The solution was emptied into a vial containing *p*-MeArI$(OAc)_2$ (18.5 mg, 0.55 mmol), *p*-ClArI$(OAc)_2$ (19.6 mg, 0.55 mmol), and CSA (27.9 mg, 0.12 mmol) and the mixture was shaken, then pipetted back into the NMR tube. A ^1H NMR spectrum at t_1 was then obtained, where t_1 is the time between mixing all the components and the midpoint of the time it takes to acquire the first spectrum. A ^1H NMR spectrum was then obtained every 120 seconds, with 8 scans.

Reaction 3

A: **C9** (344 mg, 1.25 mmol) and CD_3OD (245 μL) were mixed, and the solution made up to 10 mL with $CDCl_3$.
B: (tht)Au$(Br)_3$ (26.2 mg, 0.05 mmol) was dissolved and made up to 5 mL with $CDCl_3$.

Stock solution **A** (0.80 mL), stock solution **B** (0.20 mL), and 2-bromothiophene (0.69 μL, 7 mol%) were combined in an NMR tube. The ^1H NMR spectrum at t_0 was obtained at this point, and the spectrometer was tuned and shimmed. The solution was emptied into a vial containing *p*-MeArI$(OAc)_2$ (16.8 mg, 0.50 mmol), *p*-ClArI$(OAc)_2$ (17.8 mg, 0.50 mmol), and CSA (27.9 mg, 0.12 mmol) and the mixture was shaken, then pipetted back into the NMR tube. A ^1H NMR spectrum at t_1 was then obtained, where t_1 is the time between mixing all the components and the midpoint of the time it takes to acquire the first spectrum. A ^1H NMR spectrum was then obtained every 120 seconds, with 8 scans.

Reaction 4

As described in the general procedure

Reaction 5

A: **C9** (344 mg, 1.25 mmol) and CD_3OD (245 μL) were mixed, and the solution made up to 10 mL with $CDCl_3$.

Stock solution **A** and (tht)Au(Cl) (0.64 mg, 2 mol%) were combined in an NMR tube. The ^1H NMR spectrum at t_0 was obtained at this point, and the spectrometer was tuned and shimmed. The solution was emptied into a vial containing *p*-MeArI$(OAc)_2$ (16.8 mg, 0.50 mmol), *p*-CF_3ArI$(OAc)_2$ (19.5 mg, 0.50 mmol), and CSA (27.9 mg, 0.12 mmol) and the mixture was shaken, then pipetted back into the NMR tube. A ^1H NMR spectrum at t_1 was then obtained, where t_1 is the time between mixing all the components and the midpoint of the time it takes to acquire the first spectrum. A ^1H NMR spectrum was then obtained every 120 seconds, with 8 scans.

7.4.3. Procedure relating to Figure 31

A: **C9** (344 mg, 1.25 mmol) and CD_3OD (245 μL) were mixed, and the solution made up to 10 mL with $CDCl_3$.
B: (tht)Au$(Br)_3$ (26.2 mg, 0.05 mmol) was dissolved and made up to 5 mL with $CDCl_3$.
C: Bu_4NBr (6.44 mg, 0.02 mmol) was dissolved and made up to 2 mL with $CDCl_3$.

CF_3CH_2I (9.8 μL, 0.1 mmol), *p*-BrArI$(OAc)_2$ (40.1 mg, 0.1 mmol), and CSA (28.4 mg, 0.12 mmol) were dissolved in $CDCl_3$ (0.5 mL) in a small vial. Stock solution **C** (100 μL) was added and the vial was shaken vigorously, then left to stand for 15 minutes. A small amount of *m*-OMeArI was added to the solution, and the vial was shaken. The cap of the vial was left off to allow for the solvent to evaporate.

Stock solution **A** (0.8 mL) and stock solution **B** (0.2 mL) were combined in an NMR tube. The ^1H NMR spectrum at t_0 was obtained at this point, and the spectrometer was tuned and shimmed. The solution was emptied into the vial holding the oxidants and CSA described above, and the mixture was shaken, then pipetted back into the NMR tube. A ^1H NMR spectrum at t_1 was then obtained, where t_1 is the time between mixing all the components and the midpoint of the time it takes to acquire the first spectrum. A ^1H NMR spectrum was then obtained every 60 seconds, with 1 scan.

7.5. Procedures and data relevant to Chapter 4

7.5.1. Monitoring the resting state

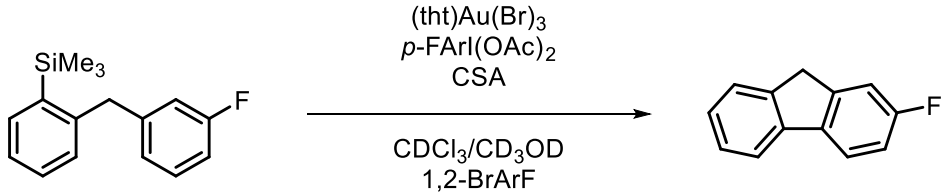

D4 **D5**

A: **D4** (129 mg, 0.5 mmol), CD_3OD (49 μL), and 1,3-$C_6H_4F_2$ (12 μL) were combined and made up to 1 mL with $CDCl_3$.

B: (tht)Au$(Br)_3$ (26.2 mg, 0.05 mmol) and 1,2-BrArF were combined and made up to 2 mL with $CDCl_3$.

0.010 M [Au]

Stock solution **A** (200 μL), stock solution **B** (100 μL), and $CDCl_3$ (200 μL) were mixed together in an NMR tube. The ^{19}F NMR spectrum at t_0 was obtained at this point, and the spectrometer was tuned and shimmed. CSA (19.2 mg, 0.083 mmol) and *p*-FArI$(OAc)_2$ (25.5 mg, 0.075 mmol) were added to the tube, and the tube was shaken vigorously. A ^{19}F NMR spectrum at t_1 was then obtained, where t_1 is the time between mixing all the components and the midpoint of the time it takes to acquire the first spectrum. Subsequent spectra were taken every 5 seconds, with 1 scan.

0.006 M [Au]

Stock solution **A** (200 μL), stock solution **B** (60 μL), and $CDCl_3$ (240 μL) were mixed together in an NMR tube. The ^{19}F NMR spectrum at t_0 was obtained at this point, and the spectrometer was tuned and shimmed. CSA (19.2 mg, 0.083 mmol) and *p*-FArI$(OAc)_2$ (25.5 mg, 0.075 mmol) were added to the tube, and the tube was shaken vigorously. A ^{19}F NMR spectrum at t_1 was then obtained, where t_1 is the time between mixing all the components and the midpoint of the time it takes to acquire the first spectrum. Subsequent spectra were taken every 5 seconds, with 1 scan.

0.014 M [Au]

Stock solution **A** (200 μL), stock solution **B** (140 μL), and $CDCl_3$ (60 μL) were mixed together in an NMR tube. The ^{19}F NMR spectrum at t_0 was obtained at this point, and the spectrometer was tuned and shimmed. CSA (19.2 mg, 0.083 mmol) and *p*-FArI$(OAc)_2$ (25.5 mg, 0.075 mmol) were added to the tube, and the tube was shaken vigorously. A ^{19}F NMR spectrum at t_1 was then obtained, where t_1 is the time between mixing all the components and the midpoint of the time it takes to acquire the first spectrum. Subsequent spectra were taken every 5 seconds, with 1 scan.

7.5.2. Reaction shown in Figure 37

A: CD_3OD (39 μL) and 1,3-$C_6H_4F_2$ (10 μL) were combined and made up to 2 mL with $CDCl_3$**.**

D7 (25.8 mg, 0.1 mmol) and (tht)Au$(Br)_3$ (2.64 mg, 0.005 mmol, 5 mol%) were dissolved in **A** (0.5 mL). The ^{19}F NMR spectrum at t_0 was obtained at this point, and the spectrometer was tuned and shimmed. CSA (18.5 mg, 0.080 mmol) and *p*-FArI$(OAc)_2$ (25.5 mg, 0.075 mmol) were added to the tube, and the tube was shaken vigorously. A ^{19}F NMR spectrum at t_1 was then obtained, where t_1 is the time between mixing all the components and the midpoint of the time it takes to acquire the first spectrum. Subsequent spectra were taken every 10 seconds, with 1 scan.

7.5.3. Reoxidation of gold

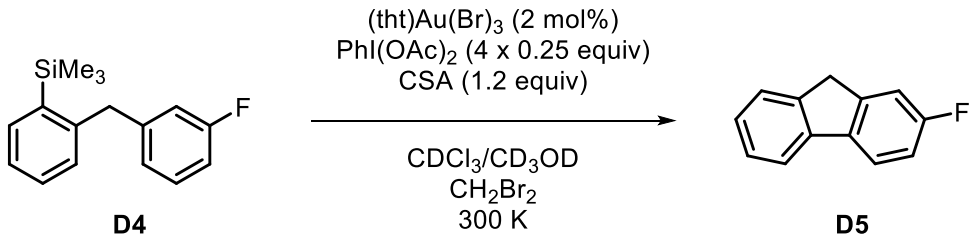

D4 **D5**

A: **D4** (323 mg, 1.25 mmol), CD_3OD (245 μL), and CH_2Br_2 (50 μL) were combined and made up to 10 mL with $CDCl_3$.

B: (tht)Au$(Br)_3$ (26.3 mg, 0.05 mmol) was made up to 5 mL with $CDCl_3$.

Stock solution **A** (0.8 mL) and stock solution **B** (0.2 mL) were combined in an NMR tube. The ^1H NMR spectrum at t_0 was obtained at this point, and the spectrometer was tuned and shimmed. CSA (27.9 mg, 0.12 mmol) and PhI$(OAc)_2$ (8.05 mg, 0.025 mmol) were added to the tube, and the tube was shaken vigorously. A ^1H NMR spectrum at t_1 was then obtained, where t_1 is the time between mixing all the components and the midpoint of the time it takes to acquire the first spectrum. Subsequent spectra were taken every 30 seconds, with 1 scan.

When the oxidant was completely consumed, the sample was ejected and more $PhI(OAc)_2$ (8.05 mg, 0.025 mmol) was added after approximately 30 seconds. The tube was returned to the spectrometer and monitored further by ^1H NMR spectroscopy. This was repeated three times, until **D4** was completely consumed.

The experiment was repeated with varying delay times before more oxidant was added.

7.5.4. Setup 1.0

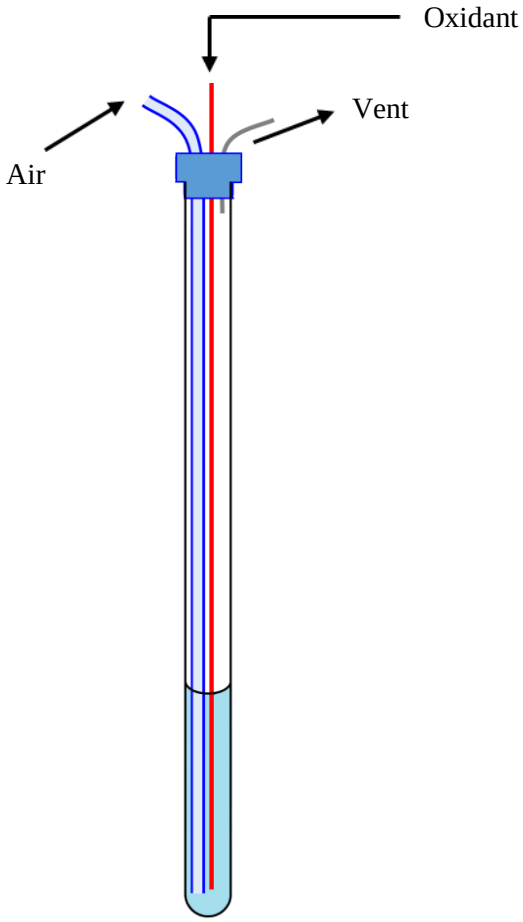

NMR tube insert

PEEK tubing (1.59 mm OD, 1.0 mm ID) was used to deliver air into the tube. The tubing was connected using HPLC fittings to a 50 mL disposable syringe. Air was bubbled into the system using a syringe pump. The same tubing was used for the vent. Tefzel® tubing (0.80 mm OD, 0.25 mm ID) was used to deliver reagents into the tube. This tubing was connected using HPLC fittings to a three-way valve, with a 50 µL syringe attached on one end, and a 2.5 mL syringe attached on the other end. (Chapter 5, Figure 43)

The NMR tube used was a standard 7-inch tube with a plastic cap. The plastic cap was pierced with three holes so that the NMR tube insert described above can be fitted in. The insert was placed so that the end of the tubing reached the bottom of the NMR tube.

Mixing test with a blue solution

Blue solution was obtained by stirring chloroform (15 mL) with the nib of a permanent pen (edding® 142 M blue) suspended in solution for 20 minutes.

Chloroform (0.5 mL) was added to an NMR tube. The bubbler was switched on, and when a constant stream of bubbles was produced, **blue solution** (20 μL) was injected, and the bubbler was immediately switched off.

Reaction monitoring

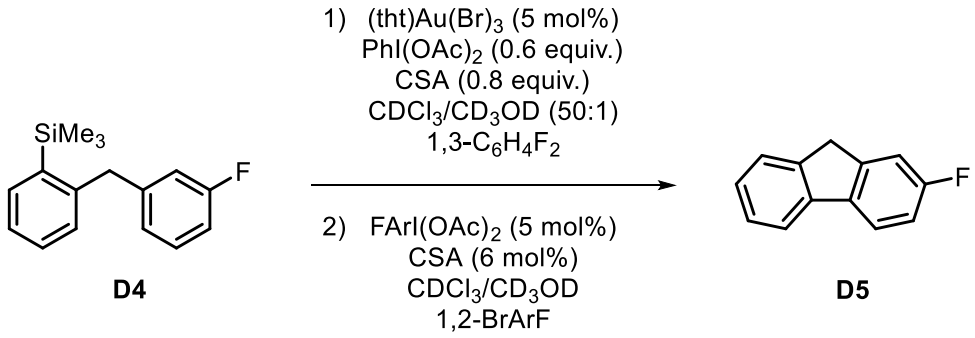

A: **D4** (103 mg, 0.40 mmol), (tht)Au(Br)$_3$ (10.6 mg, 0.020 mmol), 1,3-$C_6H_4F_2$ (9.8 μL, 0.1 mmol), and CD_3OD (39 μL) were mixed and made up to 2 mL with $CDCl_3$.

B: *p*-FArI(OAc)$_2$ (170 mg, 0.5 mmol), CSA (139 mg, 0.6 mmol), CD_3OD (39 μL), and 1,2-BrArF (55 μL, 0.5 mmol) were combined and made up to 2 mL with $CDCl_3$.

The reagent tubing in the NMR tube insert was primed with solution **B**.

Stock solution **A** (0.5 mL) was added into an NMR tube with the NMR tube insert, and the ^{19}F NMR spectrum at t_0 was obtained after tuning and shimming the spectrometer. The insert was removed and PhI(OAc)$_2$ (18.9 mg, 0.059 mmol) and CSA (18.2 mg, 0.078 mmol) were added to the tube. The tube was capped and shaken vigorously to dissolve all the reagents. The insert was placed back into the tube, and a ^{19}F NMR spectra were acquired using a pseudo-2D pulse program, with a single scan per spectrum and a 20 second delay between spectra. When the oxidant was completely consumed, the acquisition of spectra was stopped, and restarted with identical parameters with the exception of a delay time of 2.5 seconds between spectra.

The bubbler was switched on, and the lock display was observed for a constant lock signal, indicating a constant stream of bubbles was being produced. Solution **B** (20 μL) in the NMR tube insert was injected and the bubbler was immediately switched off. The resulting reaction was monitored by ^{19}F NMR spectroscopy as set up previously.

7.5.5. Setup 1.1

Acid/base mixing test

A: *p*-fluoroaniline (95 μL, 1.0 mmol) was made up to 5 mL with $CDCl_3$.

B: AcOH (286 μL, 5 mmol) was made up to 5 mL with $CDCl_3$.

The reagent tubing in the NMR tube insert was primed with solution **B**.

Stock solution **A** (0.5 mL) was added into an NMR tube with the NMR tube insert. A ^1H NMR spectrum at t_0 was obtained after tuning and shimming the spectrometer. The bubbler was switched on, and the lock display was observed for a constant lock signal, indicating a constant stream of bubbles was being produced. Solution **B** (20 μL) in the NMR tube insert was injected and the bubbler was immediately switched off. The trigger from the injection initiated the pseudo-2D pulse program and started acquisition of ^1H NMR spectra with 1 scan and a delay time of 3 seconds between spectra.

Reaction monitoring

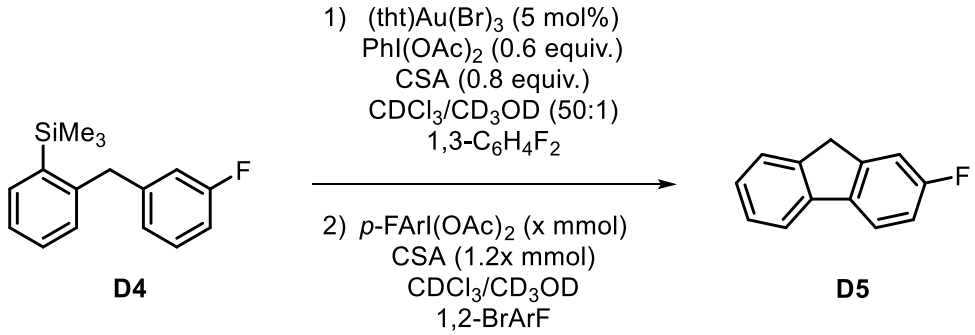

A: **D4** (103 mg, 0.40 mmol), (tht)$Au(Br)_3$ (10.6 mg, 0.020 mmol), 1,3-$C_6H_4F_2$ (9.8 μL, 0.1 mmol), and CD_3OD (39 μL) were mixed and made up to 2 mL with $CDCl_3$.

B: *p*-$FArI(OAc)_2$ (425 mg, 1.25 mmol), CSA (319 mg, 1.38 mmol), CD_3OD (98 μL), and 1,2-BrArF (137 μL, 1.25 mmol) were combined and made up to 5 mL with $CDCl_3$.

The reagent tubing in the NMR tube insert was primed with solution **B**.

Stock solution **A** (0.5 mL) was added into an NMR tube with the NMR tube insert, and the ^{19}F NMR spectrum at t_0 was obtained after tuning and shimming the spectrometer. The insert was removed and $PhI(OAc)_2$ (18.9 mg, 0.059 mmol) and CSA (18.2 mg, 0.078 mmol) were added to the tube. The tube was capped and shaken vigorously to dissolve all the reagents. The insert was placed back into the tube, and a ^{19}F NMR spectra were acquired using a pseudo-2D pulse program, with a single scan per spectrum and a 20 second delay between spectra. When the oxidant was completely consumed, the acquisition of spectra was stopped, and restarted with identical parameters with the exception of a delay time of 2.5 seconds between spectra.

The bubbler was switched on, and the lock display was observed for a constant lock signal, indicating a constant stream of bubbles was being produced. Solution **B** (10 μL, 20 μL, or 30 μL) in the NMR tube insert was injected and the bubbler was immediately switched off. The resulting reaction was monitored by ^{19}F NMR spectroscopy as set up previously.

7.5.6. Setup 2.0

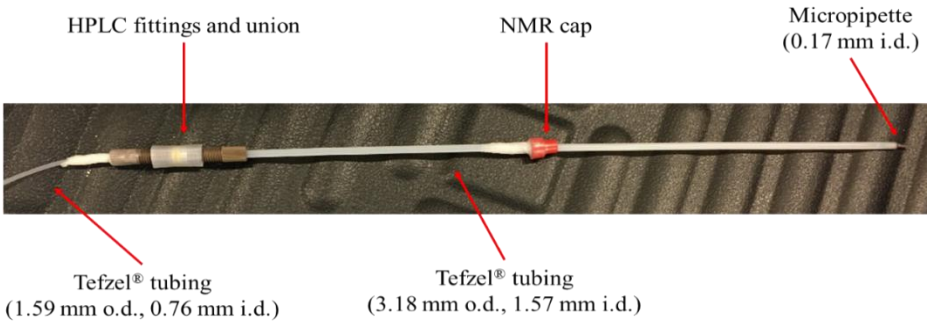

NMR tube insert

A glass micropipette was glued into the Tefzel® tubing using LOCTITE® EA 9497. To the other end of the Tefzel® tubing, another piece of Tefzel® tubing with a larger internal diameter was attached using HPLC fittings. The end of the Tefzel® tubing was connected to the syringe setup described in Figure 48.

An NMR cap was pierced, and the tubing was inserted through it. The position of the cap allowed adjustments of the height of the tubing inside a Shigemi tube.

Mixing test with a blue solution

Blue solution was obtained by stirring chloroform (15 mL) with the nib of a permanent pen (edding® 142 M blue) suspended in solution for 20 minutes.

General procedure:

Chloroform was added to a Shigemi tube. The NMR tube insert was primed with the **blue solution** and placed inside the tube. The **blue solution** was injected with a driven pressure from a compressed air drive against the syringe setup shown in Figure 48. The different conditions tested are summarised in Table 9.

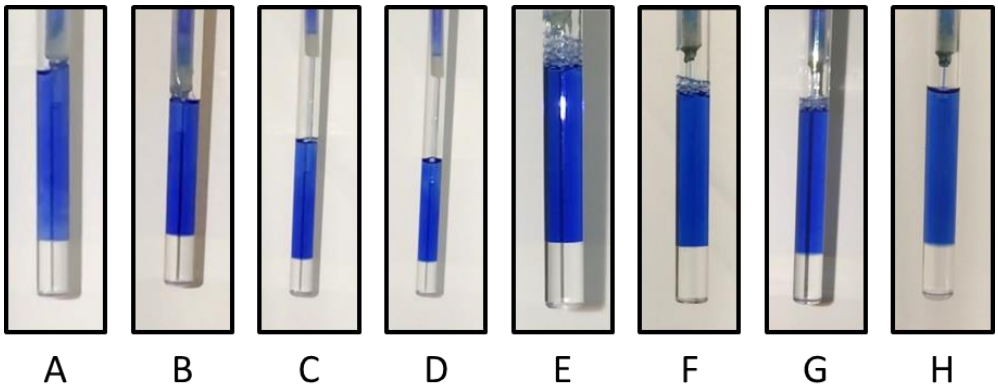

Table 9: Testing mixing efficiency under different conditions.

Run	$CHCl_3$ / µL	Micropipette tip / mm	Blue solution / µL	Pressure / bar
A	300	0.7	60	5
B	250	0.7	60	5
C	300	2.5	60	8
D	300	2.5	50	8
E	250	0.7	60	9
F	250	0.7	60	9
G	250	0.7	60	5
H	250	0.7	60	5

Acid/base mixing test

Using condition G (and H) from Table 9.

A: *p*-fluoroaniline (60 μL, 0.633 mmol) was made up to 4 mL with $CDCl_3$.

B: AcOH (286 μL, 5 mmol) was made up to 10 mL with $CDCl_3$.

The reagent tubing in the NMR tube insert was primed with solution **B**. Tuning and shimming of the NMR spectrometer was carried out on a dummy sample with the NMR tube insert placed inside the Shigemi tube.

Stock solution **A** (0.25 mL) was added into a Shigemi tube with the NMR tube insert. ^1H NMR specta were obtained using a pseudo-2D pulse program with a single scan and a delay time of 2 seconds between each spectrum. Solution **B** (60 μL) in the NMR tube insert was injected, and the resulting reaction was monitored.

Reaction monitoring

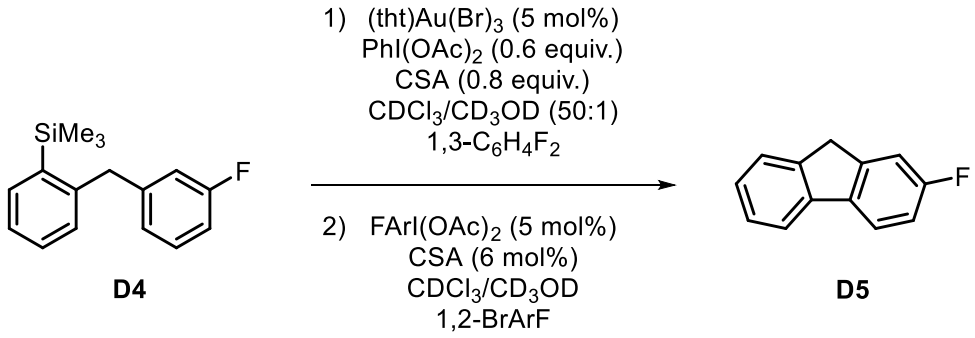

Using conditions G (and H) from Table 9

A: **D4** (206 mg, 0.80 mmol), (tht)Au(Br)$_3$ (21.15 mg, 0.040 mmol), 1,3-$C_6H_4F_2$ (19.6 μL, 0.2 mmol), and CD_3OD (78 μL) were mixed and made up to 4 mL with $CDCl_3$.

B: *p*-FArI(OAc)$_2$ (142 mg, 0.418 mmol), CSA (106 mg, 0.457 mmol), CD_3OD (196 μL), and 1,2-BrArF (45 μL, 0.418 mmol) were combined and made up to 10 mL with $CDCl_3$.

The reagent tubing in the NMR tube insert was primed with solution **B**. Tuning and shimming of the NMR spectrometer was carried out on a dummy sample with the NMR tube insert placed inside the Shigemi tube.

Stock solution **A** (0.25 mL) was added into an NMR tube with the NMR tube insert, and the ^{19}F NMR spectrum at t_0 was obtained. The insert was removed and $PhI(OAc)_2$ (24.2 mg, 0.0751 mmol) and CSA (18.6 mg, 0.0801 mmol) were added to the tube. The tube was capped and shaken vigorously to dissolve all the reagents. The insert was placed back into the tube, and a ^{19}F NMR spectra were acquired using a pseudo-2D pulse program, with a single scan per spectrum and a 15 second delay between spectra. When the oxidant was completely consumed, the acquisition of spectra was stopped, and restarted with identical parameters with the exception of a delay time of 2 seconds between spectra. Solution **B** (60 μL) in the NMR tube insert was injected. The resulting reaction was monitored by ^{19}F NMR spectroscopy as set up previously.

7.6. Procedures and data relevant to Chapter 5

7.6.1. General considerations

^1H NMR spectroscopy and $^{31}P\{^1H\}$ NMR spectroscopy were carried out with a 90° pulse angle. Integrations from $^{31}P\{^1H\}$ NMR spectroscopy were obtained relative to pre-calibrated H_3PO_4 standards in glass capillaries.

7.6.2. Oxidation of $(Ph_3P)Au(X)$

Oxidation of $(Ph_3P)Au(Cl)$

A: $(Ph_3P)Au(Cl)$ (24.7 mg, 0.050 mmol) was made up to 1 mL with $CDCl_3$.

$PhI(OAc)_2$ (32.2 mg, 0.100 mmol) and CSA (28.4 mg, 0.120 mmol) were dissolved in an NMR tube with $CDCl_3$ (0.600 mL) and CD_3OD (0.015 mL). The ^1H NMR spectrum at t_0 was obtained at this point. 0.100 mL of stock solution **A** was added to the tube, and the tube was shaken vigorously. A ^1H NMR spectrum at t_1 was then obtained, where t_1 is the time between mixing all the components and the midpoint of the time it takes to acquire the first spectrum. A ^1H NMR spectrum was then obtained every 3.5 minutes, with 8 scans where d1 = 20 s. The NMR spectrometer was tuned and shimmed on a dummy sample prior to starting the experiment.

Oxidation of $(Ph_3P)Au(OTs)$

$(Ph_3P)Au(OTs)$ (3.15 mg, 0.005 mmol) was dissolved in an NMR tube with $CDCl_3$ (0.700 mL) and CD_3OD (0.015 mL). The NMR spectrometer was tuned and shimmed, and the ^1H NMR spectrum at t_0 was obtained at this point. $PhI(OAc)_2$ (32.2 mg, 0.100 mmol) and CSA (28.4 mg, 0.120 mmol) were added to the tube, and the tube was shaken vigorously. A ^1H NMR spectrum at t_1 was then obtained, where t_1 is the time between mixing all the components and

the midpoint of the time it takes to acquire the first spectrum. A ^{1}H NMR spectrum was then obtained every 90 s, with 2 scans where d1 = 20 s.

7.6.2. Oxidation of $(Ph_3P)Au(Cl)$ with $ArI(OAc)_2$

$(Ph_3P)Au(Cl)$ (1.02 mg, 0.002 mmol) was dissolved in $CDCl_3$ (0.600 mL) and CD_3OD (0.015 mL) in an NMR tube. The NMR spectrometer was tuned and shimmed, and the ^{1}H NMR spectrum at t_0 was obtained at this point. Oxidant (0.100 mmol) and CSA (28.4 mg, 0.120 mmol) was added to the tube and the tube was shaken vigorously. A ^{1}H NMR spectrum at t_1 was then obtained, where t_1 is the time between mixing all the components and the midpoint of the time it takes to acquire the first spectrum. A ^{1}H NMR spectrum was then obtained every 3 minutes, with 6 scans where d1 = 20 s.

The same experiment was repeated, but monitored by $^{31}P\{^{1}H\}$ NMR spectroscopy, where spectra were obtained every 5 minutes, with 6 scans and d1 = 45 s.

7.6.3. Stoichiometric amounts of oxidant

A: $(Ph_3P)Au(Cl)$ (24.7 mg, 0.050 mmol) was made up to 1 mL with $CDCl_3$.

$PhI(OAc)_2$ (3.22 mg, 0.010 mmol) and CSA (2.84 mg, 0.012 mmol) were dissolved in an NMR tube with $CDCl_3$ (0.600 mL) and CD_3OD (0.015 mL). The ^{1}H NMR spectrum at t_0 was obtained at this point. 0.100 mL of stock solution **A** was added to the tube, and the tube was shaken vigorously. A ^{1}H NMR spectrum at t_1 was then obtained, where t_1 is the time between mixing all the components and the midpoint of the time it takes to acquire the first spectrum. A ^{1}H NMR spectrum was then obtained every 60 seconds, with 2 scans where d1 = 20 s. The NMR spectrometer was tuned and shimmed on a dummy sample prior to starting the experiment.

The same experiment was repeated, but monitored by $^{31}P\{^{1}H\}$ NMR spectroscopy, where spectra were obtained every 2.5 minutes, with 3 scans and d1 = 45 s.

7.6.4. Effect of product addition

A: $(Ph_3P)Au(Cl)$ (24.7 mg, 0.050 mmol) was made up to 1 mL with $CDCl_3$.

Addition of triphenylphosphine oxide

$PhI(OAc)_2$ (3.22 mg, 0.010 mmol), CSA (2.84 mg, 0.012 mmol) and Ph_3PO (1.38 mg, 0.005 mmol) were dissolved in an NMR tube with $CDCl_3$ (0.600 mL) and CD_3OD (0.015 mL). The ^1H NMR spectrum at t_0 was obtained at this point. 0.100 mL of stock solution **A** was added to the tube, and the tube was shaken vigorously. A ^1H NMR spectrum at t_1 was then obtained, where t_1 is the time between mixing all the components and the midpoint of the time it takes to acquire the first spectrum. A ^1H NMR spectrum was then obtained every 60 seconds, with 2 scans where d1 = 20 s. The NMR spectrometer was tuned and shimmed on a dummy sample prior to starting the experiment.

Addition of para-fluoroaryliodine

$PhI(OAc)_2$ (3.22 mg, 0.010 mmol), CSA (2.84 mg, 0.012 mmol) and *p*-FArI (1.15 μL, 0.010 mmol) were mixed in an NMR tube with $CDCl_3$ (0.600 mL) and CD_3OD (0.015 mL). The ^1H NMR spectrum at t_0 was obtained at this point. 0.100 mL of stock solution **A** was added to the tube, and the tube was shaken vigorously. A ^1H NMR spectrum at t_1 was then obtained, where t_1 is the time between mixing all the components and the midpoint of the time it takes to acquire the first spectrum. A ^1H NMR spectrum was then obtained every 60 seconds, with 2 scans where d1 = 20 s. The NMR spectrometer was tuned and shimmed on a dummy sample prior to starting the experiment.

7.6.4. Addition of more starting complex (Figure 71)

A: $(Ph_3P)Au(Cl)$ (24.7 mg, 0.050 mmol) was made up to 1 mL with $CDCl_3$.

Run 1

$PhI(OAc)_2$ (16.1 mg, 0.050 mmol) and CSA (14.2 mg, 0.060 mmol) dissolved in an NMR tube with $CDCl_3$ (0.600 mL) and CD_3OD (0.015 mL). The ^1H NMR spectrum at t_0 was obtained at this point. 0.100 mL of stock solution **A** was added to the tube, and the tube was shaken vigorously. A ^1H NMR spectrum at t_1 was then obtained, where t_1 is the time between mixing all the components and the midpoint of the time it takes to acquire the first spectrum. A ^1H NMR spectrum was then obtained every 2 minutes, with 4 scans where d1 = 20 s. The NMR spectrometer was tuned and shimmed on a dummy sample prior to starting the experiment.

When no more product formed, the tube was ejected from the spectrometer and 0.100 mL of stock solution **A** was added, the tube was shaken vigorously and placed back inside the spectrometer. The reaction was then monitored as previously described.

Run 2

$PhI(OAc)_2$ (16.1 mg, 0.050 mmol) and CSA (14.2 mg, 0.060 mmol) dissolved in an NMR tube with $CDCl_3$ (0.600 mL) and CD_3OD (0.015 mL). The ^1H NMR spectrum at t_0 was obtained at this point. 0.100 mL of stock solution **A** was added to the tube, and the tube was shaken vigorously. A ^1H NMR spectrum at t_1 was then obtained, where t_1 is the time between mixing all the components and the midpoint of the time it takes to acquire the first spectrum. A ^1H NMR spectrum was then obtained every 3.5 minutes, with 8 scans where d1 = 20 s. The NMR spectrometer was tuned and shimmed on a dummy sample prior to starting the experiment.

Run 3

$PhI(OAc)_2$ (12.8 mg, 0.040 mmol) and CSA (14.2 mg, 0.060 mmol) dissolved in an NMR tube with $CDCl_3$ (0.700 mL) and CD_3OD (0.015 mL). The ^1H NMR spectrum at t_0 was obtained at this point. 0.100 mL of stock solution **A** was added to the tube, and the tube was shaken vigorously. A ^1H NMR spectrum at t_1 was then obtained, where t_1 is the time between mixing all the components and the midpoint of the time it takes to acquire the first spectrum. A ^1H NMR spectrum was then obtained every 3.5 minutes, with 8 scans where d1 = 20 s. The NMR spectrometer was tuned and shimmed on a dummy sample prior to starting the experiment.

7.6.5. Changing [CSA]

A: $(Ph_3P)Au(Cl)$ (24.7 mg, 0.050 mmol) was made up to 1 mL with $CDCl_3$.

$PhI(OAc)_2$ (3.22 mg, 0.010 mmol) and CSA (0.012 mmol, 0.030 mmol, 0.060 mmol or 0.090 mmol) were dissolved in an NMR tube with $CDCl_3$ (0.600 mL) and CD_3OD (0.015 mL). The ^1H NMR spectrum at t_0 was obtained at this point. 0.100 mL of stock solution **A** was added to the tube, and the tube was shaken vigorously. A ^1H NMR spectrum at t_1 was then obtained, where t_1 is the time between mixing all the components and the midpoint of the time it takes to acquire the first spectrum. A ^1H NMR spectrum was then obtained every 60 seconds, with 2 scans where d1 = 20 s. The NMR spectrometer was tuned and shimmed on a dummy sample prior to starting the experiment.

7.6.6. Using HCIB as oxidant

A: $(Ph_3P)Au(Cl)$ (24.7 mg, 0.050 mmol) was made up to 1 mL with $CDCl_3$.

HCIB (4.52 mg, 0.010 mmol) was dissolved in an NMR tube with $CDCl_3$ (0.600 mL) and CD_3OD (0.015 mL). The ^1H NMR spectrum at t_0 was obtained at this point. 0.100 mL of stock solution **A** was added to the tube, and the tube was shaken vigorously. A ^1H NMR spectrum at t_1 was then obtained, where t_1 is the time between mixing all the components and the midpoint of the time it takes to acquire the first spectrum. A ^1H NMR spectrum was then obtained every 60 seconds, with 2 scans where d1 = 20 s. The NMR spectrometer was tuned and shimmed on a dummy sample prior to starting the experiment.

7.6.7. Premixing CSA and $(Ph_3P)Au(Cl)$ (Figure 75)

A: $(Ph_3P)Au(Cl)$ (24.7 mg, 0.050 mmol) was made up to 1 mL with $CDCl_3$.

Run 1:

CSA (14.2 mg, 0.060 mmol) was dissolved in an NMR tube with $CDCl_3$ (0.600 mL) and CD_3OD (0.015 mL). 0.100 mL of stock solution **A** was added to the tube, and the mixture was left for 20 minutes. The ^1H NMR spectrum at t_0 was obtained after this. $PhI(OAc)_2$ (16.1 mg, 0.050 mmol) was added, and the tube was shaken vigorously. A ^1H NMR spectrum at t_1 was then obtained, where t_1 is the time between mixing all the components and the midpoint of the time it takes to acquire the first spectrum.

Run 1':

$PhI(OAc)_2$ (16.1 mg, 0.050 mmol) and CSA (14.2 mg, 0.060 mmol) were dissolved in an NMR tube with $CDCl_3$ (0.600 mL) and CD_3OD (0.015 mL). The ^1H NMR spectrum at t_0 was obtained at this point. 0.100 mL of stock solution **A** was added to the tube, and the tube was shaken vigorously. A ^1H NMR spectrum at t_1 was then obtained, where t_1 is the time between mixing all the components and the midpoint of the time it takes to acquire the first spectrum. A ^1H NMR spectrum was then obtained every 60 seconds, with 2 scans where d1 = 20 s. The NMR spectrometer was tuned and shimmed on a dummy sample prior to starting the experiment.

Run 2:

CSA (2.83 mg, 0.012 mmol) was dissolved in an NMR tube with $CDCl_3$ (0.600 mL) and CD_3OD (0.015 mL). 0.100 mL of stock solution **A** was added to the tube, and the mixture was left for 20 minutes. The ^1H NMR spectrum at t_0 was obtained after this. $PhI(OAc)_2$ (3.22 mg, 0.010 mmol) was added, and the tube was shaken vigorously. A ^1H NMR spectrum at t_1 was then obtained, where t_1 is the time between mixing all the components and the midpoint of the time it takes to acquire the first spectrum.

Run 2':

$PhI(OAc)_2$ (3.22 mg, 0.010 mmol) and CSA (2.84 mg, 0.012 mmol) were dissolved in an NMR tube with $CDCl_3$ (0.600 mL) and CD_3OD (0.015 mL). The ^1H NMR spectrum at t_0 was obtained at this point. 0.100 mL of stock solution **A** was added to the tube, and the tube was shaken vigorously. A ^1H NMR spectrum at t_1 was then obtained, where t_1 is the time between mixing all the components and the midpoint of the time it takes to acquire the first spectrum. A ^1H NMR spectrum was then obtained every 60 seconds, with 2 scans where d1 = 20 s. The NMR spectrometer was tuned and shimmed on a dummy sample prior to starting the experiment.

7.6.8. Addition of HCl

A: $(Ph_3P)Au(Cl)$ (24.7 mg, 0.050 mmol) was made up to 1 mL with $CDCl_3$.

$PhI(OAc)_2$ (3.22 mg, 0.010 mmol) and CSA (0.012 mmol, 0.030 mmol, 0.060 mmol or 0.090 mmol) were dissolved in an NMR tube with $CDCl_3$ (0.600 mL) and HCl in methanol (0.015 mL, 1.25 M) was added to the mixture. The ^1H NMR spectrum at t_0 was obtained at this point. 0.100 mL of stock solution **A** was added to the tube, and the tube was shaken vigorously. A ^1H NMR spectrum at t_1 was then obtained, where t_1 is the time between mixing all the components and the midpoint of the time it takes to acquire the first spectrum. A ^1H NMR spectrum was then obtained every 60 seconds, with 2 scans where d1 = 20 s. The NMR spectrometer was tuned and shimmed on a dummy sample prior to starting the experiment.

The same experiment as above was carried out, but monitored by $^{31}P\{^1H\}$ NMR spectroscopy, where spectra were obtained every 2.5 minutes, with 3 scans and d1 = 45 s.

7.6.9. Addition of Bu_4NCl

A: $(Ph_3P)Au(Cl)$ (24.7 mg, 0.050 mmol) was made up to 1 mL with $CDCl_3$.

Bu_4NCl (1.39 mg, 0.005 mmol), $PhI(OAc)_2$ (3.22 mg, 0.010 mmol), and CSA (2.84 mg, 0.012 mmol) were dissolved in an NMR tube with $CDCl_3$ (0.600 mL) and CD_3OD (0.015 mL). The $^{31}P\{^1H\}$ NMR spectrum at t_0 was obtained at this point. 0.100 mL of stock solution **A** was added to the tube, and the tube was shaken vigorously. A $^{31}P\{^1H\}$ NMR spectrum at t_1 was then obtained, where t_1 is the time between mixing all the components and the midpoint of the time it takes to acquire the first spectrum. A $^{31}P\{^1H\}$ NMR spectrum was then obtained every 2.5 min, with 3 scans where d1 = 45 s. The NMR spectrometer was tuned and shimmed on a dummy sample prior to starting the experiment.

7.6.10. Reaction of $(Ph_3P)Au(Cl)_3$ with $PhI(X)_2$

$PhI(OAc)_2$ (3.22 mg, 0.010 mmol), and CSA (2.84 mg, 0.012 mmol) were dissolved in an NMR tube with $CDCl_3$ (0.700 mL) and CD_3OD (0.015 mL). The ^1H NMR spectrum at t_0 was obtained at this point. $(Ph_3P)Au(Cl)_3$ (2.78 mg, 0.005 mmol) was added to the tube, and the tube was shaken vigorously. A ^1H NMR spectrum at t_1 was then obtained, where t_1 is the time between mixing all the components and the midpoint of the time it takes to acquire the first spectrum. A ^1H NMR spectrum was then obtained 30 seconds, with 1 scan. The NMR spectrometer was tuned and shimmed on a dummy sample prior to starting the experiment.

The same experiment was repeated, but monitored by $^{31}P\{^1H\}$ NMR spectroscopy, where spectra were obtained every 2.5 minutes, with 3 scans and d1 = 45 s.

7.6.11. Effect of $(Ph_3P)Au(Cl)_3$ addition

A: $(Ph_3P)Au(Cl)$ (24.7 mg, 0.050 mmol) was made up to 1 mL with $CDCl_3$.

Bu_4NCl (1.35 mg, 0.005 mmol), $PhI(OAc)_2$ (3.22 mg, 0.010 mmol), and CSA (2.84 mg, 0.012 mmol) were dissolved in an NMR tube with $CDCl_3$ (0.600 mL) and CD_3OD (0.015 mL). The $^{31}P\{^1H\}$ NMR spectrum at t_0 was obtained at this point. 0.100 mL of stock solution **A** was added to the tube, and the tube was shaken vigorously. A $^{31}P\{^1H\}$ NMR spectrum at t_1 was then obtained, where t_1 is the time between mixing all the components and the midpoint of the time it takes to acquire the first spectrum. A $^{31}P\{^1H\}$ NMR spectrum was then obtained every 2.5 min, with 3 scans where d1 = 45 s. The NMR spectrometer was tuned and shimmed on a dummy sample prior to starting the experiment.

After the 15th spectrum was obtained, $(Ph_3P)Au(Cl)_3$ (2.88 mg, 0.010 mmol) was added to the NMR tube, and the tube was shaken vigorously. The reaction was monitored as previously described.

Chapter 8

References

1 E. H. Macdonald, in *Handbook of Gold Exploration and Evaluation*, ed. E. H. Macdonald, Woodhead Publishing, Cambridge, UK, 2007, pp. 1–61.

2 Gold Supply, https://www.gold.org/about-gold/gold-supply/gold-mining/how-much-gold, (accessed 15 June 2019).

3 Gold Mine Production, https://www.gold.org/goldhub/data/historical-mine-production, (accessed 15 June 2019).

4 Gold Demand Sectors, https://www.gold.org/about-gold/gold-demand/sectors-of-demand, (accessed 15 June 2019).

5 P. J. Loferski, Z. T. Ghalayini and S. A. Singerling, 2016 Minerals Yearbook - Platinum-Group Metals, https://www.usgs.gov/centers/nmic/platinum-group-metals-statistics-and-information, (accessed 18 June 2019).

6 G. C. Bond and D. T. Thompson, *Catal. Rev. Sci. Eng.*, 1999, **41**, 319–388.

7 L. Pauling, *J. Am. Chem. Soc.*, 1932, **54**, 3570–3582.

8 D.-A. Roşca, J. A. Wright and M. Bochmann, *Dalt. Trans.*, 2015, **44**, 20785–20807.

9 J. W. Taylor, A. McSkimming, M.-E. Moret and W. H. Harman, *Angew. Chem. Int. Ed.*, 2017, **56**, 10413–10417.

10 M. Rudolph and A. S. K. Hashmi, *Chem. Commun.*, 2011, **47**, 6536–6544.

11 E. Jiménez-Núñez and A. M. Echavarren, *Chem. Commun.*, 2007, 333–346.

12 Z. Li, C. Brouwer and C. He, *Chem. Rev.*, 2008, **108**, 3239–3265.

13 A. Arcadi, *Chem. Rev.*, 2008, **108**, 3266–3325.

14 D. J. Gorin, B. D. Sherry and F. D. Toste, *Chem. Rev.*, 2008, **108**, 3351–3378.

15 C. Nevado, *Chimia*, 2010, **64**, 247–251.

16 A. Corma, A. Leyva-Pérez and M. J. Sabater, *Chem. Rev.*, 2011, **111**, 1657–1712.

17 R. Skouta and C.-J. Li, *Tetrahedron*, 2008, **64**, 4917–4938.

18 A. S. K. Hashmi, *Chem. Rev.*, 2007, **107**, 3180–3211.

19 S. Sengupta and X. Shi, *ChemCatChem*, 2010, **2**, 609–619.

20 A. S. K. Hashmi and M. Rudolph, *Chem. Soc. Rev.*, 2008, **37**, 1766–1775.

21 A. S. K. Hashmi and M. Rudolph, *Chem.Soc.Rev.*, 2012, **41**, 2448–2462.

22 M. N. Hopkinson, A. D. Gee and V. Gouverneur, *Chem. Eur. J*, 2011, **17**, 8248–8262.

23 Y. Ito, M. Sawamura and T. Hayashi, *J. Am. Chem. Soc.*, 1986, **108**, 6405–6407.

24 A. S. K. Hashmi, L. Schwarz, J.-H. Choi and T. M. Frost, *Angew. Chem. Int. Ed.*, 2000, **39**, 2285–2288.

25 A. S. K. Hashmi, T. M. Frost and J. W. Bats, *J. Am. Chem. Soc.*, 2000, **122**, 11553–11554.

26 M. S. Kharasch and H. S. Isbell, *J. Am. Chem. Soc.*, 1931, **53**, 3053–3059.

27 P. Lu, T. C. Boorman, A. M. Z. Slawin and I. Larrosa, *J. Am. Chem. Soc.*, 2010, **132**, 5580–5581.

28 C. Jones, D. Taube, V. R. Ziatdinov, R. A. Periana, R. J. Nielsen, J. Oxgaard and W. A. Goddard III, *Angew. Chem. Int. Ed.*, 2004, **43**, 4626–4629.

29 A. S. K. Hashmi, M. C. Blanco, D. Fischer and J. W. Bats, *Eur. J. Org. Chem*, 2006, 1387–1389.

30 A. Kar, N. Mangu, H. M. Kaiser, M. Beller and M. K. Tse, *Chem. Commun.*, 2008, 386–388.

31 A. Kar, N. Mangu, H. M. Kaiser and M. K. Tse, *J. Organomet. Chem.*, 2009, **694**, 524–537.

32 X. C. Cambeiro, T. C. Boorman, P. Lu and I. Larrosa, *Angew. Chem. Int. Ed.*, 2013, **52**, 1781–1784.

33 X. C. Cambeiro, N. Ahlsten and I. Larrosa, *J. Am. Chem. Soc.*, 2015, **137**, 15636–15639.

34 C. González-Arellano, A. Corma, M. Iglesias and F. Sánchez, *J. Catal.*, 2006, **238**, 497–501.

35 G. Zhang, Y. Peng, L. Cui and L. Zhang, *Angew. Chem. Int. Ed.*, 2009, **48**, 3112–3115.

36 W. E. Brenzovich, Jr., D. Benitez, A. D. Lackner, H. P. Shunatona, E. Tkatchouk, W. A. Goddard, III and F. D. Toste, *Angew. Chem. Int. Ed.*, 2010, **49**, 5519–5522.

37 G. Zhang, L. Cui, Y. Wang and L. Zhang, *J. Am. Chem. Soc.*, 2010, **132**, 1474–1475.

38 A. D. Melhado, W. E. Brenzovich, Jr., A. D. Lackner and F. D. Toste, *J. Am. Chem. Soc.*, 2010, **132**, 8885–8887.

39 Q. Wu, C. Du, Y. Huang, X. Liu, Z. Long, F. Song and J. You, *Chem. Sci.*, 2015, **6**, 288–293.

40 L. T. Ball, M. Green, G. C. Lloyd-Jones and C. A. Russell, *Org. Lett.*, 2010, **12**, 4724–4727.

41 W. Brenzovich, Jr., J.-F. Brazeau and F. Toste, *Org. Lett.*, 2010, **12**, 4728–4731.

42 L. T. Ball, G. C. Lloyd-Jones and C. A. Russell, *Science*, 2012, **337**, 1644–1648.

43 L. T. Ball, G. C. Lloyd-Jones and C. A. Russell, *J. Am. Chem. Soc.*, 2014, **136**, 254–264.

44 A. J. Cresswell and G. C. Lloyd-Jones, *Chem. Eur. J*, 2016, **22**, 12641–12645.

45 M. Hofer, A. Genoux, R. Kumar and C. Nevado, *Angew. Chem. Int. Ed.*, 2017, **56**, 1021–1025.

46 P. A. Cox, M. Reid, A. G. Leach, A. D. Campbell, E. J. King and G. C. Lloyd-Jones, *J. Am. Chem. Soc.*, 2017, **139**, 13156–13165.

47 P. A. Cox, A. G. Leach, A. D. Campbell and G. C. Lloyd-Jones, *J. Am. Chem. Soc.*, 2016, **138**, 9145–9157.

48 J. Lozada, Z. Liu and D. M. Perrin, *J. Org. Chem.*, 2014, **79**, 5365–5368.

49 T. Kinzel, Y. Zhang and S. L. Buchwald, *J. Am. Chem. Soc.*, 2010, **132**, 14073–14075.

50 T. J. A. Corrie, L. T. Ball, C. A. Russell and G. C. Lloyd-Jones, *J. Am. Chem. Soc.*, 2017, **139**, 245–254.

51 R. J. Phipps, N. P. Grimster and M. J. Gaunt, *J. Am. Chem. Soc.*, 2008, **130**, 8172–8174.

52 X. Wang, Y. Lu, H. X. Dai and J. Q. Yu, *J. Am. Chem. Soc.*, 2010, **132**, 12203–12205.

53 K. B. McMurtrey, J. M. Racowski and M. S. Sanford, *Org. Lett.*, 2012, **14**, 4094–4097.

54 G. Shan, X. Yang, Y. Zong and Y. Rao, *Angew. Chem. Int. Ed.*, 2013, **52**, 13606–13610.

55 V. V. Zhdankin and P. J. Stang, *Chem. Rev.*, 2008, **108**, 5299–5358.

56 M. Ochiai, T. Sueda, K. Miyamoto, P. Kiprof and V. V. Zhdankin, *Angew. Chem. Int. Ed.*, 2006, **45**, 8203–8206.

57 R. M. Moriarty and O. Prakash, *Acc. Chem. Res.*, 1986, **19**, 244–250.

58 S. Kajigaeshi, T. Kakinami and M. Masayuky, *Tetrahedron Lett.*, 1988, **29**, 5783–5786.

59 A. J. Edwards, *J. Chem. Soc., Dalt. Trans.*, 1978, **42**, 1723–1725.

60 E. M. Archer and T. G. D. van Schalkwyk, *Acta Crystallogr.*, 1953, **6**, 88–92.

61 N. W. Alcock, R. M. Countryman, S. Esperas and J. F. Sawyer, *J. Chem. Soc., Dalt. Trans.*, 1979, 854–860.

62 G. Kokkinidis, M. Papadopoulou and A. Varvoglis, *Electrochim. Acta*, 1989, **34**, 133–139.

63 A. J. Bard and L. R. Faulkner, *Electrochemical Methods: Fundamentals and Applications*, John Wiley & Sons, New York, 2nd ed., 2001.

64 C. Amatore, G. Le Duc and A. Jutand, *Chem. Eur. J.*, 2013, **19**, 10082–10093.

65 C. Amatore, A. Jutand and G. Le Duc, *Chem. Eur. J.*, 2011, **17**, 2492–2503.

66 E. Blattes, M. B. Fleury and M. Largeron, *J. Org. Chem.*, 2004, **69**, 882–890.

67 S. Tang, D. Wang, Y. Liu, L. Zeng and A. Lei, *Nat. Commun.*, 2018, **9**, 1–7.

68 A. Shrestha, M. Lee, A. L. Dunn and M. S. Sanford, *Org. Lett.*, 2018, **20**, 204–207.

69 L. Ramaley and M. S. Krause, *Anal. Chem.*, 1969, **41**, 1361–1365.

70 J. J. O'Dea, J. Osteryoung and R. A. Osteryoung, *Anal. Chem.*, 1981, **53**, 695–701.

71 G. Kokkinidis, E. Hatzigrigoriou, D. Sazou and A. Varvoglis, *Electrochim. Acta*, 1991, **36**, 1391–1395.

72 S. Bhunia, K. C. Wang and R. S. Liu, *Angew. Chem. Int. Ed.*, 2008, **47**, 5063–5066.

73 D. C. Braddock, G. Cansell, S. A. Hermitage and A. J. P. White, *Chem. Commun.*, 2006, 1442–1444.

74 C. Hansch, A. Leo and R. W. Taft, *Chem. Rev.*, 1991, **91**, 165–195.

75 L. Cui, G. Zhang and L. Zhang, *Bioorg. Med. Chem. Lett.*, 2009, **19**, 3884–3887.

76 M. N. Hopkinson, A. Tessier, A. Salisbury, G. T. Giuffredi, L. E. Combettes, A. D. Gee and V. Gouverneur, *Chem. Eur. J.*, 2010, **16**, 4739–4743.

77 N. P. Mankad and F. D. Toste, *J. Am. Chem. Soc.*, 2010, **132**, 12859–12861.

78 A. Iglesias and K. Muñiz, *Chem. Eur. J.*, 2009, **15**, 10563–10569.

79 T. De Haro and C. Nevado, *J. Am. Chem. Soc.*, 2010, **132**, 1512–1513.

80 M. Hofer and C. Nevado, *Tetrahedron*, 2013, **69**, 5751–5757.

81 L. Marchetti, A. Kantak, R. Davis and B. DeBoef, *Org. Lett.*, 2015, **17**, 358–361.

82 M. Hofer and C. Nevado, *Eur. J. Inorg. Chem.*, 2012, 1338–1341.

83 N. P. Mankad and F. D. Toste, *J. Am. Chem. Soc.*, 2010, **132**, 12859–12861.

84 A. Collado, J. Bohnenberger, M.-J. Oliva-Madrid, P. Nun, D. B. Cordes, A. M. Z. Slawin and S. P. Nolan, *Eur. J. Org. Chem.*, 2016, **2**, 4111–4122.

85 A. C. Hillier, W. J. Sommer, B. S. Yong, J. L. Petersen, L. Cavallo and S. P. Nolan, *Organometallics*, 2003, **22**, 4322–4326.

86 T. De Haro and C. Nevado, *J. Am. Chem. Soc.*, 2010, **132**, 1512–1513.

87 A. Kar, N. Mangu, H. M. Kaiser, M. Beller and M. K. Tse, *Chem. Commun.*, 2008, 386–388.

88 V. Lavallo, G. D. Frey, S. Kousar, B. Donnadieu and G. Bertrand, *Proc. Natl. Acad. Sci.*, 2007, **104**, 13569–13573.

89 R. M. Moriarty, R. K. Vaid and G. F. Koser, *Synlett*, 1990, 365–383.

90 L. Fra, A. Millán, J. A. Souto and K. Muñiz, *Angew. Chem. Int. Ed.*, 2014, **53**, 7349–7353.

91 D. A. Singleton and A. A. Thomas, *J. Am. Chem. Soc.*, 1995, **117**, 9357–9358.

92 J. Bigeleisen and M. Wolfsberg, in *Advances in Chemical Physics, Volume 1*, eds. I. Prigogine and P. Debye, John Wiley & Sons, New York, 1958, p. 38.

93 V. V. Zhdankin, C. J. Kuehl and A. J. Simonsen, *Tetrahedron Lett.*, 1995, **36**, 2203–2206.

94 V. V. Zhdankin, C. J. Kuehl and A. J. Simonsen, *J. Org. Chem.*, 1996, **61**, 8272–8276.

95 K. C. Caster, A. S. Rao, H. R. Mohan, N. A. McGrath and M. Brichacek, in *Encyclopedia of Reagents for Organic Synthesis*, John Wiley & Sons, New York, 2012.

96 T. Umemoto and Y. Gotoh, *Bull .Chem. Soc. Jpn.*, 1987, **60**, 3307–3313.

97 D. M. Hossain and T. Kitamura, *J. Org. Chem.*, 2005, **70**, 6984–6986.

98 T. Corrie, PhD Thesis, The University of Edinburgh, 2017.

99 J. A. Gonzalez, O. M. Ogba, G. F. Morehouse, N. Rosson, K. N. Houk, A. G. Leach, P. H.-Y. Cheong, M. D. Burke and G. C. Lloyd-Jones, *Nat. Chem.*, 2016, **8**, 1067–1075.

100 P. D. Boyer and H. L. Segal, *A Symposium on the Mechanism of Enzyme Action*, John Hopkins Press, Baltimore, 1954.

101 E. Ackerman and R. L. Berger, *Biophys. J.*, 1963, **3**, 493–505.

102 O. J. Koeppe, P. D. Boyer and M. P. Stulberg, *J. Biol. Chem.*, 1956, **219**, 569–583.

103 K. H. Mok, T. Nagashima, I. J. Day, J. A. Jones, C. J. V. Jones, C. M. Dobson and P. J. Hore, *J. Am. Chem. Soc.*, 2003, **125**, 12484–12492.

104 K. H. Mok, L. T. Kuhn, M. Goez, I. J. Day, J. C. Lin, N. H. Andersen and P. J. Hore, *Nature*, 2007, **447**, 106–109.

105 G. F. Koser and R. H. Wettach, *J. Org. Chem.*, 1977, **42**, 1476–1478.

106 T. S. Teets and D. G. Nocera, *J. Am. Chem. Soc.*, 2009, **131**, 7411–7420.

107 M. Bonamico, G. Dessy, C. Furlani and F. M. Capece, *Acta Crystallogr.*, 1973, **B29**, 1737–1739.

108 M. Bonamico and G. Dessy, *Acta Crystallogr.*, 1973, **B29**, 1735–1736.

109 M. P. Robinson and G. C. Lloyd-Jones, *ACS Catal.*, 2018, **8**, 7484–7488.

110 M. Stodulski, A. Goetzinger, S. V. Kohlhepp and T. Gulder, *Chem. Commun.*, 2014, **50**, 3435–3438.

111 C. Nottingham, V. Barber and G. C. Lloyd-Jones, *Org. Synth.*, 2019, **96**, 150–178.

112 P. Roembke, H. Schmidbaur, S. Cronje and H. Raubenheimer, *J. Mol. Catal. A Chem.*, 2004, **212**, 35–42.

113 R. Uson, A. Laguna and M. Laguna, *Inorg Synth*, 1989, vol. 26.

114 P. De Frémont, R. Singh, E. D. Stevens, J. L. Petersen and S. P. Nolan, *Organometallics*, 2007, **26**, 1376–1385.